EXPLORING GRAVITY THEORIES WITH GRAVITATIONAL WAVES AND COMPACT OBJECTS

Thesis submitted for the degree of
"Doctor Philosophiæ"

24 October 2008

CANDIDATE

Enrico Barausse

SUPERVISORS

Luciano Rezzolla and John C. Miller

International School for Advanced Studies
Via Beirut 2-4, 34014 Trieste, Italy.

E-mail: barausse@sissa.it

a Elena

If you can dream - and not make dreams your master,
If you can think - and not make thoughts your aim

("If", R. Kipling)

Abstract

This thesis is devoted to the study of tests of General Relativity which could be performed using astrophysical observations of stars or compact objects. The thesis consists of two parts.

In the first one, I have investigated how the future gravitational wave observations by the space-based detector LISA will permit mapping the spacetime of the supermassive black holes which are thought to reside in galactic centres. In particular, I have analysed the dynamics of a stellar black hole orbiting around a supermassive black hole and have investigated under which conditions the gravitational wave signal emitted by such a system can allow one to detect the presence of an accretion torus around the supermassive black hole. I have also studied the motion of a stellar black hole in the very strong field region of a nearly extreme supermassive black hole: contrary to our expectations and to suggestions present in the literature, we have found that although the motion presents peculiar characteristics, the emitted gravitational waves do not retain an observable imprint of the almost maximal rotation of the supermassive black hole. Also, I considered black hole binaries with arbitrary masses and spins. Although the coalescence of such systems can be studied only with numerical simulations, I have derived a compact analytic formula for the spin of the final remnant. This formula is in agreement with all the numerical simulations available to date.

In the second part, I have investigated the viability of two phenomenological theories of gravity alternative to General Relativity: $f(R)$ gravity in the Palatini variational formalism and Gauss-Bonnet gravity. While these two theories have been introduced to explain the cosmological acceleration without introducing Dark Energy, little attention has been paid to whether they are consistent with other astrophysical data. To partially fill this gap, I have studied non-vacuum static spherically symmetric solutions in Palatini $f(R)$ gravity, showing that for widely-used equations of state they all present a curvature singularity at the surface and giving some insight on the physical reason behind the onset of this singularity, and I have derived the parameterised post-Newtonian expansion of Gauss-Bonnet gravity, showing that it passes all of the solar system tests. Finally, I briefly present some work in progress aiming at testing modified gravity theories using gravitational wave observations, and discuss future research prospects.

Collaborations

The research presented in this thesis was mainly conducted in SISSA-International School for Advanced Studies between November 2004 and October 2008. This thesis is the result of my work, as well as the outcome of scientific collaborations stated below, except where explicit reference is made to the results of others.
The content of this thesis is based on the following papers:

- Chapter 2:
  - E. Barausse, *Relativistic dynamical friction in a collisional fluid*, Mon. Not. Roy. Astron. Soc. **382**, 826 (2007) [arXiv:0709.0211 astro-ph]
- Chapter 3:
  - E. Barausse and L. Rezzolla, *The influence of the hydrodynamic drag from an accretion torus on extreme mass ratio inspirals*, Phys. Rev. D **77**, 104027 (2008) [arXiv:0711.4558 gr-qc]
- Chapter 4:
  - E. Barausse, L. Rezzolla, D. Petroff and M. Ansorg, *Gravitational waves from extreme mass ratio inspirals in non-pure Kerr spacetimes*, Phys. Rev. D **75**, 064026 (2007) [arXiv:gr-qc/0612123]
  - E. Barausse, *EMRIs in non-pure Kerr spacetimes*, AIP Conf. Proc. **873**, 264 (2006)
- Chapter 5:
  - E. Barausse, S. A. Hughes and L. Rezzolla, *Circular and non-circular nearly horizon-skimming orbits in Kerr spacetimes*, Phys. Rev. D **76**, 044007 (2007) [arXiv: 0704.0138 gr-qc]
- Chapter 6:
  - L. Rezzolla, E. Barausse, E. N. Dorband, D. Pollney, C. Reisswig, J. Seiler and S. Husa, *On the final spin from the coalescence of two black holes*, Phys. Rev. D **78**, 044002 (2008) [arXiv:0712.3541 gr-qc].

- Chapter 8:
  - E. Barausse, T. P. Sotiriou and J. C. Miller, *A no-go theorem for polytropic spheres in Palatini $f(R)$ gravity*, Class. Quant. Grav. **25**, 062001 (2008) [arXiv:gr-qc/0703132]
  - E. Barausse, T. P. Sotiriou and J. C. Miller, *Curvature singularities, tidal forces and the viability of Palatini $f(R)$ gravity*, Class. Quant. Grav. **25**, 105008 (2008) [arXiv:0712.1141 gr-qc]
  - E. Barausse, T. P. Sotiriou and J. C. Miller, *Polytropic spheres in Palatini f(R) gravity*, EAS Publications Series **30**, 189 (2008).
- Chapter 9:
  - T. P. Sotiriou and E. Barausse, *Post-Newtonian expansion for Gauss-Bonnet Gravity*, Phys. Rev. D **75**, 084007 (2007) [arXiv:gr-qc/0612065]
- Chapter 10:
  - E. Barausse and T. P. Sotiriou, *Perturbed Kerr Black Holes can probe deviations from General Relativity*, Phys. Rev. Lett. **101**, 099001 (2008) [arXiv:0803.3433 gr-qc].

Contents

Preface

The first problem that I faced when I started to write this thesis, which presents the research that I conducted in SISSA between November 2004 and October 2008, was the choice of the title. When I arrived in Trieste, I was a (wanna-be) cosmologist. I wanted to know where the Universe is coming from and why, where it is going, how it will end. A bit ingenuous perhaps, but this is why we all have become astrophysicists in the first place.

Of course, I soon got the confirmation that I was not good enough to answer these questions... But I did not lose heart, and I remembered Galileo: "Io stimo più il trovar un vero, benché di cosa leggiera, che 'l disputar lungamente delle massime questioni senza conseguir verità nissuna"[1]. Perhaps I could do something useful anyway, maybe just a tiny piece in our understanding of the Universe, but it would be my own one. That was the moment when I became interested in something more "down to Earth" like gravitational waves. Something so "trivial" that they must exist, otherwise we will have to rewrite gravity books and the whole history of the Universe...

That is how the main branch of my PhD research, which was about sources of gravitational waves for the future space-based detector LISA, started off. But one nice day I moved to an office close to Thomas Sotiriou's, who soon re-infected me with his contagious enthusiasm for deep questions. That was the start of the second branch of my PhD work, the one about testing phenomenological theories of gravity which can "explain" the cosmological acceleration without introducing Dark Energy but modifying General Relativity.

I think that the only connection between these two lines of research is that they were both concerned with exploring gravity on the lengthscale of stars, stellar-mass black holes or supermassive black holes. In spite of this loose connection, there is a major difference between the two approaches. The one about gravitational wave sources for LISA assumes that General Relativity is the correct theory of gravity and works out some consequences of this assumption, which might be observable by gravitational wave detectors. However, this is no more than a consistency test of the theory. In order to really understand

[1] "I hold in higher esteem to find a truth, even a small one, rather than disputing endlessly about big questions without obtaining any results".

whether General Relativity is the correct theory of gravity, we should compare its predictions with those of *other* gravity theories: this is indeed the issue which I tried to address in the second branch of my research.

Essentially because of this major conceptual difference, I have decided to keep the two parts of which this thesis is made somewhat distinct. In the first part, after a brief overview of the LISA mission (chapter 1), I have considered the future observations of the gravitational waves emitted by stellar-mass black holes orbiting around the supermassive black holes which are thought to reside in galactic centres, and examined whether these observations can permit mapping the spacetime of the supermassive black holes. In particular, in chapter 2 I have examined the mechanisms which can affect the dynamics of the stellar-mass black hole, focusing in particular on the dynamical friction exerted by matter which could be present around the supermassive black hole. In chapter 3, I have applied the results of chapter 2 to the study of the inspiral of a stellar-mass black hole into a supermassive black hole surrounded by a thick accretion disk (*i.e.,* a torus), and I have investigated under which conditions the gravitational wave signal emitted by such a system can allow one to detect the presence of the disk. In chapter 4, instead, I have considered the purely gravitational effect of a very compact torus surrounding the supermassive black hole, examining its effect on the orbit of the stellar-mass black hole and analysing whether LISA observations of these systems could provide evidence of the presence of such a torus. In chapter 5, I have studied the motion of a stellar-mass black hole in the very strong field region of a nearly extreme supermassive black hole: contrary to my expectations and to some suggestions present in the literature, I have found that although the motion presents peculiar characteristics, the emitted gravitational waves do not retain any peculiar imprint of the almost maximal rotation of the supermassive black hole. In chapter 6, I finally considered black hole binaries with arbitrary masses and spins. Although the coalescence of such systems can be studied only with numerical simulations, I have derived a compact analytic formula for the spin of the final remnant: this formula is in agreement with all of the numerical simulations available to date.

In the second part of this thesis, I have investigated the viability of two phenomenological theories of gravity alternative to General Relativity: Gauss-Bonnet gravity and $f(R)$ gravity in the Palatini variational formalism. While these two theories have been introduced to explain the cosmological acceleration without introducing Dark Energy, little attention has been paid to whether they are consistent with other astrophysical data. To partially fill this gap, after a brief introduction on the motivation for modified theories of gravity (chapter 7), I have studied non-vacuum static spherically symmetric solutions in Palatini $f(R)$ gravity, showing that for widely-used equations of state they all present a curvature singularity at the surface, and giving some insight on the physical reason behind the onset of this singularity (chapter 8). In chapter 9, I have then derived the parameterised post-Newtonian expansion of Gauss-Bonnet gravity, showing that it passes all of the solar system tests. Finally, in a concluding section I briefly present some work in progress aiming at testing modified gravity theories using gravitational wave observations, and I stress how this line of research, which I will pursue in the coming future, offers a potential way of connecting the two lines of research which this thesis is about.

Writing this thesis and developing the work behind it would have been impossible without the help of a number of people. First, I would like to thank my PhD advisors, Luciano Rezzolla and John Miller, for their constant help, patience and encouragement during these years. Special thanks to John for his relentless correction of my English.

Particular thanks to my collaborators Thomas Sotiriou, Scott Hughes, David Petroff and Marcus Ansorg for their hard work on our common projects. It has really been a great pleasure for me to collaborate with them. I am also very grateful to Leor Barack and Monica Colpi, my thesis examiners, for reviewing this manuscript and for their useful suggestions and comments.

SISSA has provided an ideal environment for conducting my research over the last four years: I would like to thank all of the Astrophysics and Astroparticle Sectors for contributing to that. Very special thanks to Michael Cook, Christiane Frigerio-Martins, Kostas Glampedakis (and his Romanian lady...:-)), Luca Naso, Christoph Rahmede, Andrew Schurer, Thomas Sotiriou and Marcos Valdes, for all the fun we had together, the pizzas and the bets, the football games and the hangovers. I'll keep your faces locked in my heart.

But most of all, I would like to thank Elena and my family for all the strength and serenity that they gave to me in troubles, for their unfaltering faith in me, for their tender love. Without them, I would have never become the person I am.

Trieste, 24 October 2008 Enrico Barausse

Notation

- Unless stated otherwise, I use units in which $G = c = 1$;
- I adopt the signature $(-, +, +, +)$ for the metric and denote the spatial indices (from 1 to 3) by Latin letters and the space-time indices (from 0 to 3) with Greek letters;
- I adopt the definition of the Riemann tensor used in Ref. [1]:

$$R^{\alpha}_{\beta\gamma\delta} = \partial_{\gamma}\Gamma^{\alpha}_{\beta\delta} - \partial_{\delta}\Gamma^{\alpha}_{\beta\gamma} + \Gamma^{\sigma}_{\beta\delta}\Gamma^{\alpha}_{\gamma\sigma} - \Gamma^{\sigma}_{\beta\gamma}\Gamma^{\alpha}_{\delta\sigma} \ ;$$

- $\eta_{\mu\nu}$ is the Minkowski metric;
- I denote covariant derivatives as ∇_{μ} or $_{;\mu}$.
- I denote the determinant of the metric $g_{\mu\nu}$ as g.

Chapter 1

LISA: a tool to explore General Relativity

> Education is an admirable thing, but it is well to remember from time to time that nothing that is worth knowing can be taught.
>
> O. Wilde

1.1 The mission

The *Laser Interferometer Space Antenna* (LISA) [2] is a space mission planned jointly by ESA and NASA (although the NASA involvement in the mission is being currently rediscussed after the priorities in the "Beyond Einstein" program have been redefined [3]). Its purpose consists in detecting gravitational waves in the low-frequency band (from 10^{-5} Hz to 1 Hz), being therefore complementary to ground-based interferometers (such as LIGO [4], Virgo [5], GEO600 [6], Tama300 [7]), which, due to seismic noise, are designed to explore higher frequencies (from 10 Hz to 10^4 Hz).

The launch of LISA is expected to happen around 2017. The experiment setup will include three spacecraft orbiting around the Sun approximately 20 degrees behind the Earth, forming a nearly equatorial triangle with sides of 5 million kilometres and inclined 60 degrees to the Earth's ecliptic plane (see Fig. 1.1). Each spacecraft is equipped with two lasers working in a "transponder mode". Let us consider for instance spacecraft 1 (but the other two spacecraft obviously work in the same way). Spacecraft 1 sends a beam to spacecraft 2 and another beam to spacecraft 3. The laser in spacecraft 2 (spacecraft 3) is phase-locked to the incoming beam and returns a high-power beam to spacecraft 1, where this returning beam can be compared to the corresponding local beam. The phase

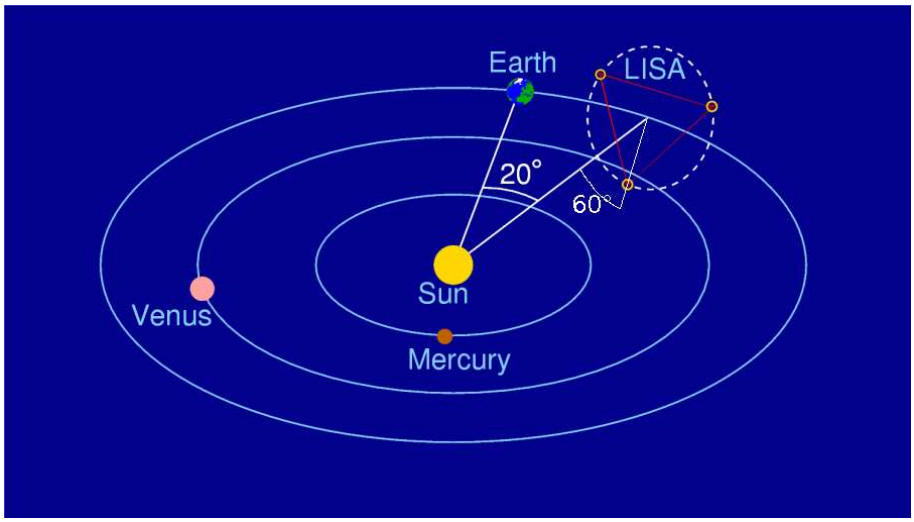

Figure 1.1: *A schematic view of the LISA constellation. Credit: Max Planck Institute for Gravitational Physics (Albert Einstein Institute)/Einstein Online.*

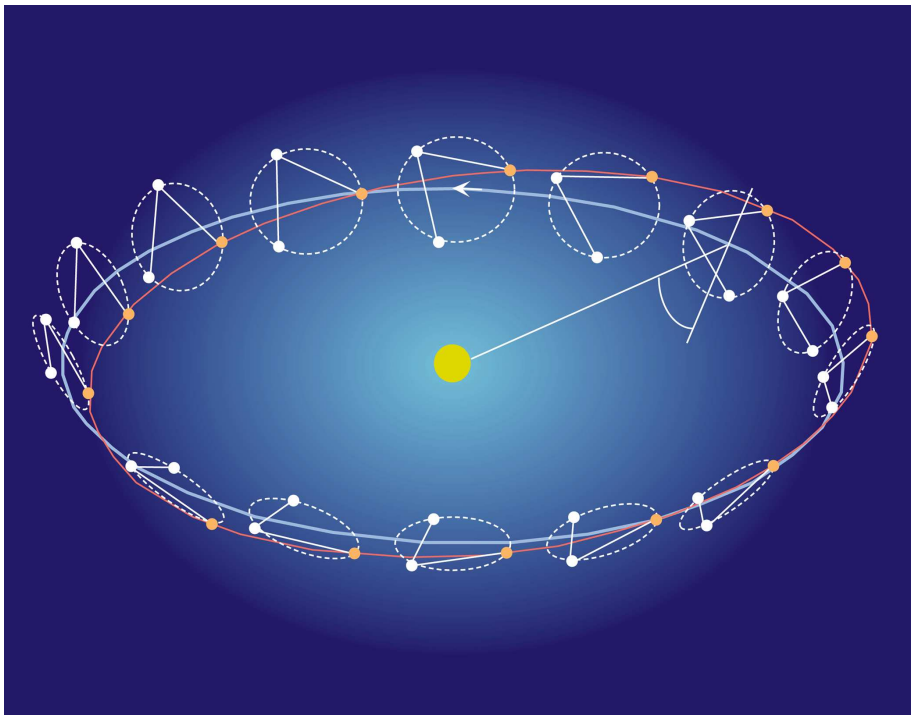

Figure 1.2: *The annual motion of the LISA constellation: the orange line represents the orbit of one spacecraft. From* `http://lisa.nasa.gov/`

difference between the beam returned by spacecraft 2 and the corresponding local beam is then subtracted from the phase difference between the beam returned from spacecraft 3 and the corresponding local beam. Therefore, each LISA arm will work in practice like the arm of a Michelson-Morley interferometer, with the laser phase-lock working as the mirror (the use of lasers in transponder mode instead of mirrors ensures that the beam is sufficiently strong when returning to the emitting spacecraft). LISA will therefore work as a three-arm interferometer, but it is clear that only two of them will be independent. Note that the presence of two independent arms will allow LISA to measure not only the amplitude of gravitational waves, but also their polarisation.

For the experiment to work, it is crucial that the distances between the spacecraft are known with an accuracy ranging from 30 to 800 meters (depending on the frequency of the gravitational wave signal) [8] during the mission lifetime (which will probably be of the order of 1-5 years), in spite of these distances being as large as 5 million kilometres. The existence of orbits particularly suitable for this purpose was first discovered by Vincent and Bender [9] (see also references [10] for further discussion). The key point is that each spacecraft moves along an inclined and eccentric orbit (see Fig. 1.2, in which the orbit of a single spacecraft is denoted by an orange line): it is possible to show that with an appropriate choice of the orbital parameters, the spacecraft maintain their distances constant to linear order in the orbital eccentricities. The changes in the distance due to effects which are of higher order in the eccentricity cause only low-frequency disturbances, which do not compromise the experiment. Note also that the LISA formation changes orientation over one year (see again Fig. 1.2): this makes it possible to measure the position of a source of gravitational waves in the sky.

Moreover, the laser emitters have to move exactly along free-fall orbits, in spite of possible disturbances such as magnetic fields, solar wind, *etc.*, in order to abate the high-frequency noise, which would jeopardize the experiment. To this purpose, the optical bench of each spacecraft is equipped with a proof mass, which is protected from disturbances thanks to careful design and which is allowed to free-fall. A housing around each mass senses its position relative to the spacecraft, which can adjust its position thanks to a system of thrusters.

1.2 Gravitational waves: basic concepts

Gravitational waves are spacetime perturbations which have the characteristic of propagating as waves (as opposed for instance to a Newtonian potential, which does not propagate because it satisfies the Poisson equation). As an example, let us briefly recall gravitational waves in a flat background. Let us write the metric as the Minkowski metric $\eta_{\mu\nu}$ plus a small perturbation $h_{\mu\nu}$, and assume that the stress-energy tensor of matter, $T_{\mu\nu}$, is also small (*i.e.* of the same order as $h_{\mu\nu}$). Linearising the Einstein equations, one easily gets equations for $h_{\mu\nu}$. What we are interested in, however, is the transverse and traceless ("TT") part of the spatial perturbation h_{ij}, which we denote by $h_{ij}^{\rm TT}$. This TT perturbation, which is what we call a gravitational wave, can be shown to be gauge invariant and

satisfies the gauge conditions

$$\delta^{ki}\partial_k h_{ij}^{\rm TT} = 0\,, \tag{1.1}$$

$$\delta^{ij} h_{ij}^{\rm TT} = 0\,, \tag{1.2}$$

where δ_{ij} is the Kronecker delta. It is also possible to get an explicit expression for the TT perturbation in terms of the full spatial perturbation h_{ij}:

$$h_{ij}^{\rm TT} = P_i^k P_j^l h_{kl} - \frac{1}{2} P^{kl} h_{kl} P_{ij}\,, \tag{1.3}$$

where Latin indices are raised and lowered using the Kronecker delta and $\boldsymbol{P}$ is the projection operator

$$P_{ij} \equiv \delta_{ij} - \partial_i \partial_j \nabla^{-2}\,, \tag{1.4}$$

($\partial_i \equiv \partial/\partial x^i$ and ∇^{-2} is the inverse of the Laplacian operator $\nabla^2 \equiv \delta^{ij}\partial_i\partial_j$[1]).

Using the TT gauge conditions (1.1) and the linearised Einstein equations, it is easy to see that $h_{ij}^{\rm TT}$ satisfies the wave equation

$$\Box h_{ij}^{\rm TT} = -16\pi T_{ij}^{\rm TT}\,, \tag{1.5}$$

where $\Box = \eta^{\mu\nu}\partial_\mu\partial_\mu$ and $T_{ij}^{\rm TT}$ is the TT part of the stress-energy tensor (this gauge invariant quantity is defined in the same way as $h_{ij}^{\rm TT}$).

A solution to this equation, at distances sufficiently far from the source, which is assumed to be located around the origin, and under the hypothesis that the internal motions of the matter source are slow, can be written in terms of the quadrupole moment $Q_{ij}(t) = \int T_{00}(t,\boldsymbol{x}) x^i x^j d^3x$:

$$h_{ij}^{\rm TT}(t,\boldsymbol{x}) = 2P_i^k P_j^l \frac{\ddot{Q}_{kl}(t-|\boldsymbol{x}|)}{|\boldsymbol{x}|} - P^{kl}\frac{\ddot{Q}_{kl}(t-|\boldsymbol{x}|)}{|\boldsymbol{x}|} P_{ij}\,, \tag{1.6}$$

where an overdot denotes a derivative with respect to time.[2]

Far away from the source and in a limited spatial region, the spherical gravitational wave (1.6) can be approximated with a plane wave. Assuming that the propagation direction is $\boldsymbol{n} = \boldsymbol{e}_z$ (propagation along the z-axis; $\boldsymbol{e}_k$, with $k = x, y, z$, denotes unit vectors in the axis directions), the plane gravitational wave tensor can be written as

$$\boldsymbol{h}^{\rm TT} = h^+(t-z)\boldsymbol{e}^+ + h^\times(t-z)\boldsymbol{e}^\times\,, \tag{1.7}$$

[1] The inverse of the Laplacian is well-defined for functions that go to zero sufficiently fast at infinity.

[2] In order to derive eq. (1.6), one has to use the conservation of the stress-energy tensor with respect to the background (Minkowski) metric, $\partial_\nu T^{\mu\nu} = 0$. Because $\partial_\nu T^{\mu\nu} = 0$ is equivalent to the geodesic equation of the background spacetime, eq. (1.6) is not, rigorously speaking, valid for a source moving under the effect of gravity (*e.g.* a binary system of stars). Nevertheless, it turns out that eq. (1.6) is a good approximation even in that case, if the source motion is Newtonian (*cf.* refs. [1, 11]) or, in some cases, even in the strong-gravity regime [12].

where the polarisation tensors $\boldsymbol{e}^+$ and $\boldsymbol{e}^\times$ are defined as

$$\boldsymbol{e}^+ \equiv \boldsymbol{e}_x \otimes \boldsymbol{e}_x - \boldsymbol{e}_y \otimes \boldsymbol{e}_y \,, \tag{1.8}$$

$$\boldsymbol{e}^\times \equiv \boldsymbol{e}_x \otimes \boldsymbol{e}_y + \boldsymbol{e}_y \otimes \boldsymbol{e}_x \,. \tag{1.9}$$

$$\tag{1.10}$$

The gravitational wave is said to be *linearly polarised* along the direction identified by the polarisation angle λ in the (x, y)-plane if $h^+(t-z) = h(t-z)\cos 2\lambda$ and $h^\times(t-z) = h(t-z)\sin 2\lambda$ (*i.e.*, h^+ and $h^\times$ oscillate in phase or in phase opposition, but can have different amplitudes), whereas the polarisation is *circular* if $h^+(t-z) = h(t-z)$ and $h^\times(t-z) = \pm i h(t-z)$ (*i.e.*, h^+ and $h^\times$ oscillate with a phase difference of $\pm\pi/2$, but with the same amplitude). If neither of these conditions is satisfied, the polarisation is *elliptical*.

The polarisation of the gravitational wave depends on the inclination of the source with respect to the line of sight to the observer. This can be easily understood by applying the quadrupole formula (1.6) to the case of a binary system in circular motion with masses m_1 and m_2 and separation R. If $R \gg m \equiv m_1 + m_2$, the motion of the system is governed by Newtonian gravity and the revolution frequency is $\Omega = (m/R^3)^{1/2}$. Using then eq. (1.6), in a region sufficiently small so as to be able to approximate the gravitational wave with a plane one, we have

$$\begin{aligned} h^+ &= \frac{2m_1 m_2}{rR}(1+\cos^2\theta)\cos[2\Omega(t-r)+2\Delta\phi]\,, \\ h^\times &= -\frac{4m_1 m_2}{rR}\cos\theta\sin[2\Omega(t-r)+2\Delta\phi]\,, \end{aligned} \tag{1.11}$$

where θ is the angle between the orbital angular momentum of the binary and the direction to the observer, while the phase $\Delta\phi$ depends on the position of the masses at $t = 0$ and on the orientation of the axes of the observer's frame. Note that in order to derive eq. (1.11) we have used the fact that the projection operator $\boldsymbol{P}$ defined in eq. (1.4) reduces to $P_{ij} = \delta_{ij} - n_i n_j$ for a plane wave with propagation direction $\boldsymbol{n}$. Clearly, the gravitational wave is circularly polarised if the observer sees the source "face-on" (*i.e.*, $\theta = 0, \pi$), while it is linearly polarised if the observer is located "edge-on" (*i.e.*, $\theta = \pi/2$).

1.3 The LISA sensitivity function

The way in which LISA will detect a gravitational wave signal is based on the shift of the laser frequency ν induced by the passage of the wave. This shift has been calculated by Estabrook and Wahlquist [13], basically by solving the null geodesic equation. In particular, if the unit vectors $\boldsymbol{n}$ and $\boldsymbol{\sigma}$ are the propagation directions respectively of the

gravitational wave and of the laser, one can define

$$\cos\theta \equiv \boldsymbol{\sigma}\cdot\boldsymbol{n}\,, \tag{1.12}$$

$$\Psi(t) \equiv \frac{h_{ij}^{\rm TT}\sigma^i\sigma^j}{\sin^2\theta}\,, \tag{1.13}$$

and the frequency-shift at the detector is

$$\frac{\Delta\nu}{\nu} = \frac{1}{2}(1+\cos\theta)\Psi(t) - \cos\theta\,\Psi(t+\tau(1-\cos\theta)/2) - \frac{1}{2}(1-\cos\theta)\Psi(t+\tau)\,, \tag{1.14}$$

where τ is the laser travel time between the end masses of interferometer. The direction $\boldsymbol{\sigma}$ will vary as the interferometer orbits around the Sun with period $T_{\rm orb}$. When calculating the interferometer response to a gravitational wave with period $T_{\rm GW}$, assuming $\boldsymbol{\sigma}$ constant introduces a relative error $(T_{\rm GW}/T_{\rm orb})^2 \ll 1$ in the power spectra [14].

However, the quantity which will be read by the laser interferometer tracking system is not the frequency-shift but the phase-shift ("the number of fringes")

$$\Delta\Phi = \int_0^t \Delta\nu(t')dt'\,. \tag{1.15}$$

The aim of a detector is to measure the phase-shift produced by a gravitational wave signal, in the presence of competing noise. It is this noise which determines the sensitivity of the detector.

In order to introduce the LISA sensitivity function, let us first briefly recall the concept of a power spectrum. If we consider a signal $h(t)$, this is related to its Fourier transform by

$$h(t) = \sqrt{T}\int_{-\infty}^{+\infty}\tilde{h}(f)e^{i2\pi ft}df\,, \tag{1.16}$$

where T is the sampling time and where the normalisation factor $\sqrt{T}$ is introduced to keep the power spectrum roughly independent of time. In fact, if $\tilde{h}(f)$ does not change significantly over a frequency bin of width $1/T$, the variance of $h(t)$ over the time T can be easily calculated to be

$$\begin{aligned}
\langle h^2\rangle_T &= \int_{t=0}^{t=T}\int_{f=-\infty}^{f=+\infty}\int_{f'=-\infty}^{f'=+\infty}\tilde{h}(f)\tilde{h}^*(f')\exp(i2\pi(f-f')t)df'dfdt \\
&= \int_{f=-\infty}^{f=+\infty}\int_{\Delta f=-\infty}^{\Delta f=+\infty}\left[\tilde{h}(f)\tilde{h}^*(f+\Delta f)\exp(-i\pi\Delta fT)\frac{\sin(\pi\Delta fT)}{\pi\Delta f}\right]d\Delta fdf \\
&\approx \int_{-\infty}^{\infty}|\tilde{h}(f)|^2df\times\int_{-\infty}^{+\infty}\exp(-i\pi\Delta fT)\frac{\sin(\pi\Delta fT)}{\pi\Delta f}d\Delta f \\
&\approx \int_0^{\infty}|\tilde{h}(f)|^2df\,,
\end{aligned} \tag{1.17}$$

where the normalisation factor cancels out. As such, defining the power spectrum $S_h(f)$ by means of

$$\langle h^2 \rangle_T \equiv \int_0^\infty S_h(f) df \ , \tag{1.18}$$

one obtains

$$S_h(f) = |\tilde{h}(f)|^2 \ . \tag{1.19}$$

The sensitivity function of a detector is basically the power spectrum of the noise. The main source of *experimental* noise for LISA is given by the laser frequency fluctuations, but this noise can be eliminated by considering suitable combinations of the phase-shifts produced in each of the two independent LISA arms. This is known as "Time Delay Interferometry" (TDI) [15] and amounts to considering, rather than simply the difference between the phase shifts $z_1(t)$ and $z_2(t)$ produced in the two arms, the combination $X(t) = z_1(t) - z_2(t) - z_1(t - 2\tau_2) + z_2(t - 2\tau_1)$ (τ_1 and τ_2 being the laser travel times in the two arms). The cancellation of the laser frequency fluctuations in the quantity $X(t)$ is exact if τ_1 and τ_2 are known exactly, but in practice they only need to be known well enough to make the effect of laser frequency fluctuations negligible with respect to the other sources of noise. More precisely, as we have already mentioned, it turns out that the accuracy with which the arm lengths (and therefore the travel times) need to be known is between 30 and 800 meters depending on the frequency of the gravitational wave signal [8].

Other sources of noise, which cannot be eliminated using TDI techniques, are the acceleration noise from the proof masses (due to external forces), the laser shot noise (due to the quantum nature of the laser photons),the thermal noise in the receiver electronics, the laser pointing errors, *etc.* [14]. Besides these sources of experimental noise, the LISA sensitivity is also affected by the *astrophysical* noise, *i.e.* the sources of gravitational waves which are not resolvable by the instrument and which therefore cause a "confusion" noise. These unresolved sources, as we will see in the next section, are mostly unresolvable white-dwarf binaries and they cause a decrease in the LISA sensitivity at frequencies smaller than ~ 2 mHz [16].

Let us now consider a linearly polarised[3] gravitational wave with amplitude $h(t)$. The amplitude reconstructed from the detector output, $s(t)$, will be the sum of the true amplitude $h(t)$ plus the noise $n(t)$ due to the sources mentioned above:

$$s(t) = h(t) + n(t) \, . \tag{1.20}$$

We define the LISA sensitivity function as

$$h_n(f) \equiv \sqrt{S_n(f)} \, , \tag{1.21}$$

where $S_n(f)$ is the noise power spectrum. A plot of h_n, produced with the online gener-

[3]This is not restrictive because a gravitational wave can always be decomposed into two linearly polarised waves [*cf.* eq. (1.7)].

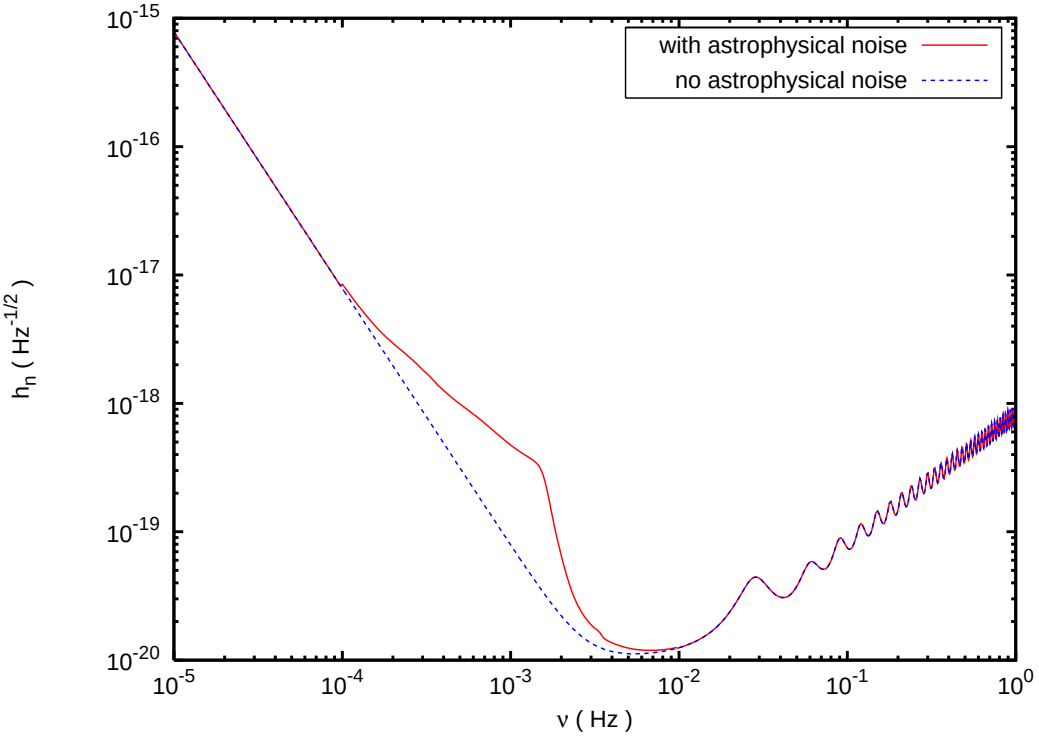

Figure 1.3: *The LISA sensitivity function $h_n(f)$, with and without astrophysical noise. Produced with the online generator [14].*

ator [14], is shown in Fig. 1.3.

To understand the meaning of h_n, let us consider a monochromatic signal $h(t) = \Re[A\exp(2\pi i f_0 t)]$, sampled for a long period T. Using eqs. (1.16) and (1.19), it is easy to check that the power spectrum of the signal goes to zero for $f \neq f_0$ if the sampling time is large, while $S_h(f_0) = |\tilde{h}(f_0)|^2 \approx A^2 T$. As such, in order to understand if a periodic signal is large or small with respect to the noise, its amplitude A has to be compared to $h_n/\sqrt{T}$ rather than simply to h_n [14]. Hence, a long sampling time T can significantly enhance the signal-to-noise ratio (SNR).

Similarly, for a burst signal with characteristic pulse width τ, *i.e.* $h(t) = A\exp[-t^2/(2\tau^2)]$, if $T \gtrsim \tau$ one has

$$\tilde{h}(f) \approx \frac{A}{\sqrt{T}} \int_{-\infty}^{+\infty} \exp[-t^2/(2\tau^2)] \exp(-2\pi i f t) dt = \frac{A\tau}{\sqrt{T}} \sqrt{2\pi} \exp(-2f^2\pi^2\tau^2)\,. \qquad (1.22)$$

From this equation, it follows that the power spectrum of the burst signal is largest when the sampling time T is not much larger than the pulse width τ. In this optimal condition ($\tau \sim T$), eq. (1.22) gives that the maximum of $\tilde{h}$ is $A\sqrt{\tau}$. Therefore, in order to understand

if a burst signal is detectable, one has to compare its amplitude A with $h_n/\sqrt{\tau}$ [14].

Finally, if one considers a stochastic background h of gravitational waves, one has to compare directly the root spectral density $\sqrt{S_h(f)}$ with h_n [14]. The reason is, of course, that both the noise and the stochastic background are (at least approximately) Gaussian random processes and are therefore uniquely identified by their power spectra.

As we will see in the next section, LISA sources usually present small SNRs (with the exception of supermassive black hole mergers, which usually have higher SNRs), but they are very numerous. As such, one needs a way of extracting one particular signal from the "choir" of all the possible signals. This is done by the so called *matched-filtering* technique, which basically consists of cross-correlating the incoming gravitational wave with a bank of theoretical templates representing the expected signal as a function of the source parameters. This will not only allow one to detect the source, but also to extract its properties. However, it should be mentioned that matched-filtering poses serious challenges both in building the templates and in accessing them, because the number of templates that need to be built increases exponentially with the number of parameters involved in the source description (see ref. [17] for a detailed discussion).

We recall that if a signal $s(t)$ is the sum of a gravitational wave $h(t)$ and of some noise $n(t)$ which we assume to be Gaussian, the SNR for a template $\hat{h}(t)$ is given by [18]

$$\frac{S}{N}[\hat{h}] = \frac{\int \hat{h}(t)\, w(t-\tau)\, s(\tau)\, d\tau dt}{\mathrm{rms}\left[\int \hat{h}(t)\, w(t-\tau)\, n(\tau)\, d\tau dt\right]} \tag{1.23}$$

where $w(t)$ is a filter function introduced to suppress the frequencies of the signal at which the noise is too large and "rms" denotes the root mean square over the sampling time. It can be shown, in particular, that the SNR is maximised if $w(t)$ is the Wiener optimal filter (*i.e.* if the Fourier transform of the function $w(t)$ is given by $\tilde{w}(f) = 1/S_n(f)$, with $S_n(f)$ being the power spectrum of the noise). If the noise is Gaussian and there is no gravitational wave signal, $S/N[\hat{h}]$ is clearly a random variable with a Gaussian distribution and a standard deviation of 1. Conversely if $S/N[\hat{h}]$ is so large that it cannot be given by noise alone, a gravitational wave with a shape similar to $\hat{h}$ has been identified with high confidence.

Eq. (1.23) can be put in a more useful form by defining internal product "$(\ ,\ )$" between two signals h_1 and h_2:

$$(h_1, h_2) \equiv 2\int_0^\infty \frac{\tilde{h}_1^*(f)\tilde{h}_2(f) + \tilde{h}_1(f)\tilde{h}_2^*(f)}{S_n(f)} df\ . \tag{1.24}$$

With this definition, it is easy to write

$$\frac{S}{N}[\hat{h}] = \frac{(\hat{h}, s)}{\mathrm{rms}(\hat{h}, n)} = \frac{(\hat{h}, s)}{(\hat{h}, \hat{h})^{1/2}} \approx \frac{(\hat{h}, h)}{(\hat{h}, \hat{h})^{1/2}}\,. \tag{1.25}$$

Note that in order to go from the second to the third expression we have used the fact that for a Gaussian field the ensemble average ("$\langle\ \ \rangle$") coincides with the time average

("$\langle \quad \rangle_T$") if the sampling time is sufficiently long (this characteristic of Gaussian random fields is known as "ergodicity": see for instance ref. [19], paragraph 6.5). Moreover, we have used the identity $\langle (g,n)(n,k)\rangle_T = \langle (g,n)(n,k)\rangle = (g,k)$, which immediately follows from the fact that for a Gaussian field n the different Fourier modes are independent:

$$\langle \tilde{n}(f)\tilde{n}(f')\rangle = \frac{1}{2T} S_n(f)\delta(f+f') \tag{1.26}$$

(the unusual factor $1/T$ on the right-hand side is due to our Fourier transform definition, eq. (1.16)). In order to go instead from the third to the fourth expression of eq. (1.25), we have decomposed $s = h + n$ and used the fact that $(\hat{h}, n)$ averages to zero over long sampling times.

From eq. (1.25) it is eventually clear that the SNR is maximum if $\hat{h} = h$, in which case

$$\frac{S}{N}[h] = (h,h)^{1/2}\,. \tag{1.27}$$

1.4 Sources of gravitational waves for LISA

The simplest sources of gravitational waves are binary systems of compact objects. We have already seen [eq. (1.11)] that a system of two masses m_1 and m_2 in circular Newtonian motion with separation R emits gravitational waves at a frequency which is the double of the orbital frequency $\Omega/(2\pi) = (m/R^3)^{1/2}/(2\pi)$ ($m = m_1 + m_2$). Expressing $f_{\rm GW} = \Omega/\pi$ in Hz, one gets

$$f_{\rm GW} = \frac{6\times 10^4}{\tilde{m}\tilde{R}^{3/2}}\text{Hz}\,, \tag{1.28}$$

where $\tilde{R} = R/m$ and $\tilde{m} = m/M_\odot$. Therefore, in order for the signal to fall within the LISA band ($10^{-5} - 1$ Hz) one needs to have either $\tilde{m} \sim 10^5 - 10^7$ and $\tilde{R} \sim 1 - 100$, or a lower $\tilde{m}$ and a higher separation (for instance, $\tilde{m} \sim 1$ and $\tilde{R} \sim 10^3 - 10^6$).

The first case corresponds to a very compact binary system in which at least one component is a supermassive black hole (SMBH).[4] The other component can be either another SMBH (in which case one has an SMBH binary) or by a stellar mass black hole or compact object (in which case one has an extreme mass-ratio inspiral, EMRI). Let us note that both in the case of an SMBH binary and in the case of an EMRI, the dimensionless separation $\tilde{R}$ needs to be of order $1 - 100$. This means that both SMBH mergers and EMRIs are strong gravity sources and need General Relativity (GR) to be described correctly. This also clarifies why in the case of EMRIs the smaller object must be a compact star or a black hole: in the strong field region of the SMBH the tidal forces become so large as to disrupt ordinary stars.

The second case considered above corresponds instead to a binary system of compact stars (mostly white-dwarf binaries). In this case the separation, expressed in gravitational

[4] As we will see in sections 1.4.2 and 1.4.3, galaxy formation models predict that a considerable number of these sources will be detected by LISA.

radii, is much larger than in the case of SMBH mergers or EMRIs, implying that for describing these sources one does not need full GR because a post-Newtonian expansion is sufficient. However, one should consider that a separation $\tilde{R} \sim 10^3 - 10^6$ is not much larger than the stellar radii (which are $\sim 10^2 - 10^3 M_\odot$ for white dwarfs), so these binaries are actually very compact.

One could also consider binary systems in which at least one of the components is an intermediate mass black hole (IMBH) *i.e.,* one with mass $\sim 10^2 - 10^4 M_\odot$: one could have a binary system of IMBHs, or a system composed of one IMBH and a stellar mass black hole or an SMBH (in both cases, the system would be an intermediate mass-ratio inspiral, IMRI). Nevertheless, too little is presently known about these objects to draw any sound conclusions about their event rate for LISA and even about their very existence (see however ref. [20] for intermediate mass black holes as possible sources for LISA).

In the next subsections we will examine the sources outlined above, referring the reader to ref. [21] and references therein for more details.

1.4.1 Compact stellar binaries

It is possible to show that the gravitational waves emitted by a binary system carry energy and angular momentum. As a result of this loss of energy and angular momentum, the orbital parameters of the system evolve secularly. The situation is particularly simple for a binary on a circular orbit, as in this case the orbit remains circular [22] and the emission of gravitational waves simply decreases the separation between the two components, consequently increasing the revolution frequency. Since the gravitational wave frequency is twice the revolution frequency, this increases too. In particular, in the quadrupole approximation one has [22, 23]

$$\dot{f}_{\rm GW} = \frac{48}{5\pi} \mu m^{2/3} (2\pi f_{\rm GW})^{11/3} \tag{1.29}$$

where $\mu = m_1 m_2/m$ is the reduced mass. Specialising for simplicity to equal masses ($\mu = m/4$), we have

$$\dot{f}_{\rm GW} = 9.2 \times 10^{-18} {\rm Hz/s} \times \tilde{m}^{5/3} \left(\frac{f_{\rm GW}}{1\,{\rm mHz}} \right)^{11/3} . \tag{1.30}$$

Using this formula it is easy to check that the frequency of a stellar compact binary barely changes over the LISA mission lifetime (which will probably be between 1 and 5 years). In particular, since $\dot{f}_{\rm GW} T_{\rm mission}$ is much less than the binwidth $1/T_{\rm mission}$, except at the high end of the band ($f_{\rm GW} \gtrsim 0.01$ Hz), these sources are practically monochromatic as far as LISA is concerned.[5] These sources are therefore quite simple and play an important

[5] Here and in what follows, we use the term "monochromatic" to refer to sources whose frequencies keep constant during the mission's lifetime, as opposed to "chirping" sources, whose frequencies vary significantly over that timescale. It is understood that what we call "monochromatic" sources generally contain more than one frequency, due to the presence of higher order harmonics.

role for LISA, as each galaxy (including the Milky Way) contains millions of them (mostly white dwarf binaries) [24]. Most of these sources will not be resolvable and will give origin, at frequencies $f_{\rm GW} \lesssim 2$ mHz, to the astrophysical noise that we have mentioned in the previous section and that we have plotted in Fig. 1.3. However, between 5000 and 10000 Galactic binaries are expected to be individually resolvable with LISA, and a few of them have been directly identified using X-ray and optical observations and *should* be detectable by LISA: these are known as *guaranteed sources* or *verification binaries*.

1.4.2 Supermassive black hole binaries and mergers

Applying eq. (1.29) to an SMBH binary, it is easy to see that this class of sources is *not* monochromatic, because the frequency rapidly moves across the LISA band in times comparable with the LISA lifetime. As such, SMBH binaries are *chirping* sources, and their evolution can be initially described by means of a post-Newtonian expansion [25]. However, as the SMBH separation gets smaller and smaller, the post-Newtonian expansion breaks down and one needs to solve the full Einstein equations to follow the evolution accurately. A lot of work has been done in this direction in the last ten years, and today several groups around the world can follow numerically the last stages of the inspiral of two spinning SMBHs, their coalescence and the ring-down of the final remnant, producing accurate waveforms that will be suitable for LISA data analysis [26]. (It should be noted that the ring-down of the final black hole produced by the merger could in principle be described by means of semi-analytic techniques, although the matching of the ring-down waveforms with the numerical waveforms describing the merger is problematic [25].) In Fig. 1.4 we show an example of binary SMBH waveform in which the inspiral ("chirp") phase, the merger and the ring-down are clearly visible. This figure uses the data of ref. [27] and shows the gravitational-wave signal $h(t)$ at the detector for a system of two equal-mass Schwarzschild black holes with masses of $10^6 M_\odot$, distance of 1 Mpc, inclination $\theta = 0$ degrees with respect to the observer (*i.e.* the system is observed face-on and the signal is therefore circularly polarised).

SMBH binaries are expected to form when two galaxies, and the dark matter halos which host them, merge. Within the presently favoured scenario for the cosmological evolution, there is a wide consensus that galaxies indeed form hierarchically, *i.e.* through repeated mergers [28]. Since it is nowadays accepted that most galactic nuclei host an SMBH [29], when the two parent halos merge the two SMBHs sink towards the centre of the newly-born galaxy by dynamical friction and there they form a binary [30]. The binary then continues to harden through "slingshot" interactions [31], in which stars intersecting the binary are ejected at velocities comparable to the binary orbital velocity, thus increasing the binding energy of the binary. However, the binary will soon eject all the intersecting stars, thus making the slingshot hardening inefficient. This will cause the binary to stall at a separation of ~ 1 pc, unless other mechanisms intervene to make the binary decay to a separation of ~ 0.01 pc, where gravitational wave emission becomes sufficiently strong so as to be able to drive the evolution of the binary until the merger in a time shorter than the Hubble time. Since there is not, at present, a generally accepted

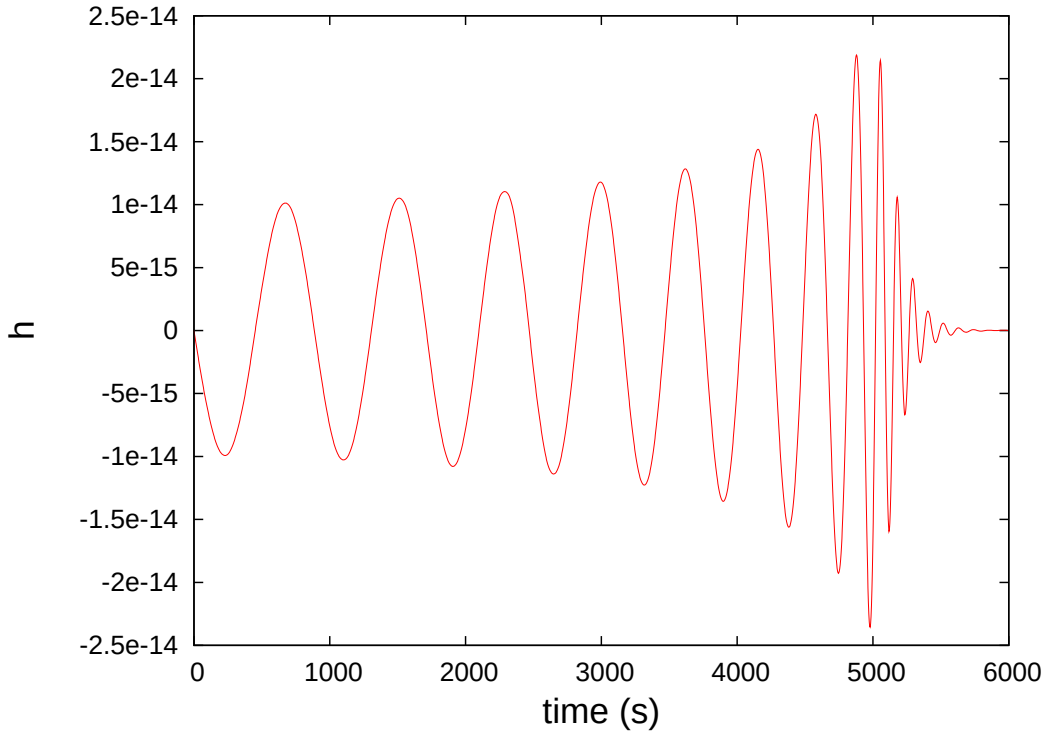

Figure 1.4: *The gravitational wave signal $h(t)$ at the detector for a system of two equal-mass Schwarzschild black holes with masses of $10^6 M_\odot$, distance of 1 Mpc, inclination $\theta = 0$ degrees with respect to the observer (i.e. the system is observed face-on and the signal is therefore circularly polarised). This figure uses the data of ref. [27].*

scenario to overcome the stalling of the binary evolution at ~ 1 pc, this bottleneck is generally referred as "the final parsec problem" [32]. Provided that this problem is somehow solved in nature[6], the expected number of SMBH binary and merger events during the LISA lifetime ranges from ~ 1 to ~ 1000 [33]. The SNR of these events is expected to be very large (SNR$\sim 100 - 1000$) and will permit detecting them up to very high redshifts (even $z \sim 10$ and beyond, if SMBHs are already present) and measuring the masses and spins of the SMBHs involved with an accuracy of $\sim 1\%$ [34].

1.4.3 Extreme mass-ratio inspirals

From eq. (1.29), it is clear that EMRIs cannot be considered monochromatic sources over the LISA lifetime. Actually, the orbit of the satellite (a stellar mass black hole or a com-

[6]It is generally accepted that this is the case, as uncoalesced binaries would result in slingshot ejection of SMBHs when additional SMBHs were brought in by successive mergers, thus resulting in off-centre SMBHs which are not observed [32].

pact object) is indistinguishable from (*i.e.*, it keeps in phase with) a geodesic of the central SMBH only over a timescale of days or at most weeks (this time is known as the *dephasing time* [35]). After this time, the loss of energy and angular momentum through gravitational waves ("radiation reaction") becomes important and makes the satellite inspiral down to the central SMBH in $10^4 - 10^5$ revolutions. From a more general viewpoint, these deviations from geodetic motion are due to the force arising from the interaction of the satellite with the gravitational field produced by itself.[7] This force, usually called *self-force*, contains the effect of the losses of energy and angular momentum via gravitational waves (in its dissipative part: see ref. [36]) and also additional conservative effects (see ref. [37]). However, the self-force is hard to compute because the gravitational potential produced by the satellite diverges as $1/r$ when one approaches the satellite, and a regularization procedure is therefore needed to perform practical calculations (see refs. [38, 39] for a review).

Even on timescales shorter than the dephasing time, though, EMRI orbits can be quite complicated. Kerr geodesics can indeed be characterised by three frequencies: ω_ϕ describing the revolution motion, ω_r describing radial oscillations and ω_θ describing poloidal oscillation.[8] These three frequencies are equal in the Newtonian regime, but in the strong field region of the SMBH one has $\omega_r < \omega_\theta \leq \omega_\phi$ (note that $\omega_\theta = \omega_\phi$ only if the SMBH is Schwarzschild, because in that case the geodetic motion is planar). As a result of this mismatch, the orbit can be rather involved: for instance, if $\omega_r \ll \omega_\phi$ the satellite can "whirl" many times close to the SMBH before "zooming" out to the apoastron [40]. If one can build a model for the secular evolution of these three frequencies[9] and if this model is suitable for tracking the inspiral until the final plunge into the SMBH (*i.e.*, as we were mentioning above, for $10^4 - 10^5$ revolutions), it should be possible to map the spacetime geometry with high precision, measuring the SMBH spin and mass with an accuracy of 10^{-4} [43] and possibly testing its Kerr nature. However, it should be noted that EMRIs are expected to have lower SNR than SMBH binaries and mergers, and for this reason they will be detectable only at redshifts $z \lesssim 1$.

EMRIs can be formed in galactic nuclei either by direct or indirect capture of compact objects by the central SMBH, and these two scenarios produce EMRIs with very different eccentricities. Direct capture happens when compact objects moving on wide orbits in the galactic nucleus are scattered by star-star interactions to an orbit inspiralling into the SMBH under the effect of gravitational wave emission [45]. The semi-major axis of these orbits must be sufficiently small so as to make gravitational wave emission dominant over two-body relaxation (*i.e.*, star-star interaction) [46]. In fact, if the time needed

[7] Actually, the satellite can be thought of as moving along a geodesic of a spacetime the metric of which is given by the background metric (*i.e.*, the Kerr metric due to the central SMBH) plus the metric perturbations (suitably regularized because otherwise they would be divergent at the position of the satellite) produced by the satellite itself.

[8] In the case of equatiorial or circular orbits, it is still possible to define ω_θ and ω_r by taking the limit of small oscillations.

[9] This can be done either by considering only the effect of radiation reaction [41] or, better, the full self-force (see ref. [42] for the self-force driven evolution of circular orbits around non-spinning SMBHs).

for gravitational waves to drive the compact object down to the SMBH (*i.e.,* the inspiral timescale) is large with respect to the timescale of two-body relaxation (*i.e.,* the time needed for star-star interactions to change the energy or the angular momentum of the compact object by an amount of order unity), the captured compact object will start inspiralling under the effect of gravitational waves, but before reaching the SMBH it will most likely be scattered into the horizon on a plunging orbit or back to the outer region of the galactic nucleus. Conversely, if the semi-major axis of the orbit is smaller than $a_{\rm GW} \sim$ a few 0.01 pc, it is possible to show that the inspiral timescale is small with respect to the two-body relaxation timescale and the compact object will give origin to an EMRI. Numerical simulations show that the eccentricity distribution of the EMRIs produced in this manner is skewed towards high eccentricities [46]. This is easy to understand because the inspiral timescale has a strong dependence on the orbital eccentricity e: $t_{\rm inspiral} \propto (1-e^2)^{7/2}$ at high eccentricities [22]. As such, highly eccentric orbits inspiral faster under the effect of gravitational wave emission (this makes sense because if the semi-major axis is large, only orbits with high eccentricity will get sufficiently close to the SMBH so as to emit gravitational waves) and are therefore less likely to be scattered by other stars. Let us note that the fact that direct capture gives origin to high eccentricity EMRIs is intuitive, because the SMBH horizon radius is of order $10^6 M_\odot \sim 5 \times 10^{-8}$ pc, which is tiny with respect to the size of the galactic nucleus ($\sim 1-10$ pc) and to the star-star average separation in the galactic nucleus (~ 0.01 pc [44]). In other words, the space surrounding the SMBH is almost *empty* and the SMBH will only be able to capture compact stars which happen to pass very close to it on very eccentric orbits.

As we have already mentioned, however, two body-relaxation not only determines the semi-major axis $a_{\rm GW}$ under which gravitational wave emission becomes the dominant mechanism affecting the orbital evolution, but also plays another important role in direct capture rates, because it continously scatters new stars into orbits with semi-major axis smaller than $a_{\rm GW}$, thus giving rise to new EMRI events. This process is known as *loss cone replenishment* [45] and is clearly crucial for event rate calculations. For this reason, any process which changes the relaxation time will have an important effect on EMRI direct capture rates. This is indeed the case of *resonant relaxation* [48]. The idea behind this mechanism is simple. Star interactions are not random, as is assumed when calculating the standard two-body relaxation timescale, because the relaxation timescale is much larger than the orbital periods of the stars. As such, the gravitational interaction between stars is *periodic* on timescales shorter than the relaxation time (which is ~ 1 Gyr in galactic nuclei). On a timescale larger than the orbital period and shorter than the relaxation time one can then imagine to "smooth" the mass of each star over its orbit. In other words, one can represent each star by a wire whose mass is the stellar mass, whose shape is the shape of the orbit and whose linear mass density is inversely proportional to the local velocity of the star. Resonant relaxation consists indeed in the gravitational interaction of these wires, which exert mutual torques leading to a decrease of the relaxation time. However, it is not currently known whether this will lead to an increase or a decrease of the EMRI direct capture rate. State-of-the-art simulations seem to suggest that this rate should increase and should be between 1 and 1000 events during LISA's lifetime [17].

However, if resonant relaxation should be larger than assumed in these simulations, the event rate would decrease, settling eventually to zero [49].

Another process which affects EMRI direct capture is *mass segregation* [50]. While the details of this mechanism are quite technical (a rigorous treatment requires solving the Fokker-Planck equation for the stellar distribution function in the presence of two-body relaxation and different star species), the bottom line is easy to understand. When stars interact gravitationally, they tend to have the same kinetic energy (*equipartition of energy*). Although equipartition is never reached in a star cluster, this tendency causes the most massive stars to sink to the centre, where velocities are smaller[10]. This phenomenon is called mass segregation and plays an important role for direct capture of EMRIs. For instance, stellar black holes are more massive than neutron stars or white dwarfs and they are therefore more numerous near the SMBH: this makes stellar-mass black-hole EMRIs more frequent than compact-star EMRIs.

Other astrophysical processes that could produce EMRIs are the so-called "indirect capture processes". These include stellar formation in gaseous self-gravitating accretion disks [51] and tidal disruption of binaries by the SMBH (a binary may be scattered on a very eccentric orbit passing close to the SMBH: as a result of tidal forces, one star is ejected at very high velocity, while the other star gets tightly bound to the SMBH) [52]. The event rates of these processes are very uncertain, but they could be comparable with that of the direct capture process. Moreover, and differently from the case of direct capture EMRIs, these scenarios produce EMRIs with small eccentricities, thus giving the possibility of obtaining information about galactic dynamics using only the EMRI eccentricity distribution observed by LISA.

[10] For instance, in a self-gravitating Newtonian sphere with constant density, the velocity increase linearly with the distance from the centre

Chapter 2

Relativistic dynamical friction in a collisional fluid

Karma police
arrest this man
he talks in maths
he buzzes like a fridge
he's like a detuned radio

Radiohead (Karma Police)

I will now introduce some technical tools that I will need in chapter 3 to study EMRIs in a system consisting of a central SMBH and a thick accretion disk. In particular, in this chapter I will study one of the most important effects that influence the motion of a body through a fluid, that is *dynamical friction*, focussing on the case in which the body moves at *relativistic* velocities through a *collisional* fluid.

2.1 An introduction to dynamical friction

The mechanism of dynamical friction (DF), which arises because of the gravitational interaction between a massive perturber moving in a medium and its own gravitationally-induced wake, was first studied in collisionless systems by ref. [53], and has had widespread applications in astrophysics (*e.g.,* stars moving in clusters or galaxies, globular clusters in galaxies, galaxies in galaxy clusters, etc.: see ref. [54] section 7.1, and references therein). In particular, the Newtonian dynamical friction drag acting on a perturber of gravitational mass M moving with velocity $\boldsymbol{v}_M$ in a collisionless system of "particles" with gravitational mass m and isotropic velocity distribution $f(v_m) \equiv dN/(d^3x d^3v_m)$ is given [53] by

$$\boldsymbol{F}_{\rm DF} = -16\pi^2 M(M+m)\frac{m\int_0^{v_M} f(v_m)v_m^2 dv_m}{v_M^3}\boldsymbol{v}_M \ln\Lambda \tag{2.1}$$

where $\Lambda \approx b_{\max} v_{\rm typ}^2/(M+m)$, $b_{\max}$ and $v_{\rm typ}$ being respectively the maximum impact parameter and the typical velocity of the particles with respect to the perturber (see also ref. [54] section 7.1 for a derivation). The intuitive reason for the presence of this drag is the fact that the particles are attracted by the perturber, which in the meantime moves: the particles therefore build up a slight density enhancement behind it (the wake). It is the gravitational attraction of the wake that pulls the perturber back. Note that in the case of a perturber moving through a collisionless fluid, dynamical friction is essentially the only drag force acting on the perturber, besides that due to capture of particles by the perturber and that due to gravitational-wave emission (which is usually subdominant because it appears at 2.5 post-Newtonian order: see ref. [55], and also ref. [56] and references therein).

Eq. (2.1) was improved by including post-Newtonian corrections in ref. [57], and was generalised to relativistic velocities, although only in the weak scattering limit, in ref. [58]. The case of a *collimated* flow of collisionless particles of gravitational mass m moving at relativistic speed and impacting on a perturber of gravitational mass M was instead worked out in ref. [59] [eq. (B17)], where it was found that in the rest frame of the perturber the 3-momentum change is given by

$$\left(\frac{d\boldsymbol{p}}{dt}\right)_{\rm DF} = -\frac{4\pi m n_\infty M^2 \gamma^2 (1+v^2)^2}{v^2} \ln\left(\frac{b_{\max}}{b_{\min}}\right) \frac{\boldsymbol{v}}{v}\,, \tag{2.2}$$

where n_∞ is the number density of particles in the flow far away from the perturber and before deflection, $\boldsymbol{v}$ and $\gamma = (1-v^2)^{-1/2}$ are the velocity and the Lorentz factor of the perturber relative to the flow, and $b_{\min}$ is the size of the perturber or the capture impact parameter $b_{\min} \approx 2M(1+v^2)/v^2$ if this is a black hole.

Dynamical friction acts also in collisional fluids, together with the two other effects mentioned above for collisionless systems (*i.e.*, gravitational-wave emission and accretion onto the perturber) and ordinary viscous forces, which are *not* present if the perturber is a black hole but instead act if the perturber is a star[1]. However, unlike in the collisionless case, it presents different features depending on the Mach number of the perturber. The correct behaviour in the supersonic case has long been recognised by several authors: the steady state Newtonian drag on a perturber M moving on a straight line with velocity $\boldsymbol{v}$ relative to a homogeneous fluid with rest-mass density ρ_0 and sound speed $c_s = v/\mathcal{M}$ ($\mathcal{M} > 1$) was found in ref. [62] and in ref. [63] to be

$$\boldsymbol{F}_{\rm DF} = -\frac{4\pi M^2 \rho_0}{v^2} \ln\left[\frac{b_{\max}}{b_{\min}} \frac{\mathcal{M}}{(\mathcal{M}^2-1)^{1/2}}\right] \frac{\boldsymbol{v}}{v}\,, \tag{2.3}$$

where the maximum impact parameter $b_{\max}$ is the Jeans length (or the size of the medium

[1]The drag due to ordinary viscosity is given, for non-relativistic velocities and in the laminar regime, by Stokes' law: $\boldsymbol{F}_{\rm Stokes} = -6\pi\eta\, a\boldsymbol{v}$, a being the radius of the perturber and η the viscosity coefficient. For instance, in a thin accretion disc [60] one has $\eta = \alpha\rho_0 c_s H$, where ρ_0 and c_s are the rest-mass density and the sound velocity in the disc, H is its height and $\alpha \sim 0.1 - 0.4$ [61]. Note that this drag can be calculated independently of the dynamical friction effects considered in this chapter.

if this is smaller than the Jeans length). Note that the dynamical friction drag given by eq. (2.3) is comparable to the drag due to Bondi accretion onto the perturber: the latter is in fact given by $\boldsymbol{F}_{\rm Bondi} = -\boldsymbol{v}\dot{M}$, where $\dot{M} = 4\lambda\pi M^2\rho_0/(v^2+c_s^2)^{3/2}$ [64, 65], λ being a parameter of order unity.

Eq. (2.3) was confirmed by ref. [66] with a finite-time analysis and was generalised to the relativistic case in ref. [59], where it was found that eq. (2.2) remains valid also in the collisional supersonic case if the rest-mass density mn_∞ is replaced by $p+\rho$, p and ρ being the pressure and energy-density of the fluid. The physical reason for the presence of a non-zero drag in the supersonic case is the fact that sound waves can propagate only downwind, inside the Mach cone, producing a non-symmetric pattern of density perturbations, which gives rise to a drag by gravitational interaction.

The subsonic case proved instead to be more elusive. Because sound waves can propagate both downwind and upwind, the drag is expected to be lower than in the supersonic case. In particular, ref. [62] in the Newtonian case and ref. [59] in the relativistic one argued that the drag should be exactly zero for subsonic motion in a homogeneous fluid, because of the upwind-downwind symmetry of the stationary solution for the density perturbations excited by the perturber. However, although a zero drag can be a useful approximation in many cases, this result does not rigorously hold if one performs a finite-time analysis [66]. In fact, if the perturber is formed at $t=0$ and moves at non-relativistic subsonic speed on a straight line in a homogeneous fluid, the density perturbations are given by the stationary solution found by ref. [62] only inside a sphere of radius $c_s t$ centred on the initial position of the perturber, and are instead exactly zero (because of causality) outside. The upwind-downwind symmetry of the stationary solution is therefore broken and the perturber experiences a finite drag, which reads [66]

$$\boldsymbol{F}_{\rm DF} = -\frac{4\pi M^2\rho_0}{v^2}\left[\frac{1}{2}\ln\left(\frac{1+\mathcal{M}}{1-\mathcal{M}}\right)-\mathcal{M}\right]\frac{\boldsymbol{v}}{v} \tag{2.4}$$

as long as $(c_s+v)t$ is smaller than the size of the medium. This result was confirmed by numerical simulations [67] and was extended to the case of a perturber moving at non-relativistic speed on a circular orbit in a homogeneous medium by ref. [68]. In particular, ref. [68] found that in the subsonic case the perturber experiences a tangential drag, given roughly by eq. (2.4), and a drag in the radial direction (towards the centre of the orbit), whose contribution to the orbital decay is however subdominant with respect to the tangential drag. Similarly, in the supersonic case the tangential drag is roughly given by eq. (2.3) with $b_{\max}$ equal to the orbital radius, while a radial drag is present but again remains subdominant with respect to the tangential one.

The purpose of this chapter is to generalise to the relativistic case the finite-time drag found by ref. [66] and by ref. [68]. While a Newtonian treatment of dynamical friction is satisfactory in many astrophysical scenarios, relativistic expressions are needed in order to study the interaction of solar-mass compact objects or black holes with the gaseous matter (*e.g.*, an accretion disc) which could be present in the vicinity of an SMBH, where orbital velocities close to that of light are reached. As we have already seen in chapter 1,

these systems are known as extreme mass-ratio inspirals (EMRIs) and are expected to be among the most interesting sources of gravitational waves for LISA, and considerable effort has been spent trying to understand whether different kinds of accretion disc, when present, can produce an observable signature in the emitted gravitational-wave signal. In a series of papers Karas, Subr and Vokrouhlicky considered the interaction between stellar satellites and thin disks [69, 70, 71, 72]. In ref. [72], in particular, Subr and Karas found that the effect of the star-disk interaction on EMRIs dominates over radiation reaction for thin disks, both for non-equatorial orbits crossing the disk only twice per revolution and for equatorial orbits embedded in the disk. The only exceptions to these conclusions come if the satellite is very compact (a neutron star or a black hole) or the disk has a low density (*e.g.*, in the region close to the SMBH if the flow becomes advection-dominated). These results agree with those found by Narayan [73], who focused on Advection Dominated Accretions Flows (ADAFs), which were believed to describe accretion onto "normal" galactic nuclei (*i.e.*, ones much dimmer than AGNs)[2]. Overall, he found that for compact objects and white dwarfs the effect of the hydrodynamic drag is negligible with respect to radiation reaction, whereas it is not negligible for main sequence and giant stars. More recently, Levin [51] has proposed a scenario in which massive stars form in a thin accretion disk in an AGN, ultimately producing stellar-mass black holes embedded in the disk. The small black holes are then dragged towards the (non-rotating) SMBH, but if this is accreting at a rate comparable to the Eddington limit, the drag from the accreting gas will not significantly affect the final part of the inspiral (*i.e.*, at radii smaller than 10 Schwarzschild radii). Finally, Chakrabarti [76, 77], studied instead the orbital evolution of a black hole satellite on a circular equatorial orbit embedded in a disk with a non-Keplerian distribution of angular momentum, and found that the exchange of angular momentum between the disk and the satellite can lead to significant orbital modifications.

Although we do not expect our results to change significantly the picture outlined above for ADAFs or ADIOS's, whose density is too low to make the effect of the hydrodynamic drag, and of dynamical friction in particular, comparable to the effects of gravitational-wave emission even if one includes relativistic corrections, we think that our relativistic corrections could play a more important role, under certain circumstances, for black holes or compact objects moving in higher density environments (Active Galactic Nuclei, quasars, Seyfert galaxies, etc.). In the next chapter, we will apply our results to the case of an accretion flow with a toroidal structure.

While our results rigorously apply only to a non self-gravitating fluid in either a flat background spacetime (in the case of straight-line motion) or the weak field region of a curved spacetime (in the case of circular motion), and additional work may be needed in order to evaluate the effect of a curved background, we argue that such an approximation is suitable at least for a preliminary study of dynamical friction effects on EMRIs (chapter 3). Indeed, for many purposes a similar approximation is adequate to study

[2] Accretion onto "normal" galactic nuclei is now believed to be better described by Advection Dominated Inflow Outflow Solutions (ADIOS) [75]. However, this is not expected to change significantly Narayan's results since ADIOS's, like ADAFs, have very low densities in the vicinity of the SMBH.

gravitational-wave emission by EMRIs around a Kerr SMBH: the flat-spacetime quadrupole formula, combined with geodesic motion for the solar-mass satellite, gives results which are in surprisingly good agreement with rigorously computed waveforms [12].

Our analysis closely follows that of refs. [66] and [68], and we find that their results still hold for relativistic velocities provided that the rest-mass density appearing in the Newtonian formulae is replaced by $p + \rho$ (p and ρ being the pressure and energy-density of the fluid), and a multiplicative factor is included: $\gamma^2(1+v^2)^2$ in the straight-line motion case and for the tangential component of the drag in the circular motion case; $\gamma^3(1+v^2)^2$ for the radial component of the drag in the circular motion case.

2.2 Equations and variables

Let us consider a perturber with gravitational mass M, formed at $t = 0$ and moving in a perfect fluid at rest at the initial position of the perturber[3] and having energy density ρ and pressure p there. We write the metric as a Minkowski background plus some perturbations produced by the presence of the fluid and the perturber: the general form of such a metric is known to be [11, 78, 79, 80]

$$d\tilde{s}^2 = \tilde{g}_{\mu\nu}dx^\mu dx^\nu = -(1+2\phi)\,dt^2 + 2\omega_i dx^i dt \tag{2.5}$$

$$+ \left[\delta_{ij}(1-2\psi) + \chi_{ij}\right] dx^i dx^j\,, \qquad \chi^i{}_i = 0\,, \tag{2.6}$$

where the 3-vector ω_i can be decomposed into a gradient and a divergence-free part,

$$\omega_i = \partial_i \omega^{\parallel} + \omega_i^{\perp}, \qquad \partial^i \omega_i^{\perp} = 0\,, \tag{2.7}$$

while the traceless 3-tensor χ_{ij} can be split in a gradient part, a divergence-free vector part and a (gauge invariant) transverse pure-tensor part,

$$\chi_{ij} = D_{ij}\chi^{\parallel} + \partial_{(i}\chi_{j)}^{\perp} + \chi_{ij}^{\top}\,,\ D_{ij} \equiv \partial_i\partial_j - \frac{1}{3}\delta_{ij}\nabla^2\,,$$
$$\partial^i \chi_i^{\perp} = \partial^i \chi_{ij}^{\top} = \chi_i^{\top i} = 0\,, \tag{2.8}$$

where $\nabla^2 = \delta^{ij}\partial_i\partial_j$. Note that Latin indices are raised and lowered with the Kronecker delta δ_{ij}. Similarly, the stress-energy tensor can be written as

$$T_{\mu\nu}dx^\mu dx^\nu = T_{tt}dt^2 + 2(\partial_i S^{\parallel} + S_i^{\perp})dt dx^i \tag{2.9}$$

$$+ \left[\frac{T}{3}\delta_{ij} + D_{ij}\Sigma^{\parallel} + \partial_{(i}\Sigma_{j)}^{\perp} + \Sigma_{ij}^{\top}\right] dx^i dx^j\,, \tag{2.10}$$

where

$$\partial^i S_i^{\perp} = \partial^i \Sigma_i^{\perp} = \partial^i \Sigma_{ij}^{\top} = \Sigma_i^{\top i} = 0\,. \tag{2.11}$$

[3]Note that this condition can always be satisfied by performing a suitable boost.

Note that the decompositions outlined in eqs. (2.5) and (2.9) are defined unambiguously if the perturbations go to zero sufficiently fast as $r \to \infty$ so as to make the Laplacian operator ∇^2 invertible. As an example, let us consider the case of eq. (2.9). First, calculating $\partial^i T_{0i}$ and using eq. (2.11) one immediately obtains

$$S^{\parallel} = \nabla^{-2}(\partial^i T_{0i})\,, \tag{2.12}$$

$$S_i^{\perp} = T_{0i} - \partial_i S^{\parallel}\,, \tag{2.13}$$

where ∇^{-2} denotes the inverse of the Laplacian ∇^2. Summing over the spatial indices trivially gives

$$T = \delta^{ij} T_{ij}\,, \tag{2.14}$$

and calculating $\partial^i \partial^j T_{ij}$ and $\partial^j T_{ij}$ using eq. (2.11) one easily obtains

$$\Sigma^{\parallel} = \nabla^{-2}\left[\frac{3}{2}\nabla^{-2}\left(\partial^i\partial^j T_{ij}\right) - \frac{1}{2}T\right]\,, \tag{2.15}$$

$$\Sigma_i^{\perp} = 2\nabla^{-2}\left(\partial^j T_{ij} - \frac{1}{3}\partial_i T\right) - \frac{4}{3}\partial_i \Sigma^{\parallel}\,. \tag{2.16}$$

Inserting eqs. (2.14), (2.15) and (2.16) into eq. (2.9), one can finally derive an explicit expression for the gauge invariant transverse traceless perturbation $\Sigma_{ij}^{\top}$. Similar considerations apply to the decomposition (2.5) of the metric.

Deviations of the metric away from a flat background are due to the presence of the fluid, which causes perturbations of dimensionless order $\lesssim \varepsilon_1 = \mathcal{O}(\mathcal{L}/\lambda_J)^2$ [$\mathcal{L}$ being the characteristic size of the medium and $\lambda_J = c_s/(4\pi(p+\rho))^{1/2}$ being a generalised Jeans length], and due to the presence of the perturber, which is expected to cause perturbations of order $\varepsilon_2 = M/r$, where r is the distance from the perturber. Note that the perturbations of the first kind are small if the fluid is not self-gravitating (*i.e.* if $\mathcal{L} \ll \lambda_J$), while those of the second kind in principle diverge if we consider a point-like perturber. In order to retain the validity of the perturbative expansion, we therefore have to introduce a cutoff $r_{\min}$, which is taken to be the size of the star acting as the perturber or, in the case where the perturber is instead a black hole, the "capture" impact parameter $r_{\min} \approx 2M(1+v^2)/v^2$ (*i.e.*, the impact parameter for which a test-particle is deflected by an angle ~ 1 by the black hole). This ensures that ε_2 is small and can be treated as an expansion parameter. The gravitational field produced by the perturber on scales smaller than the cutoff gives rise, when coupled to the fluid, to accretion onto the perturber. This gives additional contributions to the drag, but these effects can easily be calculated separately: see for instance ref. [59] [eq. (2.40)] for the drag-force due to accretion onto a black hole. As we have already mentioned in sec. 1.4.3, when acting directly on the perturber, the gravitational field produced by the perturber itself gives rise instead to the so-called *self-force* (see ref. [38, 39] for a review), the dissipative part of which accounts for the energy and angular momentum lost through gravitational waves.

In order to exploit as much as possible the calculations done in the Newtonian case in

refs. [66] and [68], let us choose the so-called Poisson gauge [81], defined by the conditions $\partial_i \omega^i = \partial_i \chi^{ij} = 0$. In this gauge the perturbed metric is

$$d\tilde{s}^2 = -(1+2\phi)\,dt^2 + 2\omega_i^{\perp} dx^i dt + \left[\delta_{ij}(1-2\psi) + \chi_{ij}^{\top}\right] dx^i dx^j \,, \tag{2.17}$$

and the linearised Einstein equations give

$$\nabla^2 \psi = 4\pi T_{tt} \,, \tag{2.18}$$

$$\partial_t \psi = 4\pi S^{\parallel} \,, \tag{2.19}$$

$$\nabla^2 \omega_i^{\perp} = -16\pi S_i^{\perp} \,, \tag{2.20}$$

$$\nabla^2 \phi = 4\pi(T_{tt} + T) - 3\partial_t^2 \psi \,, \tag{2.21}$$

$$\psi - \phi = 8\pi \Sigma^{\parallel} \,, \tag{2.22}$$

$$\partial_t \omega_i^{\perp} = -8\pi \Sigma_i^{\perp} \,, \tag{2.23}$$

$$\Box \chi_{ij}^{\top} = -16\pi \Sigma_{ij}^{\top} \,, \tag{2.24}$$

where $\Box = \eta^{\mu\nu}\partial_\nu \partial_\mu$. In particular, from the linearised Einstein equations one gets the following relations between the matter fields:

$$\nabla^2 S^{\parallel} = \partial_t T_{tt} \,, \tag{2.25}$$

$$\nabla^2 \Sigma^{\parallel} = \frac{1}{2}(3\partial_t S^{\parallel} - T) \,, \tag{2.26}$$

$$\nabla^2 \Sigma_i^{\perp} = 2\partial_t S_i^{\perp} \,, \tag{2.27}$$

which can also be derived directly from the conservation (to first order) of the stress-energy tensor with respect to the background metric, $\partial_\mu T^{\mu\nu} = 0$.

Let us now write the stress energy tensor as $T_{\mu\nu} = T_{\mu\nu}^{\rm fluid} + T_{\mu\nu}^{\rm pert}$. The stress-energy tensor of the fluid is

$$T_{\mu\nu}^{\rm fluid} = (\tilde{p} + \tilde{\rho})\tilde{u}_\mu \tilde{u}_\nu + \tilde{p}\tilde{g}_{\mu\nu} \,, \tag{2.28}$$

where the perturbed metric $\tilde{g}_{\mu\nu}$ is given by eq. (2.17) and $\tilde{\rho}$, $\tilde{p}$ and $\tilde{u}^\mu$ are the perturbed energy density, pressure and 4-velocity of the fluid:

$$\tilde{\rho} = \rho + \delta\rho \,, \quad \tilde{p} = p + \delta p \,, \tag{2.29}$$

$$\tilde{u}_i = \delta u_i \,, \quad \tilde{u}_t = -1 - \phi \tag{2.30}$$

(the equation for $\tilde{u}_i$ comes about because the fluid is at rest at the initial position of the perturber, while the equation for $\tilde{u}_t$ follows from the normalisation condition $\tilde{g}_{\mu\nu}\tilde{u}^\mu \tilde{u}^\nu = -1$). The stress-energy tensor of the perturber is (see for instance ref. [38])

$$T_{\mu\nu}^{\rm pert}(\boldsymbol{x}, t) = M \frac{\tilde{u}_\mu^{\rm pert} \tilde{u}_\nu^{\rm pert}}{\tilde{u}_{\rm pert}^t \sqrt{-\tilde{g}}} \delta^{(3)}(\boldsymbol{x} - \tilde{\boldsymbol{x}}^{\rm pert}(t)) \,, \tag{2.31}$$

where $\tilde{u}^\mu_{\rm pert}$ and $\tilde{\boldsymbol{x}}^{\rm pert}(t)$ are the perturbed 4-velocity and spatial trajectory of the perturber, which for mathematical purposes is considered to be a point-particle, and $\tilde{g}$ is the determinant of the perturbed metric (2.17). If one expands the trajectory $\tilde{\boldsymbol{x}}^{\rm pert}$ and the 4-velocity $\tilde{u}^\mu_{\rm pert}$ of the perturber as the sum of their unperturbed values $\boldsymbol{x}^{\rm pert}$ and $u^\mu_{\rm pert}$ plus some perturbations due to the presence of the fluid (and therefore of order ε_1) and some perturbations due to the interaction of the perturber with its own gravitational field (and therefore of order ε_2), and notes that $\tilde{g} = -(1+2\phi-6\psi) = -1+\mathcal{O}(\varepsilon_1,\varepsilon_2)$, eq. (2.31) can be written as

$$T^{\rm pert}_{\mu\nu}(\boldsymbol{x},t) = M\frac{u^{\rm pert}_\mu u^{\rm pert}_\nu}{u^t_{\rm pert}}\delta^{(3)}(\boldsymbol{x}-\boldsymbol{x}^{\rm pert}(t))\times[1+\mathcal{O}(\varepsilon_1,\varepsilon_2)]\,. \tag{2.32}$$

Note that because of the presence of the factor $M = r\varepsilon_2$, the stress-energy tensor $T^{\rm pert}_{\mu\nu}$ is an intrinsically first order quantity, and dropping the second order terms, as we have done earlier, we can simply write

$$T^{\rm pert}_{\mu\nu}(\boldsymbol{x},t) = M\frac{u^{\rm pert}_\mu u^{\rm pert}_\nu}{u^t_{\rm pert}}\delta^{(3)}(\boldsymbol{x}-\boldsymbol{x}^{\rm pert}(t))\,. \tag{2.33}$$

Perturbing the expression for the conservation of the baryon number in the fluid,

$$\partial_\mu[(-\tilde{g})^{1/2}\,\tilde{n}\tilde{u}^\mu] = 0 \tag{2.34}$$

($\tilde{n} = n+\delta n$ being the perturbed number density), one gets

$$\partial_t\left(\frac{\delta n}{n}\right) + \partial_i\delta u^i - 3\partial_t\psi = 0\,, \tag{2.35}$$

whereas perturbing the Euler equation

$$\tilde{a}^\mu = \tilde{u}^\alpha\tilde{\nabla}_\alpha\tilde{u}^\mu = -(\tilde{g}^{\mu\nu}+\tilde{u}^\mu\tilde{u}^\nu)\frac{\partial_\nu\tilde{h}}{\tilde{h}} \tag{2.36}$$

[$\tilde{h}\equiv(\tilde{p}+\tilde{\rho})/\tilde{n} = h+\delta h$ is the perturbed specific enthalpy] one obtains

$$\partial_t\delta u^i + \partial_i\phi + \partial_t\omega_i^\perp + c_s^2\partial_i\frac{\delta n}{n} = 0\,, \tag{2.37}$$

where $c_s = (dp/d\rho)^{1/2}$ is the velocity of sound and where we have used the first law of thermodynamics ($\delta h/h = c_s^2\delta n/n$). Combining the divergence of eq. (2.37) and the time derivative of eq. (2.35) and finally using eq. (2.21), one gets the following wave equation for the baryon density perturbations:

$$(\partial_t^2 - c_s^2\nabla^2)\frac{\delta n}{n} = \nabla^2\phi + 3\partial_t^2\psi = 4\pi(T_{tt}+T)\,. \tag{2.38}$$

In the next sections we will solve the wave eq. (2.38) and the Einstein eqs. (2.18)-(2.24). It is understood, however, that since these equations are linearised, the solutions that we find "intrinsically" have a relative error $\mathcal{O}(\varepsilon_1, \varepsilon_2)$. This error is not to be confused with those which we will introduce when solving these equations approximately. We will explicitly keep track of the latter in the next sections, while we will re-introduce the relative error $\mathcal{O}(\varepsilon_1, \varepsilon_2)$ due to the linearisation procedure only in the final results.

2.3 Straight-line motion

Let us first consider the case of a perturber moving along a straight line, which is taken to be the z-axis of a Cartesian coordinate system: the unperturbed trajectory of the perturber is therefore $x^{\rm pert}(t) = y^{\rm pert}(t) = 0$, $z^{\rm pert}(t) = vt$ and the unperturbed 4-velocity is $u^\mu_{\rm pert}\partial/\partial x^\mu = \gamma(\partial/\partial t + v\partial/\partial z)$, with $\gamma^2 = 1/(1-v^2)$. Denoting the step function by $H(t)$, eq. (2.38) can be rewritten as

$$(\partial_t^2 - c_s^2\nabla^2)\frac{\delta n}{n} = 4\pi M\gamma(1+v^2)\delta(x)\delta(y)\delta(z-vt)H(t) + 4\pi[\rho(1+2\phi) + 3p(1-2\psi)] + 4\pi(1+3c_s^2)(p+\rho)\frac{\delta n}{n}\,. \quad (2.39)$$

Solving this equation is complicated by the presence of the terms $4\pi[\rho(1+2\phi)+3p(1-2\psi)]$ and $4\pi(1+3c_s^2)(p+\rho)\delta n/n$ on the right-hand side. If these terms were not present, we could simply solve eq. (2.39) by using the Green's function of the flat wave operator $-\partial_t^2 + c_s^2\nabla^2$, and proceeding as in ref. [66] we would get

$$\frac{\delta n}{n}(\boldsymbol{x}, t) \approx f\frac{M\gamma(1+v^2)}{c_s^2[(z-vt)^2 + (x^2+y^2)(1-\mathcal{M}^2)]^{1/2}}\,, \quad (2.40)$$

where $\mathcal{M} = v/c_s$ is the Mach number and

$$f = \begin{cases} 1 \quad \text{if } x^2+y^2+z^2 < (c_s t)^2 \\ \\ 2 \quad \text{if } \mathcal{M} > 1,\, x^2+y^2+z^2 > (c_s t)^2, \\ (z-vt)/\sqrt{x^2+y^2} < -\sqrt{\mathcal{M}^2-1} \\ \text{and } z > c_s t/\mathcal{M} \\ \\ 0 \quad \text{otherwise} \end{cases} \quad (2.41)$$

Note that performing a boost to the reference frame comoving with the perturber (the "primed" frame) this "approximate" solution becomes

$$\frac{\delta n}{n} \approx f\frac{M\gamma^2(1+v^2)}{c_s^2 r'\sqrt{1-\tilde{\mathcal{M}}^2\sin^2\theta'}}\,, \quad \tilde{\mathcal{M}}^2 = \frac{1-c_s^2}{c_s^2}\gamma^2 v^2\,, \quad (2.42)$$

where r' and θ' are the radius and polar angle in the primed frame *i.e.*, $r' = \sqrt{x'^2 + y'^2 + z'^2}$ and $\cos\theta' = z'/r'$ in terms of the Cartesian coordinates x', y' and z'. Eq. (2.42) agrees with the solution found in ref. [59] [eq. (B30)], except for the different value of f (this happens because ref. [59] considered the stationary solution instead of performing a finite-time analysis: *cf.* ref. [66] for more details).

It is not difficult to see that eqs. (2.40) and (2.42) are actually approximate solutions to eq. (2.39). Indeed, the term $4\pi(\rho + 3p)$ on the right-hand side of eq. (2.39) simply gives rise to an error $\mathcal{O}(\mathcal{L}/\lambda_J)^2$ in the solution. This error represents the correction due to the fact that having a fluid with constant p and ρ together with the Minkowski metric is not a solution of the Einstein equations. When it comes to the term $8\pi(\rho\phi + 3p\psi)$, let us note that the gravitational potentials ϕ and ψ consist of a part of order $\mathcal{O}(\mathcal{L}/\lambda_J)^2$ due to the presence of the fluid and a part of order $-M/r \sim -\delta n/n$ (r being the distance from the perturber) due to the presence of the perturber. The first part of the potentials therefore gives rise, when inserted into the term $8\pi(\rho\phi + 3p\psi)$, to an error much smaller than the error $\mathcal{O}(\mathcal{L}/\lambda_J)^2$ coming from the term $4\pi(\rho+3p)$. The second part of the potentials, when inserted into the term $8\pi(\rho\phi + 3p\psi)$, gives rise instead to a Yukawa-like term similar to the term $4\pi(1 + 3c_s^2)(p + \rho)\delta n/n$ appearing on the right-hand side of eq. (2.39). It is not difficult to see that these Yukawa-like terms give rise to a relative error $\varepsilon_{\mathrm{J}} \sim \mathcal{O}(\mathcal{L}/\lambda_J)$. To see this, one can simply Fourier-transform eq. (2.39) with respect to time in order to get rid of the time derivatives. One is then left with an equation of the form

$$\nabla^2\left(\frac{\delta n}{n}(\boldsymbol{x},\omega)\right) \approx S(\boldsymbol{x},\omega) + (a/\lambda_{\mathrm{J}}^2 - \omega^2/c_s^2)\frac{\delta n}{n}(\boldsymbol{x},\omega)\ , \tag{2.43}$$

where for simplicity we have used the same symbol for $\delta n/n$ and its Fourier transform with respect to time, a is a constant and $S(\boldsymbol{x},\omega)$ is a suitably defined source function [inspection of eq. (2.39) actually reveals that $S(\boldsymbol{x},\omega) \sim \exp(i\omega z/v)$]. Using the Green's function of the Yukawa operator $\nabla^2 - \mu^2$ (μ being a constant),[4]

$$G(\boldsymbol{x}) = \frac{\exp\left(-\mu|\boldsymbol{x}|\right)}{4\pi|\boldsymbol{x}|}\ , \tag{2.44}$$

this equation can be solved and gives

$$\frac{\delta n}{n}(\boldsymbol{x},\omega) = -\int d^3x' \frac{\exp\left(-\sqrt{a/\lambda_{\mathrm{J}}^2 - \omega^2/c_s^2}|\boldsymbol{x}-\boldsymbol{x}'|\right)}{4\pi|\boldsymbol{x}-\boldsymbol{x}'|} S(\boldsymbol{x}',\omega)\ . \tag{2.45}$$

[4]Using spherical coordinates and the fact that $\nabla^2(1/|\boldsymbol{x}|) = -4\pi\delta^{(3)}(\boldsymbol{x})$, it is indeed easy to check that $(\nabla^2 - \mu^2)G(\boldsymbol{x}) = -\delta^{(3)}(\boldsymbol{x})$.

If $\omega/c_s \gg 1/\lambda_{\rm J}$, one can series expand eq. (2.45) and get

$$\begin{aligned}&\frac{\delta n}{n}(\boldsymbol{x},\omega) \approx \\ &-\int d^3x' \Big\{ \frac{\exp\left[iac_s|\boldsymbol{x}-\boldsymbol{x}'|/(2\omega\lambda_{\rm J}^2)\right]}{4\pi|\boldsymbol{x}-\boldsymbol{x}'|} \times \exp(-i\omega/c_s|\boldsymbol{x}-\boldsymbol{x}'|) S(\boldsymbol{x}',\omega) \Big\} \approx \\ &-\int d^3x' \frac{\exp(-i\omega/c_s|\boldsymbol{x}-\boldsymbol{x}'|) S(\boldsymbol{x}',\omega)}{4\pi|\boldsymbol{x}-\boldsymbol{x}'|} \times \left(1+\frac{c_s\varepsilon_{\rm J}}{\omega\lambda_{\rm J}}\right) ,\end{aligned} \tag{2.46}$$

and from the last line of this equation it is clear that one gets the solution which would have been obtained by neglecting the term $a/\lambda_{\rm J}^2 \times \delta n/n$ in eq. (2.43), with a relative error $c_s\varepsilon_{\rm J}/(\omega\lambda_{\rm J}) \ll \varepsilon_{\rm J}$. For frequencies $\omega/c_s \ll 1/\lambda_{\rm J}$ (*i.e.*, for wavelengths larger than the generalised Jeans length $\lambda_{\rm J}$) this procedure is not applicable. However, it is clear that for $\omega = 0$ eq. (2.45) becomes the solution which would have been obtained by neglecting the term $a/\lambda_{\rm J}^2 \times \delta n/n$ in eq. (2.43), corrected by a factor $\sim (1+\varepsilon_{\rm J})$. Moreover, because $S(\boldsymbol{x},\omega) \sim \exp(i\omega z/v)$, the integral appearing in eq. (2.45) averages out if $\omega \gg v/\mathcal{L}$. Therefore, the spectrum of $\delta n/n$ extends up to $\omega_{\rm cutoff} \sim v/\mathcal{L}$, and the effect of the frequencies $\omega/c_s \ll 1/\lambda_{\rm J}$ on the final solution $\delta n/n(\boldsymbol{x},t)$ is negligible because $\omega_{\rm cutoff} \sim v/\mathcal{L} \gg 1/\lambda_{\rm J}$ if the fluid is not self-gravitating.

As such, since we already know the solution of eq. (2.39) if we neglect the terms $4\pi[\rho(1+2\phi)+3p(1-2\psi)]$ and $4\pi(1+3c_s^2)(p+\rho)\delta n/n$ on the right-hand side [eq. (2.40)], we can write the following approximate solution for eq. (2.39):

$$\frac{\delta n}{n}(\boldsymbol{x},t) \,= f\frac{M\gamma(1+v^2)}{c_s^2[(z-vt)^2+(x^2+y^2)(1-\mathcal{M}^2)]^{1/2}} \times (1+\varepsilon_{\rm J}) + \mathcal{O}(\mathcal{L}/\lambda_J)^2 \,, \tag{2.47}$$

where, as explained above, the error $\mathcal{O}(\mathcal{L}/\lambda_J)^2$ comes from the term $4\pi(\rho+3p)$ on the right-hand side of eq. (2.39), while the error $\varepsilon_{\rm J}$ comes from the terms $4\pi(1+3c_s^2)(p+\rho)\delta n/n$ and $8\pi(\rho\phi+3p\psi)$. [Note that $\varepsilon_{\rm J}(x,y,z,t) = \varepsilon_{\rm J}(-x,y,z,t)$ and $\varepsilon_{\rm J}(x,y,z,t) = \varepsilon_{\rm J}(x,-y,z,t)$ due to the cylindrical symmetry of the problem.] Both of these errors are negligible if $\mathcal{L} \ll \lambda_J$ (*i.e.*, if the fluid is not self-gravitating).

The trajectory of the perturber is governed by the geodesic equation of the physical, perturbed spacetime (*i.e.*, the one with metric $\tilde{g}_{\mu\nu} = \eta_{\mu\nu} + \delta g_{\mu\nu}$)[5]. The familiar form of this equation is

$$\frac{d^2\tilde{x}^\mu_{\rm pert}}{d\tilde{\tau}^2} + \tilde{\Gamma}^\mu_{\alpha\beta}\frac{d\tilde{x}^\alpha_{\rm pert}}{d\tilde{\tau}}\frac{d\tilde{x}^\beta_{\rm pert}}{d\tilde{\tau}} = 0 \,, \tag{2.48}$$

where $\tilde{x}^\mu_{\rm pert}$ and $\tilde{\tau}$ are the perturbed trajectory and proper time while the $\tilde{\Gamma}$'s are the Christoffel symbols of the perturbed spacetime. This equation can be easily expressed in terms of the background proper time τ,

$$\frac{d^2\tilde{x}^\mu_{\rm pert}}{d\tau^2} + \tilde{\Gamma}^\mu_{\alpha\beta}\frac{d\tilde{x}^\alpha_{\rm pert}}{d\tau}\frac{d\tilde{x}^\beta_{\rm pert}}{d\tau} = -\frac{d^2\tau}{d\tilde{\tau}^2}\left(\frac{d\tilde{\tau}}{d\tau}\right)^2\frac{d\tilde{x}^\mu_{\rm pert}}{d\tau} \,, \tag{2.49}$$

[5] Actually, the metric perturbation $\delta g_{\mu\nu}$, which is produced by the fluid and by the perturber, needs to be suitably regularized (see refs. [38, 39] for details), because the metric perturbation produced by the perturber is clearly divergent at the perturber's position.

which can be also written as

$$\frac{d^2\tilde{x}^\mu_{\rm pert}}{d\tau^2}+\tilde{\Gamma}^\mu_{\alpha\beta}\frac{d\tilde{x}^\alpha_{\rm pert}}{d\tau}\frac{d\tilde{x}^\beta_{\rm pert}}{d\tau}=\frac{d\tilde{x}^\mu_{\rm pert}/d\tau}{\sqrt{-\tilde{g}_{\alpha\beta}\frac{d\tilde{x}^\alpha_{\rm pert}}{d\tau}\frac{d\tilde{x}^\beta_{\rm pert}}{d\tau}}}\frac{d}{d\tau}\sqrt{-\tilde{g}_{\alpha\beta}\frac{d\tilde{x}^\alpha_{\rm pert}}{d\tau}\frac{d\tilde{x}^\beta_{\rm pert}}{d\tau}}\,. \tag{2.50}$$

Using now $\tilde{g}_{\mu\nu}=\eta_{\mu\nu}+\delta g_{\mu\nu}$, eq. (2.50) can be easily rewritten, to first order [*i.e.*, neglecting as usual errors of order $\mathcal{O}(\varepsilon_1^2,\varepsilon_2^2,\varepsilon_1\varepsilon_2)$], as [38]

$$\tilde{a}^\mu_{\rm pert}=\frac{d^2\tilde{x}^\mu_{\rm pert}}{d\tau^2}=-\frac{1}{2}(\eta^{\mu\nu}+u^\mu_{\rm pert}u^\nu_{\rm pert})(2\partial_\rho\delta g_{\nu\lambda}-\partial_\nu\delta g_{\rho\lambda})u^\lambda_{\rm pert}u^\rho_{\rm pert}\,. \tag{2.51}$$

The metric perturbations $\delta g_{\mu\nu}$ appearing on the right-hand side of eq. (2.51) consist of a part produced by the stress-energy of the fluid ($\delta g^{\rm F}_{\mu\nu}$) and one (suitably regularized) produced by the perturber ($\delta g^{\rm P}_{\mu\nu}$). The latter contribution, as already mentioned, gives rise to accretion onto the perturber and to the self-force. The drag due to accretion is easy to calculate separately, as mentioned previously, while the self-force is in general hard to deal with [38, 39]. However, it is well-known that the self-force is zero in a Minkowski spacetime for *geodesic* (*i.e.*, straight-line) motion *in the Lorenz gauge*. Since the right-hand side of eq. (2.51) is not gauge-invariant, the self-force itself is *not* gauge-invariant [82]. Nevertheless, it is possible to show that at least the dissipative part of the self-force (*i.e.*, the average of the self-force over a time approaching infinity) *is* gauge-invariant and therefore zero also in the gauge which we are using [36].[6] (Alternatively, this can be understood from the fact that a perturber moving on a straight line does not emit energy through gravitational waves in the quadrupole approximation.) It should be noted that the presence of the fluid does not alter these results. In fact, one can insert the decomposition $\delta g_{\mu\nu}=\delta g^{\rm F}_{\mu\nu}+\delta g^{\rm P}_{\mu\nu}$ into the Einstein equations, and split them into equations for $\delta g^{\rm F}_{\mu\nu}$ and equations for $\delta g^{\rm P}_{\mu\nu}$ by including in the right-hand sides of the equations for $\delta g^{\rm P}_{\mu\nu}$ only quantities containing the stress-energy of the perturber and $\delta g^{\rm P}_{\mu\nu}$ itself. In particular from eqs. (2.18), (2.21) and (2.24), using eq. (2.28) one gets

$$\nabla^2\psi^{\rm P}=8\pi\rho\phi^{\rm P}+4\pi T^{\rm pert}_{tt}\,, \tag{2.52}$$

$$\nabla^2\psi^{\rm F}=4\pi\left[\rho+2\rho\phi^{\rm F}+(p+\rho)\frac{\delta n}{n}\right]\,, \tag{2.53}$$

$$\psi^{\rm P}-\phi^{\rm P}=8\pi\Sigma^{\parallel}_{\rm pert}\,, \tag{2.54}$$

$$\psi^{\rm F}-\phi^{\rm F}=0\,, \tag{2.55}$$

$$\Box\chi^{\top\,{\rm P}}_{ij}=-16\pi(\Sigma^{\top\,{\rm pert}}_{ij}+p\chi^{\top\,{\rm P}}_{ij})\,, \tag{2.56}$$

$$\Box\chi^{\top\,{\rm F}}_{ij}=-16\pi p\chi^{\top\,{\rm F}}_{ij}\,. \tag{2.57}$$

From eq. (2.37) it follows instead that $\delta u^\perp_i=-\omega^\perp_i$ [7] and therefore $S^{\perp\,\rm fluid}_i=-(p+\rho)\delta u^\perp_i+$

[6] Note that this "dissipative" part of the self-force can be shown to account exactly for the deceleration due to the loss of energy and angular momentum through gravitational waves [36].

[7] We are making here the simplifying but reasonable assumption that no vortical modes $\delta u^\perp_i$ and $\omega^\perp_i$ are

$p\omega_i^\perp = (2p+\rho)\omega_i^\perp$, which together with eq. (2.20) gives

$$\nabla^2 \omega_i^{\perp\,\mathrm{P}} = -16\pi S_i^{\perp\,\mathrm{pert}} - 16\pi(2p+\rho)\omega_i^{\perp\,\mathrm{P}}\,, \tag{2.58}$$

$$\nabla^2 \omega_i^{\perp\,\mathrm{F}} = -16\pi(2p+\rho)\omega_i^{\perp\,\mathrm{F}}\,. \tag{2.59}$$

From eqs. (2.52), (2.54), (2.56) and (2.58) it therefore follows that the metric perturbations $\delta g_{\mu\nu}^{\mathrm{P}}$ produced by the perturber are the same as in the absence of the fluid, except for the presence of the terms $8\pi\rho\phi^{\mathrm{P}}$, $-16\pi p\chi_{ij}^{\top\,\mathrm{P}}$ and $-16\pi(2p+\rho)\omega_i^{\perp\,\mathrm{P}}$ on the right-hand sides of eqs. (2.52), (2.56) and (2.58). Using the Green's function of the Yukawa operator it is easy to see that these terms produce a contribution of order $\mathcal{O}(\rho\, r_{\mathrm{min}}^2\, \partial\delta g_{\mu\nu}^{\mathrm{P}}) \sim \mathcal{O}(\rho\, M)$ to the gradients $\partial\delta g_{\mu\nu}^{\mathrm{P}} \sim M/r_{\mathrm{min}}^2$. To be more specific, let us consider for example the case of ψ^{P}. Using eqs. (2.44), (2.52) and (2.54), the solution for ψ^{P} reads

$$\psi^{\mathrm{P}}(\boldsymbol{x},t) = -\int d^3x' \frac{\exp\left(-\sqrt{8\pi\rho}|\boldsymbol{x}-\boldsymbol{x}'|\right)}{|\boldsymbol{x}-\boldsymbol{x}'|}\left[T_{tt}^{\mathrm{pert}}(\boldsymbol{x}',t) - 16\pi\rho\Sigma_{\mathrm{pert}}^{\parallel}(\boldsymbol{x}',t)\right].$$

Taking now the derivative with respect to $\boldsymbol{x}$ and expanding the exponential, it is easy to check that the presence of the fluid simply adds a contribution of order $\mathcal{O}(\rho\, r_{\mathrm{min}}^2\, \partial_i\psi^{\mathrm{P}})$ to the gradient $\partial_i\psi^{\mathrm{P}}$. It should be noted that a contribution of order $\mathcal{O}(\rho\, r_{\mathrm{min}}^2\, \partial\delta g_{\mu\nu}^{\mathrm{P}}) \sim \mathcal{O}(\rho\, M)$ to the gradients $\partial\delta g_{\mu\nu}^{\mathrm{P}}$ corresponds to a contribution of order $\mathcal{O}(\rho\, M^2)$ to the drag: this contribution can be interpreted, as we have mentioned, as being due to accretion onto the perturber.

We will therefore focus on the force produced by the gravitational interaction with the fluid, which includes dynamical friction. From eqs. (2.53), (2.55), (2.57) and (2.59) it follows that the fluid can only excite the metric perturbations ϕ and ψ. Using eqs. (2.44), (2.53) and (2.55), we can easily get expressions for the gradients $\partial_\mu\phi^{\mathrm{F}} = \partial_\mu\psi^{\mathrm{F}}$ evaluated at the position of the perturber $x = y = 0$, $z = vt$, which enter eq. (2.51). In particular, the solution for ψ^{F} is

$$\psi^{\mathrm{F}}(\boldsymbol{x},t) = -\int d^3x' \frac{\exp\left(-\sqrt{8\pi\rho}|\boldsymbol{x}-\boldsymbol{x}'|\right)}{|\boldsymbol{x}-\boldsymbol{x}'|}\left[\rho + (p+\rho)\frac{\delta n}{n}(\boldsymbol{x}',t)\right], \tag{2.60}$$

and taking the derivative with respect to $\boldsymbol{x}$, one easily gets

$$\partial_i\psi^{\mathrm{F}}(\boldsymbol{x}) = \int d^3x' \frac{x^i - x^{i'}}{|\boldsymbol{x}-\boldsymbol{x}'|^3}\left[\rho + (p+\rho)\frac{\delta n}{n}(\boldsymbol{x}',t)\right] \times (1 + \varepsilon_{\mathrm{Yukawa}})\,, \tag{2.61}$$

where we have introduced the error $\varepsilon_{\mathrm{Yukawa}} \sim \mathcal{O}(\rho\mathcal{L}^2)$ which arises when expanding the Yukawa exponential. In particular, note that the source ρ appearing in the integral of eq. (2.61) simply gives the gravitational force exerted by the unperturbed medium on the perturber. This force is exactly zero if the medium is spherically symmetric with respect to the perturber, but in general the net effect on the gradients $\partial_i\phi^{\mathrm{F}} = \partial_i\psi^{\mathrm{F}}$ can be non-

excited in the system before the perturber is turned on at $t = 0$.

zero and at most of order $\rho\,\mathcal{L}$, depending on the shape of the fluid configuration and on the position of the perturber. Similarly, the term $(p+\rho)\delta n/n$ appearing in eq. (2.61) can be considered as the sum of two parts, one coming from the error $\mathcal{O}(\mathcal{L}/\lambda_J)^2$ appearing in eq. (2.47) and the other coming from the rest of this equation. Note that the first part is present even if the mass of the perturber goes to zero and represents the force exerted by the density perturbations which appear because, as mentioned earlier, a fluid with constant p and ρ together with the Minkowski metric is not a solution of the Einstein equations. The contribution to the gradients $\partial_\mu\phi^{\rm F}=\partial_\mu\psi^{\rm F}$ from this term can be as large as $\rho\mathcal{L}(\mathcal{L}/\lambda_J)^2$, and in what follows we will group it together with the contribution from the term ρ appearing in eq. (2.61) into a correction $\varepsilon_{\rm not\,DF}\lesssim\mathcal{O}(\rho\,\mathcal{L})$. The rest of the term $(p+\rho)\delta n/n$ gives instead the force exerted by the density perturbations produced by the perturber *i.e.*, dynamical friction. In particular, using eq. (2.47) in eq. (2.61) one obtains, for the x and y gradients evaluated at the position of the perturber $x=y=0$, $z=vt$,

$$\partial_x\phi^{\rm F}=\partial_x\psi^{\rm F}=\partial_y\phi^{\rm F}=\partial_y\psi^{\rm F}=\varepsilon_{\rm not\,DF}\,, \tag{2.62}$$

as expected from the cylindrical symmetry of the problem, while the t and z gradients, evaluated at the position of the perturber $x=y=0$, $z=vt$, are

$$\begin{aligned}&\partial_z\psi^{\rm F}=\partial_z\phi^{\rm F}=-\frac{\partial_t\psi^{\rm F}}{v}=-\frac{\partial_t\phi^{\rm F}}{v}=\\&(p+\rho)\int d^3x'\,\frac{\frac{\delta n}{n}\left(\boldsymbol{x}',t=\frac{z}{v}\right)(z-z')}{[x'^2+y'^2+(z'-z)^2]^{3/2}}\times(1+\varepsilon_{\rm Yukawa})+\varepsilon_{\rm not\,DF}\,.\end{aligned} \tag{2.63}$$

[Note that this expression for $\partial_t\psi^{\rm F}$ is obtained by taking the derivative of eq. (2.60) with respect to t, transforming the derivative with respect to t acting on $\delta n/n$ into a derivative with respect to z' using eq. (2.47), integrating by parts and finally transforming the derivative with respect to z' into one with respect to z.] The integral in eq. (2.63) can be evaluated using eq. (2.47) as in ref. [66], and is

$$\begin{aligned}&\partial_z\psi^{\rm F}=\partial_z\phi^{\rm F}=-\frac{\partial_t\psi^{\rm F}}{v}=-\frac{\partial_t\phi^{\rm F}}{v}=\\&\frac{4\pi(p+\rho)M\gamma(1+v^2)}{v^2}\,I\times[1+\mathcal{O}(\mathcal{L}/\lambda_J)]+\varepsilon_{\rm not\,DF}\,,\end{aligned} \tag{2.64}$$

where

$$I=\begin{cases}\frac{1}{2}\ln\left(\frac{1+\mathcal{M}}{1-\mathcal{M}}\right)-\mathcal{M} & \text{if } \mathcal{M}<1\,,\\ \frac{1}{2}\ln\left(1-\frac{1}{\mathcal{M}^2}\right)+\ln\left(\frac{vt}{r_{\rm min}}\right) & \text{if } \mathcal{M}>1\end{cases} \tag{2.65}$$

and we have made the assumptions that $|c_s-v|t$ exceeds the cutoff $r_{\rm min}$ and that $|c_s+v|t$ is smaller than $\mathcal{L}$.

Inserting eq. (2.62) into eq. (2.51), one immediately finds

$$\left(\tilde{a}^x_{\rm pert}\right)_{\rm F}=\left(\tilde{a}^y_{\rm pert}\right)_{\rm F}=\varepsilon_{\rm not\,DF}\,, \tag{2.66}$$

while using eq. (2.64) in eq. (2.51) gives

$$\left(\tilde{a}^t_{\rm pert}\right)_{\rm F} = -\frac{4\pi(p+\rho)M\gamma^3(1+v^2)^2}{v} I \times [1+\mathcal{O}(\mathcal{L}/\lambda_J)+\mathcal{O}(M/r_{\rm min})] + \varepsilon_{\rm not\,DF}\,, \quad (2.67)$$

$$\left(\tilde{a}^z_{\rm pert}\right)_{\rm F} = -\frac{4\pi(p+\rho)M\gamma^3(1+v^2)^2}{v^2} I \times [1+\mathcal{O}(\mathcal{L}/\lambda_J)+\mathcal{O}(M/r_{\rm min})] + \varepsilon_{\rm not\,DF}\,, \quad (2.68)$$

where I is defined by eq. (2.65). Note that we have restored the relative error $\mathcal{O}(\varepsilon_1,\varepsilon_2)$ due to the linearisation of the equations of the previous section: this gives rise to the error $\mathcal{O}(M/r_{\rm min})$ appearing in eqs. (2.67) and (2.68).

Performing a boost we can calculate the change of 3-momentum in the rest frame of the perturber due to the gravitational interaction with the fluid, so as to compare with the results of ref. [59]:

$$\left(\frac{d\tilde{p}^{(z)}_{\rm pert}}{d\tau}\right)_{\rm F} = M\gamma\left[\left(\tilde{a}^z_{\rm pert}\right)_{\rm F} - v\left(\tilde{a}^t_{\rm pert}\right)_{\rm F}\right] =$$

$$-\frac{4\pi(p+\rho)M^2\gamma^2(1+v^2)^2}{v^2} I \times [1+\mathcal{O}(\mathcal{L}/\lambda_J)+\mathcal{O}(M/r_{\rm min})] + \varepsilon_{\rm not\,DF}\,, \quad (2.69)$$

$$\left(\frac{d\tilde{p}^{(x)}_{\rm pert}}{d\tau}\right)_{\rm F} = \left(\frac{d\tilde{p}^{(y)}_{\rm pert}}{d\tau}\right)_{\rm F} = \varepsilon_{\rm not\,DF}\,. \quad (2.70)$$

Note that the relative errors $\mathcal{O}(\mathcal{L}/\lambda_J)$ and $\mathcal{O}(M/r_{\rm min})$ are negligible – the former because the fluid is not self-gravitating and the latter because the effective cutoff radius $r_{\rm min}$ is large compared with M – whereas $\varepsilon_{\rm not\,DF}$ in general is not negligible. However, $\varepsilon_{\rm not\,DF}$ represents the standard force acting on the perturber because of the gravitational interaction with the fluid, and it can be computed separately if the global structure of the system is known. In particular, $\varepsilon_{\rm not\,DF} = 0$ if the medium is distributed in a spherically symmetric fashion around the perturber.

The relativistic correction factor $\gamma^2(1+v^2)^2$ appearing in eq. (2.69) is plotted as a function of the velocity v in Fig. 2.1. Note that, for $\mathcal{M} \gg 1$ and $vt \to r_{\rm max}$, eq. (2.69), and in particular the correction factor, agrees with eq. (B45) of ref. [59].

2.4 Circular motion

Let us now consider the case of a perturber moving on a circular orbit of radius R with velocity $v = \Omega R$. Such an orbit is clearly not allowed in a Minkowski background, unless there is an external *non-gravitational* force keeping the perturber on a circular trajectory. In astrophysical scenarios we are interested instead in a perturber maintained in circular motion by *gravitational* forces. In this case, the background spacetime is necessarily curved: one can think of a circular orbit around a Schwarzschild black hole with mass $M_{\rm BH}$ surrounded by a tenuous fluid at rest. However, if the perturber is sufficiently far from the central black hole (*i.e.*, if $R \gg M_{\rm BH}$) one can approximately consider the met-

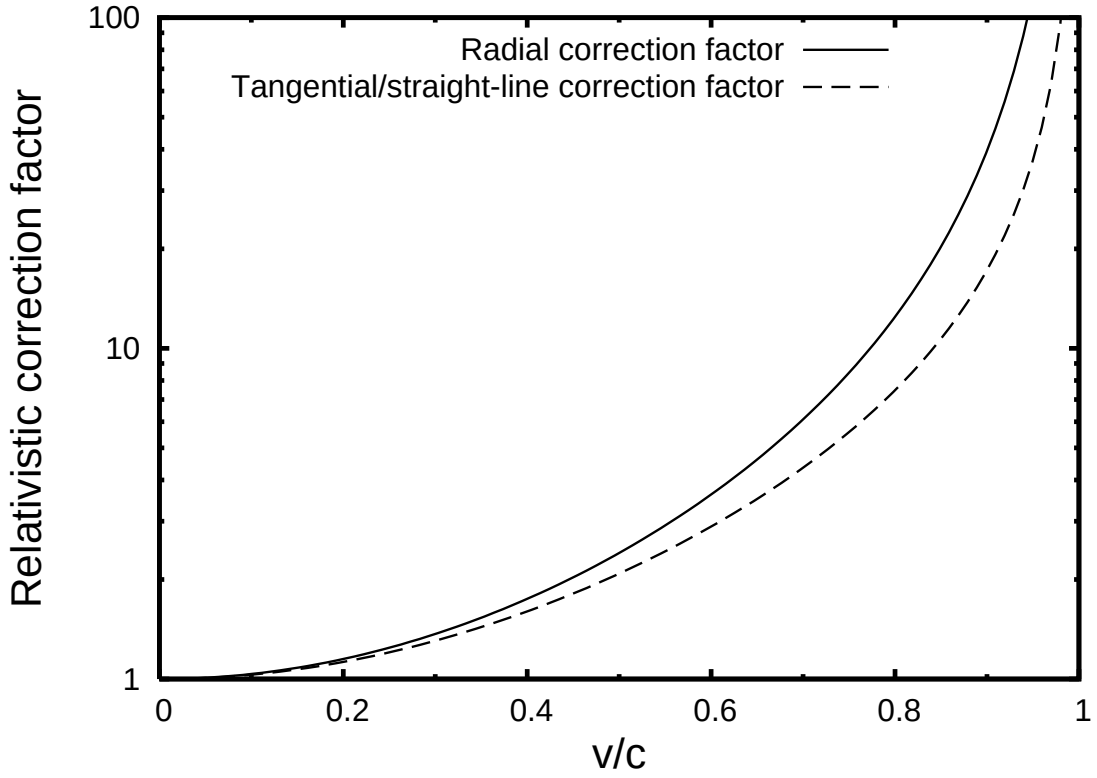

Figure 2.1: *The relativistic correction factors $\gamma^2(1+v^2)^2$, multiplying the Newtonian drag for straight-line motion and the tangential Newtonian drag for circular motion, and $\gamma^3(1+v^2)^2$, multiplying the radial Newtonian drag for circular motion, are plotted as functions of the velocity v of the perturber relative to the fluid. Note that velocities $v \sim 0.8$ can be obtained for a perturber orbiting around an accreting SMBH in the opposite direction with respect to the accretion flow.*

ric as given by eq. (2.17) (*i.e.*, Minkowski plus the perturbations produced by the presence of the fluid and of the perturber) and neglect the corrections $\mathcal{O}(M_{\rm BH}/R)$ due to the presence of the central black hole. This treatment is clearly not completely satisfactory, because orbital velocities become relativistic only close to the central black hole [in fact, $v \sim (M_{\rm BH}/R)^{1/2}$], but we argue that it may not be such a bad approximation as it might seem.

Indeed, if one uses Fermi normal coordinates comoving with the perturber (see for instance ref. [1]), all along the trajectory the metric can be written as Minkowski plus perturbations produced by the fluid and the perturber, the curvature of the background introducing just corrections of order $\mathcal{O}(r/M_{\rm BH})^2$ (r being the *spatial* distance from the perturber). Because the wake can extend out to distances of order R from the perturber [68], it will eventually feel the curvature of the background unless $R \ll M_{\rm BH}$. However, the part of the wake giving the largest gravitational attraction to the perturber will be that

closest to it, and this part will experience an approximately flat spacetime. Reasoning in the same way, we can argue that our treatment should be approximately applicable also to a perturber moving on a circular orbit in a fluid which is moving circularly in the same plane as the perturber (*e.g.*, a perturber moving inside an accretion disc), provided that the velocity $v = \Omega R$ of the perturber is taken to be the velocity *relative* to the fluid.

Considering therefore a Minkowski background spacetime, one can proceed as in the previous section, and eq. (2.38) becomes

$$(\partial_t^2 - c_s^2\nabla^2)\frac{\delta n}{n} = \frac{4\pi M\gamma(1+v^2)}{R}\delta(r-R)\delta(z)\delta(\theta-\Omega t)H(t) \\ + 4\pi[\rho(1+2\phi)+3p(1-2\psi)] + 4\pi(1+3c_s^2)(p+\rho)\frac{\delta n}{n}\,, \tag{2.71}$$

where we have introduced a system of cylindrical coordinates (r, θ, z) such that the motion of the perturber takes place at $z = 0$, $r = R$. The solution to this equation is rather complex, but has fortunately been worked out by ref. [68]. For our purposes, proceeding as in the previous section we can simply write it as

$$\frac{\delta n}{n}(\boldsymbol{x}, t) = \frac{M\gamma(1+v^2)}{R\,c_s^2}\mathcal{D}(\boldsymbol{x}, t) \times (1+\varepsilon_{\rm J}) + \mathcal{O}(\mathcal{L}/\lambda_J)^2\,, \tag{2.72}$$

where $\varepsilon_{\rm J} \sim \mathcal{O}(\mathcal{L}/\lambda_J)$ and the weight-function $\mathcal{D}(\boldsymbol{x}, t)$, whose detailed form can be found in ref. [68], defines the region of influence which sound waves sent off by the perturber do not have time to leave. From the plane-symmetry of the problem, it is clear that $\mathcal{D}(x, y, z, t) = \mathcal{D}(x, y, -z, t)$ and $\varepsilon_{\rm J}(x, y, z, t) = \varepsilon_{\rm J}(x, y, -z, t)$. Moreover, from the gradient of eq. (2.71) it also follows that

$$\partial_t\mathcal{D} = -\Omega\,\partial_\theta\mathcal{D}\,. \tag{2.73}$$

If we are again concerned with the gravitational force exerted by the fluid, which includes dynamical friction effects, rather than with the accretion drag or the self-force [8], we can restrict our attention to the metric perturbations $\phi^{\rm F} = \psi^{\rm F}$ generated by the fluid, which are again given by eq. (2.53). Using again the Green's function of the Yukawa operator and evaluating at the position of the perturber ($r = R$, $\theta = \Omega t$, $z = 0$) we easily get

$$\partial_z\phi^{\rm F} = \partial_z\psi^{\rm F} = \varepsilon_{\rm not\,DF} \tag{2.74}$$

(from the plane symmetry of the function $\mathcal{D}$). For the azimuthal gradient, instead, we

[8] Note that, differently from the case of straight-line motion, even the dissipative part of the self-force is now non-zero, as can be seen from the fact that the perturber loses energy and angular momentum through gravitational waves (*cf.* the quadrupole formula). Self-force calculations, as already mentioned, require different techniques [38, 39] and can be performed separately.

have

$$\partial_\theta \psi^{\rm F} = \partial_\theta \phi^{\rm F} = -\frac{\partial_t \psi^{\rm F}}{\Omega} = -\frac{\partial_t \phi^{\rm F}}{\Omega} = \\ (p+\rho)\int d^3x' \frac{\frac{\delta n}{n}\left(\boldsymbol{x}', t=\theta/\Omega\right)(\boldsymbol{x}-\boldsymbol{x}')\cdot\partial_\theta \boldsymbol{x}}{|\boldsymbol{x}-\boldsymbol{x}'|^3} \times (1+\varepsilon_{\rm Yukawa}) + \varepsilon_{\rm not\,DF} = \\ \frac{4\pi(p+\rho)M\gamma(1+v^2)R}{v^2} I_\theta \times [1+\mathcal{O}(\mathcal{L}/\lambda_J)] + \varepsilon_{\rm not\,DF}\ , \tag{2.75}$$

where I_θ is given by

$$I_\theta \equiv -\frac{\mathcal{M}^2}{4\pi}\int d^3\hat{x}' \frac{\mathcal{D}\left(\boldsymbol{x}', t=\theta/\Omega\right)\hat{r}'\sin(\theta'-\theta)}{[1+\hat{z}'^2+\hat{r}'^2-2\hat{r}'\cos(\theta-\theta')]^{3/2}} \tag{2.76}$$

(a hat denotes quantities scaled by the radius of the orbit: $\hat{\boldsymbol{x}}' \equiv \boldsymbol{x}'/R$, $\hat{r}' = r'/R$, $\hat{z}' = z'/R$). Similarly, for the radial gradient we obtain

$$\partial_r \psi^{\rm F} = \partial_r \phi^{\rm F} = \\ (p+\rho)\int d^3x' \frac{\frac{\delta n}{n}\left(\boldsymbol{x}', t=\theta/\Omega\right)(\boldsymbol{x}-\boldsymbol{x}')\cdot\partial_r \boldsymbol{x}}{|\boldsymbol{x}-\boldsymbol{x}'|^3} \times (1+\varepsilon_{\rm Yukawa}) + \varepsilon_{\rm not\,DF} = \\ \frac{4\pi(p+\rho)M\gamma(1+v^2)}{v^2} I_r \times [1+\mathcal{O}(\mathcal{L}/\lambda_J)] + \varepsilon_{\rm not\,DF}\ , \tag{2.77}$$

where I_r is given by

$$I_r \equiv -\frac{\mathcal{M}^2}{4\pi}\int d^3\hat{x}' \frac{\mathcal{D}\left(\boldsymbol{x}', t=\theta/\Omega\right)[\hat{r}'\cos(\theta-\theta')-1]}{[1+\hat{z}'^2+\hat{r}'^2-2\hat{r}'\cos(\theta-\theta')]^{3/2}}\ . \tag{2.78}$$

Note that the integrals I_θ and I_r have been calculated numerically in ref. [68]. They are functions of the coordinate θ of the perturber, which is thought to vary in an unbound range to count the number of revolutions, or equivalently they can be thought of as functions of time ($t = \theta/\Omega$). Fortunately, though, steady state values for these integrals are reached in times comparable to the sound crossing-time R/c_s or within one orbital period: fits to the numerical results for these steady state values in the case in which $R \gg r_{\rm min}$ and $\mathcal{L} \gtrsim (20-100)R$ are given by [68]

$$I_r = \begin{cases} \mathcal{M}^2\ 10^{\,3.51\mathcal{M}-4.22}, & \text{for } \mathcal{M} < 1.1\,, \\ \\ 0.5\ \ln\left[9.33\mathcal{M}^2(\mathcal{M}^2-0.95)\right], & \\ \text{for } 1.1 \le \mathcal{M} < 4.4\,, & \\ \\ 0.3\,\mathcal{M}^2, & \text{for } \mathcal{M} \ge 4.4\,, \end{cases} \tag{2.79}$$

and

$$I_\theta = \begin{cases} 0.7706 \ln\left(\frac{1+\mathcal{M}}{1.0004-0.9185\mathcal{M}}\right) - 1.4703\mathcal{M}, \\ \text{for } \mathcal{M} < 1.0\,, \\ \\ \ln[330(R/r_{\rm min})(\mathcal{M}-0.71)^{5.72}\mathcal{M}^{-9.58}], \\ \text{for } 1.0 \le \mathcal{M} < 4.4\,, \\ \\ \ln[(R/r_{\rm min})/(0.11\mathcal{M}+1.65)], \\ \text{for } \mathcal{M} \ge 4.4\,. \end{cases} \tag{2.80}$$

These fits are accurate to within 4% for $\mathcal{M} < 4.4$ and to within 16% for $\mathcal{M} > 4.4$.

Using eqs. (2.74), (2.75) and (2.77) in eq. (2.51) and transforming to cylindrical coordinates, for the acceleration produced by the gravitational interaction with the fluid we easily get

$$\begin{aligned} \left(\tilde{a}^t_{\rm pert}\right)_{\rm F} = &- \frac{4\pi(p+\rho)M\gamma^3(1+v^2)^2}{v}\, I_\theta \\ &\times [1 + \mathcal{O}(\mathcal{L}/\lambda_J) + \mathcal{O}(M/r_{\rm min})] + \varepsilon_{\rm not\,DF}\,, \end{aligned} \tag{2.81}$$

$$\begin{aligned} \left(\tilde{a}^\theta_{\rm pert}\right)_{\rm F} = &- \frac{4\pi(p+\rho)M\gamma^3(1+v^2)^2}{R\,v^2}\, I_\theta \\ &\times [1 + \mathcal{O}(\mathcal{L}/\lambda_J) + \mathcal{O}(M/r_{\rm min})] + \varepsilon_{\rm not\,DF}\,, \end{aligned} \tag{2.82}$$

$$\begin{aligned} \left(\tilde{a}^r_{\rm pert}\right)_{\rm F} = &- \frac{4\pi(p+\rho)M\gamma^3(1+v^2)^2}{v^2}\, I_r \\ &\times [1 + \mathcal{O}(\mathcal{L}/\lambda_J) + \mathcal{O}(M/r_{\rm min})] + \varepsilon_{\rm not\,DF}\,, \end{aligned} \tag{2.83}$$

$$\left(\tilde{a}^z_{\rm pert}\right)_{\rm F} = \varepsilon_{\rm not\,DF}\,. \tag{2.84}$$

[The error $\mathcal{O}(M/r_{\rm min})$ comes about because the equations that we have solved are linearised and are therefore subject to an "intrinsic" error $\mathcal{O}(\varepsilon_1, \varepsilon_2)$.]

Finally, in order to compute the change of 3-momentum due to the gravitational interaction with the fluid in the rest frame of the perturber, it is sufficient to project the 4-force $M(\tilde{a}^\mu_{\rm pert})_{\rm F}$ onto a tetrad comoving with the perturber, *i.e.*, $e_{(t)} = u^\mu_{\rm pert}\partial/\partial x^\mu = \gamma(\partial/\partial t + \Omega\partial/\partial\theta)$, $e_{(\theta)} = \gamma(v\partial/\partial t + 1/r\,\partial/\partial\theta)$, $e_{(r)} = \partial/\partial r$ and $e_{(z)} = \partial/\partial z$. Using eqs. (2.81)–(2.84) one then easily gets

$$\begin{aligned} \left(\frac{d\tilde{p}^{(\theta)}_{\rm pert}}{d\tau}\right)_{\rm F} = &-\frac{4\pi(p+\rho)M^2\gamma^2(1+v^2)^2}{v^2}\, I_\theta \\ &\times [1 + \mathcal{O}(\mathcal{L}/\lambda_J) + \mathcal{O}(M/r_{\rm min})] + \varepsilon_{\rm not\,DF}\,, \end{aligned} \tag{2.85}$$

$$\left(\frac{d\tilde{p}^{(r)}_{\rm pert}}{d\tau}\right)_{\rm F} = -\frac{4\pi(p+\rho)M^2\gamma^3(1+v^2)^2}{v^2}\, I_r$$
$$\times\,[1+\mathcal{O}(\mathcal{L}/\lambda_J)+\mathcal{O}(M/r_{\rm min})]+\varepsilon_{\rm not\,DF}\,, \tag{2.86}$$

$$\left(\frac{d\tilde{p}^{(z)}_{\rm pert}}{d\tau}\right)_{\rm F} = \varepsilon_{\rm not\,DF}\,. \tag{2.87}$$

As in the case of straight-line motion, the relative errors $\mathcal{O}(\mathcal{L}/\lambda_J)$ and $\mathcal{O}(M/r_{\rm min})$ are negligible, because the fluid is not self-gravitating and because the effective cutoff radius $r_{\rm min}$ is large compared with M, whereas $\varepsilon_{\rm not\,DF}$ in general is not negligible, although it is exactly zero if the medium is spherically symmetric around the perturber. The relativistic correction factors $\gamma^2(1+v^2)^2$ and $\gamma^3(1+v^2)^2$ appearing in eqs. (2.85) and (2.86) are plotted as functions of the velocity v in Fig. 2.1.

2.5 Summary

We have studied the drag experienced by a massive body because of the gravitational interaction with its own gravitationally-induced wake, when it is moving along a straight-line or a circular orbit at relativistic speed v relative to a non self-gravitating collisional fluid in a flat or weakly curved background spacetime. Thanks to a suitable choice of gauge, we could exploit the Newtonian analysis of ref. [66] and of ref. [68] to simplify our calculations. We find that their results remain valid also in the relativistic case, provided that the rest-mass density is replaced by $p+\rho$ (p and ρ being the pressure and energy density of the fluid) and a relativistic multiplicative factor is included. This factor turns out to be $\gamma^2(1+v^2)^2$ in the straight-line motion case and for the tangential component of the drag in the circular motion case, and $\gamma^3(1+v^2)^2$ for the radial component of the drag in the circular motion case. We can note that this factor involves only kinematic quantities and therefore amounts to a special-relativistic effect rather than to a general-relativistic one. This is not surprising because our analysis strictly applies only to a fluid in a flat spacetime (in the case of straight-line motion) or a weakly curved one (in the case of circular motion).

In spite of these limitations, we have argued that our results are suitable at least for a preliminary study of the effects of an accretion disc on EMRIs. Although our results are not expected to change the standard conclusion that the gas accreting onto the central SMBH does not significantly affect EMRIs in the case of "normal" Galactic Nuclei [73], they could play a role, under certain circumstances, in the case of higher density environments like Active Galactic Nuclei (quasars, Seyfert Galaxies, etc.). An investigation of this scenario, in which the accretion is modelled by a thick torus, will be presented in the next chapter.

Chapter 3

Detecting an AGN accretion torus with LISA

> We shall not cease from exploration,
> and the end of all our exploring will
> be to arrive where we started and
> know the place for the first time.
>
> T. S. Eliot

One of the most exciting prospects opened up by the scheduled launch of the space-based gravitational-wave detector LISA [2] will be the possibility of mapping accurately the spacetime of the SMBHs which are believed to reside in the centre of galaxies [29]. As we have already stressed in chapter 1, among the best candidate sources for this detector are the Extreme Mass Ratio Inspirals (EMRIs), *i.e.* stellar-mass black holes ($m \approx 1-10M_{\odot}$) or compact objects orbiting around the SMBH and slowly inspiralling due to the loss of energy and angular momentum via gravitational waves (radiation reaction). In order for the signal to fall within the sensitivity band of LISA, the SMBH must have a mass $M \approx 10^5 - 10^7 M_{\odot}$, *i.e.*, the low end of the SMBH mass function.

It is currently expected that a number of such events ranging from tens to perhaps one thousand could be measured every year [17], but since they will have small signal-to-noise ratios, their detection and subsequent parameter extraction will require the use of matched-filtering techniques. These basically consist of cross-correlating the incoming gravitational-wave signal with a bank of theoretical templates representing the expected signal as a function of the parameters of the source.

This will not only allow one to detect the source, but also to extract its properties. For instance, the accurate modelling of the motion of a satellite in a Kerr spacetime will allow one to measure the spin and the mass of the SMBH. Although producing these pure-Kerr templates has proved to be a formidable task, particularly because of the difficulty of treating rigorously the effect of radiation reaction (see refs. [38, 39] for a detailed review),

considerable effort has gone into trying to include the effects of a deviation from the Kerr geometry. These attempts are motivated by the fact that possible "exotic" alternatives to SMBHs have been proposed (*e.g.,* boson stars [83], fermion balls [84] and gravastars [85]), although the presence of these objects would require radically modifying the mechanism by which galaxies are expected to form. On the other hand, non-pure Kerr templates might allow one to really map the spacetimes of SMBHs and to test, *experimentally*, the Kerr solution.

Various approaches to this problem have been considered in the literature. EMRIs in a spacetime having arbitrary gravitational multipoles should be considered in order to maintain full generality [86, 87, 88], but this method does not work very well in practice and would only apply to vacuum spacetimes. For this reason, alternative approaches have been proposed and range from EMRIs around non-rotating boson stars [89], to EMRIs in bumpy black-hole spacetimes [90, 91] (*i.e.*, spacetimes that, although involving naked singularities, are *almost* Schwarzschild or Kerr black holes, but have some multipoles with the wrong values) or in quasi-Kerr spacetimes [92, 93] (*i.e.*, spacetimes, consisting of Kerr plus a small quadrupole moment). We will review these attempts more in detail in the next chapter.

Interestingly, however, none of these methods is suitable for taking into account the effect of the matter which is certainly present in galactic centres. SMBHs can indeed be surrounded by stellar disks (as in the case of the Galactic centre [94]) or, as in the case of Active Galactic Nuclei (AGNs) [95] (in which we are most interested) by accretion disks of gas and dust which can be even as massive as the SMBH [96]. While the gravitational attraction of a disk can have important effects on EMRIs if this disk is very massive and close to the SMBH (see the next chapter and ref. [97]), an astrophysically realistic accretion disk can influence an EMRI only if the satellite crosses it, thus experiencing a "hydrodynamic" drag force.

This drag consists of two parts. The first one is due to the accretion of matter onto the satellite. This transfers energy and momentum from the disk to the satellite, giving rise to a short-range interaction. In this chapter we will focus on the case of a satellite black hole, the accretion onto which was studied analytically by Bondi & Hoyle [64, 65] and subsequently confirmed through numerical calculations [59, 98, 99].[1] The second part of the drag is instead due the gravitational deflection of the material which is not accreted, which is therefore far from the satellite, but which can nevertheless transfer momentum to the satellite. As we have already mentioned in chapter 2, this long-range interaction can also be thought of as arising from the gravitational pull of the satellite by its own gravitationally-induced wake (*i.e.,* the density perturbations that the satellite excites, by gravitational interaction, in the medium), and is often referred to as "dynamical friction". This effect was first studied in a collisionless medium by Chandrasekar [53], but acts also for a satellite moving in a collisional fluid [62, 63, 59, 66, 67, 68, 100].

As we have already stressed in chapter 2, the effect of this disk-satellite interaction

[1] For a satellite neutron star, instead, the accretion rate will be lower than for a satellite black hole, but we expect our results to remain valid, at least qualitatively, also in that case, because we will see that for most orbits the short range drag is not the main driver of the secular evolution.

on EMRIs has been studied by different authors for a number of disk models [51, 69, 70, 71, 72, 73, 76, 77]. However, all of these studies have been been carried out within a Newtonian or pseudo-Newtonian description of gravity (with the partial exception of ref. [69], in which the orbits are Kerr geodesics, but the disk model and the hydrodynamic drag is not relativistic). In this chapter, instead, we provide a first relativistic treatment for satellites moving on generic orbits around a rotating SMBH surrounded by a thick disk (*i.e.,* a torus). We consider the torus to have constant specific angular momentum (*i.e.,* constant angular momentum per unit mass as seen from an observer at infinity) and neglect its self-gravity (*i.e.,* we consider the metric to be pure Kerr). Under these assumptions, an analytical solution exists for this system [101, 102]. This configuration can be proved to be marginally stable with respect to axisymmetric perturbations [103] (*i.e.,* if perturbed, such a torus can accrete onto the SMBH), and is expected to be a good approximation at least for the inner parts of the accretion flow [101, 102].

We have found that for a system composed of an SMBH with mass $M = 10^6 M_\odot$ and a torus with mass $M_{\rm t} \lesssim M$ and outer radius $r_{\rm out} = 10^5 M$, the effect of the hydrodynamic drag on the motion of the satellite black hole is much smaller than radiation reaction at those distances from the SMBH which can be probed with LISA (*i.e.,* $\sim 10M$ for $M = 10^6 M_\odot$). Although these values for M, $M_{\rm t}$ and $r_{\rm out}$ are plausible for AGNs, an overall uncertainty is still present and has motivated an investigation also for different masses and sizes of the torus. In this way we have found that the effect of the torus can be important in the early part of the inspiral and that it could leave an observable imprint in the gravitational waveforms detected by LISA, if the radius of the torus is decreased to $r_{\rm out} = 10^3 - 10^4 M$ or, even for $r_{\rm out}$ as large as $10^5 M$ and $M_{\rm t} \lesssim M$, if $M = 10^5 M_\odot$. In this latter case, in fact, LISA could detect an EMRI event at distances as large as $r \sim 45M$ from the SMBH, although the event needs to be sufficiently close to us because the amplitude of the gravitational-wave signal decreases as M/r.

In addition, if non-negligible, the effect of the hydrodynamic drag would have a distinctive signature on the waveforms. Radiation reaction, in fact, always drives orbits from the equatorial prograde configuration to the equatorial retrograde one (see ref. [104, 105, 106] and chapter 5). The hydrodynamic drag from a torus corotating with the SMBH, on the other hand, always makes orbits evolve towards the equatorial prograde configuration. Should such a behaviour be observed in the data, it would provide a strong qualitative signature of the presence of the torus. However, it is important to point out that even for those configurations in which the hydrodynamic drag plays a major role, this is restricted to the initial part of the inspiral detectable by LISA, whereas its effect rapidly vanishes in the very strong-field region of the SMBH (*i.e.,* $p \lesssim 5M$). As a result, the pure-Kerr templates would provide a faithful description of the last part of the inspiral even in these cases.

The rest of this chapter is organised as follows. In sec. 3.1 we review the equilibrium solutions that we used for the orbiting torus. In sec. 3.2.1 we present the equations governing the interaction between the satellite black hole and the torus, while in sec. 3.2.2 we apply the adiabatic approximation to the hydrodynamic drag. Results are then discussed in sec. 3.3.1 for equatorial circular orbits and in sec. 3.3.2 for generic (inclined and

eccentric) orbits. Finally, the conclusions are drawn in sec. 3.4.

3.1 Modelling the torus

The properties of non self-gravitating, stationary, axisymmetric and plane-symmetric toroidal fluid configurations in Kerr spacetimes are well-known in astrophysics but are less well known within the community working on EMRIs. Because of this, in this section we briefly review the basic facts, referring the interested reader to refs. [101, 102, 107, 108, 109] for additional information.

Let us consider a perfect fluid with 4-velocity $\boldsymbol{u}^{\rm fluid}$, which is described by the stress-energy tensor

$$T^{\mu\nu} = (\rho + p) u^{\mu}_{\rm fluid} u^{\nu}_{\rm fluid} + p g^{\mu\nu} = \rho_0 h u^{\mu}_{\rm fluid} u^{\nu}_{\rm fluid} + p g^{\mu\nu} \,,$$

where p, ρ_0, ρ and $h \equiv (p+\rho)/\rho_0$ are the pressure, rest-mass density, energy density and specific enthalpy of the fluid. In what follows we will model the fluid with a polytropic equation of state $p = \kappa \rho_0^{\Gamma} = \rho_0 \varepsilon (\Gamma - 1)$, where $\varepsilon = \rho/\rho_0 - 1$ is the internal energy per unit rest-mass, and κ and Γ are the polytropic constant and index, respectively. Because we are neglecting the self-gravity of the fluid, we can also consider $\boldsymbol{g}$ as given by the Kerr metric in Boyer-Lindquist coordinates, which reads [1]

$$\begin{aligned} ds^2 = &- \left(1 - \frac{2Mr}{\Sigma}\right) dt^2 + \frac{\Sigma}{\Delta}\, dr^2 + \Sigma\, d\theta^2 \\ &+ \left(r^2 + a^2 + \frac{2Ma^2 r}{\Sigma} \sin^2\theta\right) \sin^2\theta\, d\phi^2 - \frac{4Mar}{\Sigma} \sin^2\theta\, dt\, d\phi \,, \end{aligned} \tag{3.1}$$

where

$$\Sigma \equiv r^2 + a^2 \cos^2\theta, \qquad \Delta \equiv r^2 - 2Mr + a^2. \tag{3.2}$$

The fluid is assumed to be in circular non-geodesic motion with 4-velocity

$$\boldsymbol{u}^{\rm fluid} = A(r,\theta) \left[\frac{\partial}{\partial t} + \Omega(r,\theta) \frac{\partial}{\partial \phi}\right] = U(r,\theta) \left[-dt + \ell(r,\theta) d\phi\right] \,, \tag{3.3}$$

where the second equals sign underlines that the vector and the 1-form are each the dual of the other. Here, $\Omega \equiv u^{\phi}_{\rm fluid}/u^{t}_{\rm fluid}$ is the angular velocity, $A \equiv u^{t}_{\rm fluid}$ is called the redshift factor, $U \equiv -u_t^{\rm fluid}$ is the energy per unit mass as measured at infinity and $\ell \equiv -u_\phi^{\rm fluid}/u_t^{\rm fluid}$ is the specific angular momentum as measured at infinity (*i.e.,* the angular momentum per unit energy as measured at infinity). Note that ℓ is conserved for stationary axisymmetric flows, as can easily be shown using Euler's equation. The specific angular momentum and the angular velocity are trivially related by

$$\Omega = -\frac{g_{t\phi} + g_{tt}\ell}{g_{\phi\phi} + g_{t\phi}\ell} \,, \quad \ell = -\frac{g_{t\phi} + g_{\phi\phi}\Omega}{g_{tt} + g_{t\phi}\Omega} \,, \tag{3.4}$$

while the normalisation condition $\boldsymbol{u}^{\rm fluid}\cdot\boldsymbol{u}^{\rm fluid}=-1$ gives

$$U=\sqrt{\frac{\varpi^2}{g_{tt}\ell^2+2g_{t\phi}\ell+g_{\phi\phi}}}\,, \tag{3.5}$$

$$A=\sqrt{\frac{-1}{g_{tt}+2g_{t\phi}\Omega+g_{\phi\phi}\Omega^2}}\,, \tag{3.6}$$

$$AU=\frac{1}{1-\Omega\ell}\,, \tag{3.7}$$

where $\varpi^2=g_{t\phi}^2-g_{tt}\,g_{\phi\phi}=\Delta\sin^2\theta$. Note that in this chapter we will always consider $\ell>0$ (torus rotating in the positive ϕ-direction), while we will allow the spin parameter a of the black hole to be either positive (black hole corotating with the torus) or negative (black hole counter-rotating with respect to the torus).

To calculate the structure of the torus, we need to use Euler's equation, which in its general form is

$$a^\mu_{\rm fluid}=-\frac{(g^{\mu\nu}+u^\mu_{\rm fluid}u^\nu_{\rm fluid})\partial_\nu p}{p+\rho}\,, \tag{3.8}$$

where $a^\mu_{\rm fluid}$ is the 4-acceleration of the fluid. In particular, if the pressure is assumed to depend only on r and θ and if the equation of state is barotropic [*i.e.*, if $\rho=\rho(p)$][2], from eq. (3.8) one easily gets that the 4-acceleration can be expressed as the gradient of a scalar potential $W(p)$:

$$a^{\rm fluid}_\mu=\partial_\mu W\,,\quad W(p)=-\int^p\frac{dp'}{p'+\rho(p')}\,. \tag{3.9}$$

On the other hand, from the definition of the 4-acceleration ($a^\mu_{\rm fluid}=u^\nu_{\rm fluid}\nabla_\nu u^\mu_{\rm fluid}$), eqs. (3.3), (3.6) and (3.7), and the Killing equation $\nabla_{(\mu}\xi_{\nu)}=0$ for $\xi=\partial/\partial t$ and $\xi=\partial/\partial\phi$, one easily gets

$$a^{\rm fluid}_\mu=\partial_\mu W=-\frac{\partial_\mu p}{p+\rho}=\partial_\mu\ln U-\frac{\Omega}{1-\Omega\ell}\partial_\mu\ell\,. \tag{3.10}$$

In particular, taking the derivative of this equation, anti-symmetrising and using the trivial fact that $\partial_{[\mu\nu]}W=\partial_{[\mu\nu]}\ell=\partial_{[\mu\nu]}U=0$, we obtain that $\partial_{[\mu}\Omega\,\partial_{\nu]}\ell=0$. This implies $\nabla\Omega\propto\nabla\ell$ and thus that ℓ and Ω have the same contour levels [*i.e.*, $\Omega=\Omega(\ell)$]. Using this fact, we can then write eq. (3.10) in an integral form:

$$W-W_{\rm out}=-\int_0^p\frac{dp'}{p'+\rho(p')}=\ln U-\ln U_{\rm out}-\int_{\ell_{\rm out}}^{\ell}\frac{\Omega(\ell')d\ell'}{1-\Omega(\ell')\ell'}\,, \tag{3.11}$$

where $W_{\rm out}$ and $\ell_{\rm out}$ are the potential and specific angular momentum at the outer edge of the torus.[3]

[2] This is of course the case for a polytropic equation of state, because $\rho=p/(\Gamma-1)+(p/\kappa)^{1/\Gamma}$.

[3] Of course, $W_{\rm out}$ and $\ell_{\rm out}$ can be replaced by the values of W and ℓ at the inner edge of the torus if this is present.

In the case of a torus with constant specific angular momentum [*i.e.*, $\ell(r,\theta) = \text{constant}$], eq. (3.11) provides an analytical solution, because once ℓ has been fixed the integral on the right-hand side is zero and eq. (3.5) gives an analytical expression for U:

$$W - W_{\rm out} = -\int_0^p \frac{dp'}{p' + \rho(p')} = \ln U - \ln U_{\rm out} \,. \tag{3.12}$$

Note that if one requires that $W \to 0$ when $r \to +\infty$ (*i.e.*, $W = 0$ for an equipotential surface closing at infinity), this equation gives $W = \ln U$: $W > 0$ then corresponds to open equipotential surfaces, while $W < 0$ corresponds to closed equipotential surfaces. Interestingly, the potential well can present a minimum and a saddle point. Because of the plane-symmetry, these points are located in the equatorial plane, thus corresponding to local extremes of $W(r, \theta = \pi/2)$, and mark two important positions: respectively, the centre of the torus (*i.e.*, the point where the density reaches its maximum) and its cusp (*i.e.*, the mass-shedding point). Noticeably, these points are located at the radii where the specific angular momentum of the torus, ℓ, coincides with that of the geodesic circular equatorial orbit (the "Keplerian" orbit) corotating with the torus,

$$\ell_K(r,a) = \frac{r^2 - 2a\sqrt{Mr} + a^2}{(r-2M)\sqrt{r/M} + a} \,. \tag{3.13}$$

This immediately follows from the fact that at the extremes of the function W one has $\partial_\mu W = 0$, which leads, through eq. (3.9), to $a^\mu_{\rm fluid} = 0$ (in other words, at the centre and at the cusp the pressure gradients are zero and only gravitational forces act).

In this chapter we will indeed consider constant-ℓ tori. A detailed classification of these models depending upon the values of ℓ and of $W_{\rm out}$ can be found in refs. [101, 102, 107]. Here we simply recall that in order to have a closed equipotential surface with a cusp, one needs to have a value of ℓ between the specific angular momenta $\ell_{\rm ms}$ and $\ell_{\rm mb}$ of the marginally stable and marginally bound equatorial geodesic (*i.e.*, "Keplerian") orbits corotating with the torus. This can be easily understood by noting, from eq. (3.12), that the potential $W(r, \theta = \pi/2)$ is simply the effective potential describing the equatorial motion of a test particle around a Kerr black hole. As such, $\ell_{\rm ms}$ and $\ell_{\rm mb}$ can be calculated easily using eq. (3.13) and the formulae for the radii of the marginally stable and marginally bound circular equatorial orbits in Kerr rotating in the positive ϕ-direction (*i.e.*, corotating with the torus):

$$\ell_{\rm ms} = \ell_K(r_{\rm ms}) \,, \quad \ell_{\rm mb} = \ell_K(r_{\rm mb}) \,, \tag{3.14}$$

$$r_{\rm ms}/M = 3 + Z_2 - \text{sign}(\tilde{a})\sqrt{(3-Z_1)(3+Z_1+2Z_2)} \,, \tag{3.15}$$

$$r_{\rm mb}/M = 2 - \tilde{a} + 2\sqrt{1-\tilde{a}} \,, \tag{3.16}$$

$$Z_1 = 1 + (1-\tilde{a}^2)^{1/3}\left[(1+\tilde{a})^{1/3} + (1-\tilde{a})^{1/3}\right] \,, \tag{3.17}$$

$$Z_2 = \sqrt{3\tilde{a}^2 + Z_1^2} \,, \tag{3.18}$$

where $\tilde{a} = a/M$.

In order to select the class of solutions having a finite radial extent (*i.e.,* having finite inner and an outer radii) one needs also to choose a negative value for the "potential barrier" at the inner edge of the torus,

$$\Delta W = W_{\rm in} - W_{\rm cusp} = W_{\rm out} - W_{\rm cusp} \leq 0\,. \tag{3.19}$$

If $\Delta W < 0$, the inner radius of the torus is larger than the radius at which the cusp occurs ($r_{\rm in} > r_{\rm cusp}$), while if the potential barrier ΔW reduces to zero, the torus exactly fills its outermost closed equipotential surface and $r_{\rm in} = r_{\rm cusp} \leq r_{\rm ms}$. Note that because of the considerations that we have made above about the value of ℓ, for constant-ℓ tori we have $r_{\rm cusp} \geq r_{\rm mb}$ (with $r_{\rm cusp} = r_{\rm mb}$ only if $\ell = \ell_{\rm mb}$) and $r_{\rm centre} \geq r_{\rm ms}$ (with $r_{\rm centre} = r_{\rm ms}$ only if $\ell = \ell_{\rm ms}$). If instead $\Delta W > 0$, the fluid overflows the outermost closed equipotential surface and mass transfer is possible at the cusp: for a polytropic equation of state, the accretion rate can be shown to be $\dot{M} \propto \Delta W^{\Gamma/(\Gamma-1)}$.

The integral Euler equation for constant-ℓ tori [eq. (3.12)] further simplifies if the equation of state is polytropic, because in this case

$$\int_0^p \frac{dp'}{p' + \rho(p')} = \ln \frac{h}{h_{\rm out}}\,, \tag{3.20}$$

where $h_{\rm out}$ is the specific enthalpy at the outer edge of the torus. Since for a polytropic equation of state the enthalpy is given by

$$h = 1 + \frac{\Gamma}{\Gamma - 1}\kappa\rho_0^{\Gamma-1}\,, \tag{3.21}$$

it is clear that $h_{\rm out} = 1$ (because $p = \rho_0 = 0$ at the outer edge of the torus), and eqs. (3.12) and (3.20) give

$$\rho_0(r,\theta) = \left\{\frac{\Gamma - 1}{\Gamma}\frac{\left[e^{W_{\rm out} - W(r,\theta)} - 1\right]}{\kappa}\right\}^{1/(\Gamma-1)}\,. \tag{3.22}$$

Once the rest-mass distribution is known, the total rest mass of the torus is given by

$$M_{t,0} = \int \rho_0\sqrt{-g}u^t d^3x\,, \tag{3.23}$$

where $\sqrt{-g} = \Sigma\sin\theta$ and $d^3x = dr\,d\theta\,d\phi$ is the coordinate 3-volume element, while the mass-energy is given by

$$\begin{aligned} M_{\rm t} &= \int (T^r_r + T^\phi_\phi + T^\theta_\theta - T^t_t)\sqrt{-g}\,d^3x = \\ &2\pi\int_{\rho_0>0}\left(\frac{g_{\phi\phi} - g_{tt}\ell^2}{g_{\phi\phi} + 2g_{t\phi}\ell + g_{tt}\ell^2}\rho_0 h + 2P\right) \times \left(r^2 + a^2\cos^2\theta\right)\sin\theta\; dr d\theta\,. \end{aligned} \tag{3.24}$$

Clearly, the smaller the ratio between the mass of the torus and that of the SMBH, the better the approximation of neglecting the self-gravity of the torus.

3.2 Modelling the orbital motion

This section is dedicated to the discussion of the hydrodynamic drag on the satellite black hole. Although the two aspects are closely inter-related, we first discuss the equations governing the interaction between the satellite black hole and the torus and then describe their use in the calculation of the changes of the orbital parameters within the adiabatic approximation.

3.2.1 The hydrodynamic drag

As already mentioned, the hydrodynamic drag acting on the satellite black hole can be written as the sum of a short-range part, due to accretion, and a long-range part, due to the deflection of the matter which is not accreted or, equivalently, to the gravitational interaction of the satellite with the density perturbations gravitationally induced by its own presence:

$$\frac{dp^{\mu}_{\rm sat}}{d\tau} = \frac{dp^{\mu}}{d\tau}\Big|_{\rm accr} + \frac{dp^{\mu}}{d\tau}\Big|_{\rm defl}\,, \tag{3.25}$$

where τ is the proper time of the satellite.

Accretion onto a moving black hole was studied analytically in a Newtonian framework by Bondi & Hoyle [64, 65], who found the rest-mass accretion rate to be

$$\frac{dm_0}{d\tau} = \frac{4\pi\lambda m^2\rho_0}{(v^2+v_s^2)^{3/2}}\,, \tag{3.26}$$

where m is the mass of the black hole, v and v_s are respectively the velocity of the black hole with respect to the fluid and the sound velocity, and λ is a dimensionless constant of the order of unity, which for a fluid with polytropic equation of state and polytropic index Γ has the value [110]

$$\lambda = \left(\frac{1}{2}\right)^{(\Gamma+1)/[2(\Gamma-1)]} \left(\frac{5-3\Gamma}{4}\right)^{-(5-3\Gamma)/[2(\Gamma-1)]}\,. \tag{3.27}$$

Subsequent numerical work [59, 98, 99] treated instead the problem of accretion in full General Relativity, and showed that eq. (3.26), with λ given by eq. (3.27), is correct provided that it is multiplied by a factor ~ 5 – 25 when v and v_s become relativistic (*cf.* Table 3 of ref. [98]). However, because a fit for this correction factor is, to the best of our knowledge, not yet available, and the published data is not sufficient for producing one, we use the Bondi accretion rate [eqs. (3.26) and (3.27)], bearing in mind that it could slightly underestimate the drag at relativistic velocities v and v_s.[4] Once the accretion rate

[4] As we will see in section 3.3, v and v_s can become relativistic only for orbits counter-rotating with respect

is known, the short-range part of the drag is given by [59]

$$\left.\frac{dp^\mu}{d\tau}\right|_{\rm accr} = h\,\frac{dm_0}{d\tau}\,u^\mu_{\rm fluid}\,, \tag{3.28}$$

where we recall that h is the specific enthalpy of the fluid. Note that this equation basically follows from the conservation of the total 4-momentum of the satellite and the fluid.

The long-range drag is instead more complicated. The gravitational interaction of a body with the density perturbations that it excites gravitationally in the surrounding medium was first studied by Chandrasekhar [53] in the case of a collisionless fluid, and is also known as "dynamical friction". Although less well recognised, dynamical friction acts also for a body moving in a collisional medium (see refs. [62, 63, 59, 66, 67, 68, 100] and chapter 2). In particular, a satellite moving on a circular planar orbit (*e.g.*, a circular orbit around a Schwarzschild black hole or a circular equatorial orbit around a Kerr black hole) experiences a drag in the tangential direction [62, 63, 59, 66, 67] and one in the radial direction [68]:

$$\left.\frac{dp^\mu}{d\tau}\right|_{\rm defl} = \left.\frac{dp}{d\tau}\right|^{\rm tang}_{\rm defl}\sigma^\mu + \left.\frac{dp}{d\tau}\right|^{\rm rad}_{\rm defl}\chi^\mu\,, \tag{3.29}$$

where $\boldsymbol{\sigma}$ is a unit spacelike vector orthogonal to $\boldsymbol{u}_{\rm sat}$ and pointing in the direction of the motion of the fluid,

$$\boldsymbol{\sigma} = \frac{\boldsymbol{u}_{\rm fluid} - \gamma\boldsymbol{u}_{\rm sat}}{\sqrt{\gamma^2-1}} \tag{3.30}$$

(the Lorentz factor $\gamma = -\boldsymbol{u}_{\rm fluid}\cdot\boldsymbol{u}_{\rm sat}$ encodes the relative motion of the satellite with respect to the fluid of the torus), and

$$\boldsymbol{\chi} = -\frac{u^{\rm sat}_r\boldsymbol{u}_{\rm sat} - \sigma_r\boldsymbol{\sigma} + \partial/\partial r}{[g_{rr} - (u^{\rm sat}_r)^2/(\gamma^2-1)]^{1/2}}\,, \tag{3.31}$$

is a unit spacelike vector, orthogonal to both $\boldsymbol{u}_{\rm sat}$ and $\boldsymbol{\sigma}$ and pointing in the radial direction. In particular, the tangential and radial drags are given by [68, 100]

$$\left.\frac{dp}{d\tau}\right|^{\rm tang}_{\rm defl} = \frac{4\pi(p+\rho)m^2\gamma^2(1+v^2)^2}{v^2}\,I_{\rm tang}\,, \tag{3.32}$$

$$\left.\frac{dp}{d\tau}\right|^{\rm rad}_{\rm defl} = \frac{4\pi(p+\rho)m^2\gamma^3(1+v^2)^2}{v^2}\,I_{\rm rad}\,, \tag{3.33}$$

where $I_{\rm tang}$ and $I_{\rm rad}$ are complicated integrals [given by eqs. (2.76) and (2.78)]. Fits to the numerically-computed steady-state values for these integrals are given in ref. [68] and were reported in chapter 2 [eqs. (2.80) and (2.79)]. In the present discussion, we rewrite

the torus and very close to the SMBH. For these orbits the dominant part of the hydrodynamic drag is the long-range one, and the relativistic correction factor to the Bondi accretion rate (which is roughly $5-10$ for these orbits, as can be seen comparing the middle panel of Fig. 3.1 with Table 3 of ref. [98]) does not change this conclusion.

here the form of these fits. If we denote the radius of the circular orbit by r and we define $r_{\rm min} \sim 2m(1+v^2)/v^2$ to be the capture impact parameter of the satellite black-hole[5] and $\mathcal{M} = v/v_s$ to be the Mach number, we have

$$I_{\rm tang} = \begin{cases} 0.7706 \ln\left(\frac{1+\mathcal{M}}{1.0004-0.9185\mathcal{M}}\right) - 1.4703\mathcal{M}, \\ \text{for } \mathcal{M} < 1.0\,, \\ \\ \ln[330(r/r_{\rm min})(\mathcal{M}-0.71)^{5.72}\mathcal{M}^{-9.58}], \\ \text{for } 1.0 \leq \mathcal{M} < 4.4\,, \\ \\ \ln[(r/r_{\rm min})/(0.11\mathcal{M}+1.65)], \\ \text{for } \mathcal{M} \geq 4.4\,, \end{cases} \tag{3.34}$$

and

$$I_{\rm rad} = \begin{cases} \mathcal{M}^2\ 10^{\,3.51\mathcal{M}-4.22}, \quad \text{for } \mathcal{M} < 1.1\,, \\ \\ 0.5\ \ln\left[9.33\mathcal{M}^2(\mathcal{M}^2-0.95)\right], \\ \text{for } 1.1 \leq \mathcal{M} < 4.4\,, \\ \\ 0.3\ \mathcal{M}^2, \quad \text{for } \mathcal{M} \geq 4.4\,. \end{cases} \tag{3.35}$$

As we have stressed, these fits are valid for $r \gg r_{\rm min}$ and are accurate to within 4% for $\mathcal{M} < 4.4$ and to within 16% for $\mathcal{M} > 4.4$. However, the fit for $I_{\rm tang}$ does not go to zero when $\mathcal{M}$ goes to zero, while $I_{\rm rad}$ goes to zero only as $\mathcal{M}^2$ in this limit: these behaviours would give a non-zero radial drag and a diverging tangential drag for $v \to 0$ [*cf.* eqs. (3.32) and (3.33)]. This is clearly a spurious behaviour: dynamical friction must vanish for $v = 0$, since in this case the pattern of the density perturbations is spherically symmetric around the body (as there is no preferred direction). However, as we will see in sec. 3.2.2, the effect of the radial drag vanishes if one uses the *adiabatic approximation* (as it is usually done in EMRI-studies [36, 41, 111, 112]), and therefore this artifact of the fit (3.35) cannot cause any harm in our numerical code. This is instead not the case for the tangential drag: in order to eliminate its spurious divergence, we have approximated $I_{\rm tang}$ with its straight-line functional form at low Mach numbers. Since the dynamical friction drag for straight-line subsonic motion is given by eq. (3.32) with $I_{\rm tang} = 1/2\ln[(1+\mathcal{M})/(1-\mathcal{M})] - \mathcal{M} \approx \mathcal{M}^3/3 + \mathcal{M}^5/5$, we can assume that $I_{\rm tang}$ is given, for $\mathcal{M} < 0.1$, by

$$I_{\rm tang} = 0.9563\left(\frac{\mathcal{M}^3}{3} + \frac{\mathcal{M}^5}{5}\right)\,, \tag{3.36}$$

where the factor 0.9563 is introduced to match the above fit at $\mathcal{M} = 0.1$.

Note that although eq. (3.29) is strictly valid only for circular planar motion (*i.e.*, in the case of a Kerr spacetime, for circular equatorial orbits), we expect it to be a good

[5] For a neutron star the capture parameter would be slightly larger, but but this would have only a minor effect on the results because the drag depends only logarithmically on $r_{\rm min}$ [*cf.* eq. (3.34)].

approximation also for generic orbits around a Kerr black hole. Indeed, thanks to the choice of the unit vectors $\boldsymbol{\sigma}$ and $\boldsymbol{\chi}$, eq. (3.29) gives a tangential drag parallel the direction of the flow and a drag in the radial direction perpendicular to the direction of the flow. Both of these components are expected to be present also for generic orbits[6]. In particular, the tangential drag should be given approximately by eqs. (3.32) and (3.36) if the radius r appearing in eq. (3.34) is replaced by the *semi-latus rectum* p of the orbit [see eq. (3.51) for the definition of this quantity.[7]] Although this prescription is not exact, the results of ref. [68] suggest that the relevant lengthscale in the Coulomb logarithm appearing in the second and third lines of eq. (3.34) should be one characterising the orbit, rather than the size of the medium, as commonly assumed in most of the works on dynamical friction predating refs. [66, 68] (see the introduction of ref. [68] and references therein for more details about this point). Of course, this lengthscale could be different from the semi-latus rectum of the orbit, but different choices for it would have only a slight impact on the results because of the logarithmic dependence.

The extrapolation of the radial drag given by eqs. (3.33) and (3.35) from circular planar to generic orbits is instead a bit more problematic, although one expects it to be a good approximation at least for orbits with small eccentricities and small inclinations with respect to the equatorial plane. At any rate, as we have mentioned earlier, in sec. 3.2.2 we will show that the effect of this radial drag on the orbital evolution averages to zero when adopting the *adiabatic approximation*. (Note that this agrees with ref. [68], which found that the effect of the radial drag on the orbital evolution was subdominant with respect to that of the tangential drag.) Nevertheless, a non-zero effect may still be present in cases in which the adiabatic approximation is not valid (*i.e.* if the hydrodynamic drag acts on a timescale comparable to the orbital period), or possibly even in the adiabatic approximation if more rigorous expressions for the radial drag should be derived in the future.

The rate of change of the mass of the satellite with respect to the coordinate time t follows immediately from $p^{\mu}_{\rm sat}\, p^{\rm sat}_{\mu} = -m^2$: denoting the derivative with respect to t with an overdot, we have

$$\dot{m} = -\frac{u^{\rm sat}_{\mu}}{u^{t}_{\rm sat}} \frac{dp^{\mu}_{\rm sat}}{d\tau} = -\frac{u^{\rm sat}_{\mu}}{u^{t}_{\rm sat}} \frac{dp^{\mu}_{\rm accr}}{d\tau} = \frac{h\,\gamma}{u^{t}_{\rm sat}} \frac{dm_0}{d\tau} \,. \tag{3.37}$$

It is well-known [113] that Kerr geodesics can be labelled, up to initial conditions, by

[6] Note that the tangential drag is due to the backward gravitational pull exerted by the wake, while the radial drag comes about because the wake "bends" if the satellite does not move on a straight line, thus exerting a non-zero gravitational attraction on the satellite [68]. Therefore, it is clear that both of these components must be present, unless the satellite moves on a straight line, in which case only the tangential drag is present.

[7] Note that the tangential drag given by eqs. (3.32), (3.34) and (3.36) is approximately correct also for straight-line motion, if r replaced in eq. (3.34) by vt – t being the time for which the satellite has been active [66, 100] – as long as vt is smaller than the size of the medium, and by a cutoff-length of order of the size of the medium at later times. To see this, compare eqs. (3.34) and (3.36) to the functional form of $I_{\rm tang}$ for straight-line motion [eq. (2.65)].

three constants of motion, the dimensionless energy $\tilde{E}$ and the angular momentum $\tilde{L}_z$ as measured by an observer at infinity,

$$\tilde{E} = -u_t^{\rm sat}\,, \quad \tilde{L}_z = u_\phi^{\rm sat}/M\,, \tag{3.38}$$

and the dimensionless Carter constant [113] $\tilde{Q}$,

$$\tilde{Q} = \left(\frac{u_\theta^{\rm sat}}{M}\right)^2 + \tilde{a}^2\cos^2\theta(1-\tilde{E}^2) + \cot^2\theta\tilde{L}_z^2 \tag{3.39}$$

where $\tilde{a} = a/M$. We will now derive expression for the rates of change of these quantities.

To this purpose, let us first introduce the tetrad $(\boldsymbol{u}_{\rm sat}, \boldsymbol{e}_1 = \boldsymbol{\sigma}, \boldsymbol{e}_2 = \boldsymbol{\chi}, \boldsymbol{e}_3)$ based in the position of the satellite and write the change in the 4-velocity due to accretion and deflection of the flow as

$$\delta u^\mu_{\rm sat} = \delta u^{(t)}_{\rm sat} u^\mu_{\rm sat} + \delta u^{(i)}_{\rm sat} e^\mu_{(i)}\,, \tag{3.40}$$

where $\delta u^{(t)}_{\rm sat}$ and $\delta u^{(i)}_{\rm sat}$ are the components with respect to the tetrad. In particular, perturbing $-(u^{(t)}_{\rm sat})^2 + \delta_{ij}u^{(i)}_{\rm sat}u^{(j)}_{\rm sat} = -1$ to first order one easily gets $-u^{(t)}_{\rm sat}\delta u^{(t)}_{\rm sat} + \delta_{ij}u^{(i)}_{\rm sat}\delta u^{(j)}_{\rm sat} = 0$, and using then the fact that $u^{(i)}_{\rm sat} = 0$ to zeroth order, one obtains $\delta u^{(t)}_{\rm sat} = 0$. Using now $\delta u^{(i)}_{\rm sat} = \delta p^{(i)}_{\rm sat}/m$, $\boldsymbol{e}_{(i)}\cdot\boldsymbol{u}_{\rm sat} = 0$ and $\boldsymbol{e}_{(i)}\cdot\boldsymbol{e}_{(j)} = \delta_{ij}$ $(i = 1, 2, 3)$, eq. (3.40) becomes

$$\begin{aligned}\delta u^\mu_{\rm sat} &= \left(\frac{\delta m_0\, h}{m}u^\nu_{\rm fluid}\,\sigma_\nu + \frac{\delta p^{\rm tang}_{\rm defl}}{m}\right)\sigma^\mu + \frac{\delta p^{\rm rad}_{\rm defl}}{m}\chi^\mu \\ &= \left(\frac{\delta m_0\, h}{m} + \frac{\delta p^{\rm tang}_{\rm defl}}{m\sqrt{\gamma^2-1}}\right)\left(u^\mu_{\rm fluid} - \gamma u^\mu_{\rm sat}\right) + \frac{\delta p^{\rm rad}_{\rm defl}}{m}\chi^\mu\,. \end{aligned}\tag{3.41}$$

Using now eqs. (3.3), (3.38) and (3.41), we immediately obtain

$$\frac{\dot{\tilde{E}}}{\tilde{E}} = \left(\frac{\dot{m}_0\, h}{m} + \frac{\dot{p}^{\rm tang}_{\rm defl}}{m\sqrt{\gamma^2-1}}\right)\left(\frac{U}{\tilde{E}} - \gamma\right) - \frac{\dot{p}^{\rm rad}_{\rm defl}}{m\tilde{E}}\chi_t\,, \tag{3.42}$$

$$\frac{\dot{\tilde{L}}_z}{\tilde{L}_z} = \left(\frac{\dot{m}_0\, h}{m} + \frac{\dot{p}^{\rm tang}_{\rm defl}}{m\sqrt{\gamma^2-1}}\right)\left(\frac{\ell\, U}{M\tilde{L}_z} - \gamma\right) + \frac{\dot{p}^{\rm rad}_{\rm defl}}{mM\tilde{L}_z}\chi_\phi\,. \tag{3.43}$$

In order to calculate instead the rate of change of the dimensionless Carter constant $\tilde{Q}$, let us note that from eq. (3.41) it follows that the variation of u_θ in a short time interval δt due to accretion and deflection of the flow is

$$\delta u^{\rm sat}_\theta = \left[-\gamma\left(\frac{\dot{m}_0\, h}{m} + \frac{\dot{p}^{\rm tang}_{\rm defl}}{m\sqrt{\gamma^2-1}}\right)u^{\rm sat}_\theta + \frac{\dot{p}^{\rm rad}_{\rm defl}}{m}\chi_\theta\right]\delta t\,. \tag{3.44}$$

We can then write $\dot{u}^{\rm sat}_\theta$ as the sum of a term coming from the gravitational evolution (*i.e.,*

the geodesic equation) and one coming from collisions with the surrounding gas:

$$\dot{u}_\theta^{\rm sat} = \Gamma^\mu_{\theta\nu} u_\mu^{\rm sat} \dot{x}^\nu_{\rm sat} - \gamma \left(\frac{\dot{m}_0\, h}{m} + \frac{\dot{p}^{\rm tang}_{\rm defl}}{m\sqrt{\gamma^2-1}} \right) u_\theta^{\rm sat} + \frac{\dot{p}^{\rm rad}_{\rm defl}}{m} \chi_\theta \; . \tag{3.45}$$

The evolution of $\tilde{Q}$ therefore follows from eq. (3.39):

$$\begin{aligned}
\dot{\tilde{Q}} = {} & \frac{\partial \tilde{Q}}{\partial \theta} \dot{\theta}_{\rm sat} + \frac{\partial \tilde{Q}}{\partial u_\theta^{\rm sat}} \Gamma^\mu_{\theta\nu} u_\mu^{\rm sat} \dot{x}^\nu_{\rm sat} + \frac{\partial \tilde{Q}}{\partial \tilde{E}} \dot{\tilde{E}} + \frac{\partial \tilde{Q}}{\partial \tilde{L}_z} \dot{\tilde{L}}_z \\
& - \frac{\partial \tilde{Q}}{\partial u_\theta^{\rm sat}} \gamma \left(\frac{\dot{m}_0\, h}{m} + \frac{\dot{p}^{\rm tang}_{\rm defl}}{m\sqrt{\gamma^2-1}} \right) u_\theta^{\rm sat} + \frac{\partial \tilde{Q}}{\partial u_\theta^{\rm sat}} \frac{\dot{p}^{\rm rad}_{\rm defl}}{m} \chi_\theta = \\
& \frac{\partial \tilde{Q}}{\partial \tilde{E}} \dot{\tilde{E}} + \frac{\partial \tilde{Q}}{\partial \tilde{L}_z} \dot{\tilde{L}}_z - \frac{\partial \tilde{Q}}{\partial u_\theta^{\rm sat}} \gamma \left(\frac{\dot{m}_0\, h}{m} + \frac{\dot{p}^{\rm tang}_{\rm defl}}{m\sqrt{\gamma^2-1}} \right) u_\theta^{\rm sat} + \frac{\partial \tilde{Q}}{\partial u_\theta^{\rm sat}} \frac{\dot{p}^{\rm rad}_{\rm defl}}{m} \chi_\theta,
\end{aligned} \tag{3.46}$$

where the partial derivatives are meant to be calculated with eq. (3.39). Note that the first and the second term of the first line cancel out because $\tilde{Q}$ is conserved for geodesic motion.

A useful alternative form for the evolution rate of $\tilde{Q}$ can be obtained by rewriting eq. (3.39) using the normalisation condition $\boldsymbol{u}^{\rm sat} \cdot \boldsymbol{u}^{\rm sat} = -1$:

$$\tilde{Q} = \tilde{\Delta}^{-1} \left[\tilde{E}(\tilde{r}^2 + \tilde{a}^2) - \tilde{a}\tilde{L} \right]^2 - (\tilde{L} - \tilde{a}\tilde{E})^2 - \tilde{r}^2 - \tilde{\Delta} (u_r^{\rm sat})^2 \; , \tag{3.47}$$

where $\tilde{r} = r/M$ and $\tilde{\Delta} = \Delta/M^2$. Proceeding as above and in particular using the fact that

$$\dot{u}_r^{\rm sat} = \Gamma^\mu_{r\nu} u_\mu^{\rm sat} \dot{x}^\nu_{\rm sat} - \gamma \left(\frac{\dot{m}_0\, h}{m} + \frac{\dot{p}^{\rm tang}_{\rm defl}}{m\sqrt{\gamma^2-1}} \right) u_r^{\rm sat} + \frac{\dot{p}^{\rm rad}_{\rm defl}}{m} \chi_r \tag{3.48}$$

[from eqs. (3.3) and (3.41)], one easily gets

$$\begin{aligned}
\dot{\tilde{Q}} = {} & \frac{\partial \tilde{Q}}{\partial r} \dot{r}_{\rm sat} + \frac{\partial \tilde{Q}}{\partial u_r^{\rm sat}} \Gamma^\mu_{r\nu} u_\mu^{\rm sat} \dot{x}^\nu_{\rm sat} + \frac{\partial \tilde{Q}}{\partial \tilde{E}} \dot{\tilde{E}} + \frac{\partial \tilde{Q}}{\partial \tilde{L}_z} \dot{\tilde{L}}_z \\
& - \frac{\partial \tilde{Q}}{\partial u_r^{\rm sat}} \gamma \left(\frac{\dot{m}_0\, h}{m} + \frac{\dot{p}^{\rm tang}_{\rm defl}}{m\sqrt{\gamma^2-1}} \right) u_r^{\rm sat} + \frac{\partial \tilde{Q}}{\partial u_r^{\rm sat}} \frac{\dot{p}^{\rm rad}_{\rm defl}}{m} \chi_r \\
= {} & \frac{\partial \tilde{Q}}{\partial \tilde{E}} \dot{\tilde{E}} + \frac{\partial \tilde{Q}}{\partial \tilde{L}_z} \dot{\tilde{L}}_z - \frac{\partial \tilde{Q}}{\partial u_r^{\rm sat}} \gamma \left(\frac{\dot{m}_0\, h}{m} + \frac{\dot{p}^{\rm tang}_{\rm defl}}{m\sqrt{\gamma^2-1}} \right) u_r^{\rm sat} + \frac{\partial \tilde{Q}}{\partial u_r^{\rm sat}} \frac{\dot{p}^{\rm rad}_{\rm defl}}{m} \chi_r \; ,
\end{aligned} \tag{3.49}$$

where the partial derivatives are now calculated with eq. (3.47). Note that for circular orbits eq. (3.49) becomes

$$\dot{\tilde{Q}} = \frac{\partial \tilde{Q}}{\partial \tilde{E}} \dot{\tilde{E}} + \frac{\partial \tilde{Q}}{\partial \tilde{L}_z} \dot{\tilde{L}}_z \tag{3.50}$$

[use eq. (3.47) and the fact that $u_r^{\rm sat}=0$ for circular orbits]. This condition ensures[8] that circular orbits keep circular under the hydrodynamic drag and in the adiabatic approximation, as it happens for radiation reaction.

Finally, let us note that the rates of change of $\tilde{E}$, $\tilde{L}_z$ and $\tilde{Q}$ [eqs. (3.42), (3.43), (3.46) and (3.49)] go smoothly to zero as the velocity of the satellite relative to the fluid goes to zero. This is easy to check using the fact that, when v approaches zero, $\dot{p}^{\rm tang}_{\rm defl}=\mathcal{O}(v)$ [*cf.* eqs. (3.32) and (3.36)], $\dot{p}^{\rm rad}_{\rm defl}\to 0$, $\gamma^2-1=\mathcal{O}(v^2)$, $u_r=\mathcal{O}(v)$, $u_\theta=\mathcal{O}(v)$, $\ell U-M\tilde{L}_z=\mathcal{O}(v)$ and $U-\tilde{E}=\mathcal{O}(v^2)$, and using the fact that $\boldsymbol{\chi}$ keeps finite in this limit [in particular, from eqs. (3.30) and (3.31) it follows $\chi_t=\mathcal{O}(v)$, $\chi_\phi=\mathcal{O}(1)$, $\chi_\theta=\mathcal{O}(1)$ and $\chi_r=\mathcal{O}(1)$]. Note that this is indeed the result that one would expect. First of all, a body comoving with the fluid clearly does not experience any dynamical friction and the only active mechanism is accretion. The body then accretes mass and consequently energy and angular momentum (because the fluid carries a specific energy and a specific angular momentum). However, the *dimensionless* constants of motion $\tilde{E}$, $\tilde{L}_z$ and $\tilde{Q}$ entering the geodesic equation cannot change because of the weak equivalence principle. Pictorially, one may think of a satellite comoving with a gaseous medium. Consider a sphere centred in the satellite, with radius small enough to ensure that the gas contained in the sphere has approximately the same velocity as the satellite. Suppose now that all the gas in this sphere is accreted by the satellite. The velocity of the satellite will clearly be unaffected, because of the conservation of momentum: for the weak equivalence principle this is enough to ensure that the orbit of the satellite will be unaffected, in spite of its increased mass.

3.2.2 The adiabatic approximation

At the heart of our approach is the calculation of the changes of the orbital parameters experienced by Kerr geodesics as a result of the hydrodynamic drag, and their comparison with the corresponding changes introduced by radiation reaction. To this purpose, let us recall that up to initial conditions Kerr geodesics can be labelled by a set of three parameters, the *semi-latus rectum* p, the *eccentricity* e and the *inclination angle* $\theta_{\rm inc}$. These are just a remapping of the energy, angular momentum and Carter constant introduced in sec. 3.2.1, and are defined as [116]

$$p=\frac{2r_{\rm a}r_{\rm p}}{r_{\rm a}+r_{\rm p}}\,,\quad e=\frac{r_{\rm a}-r_{\rm p}}{r_{\rm a}+r_{\rm p}}\,,\quad \theta_{\rm inc}=\frac{\pi}{2}-D\,\theta_{\rm min}\,, \tag{3.51}$$

where $r_{\rm a}$ and $r_{\rm p}$ are the apoastron and periastron coordinate radii, $\theta_{\rm min}$ is the minimum polar angle θ reached during the orbital motion and $D=1$ for orbits corotating with the SMBH whereas $D=-1$ for orbits counter-rotating with respect to it. Note that in the weak-field limit p and e correspond exactly to the semi-latus rectum and eccentricity used

[8] Note in particular that the proof presented in ref. [114], which was concerned mainly with radiation reaction, applies also to the case of the hydrodynamic drag. Note also that the resonance condition which was found in ref. [114] as the only possible case that could give rise to a non-circular evolution for an initially circular orbit is never satisfied in a Kerr spacetime [115].

to describe orbits in Newtonian gravity, and that $\theta_{\rm inc}$ goes from $\theta_{\rm inc}=0$ for equatorial orbits corotating with the black hole to $\theta_{\rm inc}=180$ degrees for equatorial orbits counter-rotating with respect to the black hole, passing through $\theta_{\rm inc}=90$ degrees for polar orbits.

In order to fix the initial conditions of a geodesic, let us first parameterise it with the Carter time λ, which is related to the proper time by [113]

$$\frac{d\tau}{d\lambda}=\Sigma\ . \tag{3.52}$$

This is a very useful choice because it makes the geodesic equation separable [113]:

$$\begin{aligned}\left(\frac{dr}{d\lambda}\right)^2&=V_r(r), &\qquad \frac{dt}{d\lambda}&=V_t(r,\theta),\\ \left(\frac{d\theta}{d\lambda}\right)^2&=V_\theta(\theta), &\qquad \frac{d\phi}{d\lambda}&=V_\phi(r,\theta)\ ,\end{aligned} \tag{3.53}$$

with

$$V_t(r,\theta)/M^2=\tilde{E}\left[\frac{(\tilde{r}^2+\tilde{a}^2)^2}{\tilde{\Delta}}-\tilde{a}^2\sin^2\theta\right]+\tilde{a}\tilde{L}_z\left(1-\frac{\tilde{r}^2+\tilde{a}^2}{\tilde{\Delta}}\right), \tag{3.54}$$

$$V_r(r)/M^4=\left[\tilde{E}(\tilde{r}^2+\tilde{a}^2)-\tilde{a}\tilde{L}_z\right]^2-\tilde{\Delta}\left[\tilde{r}^2+(\tilde{L}_z-\tilde{a}\tilde{E})^2+\tilde{Q}\right], \tag{3.55}$$

$$V_\theta(\theta)/M^2=\tilde{Q}-\tilde{L}_z^2\cot^2\theta-\tilde{a}^2(1-\tilde{E}^2)\cos^2\theta, \tag{3.56}$$

$$V_\phi(r,\theta)/M=\tilde{L}_z\csc^2\theta+\tilde{a}\tilde{E}\left(\frac{\tilde{r}^2+\tilde{a}^2}{\tilde{\Delta}}-1\right)-\frac{\tilde{a}^2\tilde{L}_z}{\tilde{\Delta}}. \tag{3.57}$$

This means, in particular, that the r- and θ-motions are periodic in λ. The initial conditions of the geodesic can then be characterised by the values t_0 and ϕ_0 of the coordinates t and ϕ when $\lambda=0$, the value λ_{r0} of the Carter time nearest to $\lambda=0$ at which $r(\lambda_{r0})=r_{\rm p}$, and the value $\lambda_{\theta 0}$ of the Carter time nearest to $\lambda=0$ at which $\theta(\lambda_{\theta 0})=\theta_{\rm min}$ [111].

Let us first fix the geodesic under consideration by choosing the parameters p, e and $\theta_{\rm inc}$ so as to obtain a bound and stable orbit (see ref. [116] for details) and by choosing the initial conditions as described above. One could in principle use eqs. (3.42), (3.43) and (3.46) [or (3.49)] to compute the rates of change of $\tilde{E}$, $\tilde{L}_z$ and $\tilde{Q}$ due to the hydrodynamic drag as a function the Carter time λ. However, because the timescale of the orbital evolution due to the interaction with the torus is much longer than the orbital period, we can apply the adiabatic approximation and compute instead the averages of $\dot{\tilde{E}}$, $\dot{\tilde{L}}_z$ and $\dot{\tilde{Q}}$ over times much longer than the orbital periods. This approximation is routinely adopted when studying the effect of radiation reaction on EMRIs [36, 41, 111, 112], and it is easy to implement when one considers instead the effect of the hydrodynamic drag. Denoting respectively with $\langle\ \rangle_t$ and $\langle\ \rangle_\lambda$ the average over an infinite coordinate time and

the average over an infinite Carter time, we can write [111]

$$\langle \dot{\Psi} \rangle_t = \frac{\langle d\Psi/d\lambda \rangle_\lambda}{\langle dt/d\lambda \rangle_\lambda} \,, \tag{3.58}$$

where Ψ is a place-holder for either $\tilde{E}, \tilde{L}_z$ or $\tilde{Q}$.

Using now eq. (3.3) (with the assumption that the torus is symmetric with respect to the equatorial plane) in eqs. (3.42), (3.43) and (3.46) [or (3.49)], it is easy to show that $d\tilde{E}/d\lambda$, $d\tilde{L}_z/d\lambda$ and $d\tilde{Q}/d\lambda$ depend, once fixed $\tilde{E}$, $\tilde{L}_z$ and $\tilde{Q}$, only on the r and $\cos^2\theta$ of the geodesic under consideration – *i.e.*, $r = r(\lambda, \lambda_{r0})$ and $\cos^2\theta = \cos^2\theta(\lambda, \lambda_{\theta 0})$ – and on the sign of $u_r^{\rm sat}$, which we will denote by ϵ_r. [The dependence on this sign arises because of the terms due to the radial drag, as the quantity $u_r^{\rm sat}$ appearing in the definitions of $\boldsymbol{\sigma}$ and $\boldsymbol{\chi}$ can be expressed in terms of r and $\cos^2\theta$ using eqs. (3.52)-(3.57) only up to such a sign.] Similarly, $dt/d\lambda$ is given by the geodesic equation (3.53) and depends, once fixed $\tilde{E}$, $\tilde{L}_z$ and $\tilde{Q}$, only on the r and $\cos^2\theta$ of the geodesic [*cf.* eq. (3.54)].

Using now the fact that the r- and θ-motions are periodic when expressed in the Carter time, we can expand the functions $d\tilde{E}/d\lambda$, $d\tilde{L}_z/d\lambda$ and $d\tilde{Q}/d\lambda$ and $dt/d\lambda$ appearing in eq. (3.58) in a Fourier series. Noting that the oscillating terms average out, one can then write these equations using only averages of these functions over the r- and θ-periods. More precisely, writing the r- and θ-motions as $r(\lambda, \lambda_{r0}) = \hat{r}(\lambda - \lambda_{r0})$ and $\theta(\lambda, \lambda_{\theta 0}) = \hat{\theta}(\lambda - \lambda_{\theta 0})$ (where we have denoted with a "hat" a fiducial geodesic having the same $\tilde{E}$, $\tilde{L}_z$ and $\tilde{Q}$ as the geodesic under consideration and $\lambda_{r0} = \lambda_{\theta 0} = 0$), using the fact that $d\tilde{E}/d\lambda$, $d\tilde{L}_z/d\lambda$ and $d\tilde{Q}/d\lambda$ depend on r, $\cos^2\theta$ and ϵ_r, and using the fact that $dt/d\lambda$ depends only on r and $\cos^2\theta$, we can easily write eq. (3.58) as [111]

$$\langle \dot{\Psi} \rangle_t = \frac{\int_0^{\Lambda_r} d\lambda_r \int_0^{\Lambda_\theta/4} d\lambda_\theta \, d\Psi/d\lambda(\hat{r}(\lambda_r), \cos^2\hat{\theta}(\lambda_\theta), \epsilon_r)}{\int_0^{\Lambda_r} d\lambda_r \int_0^{\Lambda_\theta/4} d\lambda_\theta \, V_t(\hat{r}(\lambda_r), \cos^2\hat{\theta}(\lambda_\theta))} \,, \tag{3.59}$$

where Ψ is again a place-holder for either $\tilde{E}, \tilde{L}_z$ or $\tilde{Q}$. Note that here Λ_r and Λ_θ are the r- and θ-periods and $d\tilde{E}/d\lambda$, $d\tilde{L}_z/d\lambda$ and $d\tilde{Q}/d\lambda$ and $dt/d\lambda$ are expressed using eqs. (3.42), (3.43), (3.46) [or (3.49)], (3.53) and (3.54)-(3.57). Using now the definitions of $\boldsymbol{\sigma}$ and $\boldsymbol{\chi}$ [eqs. (3.30) and (3.31)], it is easy to check that the changes of $\tilde{E}$, $\tilde{L}_z$ and $\tilde{Q}$ arising from the radial drag average out in the above equation because of the presence of the sign ϵ_r (in particular $\chi_t, \chi_\phi, \chi_\theta \propto \epsilon_r$). As a result, one can assume $\dot{p}^{\rm rad}_{\rm defl} = 0$ *ab initio* when computing eq. (3.59) and benefit from another small simplification since, as we have already mentioned, $d\tilde{E}/d\lambda$, $d\tilde{L}_z/d\lambda$ and $d\tilde{Q}/d\lambda$ would depend only on r and $\cos^2\theta$ if it were not for the radial drag, which brings in the dependence on ϵ_r. With this assumption, all of the integrals appearing in (3.59) can therefore be performed over $\lambda_r \in [0, \Lambda_r/2]$ rather than over $\lambda_r \in [0, \Lambda_r]$. Finally, note also that the rates of change (3.59) do not depend on the initial conditions λ_{r0} and $\lambda_{\theta 0}$ of the geodesic.

In order to reduce eq. (3.59) to a form suitable for numerical integration, we can express

our fiducial geodesic with the phase variables ψ and χ, defined by [41, 116, 117]

$$\hat{r}(\psi) = \frac{p}{1 + e\cos\psi}\,, \tag{3.60}$$

$$\cos\hat{\theta}(\chi) = z_- \cos\chi\,. \tag{3.61}$$

Note that ψ and χ change by 2π during respectively an r- and a θ-period. Inserting then these definitions into the geodesic equation (3.53) one gets [41, 116, 117]

$$\frac{d\psi}{d\lambda} = \frac{p}{1-e^2}\sqrt{J(\psi)}\,, \tag{3.62}$$

$$\frac{d\chi}{d\lambda} = M\sqrt{\beta(z_+ - z_-\cos^2\chi)}\,, \tag{3.63}$$

where

$$\begin{aligned} J(\psi) &= (1-\tilde{E}^2)(1-e^2) + 2\left(1 - \tilde{E}^2 - \frac{1-e^2}{\tilde{p}}\right)(1 + e\cos\psi) \\ &+ (1+e\cos\psi)^2 \times \left[(1-\tilde{E}^2)\frac{3+e^2}{1-e^2} - \frac{4}{\tilde{p}} + \frac{1-e^2}{\tilde{p}^2}(\beta + \tilde{L}_z^2 + \tilde{Q})\right]\,, \end{aligned} \tag{3.64}$$

$$\beta = \tilde{a}^2(1-\tilde{E}^2)\,, \tag{3.65}$$

$$z_+ = \frac{\tilde{Q} + \tilde{L}_z^2 + \beta + \sqrt{(\tilde{Q} + \tilde{L}_z^2 + \beta)^2 - 4\beta\tilde{Q}}}{2\beta}\,, \tag{3.66}$$

with $\tilde{p} = p/M$. Note that $d\psi/d\lambda$ and $d\chi/d\lambda$, differently from $dr/d\lambda$ and $d\theta/d\lambda$, are non-zero at the inversion points of the r- and θ-motions, making ψ and χ very useful for numerical integration.

Changing the integration variables λ_r and λ_θ to ψ and χ, eq. (3.59) becomes

$$\begin{aligned} \langle\dot{\Psi}\rangle_t = \int_0^\pi d\psi \int_0^{\pi/2} d\chi \frac{d\Psi/d\lambda|_{\dot{p}^{\rm rad}_{\rm defl}=0}(\hat{r}(\psi), \cos^2\hat{\theta}(\chi))(1-e^2)}{p\sqrt{J(\psi)\beta(z_+ - z_-\cos^2\chi)}} \times \\ \times \left[\int_0^\pi d\psi \int_0^{\pi/2} d\chi \frac{V_t(\hat{r}(\psi), \cos^2\hat{\theta}(\chi))(1-e^2)}{p\sqrt{J(\psi)\beta(z_+ - z_-\cos^2\chi)}}\right]^{-1}\,. \end{aligned} \tag{3.67}$$

Note that the two-dimensional integrals involved in these expressions can easily be computed numerically (*e.g.*, iterating Romberg's method [118]) once the orbital parameters p, e, $\theta_{\rm inc}$ of the geodesic under consideration have been fixed.

3.3 Results

In this section we will consider constant-ℓ tori around Kerr SMBHs and compare their influence on EMRIs with that of gravitational wave emission (*i.e.*, radiation reaction) in

the adiabatic approximation. In particular, we will compute the rates of change (3.67) of the energy, angular momentum and Carter constant due to the hydrodynamic drag, for circular equatorial orbits (sec. 3.3.1) and for generic (inclined and eccentric) orbits (sec. 3.3.2). Since $\tilde{E}$, $\tilde{L}_z$ and $\tilde{Q}$ can be expressed analytically as functions of the orbital parameters p, e and $\theta_{\rm inc}$ [116], it is then easy to compute the rates of change dp/dt, de/dt and $d\theta_{\rm inc}/dt$ due to the hydrodynamic drag. For the same orbits, we will consider also the radiation reaction, for which we will use the approximate fluxes $d\tilde{E}/dt$, $d\tilde{L}_z/dt$ and $d\tilde{Q}/dt$ of ref. [119] to compute dp/dt, de/dt and $d\theta_{\rm inc}/dt$. Note that these fluxes (often referred to as "kludge" fluxes in the literature) are a good approximation to the fluxes computed rigorously in the adiabatic approximation with the Teukolsky-Sasaki-Nakamura formalism [41, 120]. In fact, since they are based on a post-Newtonian expansion corrected with fits to fluxes computed with the Teukolsky-Sasaki-Nakamura formalism for circular orbits, these kludge fluxes are accurate within 3% for circular orbits and their accuracy is expected to be within $10-15\%$ also for generic orbits with $p \gtrsim 6M$. Moreover, they are expected to be off at most by $25-30\%$ even for smaller values of the semi-latus rectum p (*cf.* ref. [119], Table I).

The mass of the SMBH is fixed to $M = 10^6 M_\odot$ while its spin parameter a ranges from $-0.998M$ to $0.998M$ (note that $|a| = 0.998M$ is a reasonable upper limit for the spin attainable as the result of mass accretion [121] or binary black-hole mergers [122, 123]), and the mass of the satellite black hole is instead $m = 1M_\odot$. The constant-ℓ torus (which, as we have already mentioned, is taken to rotate in the positive ϕ-direction) is assumed to be composed of an isentropic monatomic gas (*i.e.*, a $\Gamma = 5/3$ polytrope) and is considered to be exactly filling its outermost closed equipotential surface ($\Delta W = 0$), so as to present a zero accretion rate $\dot{M}$ onto the SMBH.[9] Assuming $\Delta W = 0$ and $\Gamma = 5/3$, the specific angular momentum of the torus is then uniquely fixed by choosing the outer radius. A reasonable outer radius for a realistic accretion disk is given by $r_{\rm out} = 10^5 M$ [96], and this is indeed the value that we will use for most of our analysis, although we will briefly consider also different values for $r_{\rm out}$ in order to study the impact of this parameter on the final results. The polytropic constant κ of the equation of state is finally fixed by the requirement that $M_{\rm t} = 0.1M$. While this could be a reasonable value for the mass of a realistic accretion disk in AGNs [96], we will see that our results scale proportionally to $M_{\rm t}$, thus allowing one to extrapolate them easily to the case $M_{\rm t} = M$, which is certainly an astrophysically plausible value, but one for which our test-fluid approach is no longer valid.

[9] While realistic thick disks are generally expected to accrete onto the SMBH, these configurations are clearly non-stationary and cannot therefore be reproduced within our framework. However, it is easy to show that if one cuts-off a torus solution with $\dot{M} > 0$ at $r = r_{\rm cusp}$, the effect of the satellite-torus interaction will be enhanced with respect to the $\dot{M} = 0$ solution having the same mass and outer radius: the choice $\dot{M} = 0$ is thus useful to obtain at least a lower limit for the effect of the satellite-torus interaction on EMRIs.

Model	a	$M_{\rm t}/M$	$r_{\rm out}/M$	κ (CGS)	ℓ/M	$r_{\rm in}/M$	$r_{\rm centre}/M$	$\rho_{\rm centre}$ (g/cm^3)	$\rho_{\rm 0avg}$ (g/cm^3)
A1	0.900	0.100	1.000×10^{5}	4.198×10^{22}	2.6324500536	1.73246	3.60963	4.060×10^{-5}	1.475×10^{-11}
A2	-0.900	0.100	1.000×10^{5}	4.189×10^{22}	4.7567317819	5.65700	15.58890	3.992×10^{-6}	1.476×10^{-11}
B1	0.998	0.100	1.000×10^{5}	4.200×10^{22}	2.0894422310	1.09144	1.56484	1.868×10^{-4}	1.474×10^{-11}
B2	0.500	0.100	1.000×10^{5}	4.195×10^{22}	3.4141929560	2.91425	7.16458	1.331×10^{-5}	1.475×10^{-11}
B3	0.000	0.100	1.000×10^{5}	4.192×10^{22}	3.9999599993	4.00008	10.47174	7.355×10^{-6}	1.475×10^{-11}
B4	-0.500	0.100	1.000×10^{5}	4.190×10^{22}	4.4494291313	4.94962	13.39547	5.034×10^{-6}	1.475×10^{-11}
B5	-0.998	0.100	1.000×10^{5}	4.188×10^{22}	4.8269302324	5.82521	16.11218	3.796×10^{-6}	1.476×10^{-11}
C1	0.900	0.100	1.000×10^{3}	3.997×10^{20}	2.6319080229	1.73318	3.60622	4.323×10^{-2}	1.507×10^{-5}
C2	-0.900	0.100	1.000×10^{3}	3.607×10^{20}	4.7490561067	5.67540	15.49760	4.775×10^{-3}	1.573×10^{-5}
C3	0.900	0.100	1.000×10^{4}	4.170×10^{21}	2.6324007478	1.73253	3.60932	1.295×10^{-3}	1.479×10^{-8}
C4	-0.900	0.100	1.000×10^{4}	4.103×10^{21}	4.7560304461	5.65866	15.58057	1.297×10^{-4}	1.489×10^{-8}
C5	0.900	0.100	1.000×10^{6}	4.201×10^{23}	2.6324549842	1.73246	3.60967	1.283×10^{-6}	1.475×10^{-14}
C6	-0.900	0.100	1.000×10^{6}	4.199×10^{23}	4.7568019526	5.65683	15.58974	1.258×10^{-7}	1.475×10^{-14}

Table 3.1: *Models analysed in this chapter: all of them have $M = 10^6 M_\odot$, $\Gamma = 5/3$ and are filling exactly their outermost closed equipotential surface (i.e., they have $\Delta W = 0$). All the parameters are defined in sec. 3.1, except the average rest-mass density $\rho_{\rm 0avg} = M_{\rm t0}/V$, where $V = \int_{\rho_0>0} \sqrt{-g}\, d^3x$. Note that the specific angular momentum of the torus needs to be tuned with high accuracy in order to obtain large outer radii such as those considered in these models, and for this reason we report ℓ/M with 10 decimal digits.*

We should stress, however, that our results, when expressed in terms of the dimensionless orbital parameters p/M, e and $\theta_{\rm inc}$, are approximately independent of the mass M of the SMBH and of the mass m of the satellite black hole (provided that $M_{\rm t}/M$ and $r_{\rm out}/M$ are maintained constant). Indeed, since the ratios between the rates of change dp/dt, de/dt and $d\theta_{\rm inc}/dt$ due to the hydrodynamic drag and radiation reaction are of course dimensionless, it is not restrictive to fix $M = 1$, because this simply corresponds to choosing a system of units. Note in particular that this means that systems with different m and M but equal mass ratio m/M give exactly the same ratios between the rates of change dp/dt, de/dt and $d\theta_{\rm inc}/dt$ due to the hydrodynamic drag and radiation reaction. Moreover, these rates of change are proportional to m (in the case of the hydrodynamic drag this can be seen from eqs. (3.26), (3.32), (3.33), (3.42), (3.43) and (3.46), while in the case of radiation reaction see for instance ref. [119]), so this dependence on m cancels out when taking the ratio. The only dependence on m arises from the cutoff $r_{\rm min} \sim 2m(1+v^2)/v^2$ appearing in eq. (3.34), but this dependence clearly comes about only for supersonic velocities and is a logarithmic one. As such, the results which we present in this chapter, although derived in the case of $m = 1M_\odot$ and $M = 10^6 M_\odot$, are also valid for $m = 0.1M_\odot$ and $M = 10^5 M_\odot$ (exactly) or for $m = 1M_\odot$ and $M = 10^5 M_\odot$ (exactly for subsonic motion, and approximately – with an error comparable with those affecting the fit (3.34) or the kludge fluxes – for supersonic motion).

In all of our analysis we will focus on the region close to the SMBH ($r \lesssim 50M$), which contains only a small fraction of the mass of the torus (*e.g.*, in the case of model A1 of Table 3.1, the mass contained in a radius $r = 50M$ amounts to about $2.9\times10^{-5}M_{\rm t}$, and this fraction scales approximately as $r_{\rm out}^{-3/2}$ when considering tori with different outer radius). This is the region relevant for gravitational-wave experiments like LISA. In particular, an EMRI's signal is expected to be detectable by LISA when its frequency (which is twice the orbital frequency) increases above ≈ 2 mHz (below this frequency, in fact, there is a strong unresolvable foreground noise due to double white-dwarf binaries in our Galaxy [124]). This translates into a distance from the SMBH of $r \approx 10M$ for $M = 10^6 M_\odot$, and to $r \approx 45M$ for $M = 10^5 M_\odot$.

It should be noted, however, that the amplitude of an EMRI's signal scales with the distance from the SMBH: for a circular orbit of radius r, the Keplerian frequency is $2\pi\nu = M^{1/2}/(r^{3/2} \pm aM^{1/2}) \approx M^{1/2}/r^{3/2}$ and the amplitude of the signal is $h \sim (m/D)(2\pi\nu M)^{2/3} \sim (m/D)(M/r)$ [125], where D is the distance from the observer to the source. As such, an EMRI around a $10^5 M_\odot$ SMBH will have a gravitational-wave amplitude that at $r \sim 45M$ is about 10 times smaller than at $r \sim 5M$. Therefore, to see the details of the waveforms at $r \sim 45M$ the source must be ~ 10 times closer to us, which translates into a detection volume decreased by a factor ~ 1000. Nevertheless, this decrease of the detection volume may be compensated (at least partly) by the fact that the event-rate estimates consider only EMRIs in the strong-field region of the SMBH, even when $M = 10^5 M_\odot$ [17]. As such, since EMRIs in the early part of the inspiral are more numerous than those in the strong-field region, one expects to see a number of these events *larger* than the naive estimate given by the rate expected for strong-field EMRIs around a $10^5 M_\odot$ SMBH divided by the detection volume decrease factor ~ 1000. Of course, the event rates could be even

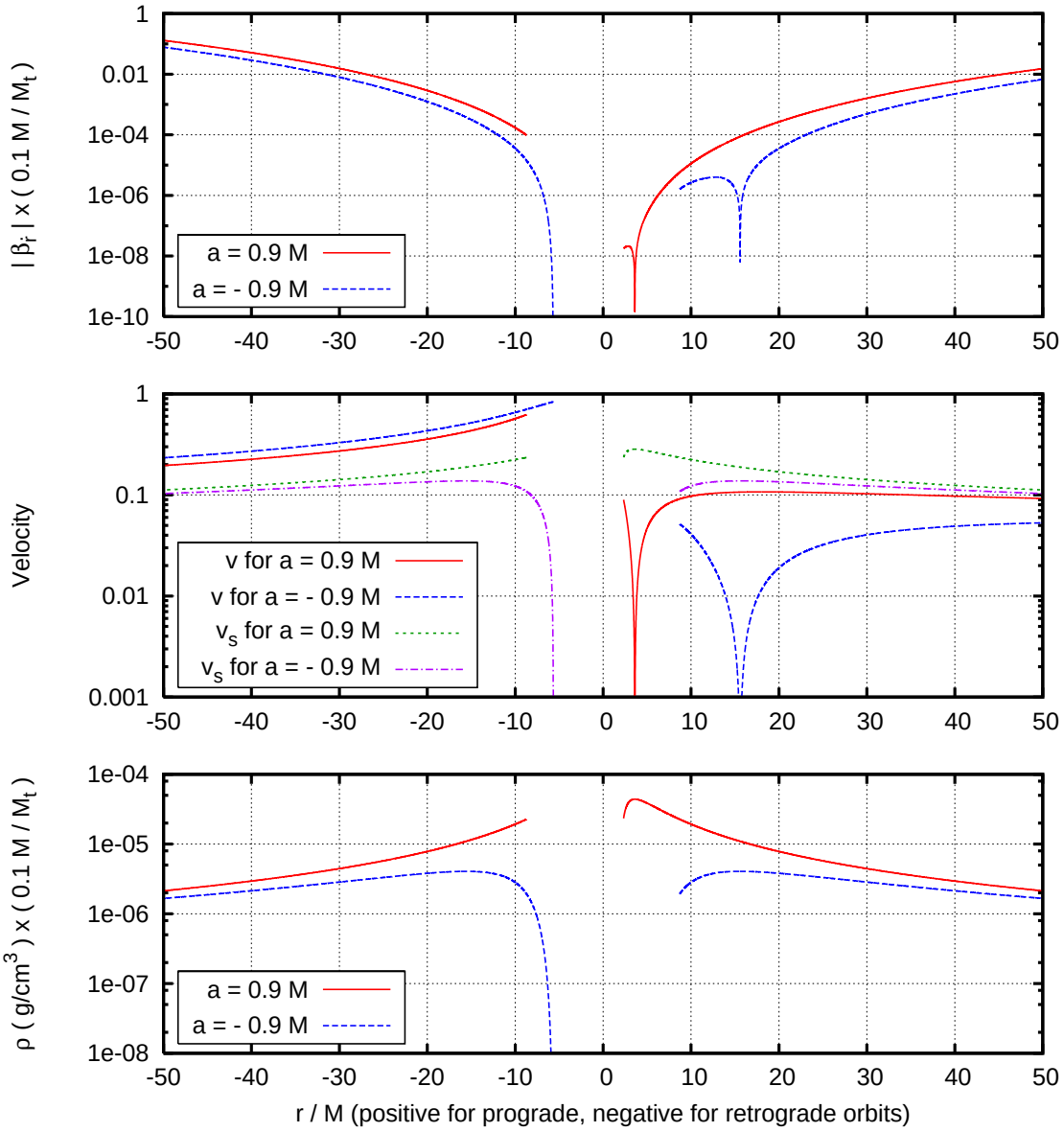

Figure 3.1: *The top plot shows the absolute value of the ratio* $\beta_{\dot{r}} \equiv (dr/dt)_{\rm hydro}/(dr/dt)_{\rm GW}$ *between the rates of change of the orbital radius due to hydrodynamic drag and radiation reaction, for circular bound stable orbits in the equatorial plane, as a function of the radius* r*. For graphical reasons* r *is considered positive for orbits in the positive* ϕ*-direction ("prograde orbits" i.e., corotating with the torus) and negative for those in the negative* ϕ*-direction ("retrograde orbits" i.e., counter-rotating with respect to the torus). Note that all the curves of this figure (including those of the middle and bottom plots) are terminated at the (prograde or retrograde) ISCO. The middle plot compares the velocity* v *of the satellite in the rest frame of the fluid with the sound velocity* v_s*, while the bottom plot shows the energy density of the torus. The curves refer to models A1 and A2 of Table 3.1, which are labelled here with the spin parameter* a *of the SMBH. Note that in all the plots the vertical axis is drawn in logarithmic scale. As such, the vertical asymptotes appearing in these plots actually correspond to a zero value for the quantity under consideration.*

larger if the satellite were a black hole with $m \sim 100M_\odot$, because the amplitude of the signal is proportional to m, but too little is presently known about these objects to draw any sound conclusions (see for instance ref. [20] for a review on intermediate mass black holes as possible sources for LISA).

3.3.1 Circular equatorial orbits

The evolution of circular equatorial orbits is very simple in the adiabatic approximation. As mentioned in sec. 3.2.1, both the radiation reaction and the hydrodynamic drag keep circular orbits circular and, due to the symmetry of the Kerr spacetime and of the torus with respect to the equatorial plane, equatorial orbits will remain equatorial. Therefore, the evolution of circular equatorial orbits under both radiation reaction and hydrodynamic drag can be characterised with only one quantity (the rate of change of the radius dr/dt), to which the rates of change of the energy and angular momentum, $d\tilde{E}/dt = (d\tilde{E}/dr)\,(dr/dt)$ and $d\tilde{L}_z/dt = (d\tilde{L}_z/dr)\,(dr/dt)$, are proportional. ($d\tilde{Q}/dt$ is instead identically zero for equatorial orbits.) Moreover, one does not need to compute the infinite-time averages (3.67), because the rates of change of $\tilde{E}$, $\tilde{L}_z$ and $\tilde{Q}$ due to the hydrodynamic drag, given by eqs. (3.42), (3.43) and (3.46) [or (3.49)], are already functions of the orbital radius alone. [Note also that the 4-vector $\boldsymbol{\chi}$ reduces to $\boldsymbol{\chi} = -\partial_r/\sqrt{g_{rr}}$.]

The ratio between the rates of change of the orbital radius due to hydrodynamic drag and radiation reaction is a convenient measure of the "efficiency" of the hydrodynamic drag. Defining this quantity simply as $\beta_{\dot{r}} \equiv (dr/dt)_{\rm hydro}/(dr/dt)_{\rm GW}$, we show in the top plot of Fig. 3.1 the absolute value of $\beta_{\dot{r}}$ as a function of the radius r of circular equatorial bound stable orbits. The two curves refer to models A1 and A2 of Table 3.1, and are labelled with the spin parameter a of the SMBH. Note that in order to present all the data in a single plot, a positive r refers to orbits rotating in the positive ϕ-direction ("prograde orbits" *i.e.*, corotating with the torus), while a negative r to orbits rotating in the negative ϕ-direction ("retrograde orbits" *i.e.*, counter-rotating with respect to the torus). The middle plot compares the velocity v of the satellite in the rest frame of the fluid with the sound velocity v_s, while the bottom plot shows instead the energy density ρ of the torus. Note that in all the plots the vertical axis is drawn in logarithmic scale. As such, the vertical asymptotes appearing in Fig. 3.1 (as well as in Figs. 3.2 and 3.3, which are in logarithmic scale too) actually correspond to a zero value for the quantity under consideration.

Note that if the torus is corotating with the black hole, the radius of the innermost stable circular orbit (ISCO) is always larger than the inner radius of the torus, both for prograde and retrograde orbits. For prograde orbits, this immediately follows from the considerations of sec. 3.1 (since our tori have $\Delta W = 0$ and $\ell_{\rm ms} < \ell < \ell_{\rm mb}$, we have $r_{\rm in} = r_{\rm cusp} < r_{\rm ms}$, and $r_{\rm ms}$ is exactly the radius of the prograde ISCO), while for retrograde orbits it is sufficient to note that the retrograde ISCO is located at a larger radius than the prograde one. Bearing this in mind, it is then easy to understand why none of the quantities plotted in Fig. 3.1 for model A1 ($a = 0.9M$) goes to zero when approaching the SMBH: although the density, the velocity of the satellite relative to the torus, the sound

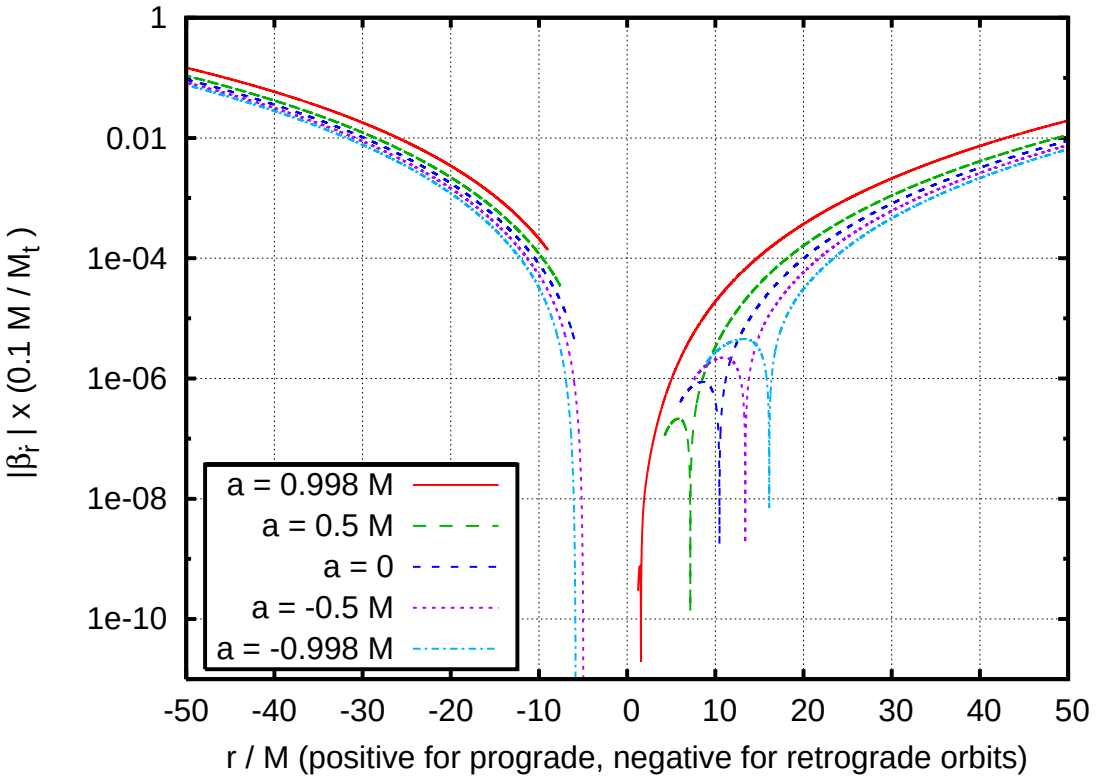

Figure 3.2: *The same as the top plot of Fig. 3.1, but for models B1-B5 of Table 3.1, which are labelled here with the spin parameter a of the SMBH.*

velocity and $(dr/dt)_{\rm hydro}$ are exactly zero at the inner radius of the torus, this radius is smaller than that of the ISCO and therefore no bound stable orbits exist there.

If instead the torus is counter-rotating with respect to the black hole (*i.e.*, $a < 0$), the radius of the ISCO is larger than $r_{\rm in}$ for prograde orbits (this follows again from $r_{\rm in} = r_{\rm cusp} < r_{\rm ms}$), but it is not possible to conclude that the radius of the ISCO is larger than $r_{\rm in}$ also for retrograde orbits. In fact, the ISCO counter-rotating with respect to the torus (*i.e.*, the "retrograde" ISCO) is corotating with the black hole and thus lies at a radius smaller than the "prograde" ISCO. Indeed, for model A2 ($a = -0.9M$) considered in Fig. 3.1 the retrograde ISCO is at a radius smaller than $r_{\rm in}$. As a consequence, the density, the sound velocity and $(dr/dt)_{\rm hydro}$ for model A2 go to zero when the radius of the retrograde orbits decreases, being in fact zero at the inner edge of the torus. (Of course, the velocity of the satellite relative to the fluid does not go to zero when the radius of the retrograde orbits decreases, because the satellite and the torus are rotating in opposite directions.)

As can be seen in the top plot, the ratio $|\beta_{\dot{r}}|$ is larger for the retrograde orbits than for the prograde ones. The reason can be easily understood from the middle plot, which shows that the retrograde motion is always supersonic. The long-range drag, which in-

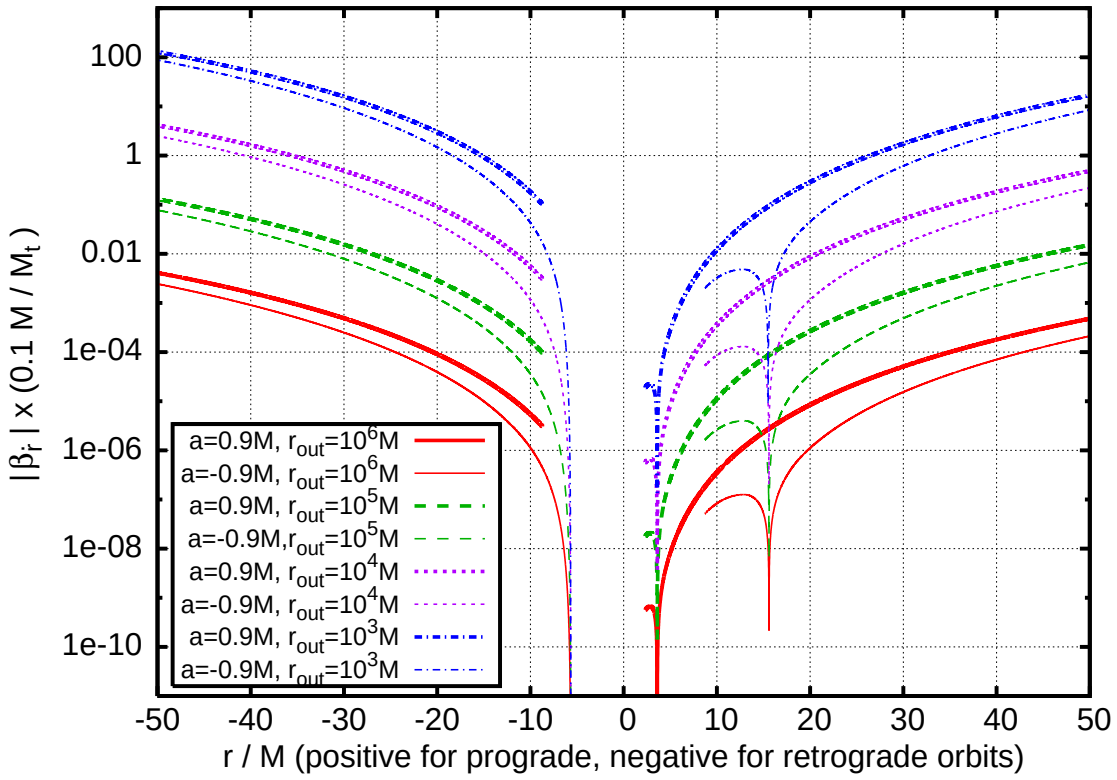

Figure 3.3: *The same as the top plot of Fig. 3.1, but for models A1-A2 and C1-C6 of Table 3.1, which are labelled here with the spin parameter a of the SMBH and the outer radius $r_{\rm out}$ of the torus.*

creases significantly when passing from the subsonic to the supersonic regime [*cf.* eq. (3.34)], then enhances the torus-satellite interaction for the retrograde orbits. From the middle plot one can also note that relativistic velocities ($v \gtrsim 0.6$) are reached in the case of retrograde orbits very close to the SMBH, thus further enhancing the hydrodynamic drag because of the relativistic correction factor $\gamma^2(1+v^2)^2$ appearing in eq. (3.32). However, we should note that when v reaches its maximum value (*i.e.*, $v \sim 0.8$ for model A2) the effect of the relativistic correction factor on the hydrodynamic drag is hindered by the small value of the density, which goes to zero at the inner edge of the torus (*cf.* the bottom plot).

As can easily be understood from the formulae reviewed in sec. 3.1, a change in the polytropic constant κ leaves all the parameters of the torus unchanged, except the energy density ρ, the rest mass density ρ_0, the pressure p [all of which scale proportionally to $\kappa^{-1/(\Gamma-1)}$] and the total mass-energy and rest-mass, $M_{\rm t}$ and $M_{\rm t0}$ (which scale proportionally to ρ). For this reason, the bottom plot of Fig. 3.1 scales linearly with the mass of the torus (*cf.* the label of the vertical axis). Noting, from the formulae of sec. 3.2.1, that the rates of change of the $\tilde{E}$, $\tilde{L}_z$ and $\tilde{Q}$ are proportional to the energy density ρ, the same scal-

ing applies to the top plot. This is a very useful feature, because although the value used for the figures of this chapter – *i.e.*, $M_{\rm t} = 0.1M$ – could be a plausible mass for the torus, very little is known about these objects and larger or smaller masses may be possible. In general, a different mass $M_{\rm t}$ could have important effects. For instance, extrapolating to the case $M_{\rm t} = M$, in which our test-fluid approximation is no longer valid, the ratio $|\beta_{\dot r}|$ would be enhanced by a factor 10, and for orbits counter-rotating with respect to the torus with $r \gtrsim 40M$ the effects of hydrodynamic drag and radiation reaction would become comparable.[10]

It is also worth pointing out that at the centre of the torus $(dr/dt)_{\rm hydro}$ changes sign for prograde orbits, being negative for $r > r_{\rm centre}$ and positive for $r < r_{\rm centre}$. [$(dr/dt)_{\rm GW}$ is instead always negative because gravitational waves carry a positive amount of energy away from the source.] This change of sign corresponds, in the top plot of Fig. 3.1, to the zero value for $|\beta_{\dot r}|$. This behaviour comes about because, although the density reaches its maximum at the centre, the motion of the fluid is exactly Keplerian (geodesic) there, and the relative velocity of the satellite is therefore exactly zero (*cf.* the middle plot). This means in particular that $\tilde{E} = -u_t^{\rm sat} = -u_t^{\rm fluid} = U$, which together with eq. (3.42) and $\chi_t = 0$ gives $\dot{\tilde{E}} = 0$ and therefore $\dot r = 0$ for prograde orbits at $r = r_{\rm centre}$. Moreover, if $r > r_{\rm centre}$ the specific angular momentum of the satellite is larger than that of the torus (*cf.* for instance ref. [101], Fig. 5), and therefore the satellite is slowed down by the interaction with the fluid (*i.e.*, $\dot r < 0$). On the other hand, if $r < r_{\rm centre}$ the specific angular momentum of the satellite is smaller than that of the torus, and the satellite is speeded up (*i.e.*, $\dot r > 0$).

Fig. 3.2 shows the absolute value of $\beta_{\dot r}$ as a function of the radius r of circular equatorial bound stable orbits for models B1-B5 of Table 3.1, whose spin parameter a goes from $-0.998M$ to $0.998M$. As it can be seen, the situation is qualitatively very similar to the one presented in the top plot of Fig. 3.1. In particular, the effect of the hydrodynamic drag can be comparable to that of radiation reaction, but only if we extrapolate to $M_{\rm t} = M$ and, even in that case, only for orbits counter-rotating with respect to the torus and with $r \gtrsim 40M$.

We can also note that the effect of the spin a on the results is negligible, except for the prograde orbits between the centre and the ISCO, for which $|\beta_{\dot r}|$ decreases as a increases. The reason for this can be easily understood by considering a satellite moving on a prograde circular equatorial orbit between the centre and the inner edge of the torus, and by recalling that the difference between $\ell_{\rm mb}$ and $\ell_{\rm ms}$ represents an upper limit for the deviation of the specific angular momentum of the satellite away from that of the torus (see ref. [101], Fig. 5). Because this deviation regulates the exchange of angular momentum between the torus and the satellite [*cf.* eq. (3.43), where $\chi_\phi = 0$ for circular orbits] and thus the rate of change of the orbital radius, $\beta_{\dot r}$ must go to zero if $\ell_{\rm mb} - \ell_{\rm ms}$ goes to zero.

[10] Note, however, that even values of $|\beta_{\dot r}|$ less than 1 can produce features detectable by LISA, because the dephasing time scales as $\sim |\dot r_{\rm GW}|^{-1/2}$ [35]. For instance, if $|\beta_{\dot r}| \approx 0.1$ the dephasing time between a waveform with only radiation reaction included and one with also the effect of the hydrodynamic drag is expected to be only ~ 3 times larger than the dephasing time between waveforms with and without radiation reaction included.

Since it is easy to verify that $\ell_{\rm mb} - \ell_{\rm ms} \to 0$ as $a \to M$ [*cf.* eq. (3.14)], it is natural to find that $|\beta_{\dot{r}}|$ decreases as a increases.

Finally, in Fig. 3.3 we plot again $|\beta_{\dot{r}}|$, but for models A1-A2 and C1-C6 of Table 3.1, in which we have considered different values for the outer radius $r_{\rm out}$ of the torus, ranging from $10^3 M$ to $10^6 M$. The reason for this is that although $r_{\rm out} \sim 10^5 M$ is a plausible value for the outer radius, little is known about the size of astrophysical accretion disks and larger or smaller outer radii may also be possible. As it can be seen from Fig. 3.3, a different outer radius will have significant effects for prograde orbits with $r \gtrsim 20M$ and retrograde orbits with $r \gtrsim 10M$, for which the effect of the hydrodynamic drag can become comparable to that of radiation reaction. In general, $|\beta_{\dot{r}}|$ progressively increases as the outer radius is decreased. This is rather simple to explain: decreasing $r_{\rm out}$ while keeping $M_{\rm t}$ constant amounts to increasing the average rest-mass density and hence the hydrodynamic drag. When considered from this point of view, the uncertainty on the value of $r_{\rm out}$ has an effect opposite to the uncertainty about the mass of the torus: a decrease of $r_{\rm out}$ (or an increase of $M_{\rm t}$) induces an increase of $|\beta_{\dot{r}}|$. For circular orbits, this overall uncertainty can be easily modelled in terms of a simple scaling of the type

$$\beta_{\dot{r}}(r_{\rm out}) \approx \beta_{\dot{r}}|_5 \left(\frac{10^5\, M}{r_{\rm out}}\right)^{3/2} , \tag{3.68}$$

where $\beta_{\dot{r}}|_5$ is the efficiency for $r_{\rm out} = 10^5\, M$. Note that the scaling power is not 3 as one may naively expect. This is because $\beta_{\dot{r}}$ is most sensitive to the changes of the rest-mass density in the inner part of the torus and this does not scale simply as $r_{\rm out}^{-3}$.

3.3.2 Generic orbits

We will now extend the analysis of sec. 3.3.1 to bound stable generic (inclined and eccentric) orbits. Although such an extension is in principle straightforward using the formulae introduced in sec. 3.2.2, the space of parameters and results which one needs to examine greatly enlarges. Not only are generic orbits characterised by the three parameters p, e, $\theta_{\rm inc}$ defined by eq. (3.51), but one also needs to consider three quantities describing the evolution of each single orbit in the parameter space *i.e.,* the rates of change dp/dt, de/dt and $d\theta_{\rm inc}/dt$.

To simplify our analysis, we will focus mainly on model A1 of Table 3.1, which could be a representative example of an astrophysical torus in an AGN, and then examine how the rates of change dp/dt, de/dt and $d\theta_{\rm inc}/dt$ due to the hydrodynamic drag compare to those due to radiation reaction throughout the space of parameters $(p, e, \theta_{\rm inc})$. The considerations that we will draw for model A1 can, however, be extended simply to the cases of different masses and radii for the torus. As in the case of circular orbits, in fact, a larger (smaller) mass $M_{\rm t}$ for the torus when $r_{\rm out}$ is held constant would simply increase (decrease) the rates dp/dt, de/dt and $d\theta_{\rm inc}/dt$ due to the hydrodynamic drag by a factor $M_{\rm t}/(0.1M)$. This scaling is *exact* (as long as the torus is not self-gravitating) and comes about because the rates of change of $\tilde{E}$, $\tilde{L}_z$ and $\tilde{Q}$ (and consequently those of p, e and $\theta_{\rm inc}$)

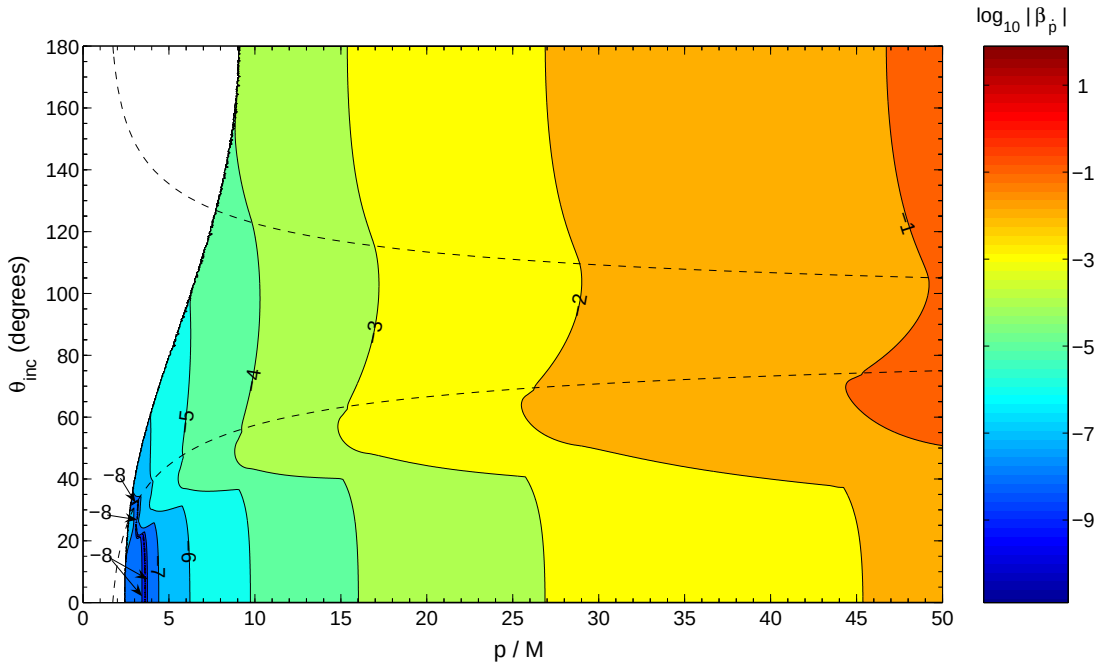

Figure 3.4: $\log_{10}|\beta_{\dot{p}}|$ *for inclined orbits with* $e = 0.1$ *as a function of the semi-latus rectum* p *and of the inclination angle* $\theta_{\rm inc}$*. The figure refers to model A1 of Table 3.1, but a larger (smaller) mass* $M_{\rm t}$ *for the torus would simply increase (decrease) the absolute ratio* $|\beta_{\dot{p}}|$ *by a factor* $M_{\rm t}/(0.1M)$*. The dashed line marks the edge of the torus.*

are proportional to the energy density $\rho \propto M_{\rm t}$. Similarly, variations of $r_{\rm out}$ will result in an effect which is similar to the one discussed for Fig. 3.3 in the case of circular orbits [*cf.*, eq. (3.68)], as we will see at the end of this section.

All of the results presented in this section have been computed by integrating numerically eqs. (3.67) using an iterated Romberg method [118], with a typical accuracy, depending on the parameters of the orbit under consideration, of 10^{-7}–10^{-4} and never worse than 4×10^{-3}. [11]

We start by analysing in detail orbits with eccentricity $e = 0.1$, and we will then study the effect of a different eccentricity on the results. In Figs. 3.4, 3.5, 3.6 the colour-code and

[11] Note that the accuracy of the numerical integration is certainly adequate, because it is considerably better than the errors affecting the fit (3.34) as well as those affecting the kludge fluxes that we use to study the effects of radiation reaction.

the contour levels show the base-10 logarithm of the "efficiencies" of $\dot{p}$, $\dot{e}$ and $\dot{\theta}_{\rm inc}$, *i.e.*,

$$\beta_{\dot{p}} \equiv \left| \left(\frac{dp}{dt}\right)_{\rm hydro} \Big/ \left(\frac{dp}{dt}\right)_{\rm GW} \right| , \tag{3.69}$$

$$\beta_{\dot{e}} \equiv \left| \left(\frac{de}{dt}\right)_{\rm hydro} \Big/ \left(\frac{de}{dt}\right)_{\rm GW} \right| , \tag{3.70}$$

$$\beta_{\dot{\theta}_{\rm inc}} \equiv \left| \left(\frac{d\theta_{\rm inc}}{dt}\right)_{\rm hydro} \Big/ \left(\frac{d\theta_{\rm inc}}{dt}\right)_{\rm GW} \right| , \tag{3.71}$$

as functions of p and $\theta_{\rm inc}$. The dashed line marks the "edge of the torus" *i.e.*, the location in the $(p, \theta_{\rm inc})$-plane of the orbits having $\theta_{\rm inc} = \theta_{\rm inc,\,t}(p)$, where $\theta_{\rm inc,\,t}(r)$ is the function giving the angle between the surface of the torus and the equatorial plane in terms of the radius r. The blank part on the left portion of these figures refers to the region where no bound stable orbits exist, and we will refer to the line marking the boundary of this region as the *separatrix* [40]

Each figure has been obtained by computing the quantity under consideration using eq. (3.67) for $\sim 5\times10^5$ orbits irregularly distributed in the $(p, \theta_{\rm inc})$-plane, and then linearly interpolating on a grid of 1500×1500 nodes using a Delaunay triangle-based method. The gridded data obtained in this way has been used to draw the contour levels. Not surprisingly, Figs. 3.4, 3.5, 3.6 show somewhat the same trend as the results presented in sec. 3.3.1 for circular equatorial orbits, with the effect of the torus becoming comparable to that of the radiation-reaction far away from the black hole and becoming instead negligible in the strong-field region of the black hole. However, these figures present also a variety of features that we will now analyse in detail.

Fig. 3.4, for instance, shows $|\beta_{\dot{p}}|$ and indicates that the effect of the hydrodynamic drag is larger for orbits with high inclination, for any given semi-latus rectum p. This is simply due to the fact that orbits with $\theta_{\rm inc} > 90$ degrees are retrograde with respect to the torus, and the velocity of the satellite relative to the fluid can easily become supersonic. Indeed this effect is visible also in the figures of sec. 3.3.1. (We recall that in those figures the retrograde orbits are mapped to negative values of the orbital radius r.) The transition between the subsonic and the supersonic regime is marked by the sharp bend of the contour levels of Fig. 3.4 at $\theta_{\rm inc} \sim 40$ degrees. This bend corresponds to the passage from orbits which are always subsonic (the orbits with $\theta_{\rm inc}$ smaller than the inclination angle at which the bend is located) to orbits which are supersonic at least for a part of their trajectory (the orbits with $\theta_{\rm inc}$ larger than the inclination angle at which the bend is located). Another small dip is barely noticeable in the contour levels at inclination angles $\theta_{\rm inc}$ just smaller than the edge of the torus (and smaller than 90 degrees, corresponding therefore to prograde orbits); this feature corresponds to the transition from orbits which are partly subsonic and partly supersonic ("below" the dip), to orbits which keep always supersonic ("above" the dip).[12] From Fig. 3.4 one can also note that $|\beta_{\dot{p}}|$ becomes lower

[12]We note that in order to better understand the fine features in the contour levels, we have built an auxiliary

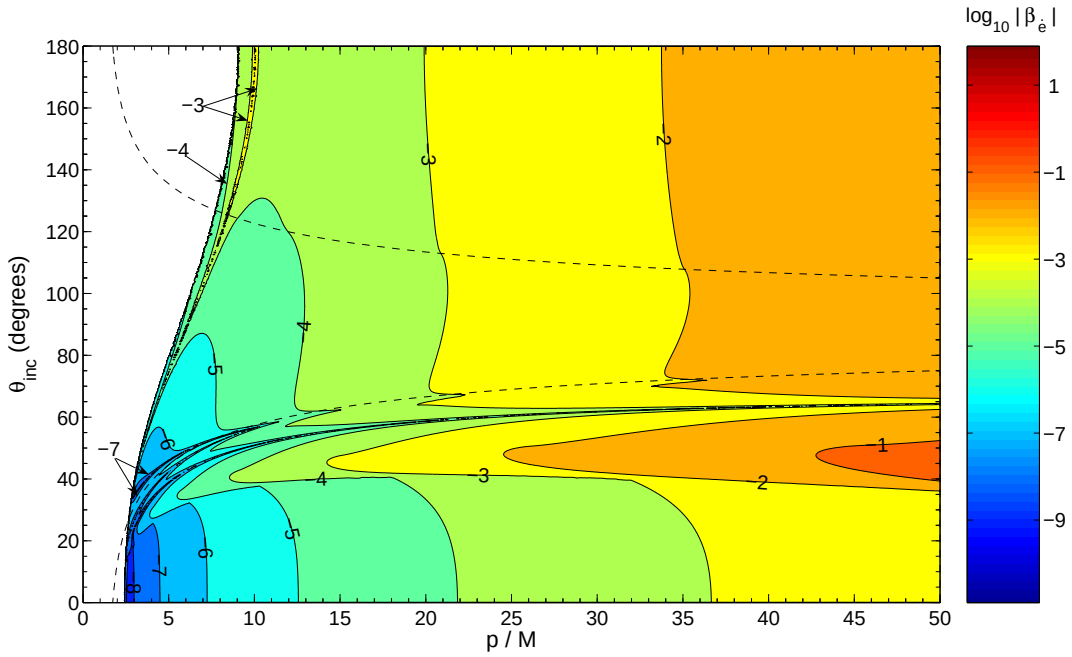

Figure 3.5: *The same as in Fig. 3.4, but for* $\log_{10}|\beta_{\dot{e}}|$.

than 10^{-8} in a narrow "strip" at $p/M < 5$. Indeed, $(dp/dt)_{\rm hydro}$ changes sign inside this "strip", being positive inside the region between the "strip" and the separatrix and negative outside, while $(dp/dt)_{\rm GW}$ is always negative. This behaviour generalises that of circular equatorial orbits, for which $(dr/dt)_{\rm hydro}$ changes sign at the centre of the torus (*cf.* sec. 3.3.1). Also in this case, however, the very small values of $|\beta_{\dot{p}}|$ cannot produce an observable imprint on the waveforms.

In a similar way, Fig. 3.5 shows the behaviour of $|\beta_{\dot{e}}|$. As can be seen, the influence of the torus is again larger at high inclinations than at low ones, for any fixed semi-latus rectum. Also in this case, this happens because the orbits counter-rotating with respect to the torus can easily become supersonic. As in Fig. 3.4, we can note the presence of a sharp bend in the contour levels at $\theta_{\rm inc} \sim 40$ degrees, due to the transition from orbits which are always subsonic to orbits which are partly supersonic, and a dip in the contour levels near the edge of the torus (at inclinations $\theta_{\rm inc} < 90$ degrees), which is more pronounced than in Fig. 3.4 but is again due to the transition from orbits which are only partly subsonic to orbits which are always supersonic. Moreover, one can note the pres-

code computing the quantities $(dp/dt)_{\rm hydro}$, $(de/dt)_{\rm hydro}$ and $(d\cos\theta_{\rm inc}/dt)_{\rm hydro}$ by direct integration of eqs. (3.42), (3.43), (3.46) and (3.49) along numerically solved geodesics, averaging over a reasonably large number of revolutions (~ 30) for each geodesic. This has not only validated the results which have been used to build the figures and which have been obtained using eqs. (3.67), but has also allowed us to examine in detail the behaviour of the geodesics in the various regions of the parameter space $(p, e, \theta_{\rm inc})$, thus helping to interpret the complicated features of the figures shown in this chapter.

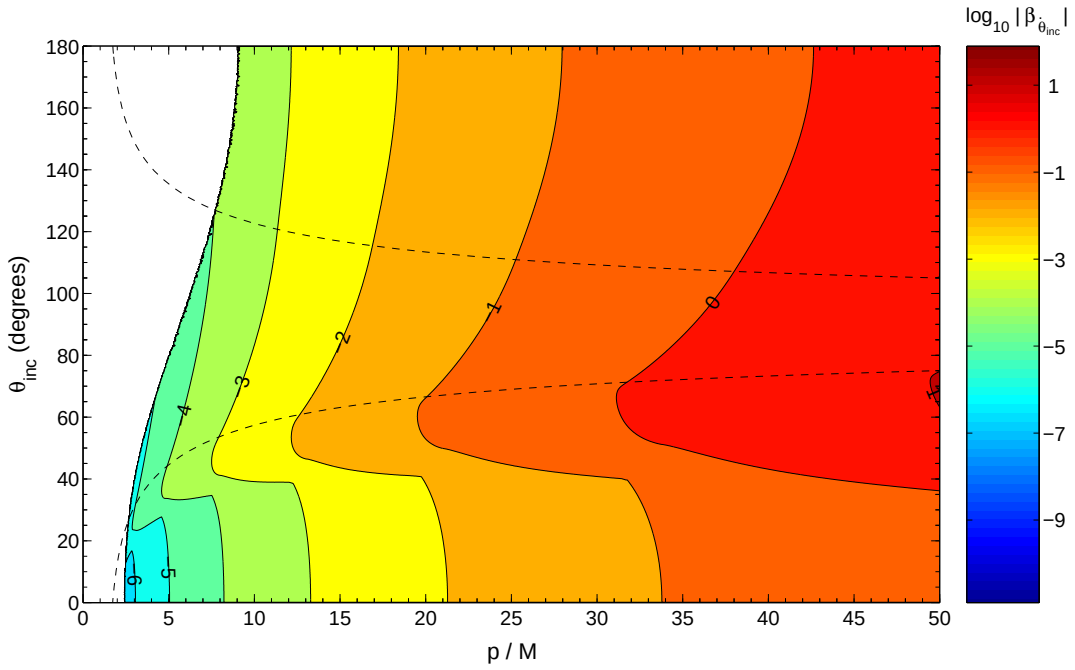

Figure 3.6: *The same as in Fig. 3.4, but for* $\log_{10}|\beta_{\dot{\theta}_{\rm inc}}|$.

ence of three "valleys" where the efficiency $|\beta_{\dot{e}}|$ becomes very small. One ("valley 1") starts at $\theta_{\rm inc} \approx 15$ degrees, very close to the separatrix, and extends as far as the right edge of the figure ($p/M = 50$, $\theta_{\rm inc} \approx 65$ degrees) and beyond. A second valley ("valley 2") starts at the same point as valley 1, but extends only until $p/M \approx 12$ and $\theta_{\rm inc} \approx 60$ degrees, where it terminates together with a third valley ("valley 3") starting on the separatrix at $\theta_{\rm inc} \approx 30$ degrees. Across these valleys, the quantity $(de/dt)_{\rm hydro}$ becomes zero and changes sign, being negative under valley 1 and in the region between the separatrix and valleys 2 and 3, and positive in the rest of the $(p, \theta_{\rm inc})$-plane. Conversely, the rate of change of the eccentricity due to radiation reaction is always negative, with the exception of orbits very close to the separatrix [119]; this is apparent also in Fig. 3.5, where the narrow "strip" corresponding to a ratio $|\beta_{\dot{e}}| \gtrsim 10^{-3}$ and running close and almost parallel to the separatrix is due to a change in sign of $(de/dt)_{\rm GW}$. Despite this markedly different behaviour of $(de/dt)_{\rm hydro}$ and $(de/dt)_{\rm GW}$, Fig. 3.5 shows that the effect of the hydrodynamic drag is always much smaller than radiation reaction unless the semi-latus rectum of the orbit is increased to $p/M \gtrsim 50$, or the mass of the torus is increased at least by a factor 10 thus extrapolating to $M_{\rm t} = M$.[13] Furthermore, while a larger semi-latus rectum increases the efficiency $\beta_{\dot{e}}$, it also reduces the frequency and amplitude of the gravitational-wave signal, moving it to a region of low sensitivity for LISA.

The effect of the hydrodynamic drag is somewhat stronger when considered in terms

[13] The test-fluid approximation of course breaks down in this limit.

of the efficiency $|\beta_{\dot{\theta}_{\rm inc}}|$, as shown in Fig. 3.6. While the qualitative behaviour is similar to the one discussed for the two preceding figures, it should be noted that the effect of the torus is comparable to that of radiation reaction already for $p/M \approx 32$ if $\theta_{\rm inc} \approx 60$ degrees, and the two effects remain comparable down to $p/M \approx 20$ if the mass of the torus is increased by a factor 10 thus extrapolating to $M_{\rm t} = M$. Moreover, while radiation reaction produces an increase in the inclination $\theta_{\rm inc}$ irrespective of the orbital parameters [106], $(d\theta_{\rm inc}/dt)_{\rm hydro}$ is always negative and thus a measurement of the evolution of the inclination angle $\theta_{\rm inc}$ in the early stages an EMRI could give important information on the presence of a torus. If such a presence were to be detected, it would not prevent high-precision tests of the Kerr nature of the SMBH being performed in the strong-field region, where the hydrodynamic drag becomes negligible.

We should also note that the decrease of $\theta_{\rm inc}$ due to the hydrodynamic drag is not surprising for orbits with $\theta_{\rm inc} > 90$ degrees (*i.e.*, orbits rotating in the opposite ϕ-direction with respect to the fluid), because the hydrodynamic drag clearly induces the orbits to rotate in the same ϕ-direction as the torus. For orbits with $\theta_{\rm inc} < 90$ degrees, instead, the decrease of $\theta_{\rm inc}$ comes directly from eq. (3.44) (we recall that the effect of the radial drag averages out when adopting the adiabatic approximation), thus following directly from the axis- and plane-symmetry of the system and being independent of the use of constant specific angular momentum tori such as the ones considered in this chapter. Indeed, since the fluid of the torus does not move in the θ-direction, eq. (3.44) states that accretion conserves the momentum of the satellite in the θ-direction, but it also increases its mass, thus reducing the velocity in the θ-direction. In addition, the dynamical friction will contribute to this reduction by damping further the oscillations around the equatorial plane.

To illustrate how the above results depend on the eccentricity, we show in Fig. 3.7 the efficiency $|\beta_{\dot{\theta}_{\rm inc}}|$ for model A1 of Table 3.1, but for different values of the eccentricity *i.e.*, $e = 0$, 0.4, and 0.8. (Equivalent figures could be made also for $|\beta_{\dot{p}}|$ and $|\beta_{\dot{e}}|$, but we omit them here because they are qualitatively similar to Fig. 3.7). For each value of the eccentricity, we have computed $|\beta_{\dot{\theta}_{\rm inc}}|$ for $\sim 4 \times 10^4$ orbits, and using the same technique employed for Figs. 3.4, 3.5, 3.6 we have drawn the contours corresponding to values of 0.01, 0.1, 1 and 10. Also in this case, a larger (smaller) mass $M_{\rm t}$ for the torus would simply increase (decrease) these absolute ratios by a factor $M_{\rm t}/(0.1M)$.

Clearly, many of the features in this plot have been discussed also for the previous figures. For instance, the contour levels present sharp bends at low inclinations (*i.e.*, $\theta_{\rm inc} \approx 10 - 40$ degrees) for $e = 0$ and $e = 0.4$, due the transition from subsonic to partly supersonic orbits, whereas the transition from partly supersonic to fully supersonic orbits causes the appearance of a pronounced "kink" in the $e = 0.4$ contour levels, for inclinations $\theta_{\rm inc} < 90$ degrees just above the edge of the torus. The $e = 0.8$ contour levels, on the other hand, are rather smooth and are less affected by the complex changes of regime as the satellite interacts with the torus. Most importantly, however, Fig. 3.7 suggests that the conclusions drawn when discussing Fig. 3.6 for orbits with $e = 0.1$ are not altered significantly by a change in the eccentricity. Indeed, even for large eccentricities the influence of the torus on the evolution of $\theta_{\rm inc}$ can be comparable to that of radiation reaction

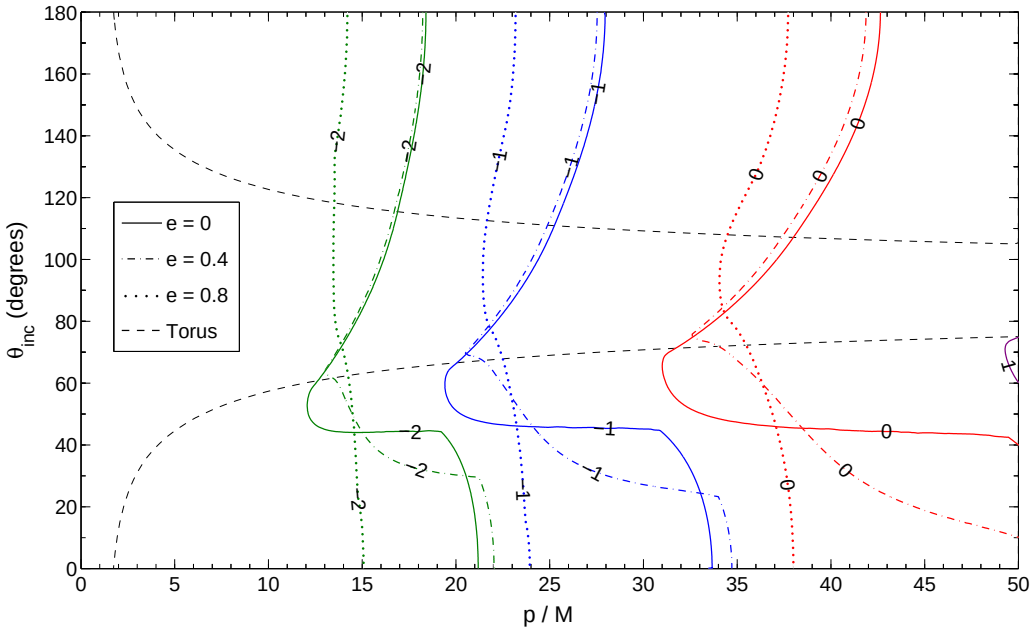

Figure 3.7: $\log_{10}|\beta_{\dot{\theta}_{\rm inc}}|$ *shown as a function of the semi-latus rectum* p *and of the inclination angle* $\theta_{\rm inc}$ *for inclined orbits with selected values of the eccentricity, i.e.,* $e = 0$ *(solid line),* $e = 0.4$ *(dot-dashed line),* $e = 0.8$ *(dotted line). The figure refers to model A1 of Table 3.1, but a larger (smaller) mass* $M_{\rm t}$ *for the torus would simply increase (decrease)* $|\beta_{\dot{\theta}_{\rm inc}}|$ *by a factor* $M_{\rm t}/(0.1M)$*. The dashed line marks the edge of the torus.*

for p/M as small as $35 - 38$, while the two effects are still equal at $p/M \approx 23 - 24$ if the mass of the torus is increased by a factor 10 thus extrapolating to $M_{\rm t} = M$. As a result, a measurement of the evolution of the inclination angle $\theta_{\rm inc}$ even for generic eccentric orbits could give important information on the presence of a torus around the SMBH.

This conclusion is finally confirmed by Fig. 3.8, in which we show how $|\beta_{\dot{\theta}_{\rm inc}}|$ changes if one considers different values of the outer radius of the torus while keeping its mass fixed. More specifically, Fig. 3.8 shows the location in the $(p, \theta_{\rm inc})$-plane of the *circular* orbits for which $|\beta_{\dot{\theta}_{\rm inc}}| = 1$. Different curves refer to different values of the outer radius, and in particular to models A1, C1, C3 and C5 of Table 3.1. As it is probably obvious by now, a different mass $M_{\rm t}$ for the torus would simply make the curves of this figure correspond to $|\beta_{\dot{\theta}_{\rm inc}}| = M_{\rm t}/(0.1M)$. As expected from the results of sec. 3.3.1, a modest variation of the outer radius can easily cause the decrease of the inclination angle due to the hydrodynamic drag to be dominant over the increase due to radiation reaction for orbits with $p/M \sim 20$ or smaller.

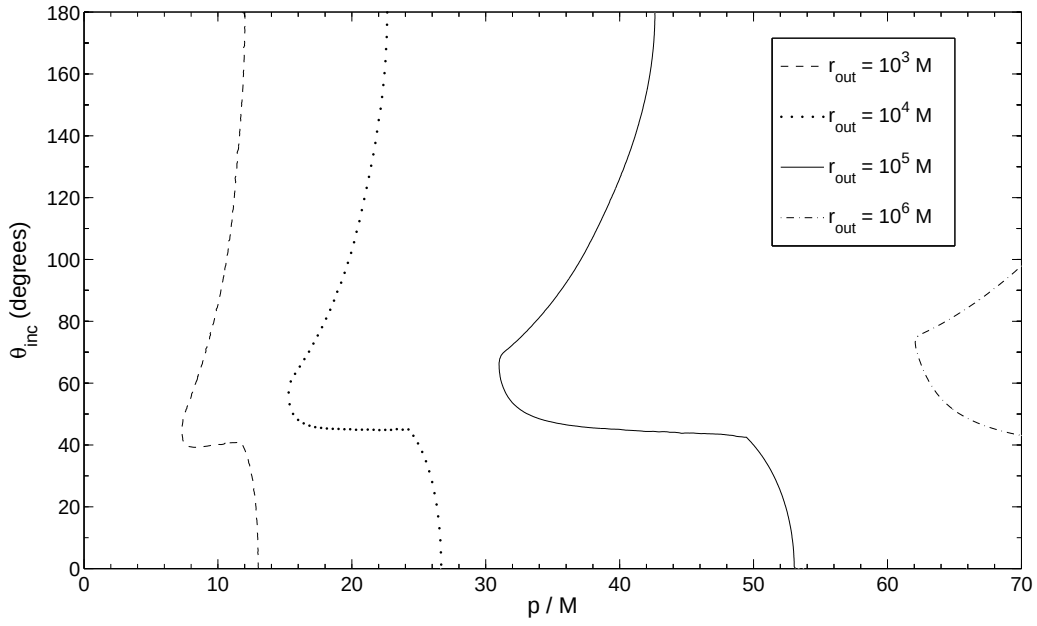

Figure 3.8: *Location in the $(p, \theta_{\rm inc})$-plane of the circular orbits for which $|\beta_{\dot{\theta}_{\rm inc}}| = 1$. Different curves refer to different values of the outer radius and thus to models A1, C1, C3 and C5 of Table 3.1. Note that a different mass $M_{\rm t}$ for the torus would simply make the curves of this figure to correspond to $|\beta_{\dot{\theta}_{\rm inc}}| = M_{\rm t}/(0.1M)$.*

3.4 Conclusions

SMBHs are expected to be surrounded by matter, either in the form of stellar disks, as in the case of "normal" galactic centres, or in the form of accretion disks of gas and dust, as in the case of AGNs. In order to assess under what conditions and to what extent the interaction with matter could modify the gravitational-wave signal from EMRIs in AGNs, we have studied EMRIs in spacetimes containing an SMBH surrounded by a non self-gravitating torus. For simplicity, and in order to handle the equilibrium solution analytically, we have considered a torus with a constant distribution of specific angular momentum, using as reference dimensions and masses those for the accretion disks expected in AGNs, but bearing in mind that these also come with rather large uncertainties. We have extrapolated our results also to cases in which the mass of the torus is comparable with that of the SMBH, although we stress that in this limit our test-fluid approximation for the torus is no longer valid.

Overall, we have found that the effect of the hydrodynamic drag exerted by the torus on the satellite black hole can have important effects sufficiently far from the central object, and that these effects are qualitatively different from those of radiation reaction. In particular, if the torus is corotating with the SMBH, the hydrodynamic drag always *de-*

creases the inclination of the orbits with respect to the equatorial plane (*i.e.,* orbits evolve towards the equatorial prograde configuration), whereas radiation reaction always *increases* the inclination (*i.e.,* orbits evolve towards the equatorial retrograde configuration). In the case of a system composed of an SMBH with mass $M = 10^6 M_\odot$ and a corotating torus with mass $M_{\rm t} \lesssim M$, the effect of the torus will be marginally observable by LISA only if the radius of the torus is as small as $r_{\rm out} \approx 10^3 - 10^4 M$. However, if the SMBH has a lower mass, EMRIs will be detectable by LISA at larger distances from the SMBH, and the effects of a torus will be more evident. For instance, for an SMBH with $M = 10^5 M_\odot$ and a corotating torus with outer radius $r_{\rm out} = 10^5 M$ and mass $M_{\rm t} = 0.1 M$ ($M_{\rm t} = M$), the inclination with respect to the equatorial plane will decrease, due to the hydrodynamic drag, for orbits with semi-latus rectum $p \gtrsim 35M$ ($p \gtrsim 25M$), while the EMRI signal will start being detectable by LISA already at a distance of $\approx 50M$ from the SMBH. Note, however, that unless one considers the satellite being an intermediate-mass black hole with $m \sim 100 M_\odot$ orbiting around a $10^5 M_\odot$ SMBH (a configuration which may be possible but about which too little is yet known), considering EMRIs at such large distances from the SMBH has the obvious drawback that the amplitude of the gravitational-wave signal will be proportionally smaller. This will considerably reduce the detection volume, although the decrease in the event rate could be mitigated by the fact that weak-field EMRIs are probably more numerous than strong-field EMRIs, which are the ones accounted for in standard calculations of event rates.

In general, we expect measurements of the evolution of the inclination angle in the early phases of EMRIs to be a potential source of important information about the presence of thick tori which could not be detected by other techniques. Moreover, because for any astrophysically plausible torus configurations, the effect of the hydrodynamic drag rapidly becomes negligible in the very strong-field region of the SMBH (*i.e.,* $p \lesssim 5M$), the presence of a torus would not prevent high-precision tests of the Kerr nature of the SMBH being performed.

Although obtained with a simple model for the torus (*i.e.*, with a constant specific angular momentum), the important feature that distinguishes the hydrodynamic drag from radiation reaction, namely the decrease of the inclination angle, cannot be affected by a change of the specific angular momentum distribution (we recall that ℓ must be increasing with radius for stability). Such a feature, in fact, is simply due to the conservation of the momentum of the satellite in the θ-direction during accretion and to the dynamical friction of the fluid: both effects force the satellite to smaller inclinations by reducing its θ-velocity. However, the calculation of the magnitude of the hydrodynamic drag and how it compares with radiation reaction for more general disk models is not straightforward.

Tori built with increasing distributions of specific angular momentum, in fact, would have two substantial differences with respect to those considered here. Firstly, the separation between the specific angular momentum of the torus and the Keplerian specific angular momentum will generally decrease for orbits corotating with the torus, thus reducing the relative motion between the satellite and the fluid and consequently the hydrodynamic drag, whereas it will increase for orbits counter-rotating relative to the torus, thus enhancing the hydrodynamic drag. The magnitude of this effect depends on the pre-

cise angular momentum distribution considered and rough estimates can be made when assuming a power-law for the specific angular momentum, *i.e.*, $\ell/M \sim (r/M)^\alpha$, with $\alpha < 0.5$ for the torus to have an outer radius and a cusp [107, 109]. Using the general formulae reported in sec. 3.1, it is easy to check that for r between $20M$ and $50M$ the relative motion decreases by $\sim 20-30\%$ for $\alpha = 0.1$ and by at least 95% for $\alpha = 0.4$ (this significant decrease is due to the fact that for $\alpha = 0.4$ the centre moves to a radius $r_{\rm centre} \sim 27M$, just in the middle of the radial interval which we are considering). Conversely, in the same radial range the increase for counter-rotating orbits is of about $8-10\%$ ($30-45\%$), for $\alpha = 0.1$ (0.4). Secondly, the density in the inner parts of the torus will generally decrease. Using again the expressions in sec. 3.1, it is easy to check that the density decreases by about 13% (90%) at $r \sim 20M$ and of about 7% (80%) at $r \sim 50M$, for $\alpha = 0.1$ (0.4).

Overall, therefore, the decrease of the inclination angle due to the hydrodynamic drag could be detectable by LISA also for non-constant ℓ tori, especially if ℓ varies slowly with the radius or, if ℓ varies rapidly with the radius, if the EMRI is counter-rotating relative to the torus.

Finally, let us comment on two further effects that can in principle occur in the systems considered in this chapter. First, the motion of the satellite will be influenced by the gravitational attraction exerted by the torus. This is clearly a conservative effect, and cannot therefore influence the infall of the satellite towards the SMBH, which is instead regulated by the dissipative forces (radiation reaction and hydrodynamic drag). However, this effect can in principle cause the periastron to advance, thus introducing a phase-shift in the gravitational waveforms. (Note that a similar advance is caused by the conservative part of the gravitational self-force [37].) To calculate the order of magnitude of this effect, let us consider for simplicity a thin disk of outer radius $r_{\rm out}$, mass $M_{\rm D}$ and constant surface density, and a satellite of mass m located on the equatorial plane at a distance $d \ll r_{\rm out}$ from the central SMBH, the mass of which we denote by M. The potential energy of the satellite due to the gravitational field of the disk can be easily calculated to be, up to a constant and to leading order,

$$U \approx \frac{m M_{\rm D}\, d^2}{2 r_{\rm out}^3}\,. \tag{3.72}$$

This potential energy can be used to compute the Newtonian periastron precession of the satellite orbit during a revolution [use for instance eq. (1) of ref. [126], chapter 3, exercise number 3]:

$$\delta\phi \approx -\frac{3 M_{\rm D} \pi d^3}{M r_{\rm out}^3} \tag{3.73}$$

for almost circular orbits. Using this equation and the well-known Newtonian formula for the revolution period, it is easy to check that, for orbits relevant for LISA, the total phase-shift accumulated in 1 year is $\ll 2\pi$ as long as $r_{\rm out} \gtrsim 10^4 M$ and $M = 10^5 - 10^6 M_\odot$. Because LISA is not expected to detect phase lags less than 1 cycle over its lifetime[14],

[14] This corresponds indeed to a dephasing time of the order of LISA's lifetime.

this periastron advance and the consequent phase-shift cannot be observed. On the other hand, for disks or tori with $r_{\rm out} \sim 10^3 M$, this effect could in principle be marginally visible by LISA (especially if $M = 10^5 M_\odot$).

A second effect which could in principle affect EMRIs in the presence of a torus is the spin of the satellite black hole, which increases due to accretion of the torus material. The spin of the satellite couples with the orbital angular momentum as well as with the spin of the SMBH, but its effect on the motion is negligible over a timescale of 1 year [127], unless it is close to its maximal value (in which case it might be marginally observable) [127].

Chapter 4

Can LISA see the unknown unknowns?

> There are more things in heaven and earth, Horatio, Than are dreamt of in your philosophy.
>
> W. Shakespeare

As we have mentioned in chapter 3, the detection of gravitational waves from EMRIs with LISA could give the possibility of mapping with high accuracy the spacetime of SMBHs. These spacetimes are commonly thought to be describable by the pure Kerr solution of GR: this is the common assumption made in most work on EMRIs. Even in chapter 3, in spite of the presence of an accretion torus, we considered the background spacetime as given by the Kerr solution, neglecting the gravitational influence of the torus (*cf.* section 3.4 for a justification of this point) and taking into account only the hydrodynamic drag exerted by the torus on the satellite.

Nevertheless, a number of other "exotic" candidates have been proposed as alternatives to the central massive object. These are, for instance, gravastars [85], boson stars [83], fermion balls [84], oscillating axion bubbles [128], *etc.* Clearly, while it is not yet possible to exclude completely these possibilities, the presence of these objects at the centres of galaxies would require a serious modification to the scenarios through which galaxies are expected to form. At the same time, the possibility that LISA observations could be used to determine the presence (or absence) of these objects, provides additional scientific value to this challenging experiment.

Hereafter, we will adopt a more conservative view and assume that the central object is indeed an SMBH. Recent observations of the near-infrared fluxes of SgrA* support this view by setting upper limits on the mass accretion rate of the Galactic centre and showing that the central massive object must have, under reasonable assumptions, an event horizon [129]. Yet, even with this assumption, the modelling of EMRIs can in principle suffer from the uncertainty of whether the spacetime in the vicinity of the SMBH can be

accurately described in terms of a (pure) Kerr solution. Of course, as we have seen in section 3.4, accretion disks such as those found in AGNs cannot cause deviations away from the Kerr solution that are detectable by LISA, because these disks have an outer radius which is very large. However, as we have mentioned, if the SMBH were surrounded by a sufficiently compact disk or torus (*i.e.*, with mass comparable with the mass M of the SMBH and $r_{\rm out} \lesssim 10^3 M$), the gravitational effect of the matter could become detectable by LISA. The aim of this chapter is indeed to study EMRIs in spacetimes which deviate considerably from Kerr due to the presence of matter. We will consider in particular spacetimes comprised of a rotating black hole and a torus which is sufficiently massive so as to distort the spacetime, but so compact (*i.e.*, close to the central SMBH) that it could not probably be detected otherwise (for instance, by means of stellar orbits), especially if made of some "dark" mass. While these configurations may be unlikely from an astrophysical point of view, we take here a phenomenological approach and investigate whether LISA could detect the presence of such an *unexpected* object.

4.1 An introduction to spacetime mapping

A number of different approaches to the "spacetime-mapping" problem have been considered in the the literature: EMRIs have been studied in spacetimes which are either approximate or exact solutions of the Einstein equations. Among the former, a multipolar expansion suitable to describe general stationary, axisymmetric, asymptotically flat spacetimes outside a central distribution of matter has been considered [86, 87, 88]. However, this multipolar expansion is in practice a series in $1/r$ (r being the distance to the central object) around a Minkowski spacetime: an accurate representation of the strong field regime would require the inclusion of many terms. Another possibility is the "quasi-Kerr" (*i.e.*, Kerr plus a small quadrupole) spacetime studied by Glampedakis and Babak [92]. This can approximately describe the spacetime outside a slowly rotating star and is *not* an expansion around Minkowski, thus being more promising in the strong field limit. Among exact solutions of the Einstein equations, only spherical boson stars [89] and "bumpy black holes" [90, 91] (*i.e.*, objects that, although involving naked singularities, are *almost* Schwarzschild or Kerr black holes, but have some multipoles with the wrong values) have been considered.

At any rate, none of these spacetimes, neither exact nor approximate, can describe satisfactorily the "astrophysical bumpiness" which is certainly present around SMBHs. With this in mind, we have studied EMRIs in stationary, axisymmetric spacetimes which are highly accurate numerical solutions of the Einstein equations and contain a rotating black hole and a torus [130].

We used these numerical spacetimes to perform a study similar to that carried out by Babak and Glampedakis for "quasi-Kerr" spacetimes [92]: we studied EMRIs in the equatorial plane and computed semi-relativistic ("kludge") waveforms, comparing them to pure-Kerr kludge waveforms. Babak and Glampedakis, in particular, find that there could be a "degeneracy" problem, because although gravitational waves emitted in a quasi-Kerr spacetime by a stellar mass black hole moving on an equatorial orbit are very

different from those emitted by the same stellar mass black hole moving along the same orbit in a pure Kerr spacetime (having the same mass and spin as the quasi-Kerr spacetime), waveforms produced by equatorial orbits having slightly different semi-latus rectum and eccentricity but the same r- and ϕ-frequencies turn out to be indistinguishable with LISA's sensitivity.[1] We therefore repeated and extended their analysis. In particular, we consider, like them, only timescales over which the emission of energy and angular momentum through gravitational waves ("radiation reaction") does not introduce significant deviations from geodesic motion: to this purpose, we introduce a suitable cut-off in time. While this could be avoided in Babak's and Glampedakis' quasi-Kerr spacetimes (probably eliminating the degeneracy problem: see the analysis in ref. [93]), this is actually a necessity in our case, since the effect of a torus on the loss of energy and angular momentum due to gravitational-wave emission is completely unknown at present.

We did not try to produce tori describing the accretion disk of AGNs, but rather adopted a more phenomenological approach. Indeed, since little is known about the strong field region near the central massive black hole, we tried to build some "extreme" configurations, *i.e.* configurations containing rather massive and compact tori (close to the event horizon of the central black hole). The purpose is to understand if LISA can detect the presence of such tori, which are so close to the horizon that they could not probably be detected otherwise (for instance, by means of stellar orbits), especially if made of some "dark" mass. We stress that the word "extreme" does not mean that these configurations are extremely far from Kerr, but just that these tori are *not* the ones astrophysicists expect in AGNs.

One possible objection is that it might be possible that these "extreme" configurations are unstable (tackling the problem of stability is indeed one of the points in which the results of ref. [130] may be improved in the future), but we do not think this should be a major concern at this stage. Our viewpoint is that considering such extreme configurations will provide a testbed to investigate the practical problems of spacetime-mapping through EMRI-gravitational waves. In particular, these configurations will also help to understand better the degeneracy problem pointed out by Glampedakis and Babak. As already stressed, while in quasi-Kerr spacetimes this degeneracy disappears when dropping the time cut-off and including radiation reaction [93], in our case it may still be present due to the practical difficulties of computing radiation reaction in our spacetimes, which *force* us to introduce a cut-off in time.

We will see, however, that this degeneracy in the orbital parameters appears in our spacetimes only for (equatorial) orbits far from the black hole-torus system, whereas it disappears in the strong field region. Nevertheless, we find another degeneracy problem, potentially more worrisome as it involves the parameters of the black hole. Of course, if we could replace the semi-relativistic approximation with a rigorous solution of the linearised Einstein equations and a proper treatment of self-force or radiation reaction,

[1] Babak and Glampedakis actually refer to this fact as a "confusion" problem. We prefer here the term "degeneracy" because "confusion" might remind the gravitational-wave savvy reader of the "confusion noise" due to white dwarfs (*cf.* section 1.3). Of course, we use here the term "degeneracy" in the sense of data-analysis, that is, meaning that that convenient changes of two or more parameters do not affect the waveforms.

this degeneracy problem may disappear as well. However, such a rigorous treatment is very hard to obtain in generic stationary and axisymmetric spacetimes (see sec. 4.2) and, as far as the self-force is considered, even in pure Kerr.

This chapter is organised as follows. In sec. 4.2 we show what the rigorous treatment of EMRIs in non-vacuum, stationary and axisymmetric spacetimes would be, and explain why this treatment has proved so hard that nobody has pursued it so far. In sec. 4.3 we review the non-Kerr spacetimes in which the problem of EMRIs has been considered to date, ranging from approximate (sec. 4.3.1) to exact (sec. 4.3.2) solutions of the Einstein equations, and we introduce the non-pure Kerr spacetimes that we will use instead (sec. 4.3.3). In sec. 4.4 we review the semi-relativistic formalism used in ref. [92] to compute gravitational waves and explain how we adapted it to our purposes: in particular we show how we integrated the geodesic equations and calculated kludge waveforms, and (in sec. 4.4.1) explain what the overlap function and the dephasing time are. In sec. 4.5 we explain in detail how we perform a comparison between our non-pure Kerr spacetimes and pure Kerr spacetimes. A summary of our results with a concluding discussion and the prospects of future work is presented in sec. 4.5.1 and 4.5.2. Finally, in the Appendix we review the connection between kludge waveforms and the linearised Einstein equations.

4.2 Waveforms from EMRIs in non-vacuum spacetimes

Let us consider a curved, non-vacuum spacetime with metric $\boldsymbol{g}$ and with a characteristic lengthscale M (for a spacetime containing an SMBH, this scale clearly coincides with the black hole mass). The spacetime is intrinsically not a vacuum one because it contains a fluid with a stress-energy tensor $\boldsymbol{T}^{\text{fluid}}$. In addition, consider the presence of a small body, such as a black hole with mass $m \ll M$.[2] The small body will of course perturb the geometry of spacetime: the metric $\widetilde{\boldsymbol{g}}$ of the physical spacetime can therefore be written as the background metric $\boldsymbol{g}$ plus some perturbations ${}_1\boldsymbol{h}$ of order $O\left(m/M\right)$, ${}_2\boldsymbol{h}$ of order $O((m/M)^2)$, *etc.*:

$$\widetilde{g}_{\mu\nu} = g_{\mu\nu} + {}_1h_{\mu\nu} + {}_2h_{\mu\nu} + O((m/M)^3) \,. \tag{4.1}$$

Similarly, the small body will excite perturbations in the background fluid: the perturbed stress-energy tensor of the fluid can be written as

$$\widetilde{T}^{\text{fluid}}_{\mu\nu} = T^{\text{fluid}}_{\mu\nu} + {}_1\delta T^{\text{fluid}}_{\mu\nu} + {}_2\delta T^{\text{fluid}}_{\mu\nu} + O((m/M)^3) \,. \tag{4.2}$$

In what follows, the background metric $\boldsymbol{g}$ is used to raise and lower tensor indices. For the sake of simplicity, we will also drop the subscript ${}_1$ indicating first order quantities: in other words, $h_{\mu\nu} \equiv {}_1h_{\mu\nu}$ and $\delta T^{\text{fluid}}_{\mu\nu} \equiv {}_1\delta T^{\text{fluid}}_{\mu\nu}$.

It is well-known that the stress-energy tensor of a small body with mass m following a

[2] Note that in this context a small black hole can be treated as a small body despite being a singularity of spacetime [131].

trajectory $z^\mu(\widetilde{\tau})$ is given by (see for instance ref. [38])

$$\widetilde{T}^{\alpha\beta}_{\text{small body}}(x) = m \int \widetilde{P}^\alpha_\mu(x,z)\widetilde{P}^\beta_\nu(x,z)\widetilde{u}^\mu\widetilde{u}^\nu \, \frac{\delta^{(4)}(x-z)}{(-\widetilde{g})^{1/2}} \, d\widetilde{\tau} \tag{4.3}$$

where $\widetilde{P}^\alpha_\mu(x,z)$, $\widetilde{\tau}$ and $\widetilde{u}^\mu \equiv dz^\mu/d\widetilde{\tau}$ are respectively the parallel propagator from z^μ to x^μ, the proper time and the 4-velocity in the physical (*i.e.* perturbed) spacetime. This stress-energy tensor can then be expanded as a series in m/M:

$$\widetilde{T}^{\alpha\beta}_{\text{small body}} = T^{\alpha\beta}_{\text{small body}} + O\left((m/M)^2\right) , \tag{4.4}$$

$$T^{\alpha\beta}_{\text{small body}}(x) = m \int P^\alpha_\mu(x,z)P^\beta_\nu(x,z)u^\mu u^\nu \, \frac{\delta^{(4)}(x-z)}{(-g)^{1/2}} \, d\tau , \tag{4.5}$$

where $P^\beta_\nu(x,z)$, τ and $u^\mu = \mathrm{d}z^\mu/\mathrm{d}\tau$ are the parallel propagator, proper time and 4-velocity in the background.

If the small body interacts only gravitationally with the matter contained in the spacetime, its stress-energy tensor is conserved in the physical spacetime:

$$\widetilde{\nabla}_\beta \widetilde{T}^{\alpha\beta}_{\text{small body}} = 0 , \tag{4.6}$$

($\widetilde{\nabla}$ is the covariant derivative in the physical spacetime). This implies that the small body follows a geodesic of the physical, perturbed spacetime (see for instance ref. [38] for a formal proof): expanding the geodesic equations in the physical spacetime ($\widetilde{u}^\nu\widetilde{\nabla}_\nu\widetilde{u}^\mu = 0$) into a series, it is possible to obtain, to first-order in m/M,

$$\frac{Du^\mu}{d\tau} = -\frac{1}{2}\left(g^{\mu\nu} + u^\mu u^\nu\right)\left(2\nabla_\rho h_{\nu\lambda} - \nabla_\nu h_{\lambda\rho}\right)u^\lambda u^\rho + O\left((m/M)^2\right), \tag{4.7}$$

where ∇ and $D/d\tau$ are the covariant derivative and the total covariant derivative in the background.

Clearly, to zeroth order eq. (4.7) reduces to the geodesic equations in the background spacetime, but it deviates from them at first-order. The right-hand-side of eq. (4.7) represents the so-called "self-force" and is physically due to the interaction of the small body with its own gravitational field $\boldsymbol{h}$; in the case of a small body orbiting around an SMBH, this self-force is responsible for its inspiral towards the black hole.

In order to compute the right-hand side of eq. (4.7) one needs to compute the metric perturbation $\boldsymbol{h}$ and because this perturbation is produced by the small body itself, some of its components will be divergent at the position of the small body. A regularization procedure to cure these divergences has been derived [131, 132] for the trace-reversed metric perturbations

$$\bar{h}_{\mu\nu} \equiv h_{\mu\nu} - \frac{1}{2}\, h^\alpha_\alpha \, g_{\mu\nu} \tag{4.8}$$

in the Lorenz gauge, which is defined as

$$\nabla_\mu \bar{h}^{\mu\nu} = 0 \, . \tag{4.9}$$

It should be noted that while this gauge allows one in principle to remove the problem of divergences and has a number of other advantages (see ref. [133] for an extensive list), self-force calculations are extremely hard to perform in practice. Indeed, no general inspirals have been computed so far using the regularised version of eq. (4.7), even in Schwarzschild or Kerr spacetimes (see ref. [38, 39] for a review). However, a simpler approach can be followed in which only the dissipative part of the self-force is taken into account, leading to the so-called "adiabatic approximation" [36][3]. Within this approximation the small body moves along a geodesic with slowly changing parameters (in Kerr, these parameters are the energy E, the angular momentum L_z and Carter's constant Q). One of the advantages of the adiabatic approximation is that it prescribes a way to compute the evolution of these parameters, demonstrating that their rates of change $\dot{E}$ and $\dot{L}_z$ (with the dot being the derivative with respect to the coordinate time t) correspond to the energy and angular momentum carried away by gravitational waves [134]. The change in Carter's constant $\dot{Q}$, on the other hand, is harder to compute, although an explicit formula has recently been derived [135].

The first-order metric perturbation $\boldsymbol{h}$ can be computed as a solution of the linearised Einstein equations [136]

$$\Box \bar{h}^{\alpha\beta} + 2R_{\mu\ \nu}^{\ \alpha\ \beta} \bar{h}^{\mu\nu} + S_{\mu\ \nu}^{\ \alpha\ \beta} \bar{h}^{\mu\nu} = -16\pi(\delta T^{\alpha\beta}_{\text{fluid}} + T^{\alpha\beta}_{\text{small body}}) \, , \tag{4.10}$$

where

$$S_{\mu\alpha\nu\beta} = 2G_{\mu(\alpha} g_{\beta)\nu} - R_{\mu\nu} g_{\alpha\beta} - 2g_{\mu\nu} G_{\alpha\beta} \, , \qquad \Box \equiv g^{\mu\nu} \nabla_\mu \nabla_\nu \tag{4.11}$$

($R_{\mu\nu\alpha\beta}$, $R_{\mu\nu}$ and $G_{\mu\nu}$ are the background Riemann, Ricci and Einstein tensors). Note that self-force effects are not contained in (4.10), which is a first order equation. In fact, since the stress-energy tensor of the small body at the lowest order, $\boldsymbol{T}_{\text{small body}}$, is an intrinsically first-order quantity [remember the factor m appearing in eq. (4.5)], the small body's contribution can be computed using a zeroth-order expression of u^μ or, equivalently, by solving the geodesic equations for the background metric. In addition to the calculation of the small body's contribution, a consistent solution at first-order for the EMRI problem in a curved and non-vacuum spacetime requires the solution of the fluid perturbation $\boldsymbol{\delta T}_{\text{fluid}}$. This can be computed by imposing the conservation of the stress-energy tensor of the fluid, $\widetilde{\nabla}_\beta \widetilde{T}^{\alpha\beta}_{\text{fluid}} = 0$, which gives, to first order,

$$-16\pi \, \nabla_\beta \, \delta T^{\alpha\beta}_{\text{fluid}} = 2G^{\beta\sigma} \nabla_\sigma \bar{h}^\alpha_\beta - 2G^{\alpha\beta} \partial_\beta \bar{h} - R^{\beta\sigma} \nabla_\gamma \bar{h}_{\beta\sigma} g^{\gamma\alpha} \, . \tag{4.12}$$

It is not difficult to realize, using eqs. (4.10) and (4.12), that the Lorenz gauge condition is

[3] It should be noted that it is not yet clear whether the adiabatic approximation is accurate enough to compute waveforms for LISA as the conservative part of the self-force could have a secular effect as well [37].

conserved since it satisfies a homogeneous equation

$$\Box(\nabla_\beta \bar{h}^{\alpha\beta}) + R^\alpha_\mu \nabla_\beta \bar{h}^{\mu\beta} = 0 \ . \tag{4.13}$$

To summarise, the solution of eqs. (4.10) with the right-hand-side given by eqs. (4.12) and the zeroth-order contribution of eq. (4.7), provides the complete and consistent solution of the EMRI problem at first-order in m/M. Unfortunately, for situations of practical interest, such as for the observations of EMRIs performed by LISA, these first-order waveforms would be sufficiently accurate only for a few days or weeks [35, 92], imposing, at least in principle, the need for solution of the second-order equations.

Clearly, the solution of the second-order perturbation equations is much harder to obtain as these will have a schematic generic form of the type

$$\mathcal{D}[{}_2\boldsymbol{h}] = O\left(\nabla \boldsymbol{h} \nabla \boldsymbol{h}, \boldsymbol{h} \nabla \nabla \boldsymbol{h}\right) \ , \tag{4.14}$$

where $\mathcal{D}[{}_2\boldsymbol{h}]$ is a differential operator acting on ${}_2\boldsymbol{h}$.

One could naïvely try to solve this equation by imposing a gauge condition on ${}_2\boldsymbol{h}$ and using the Green's function of the $\mathcal{D}$ operator, but the formal solution obtained in this way would be divergent at every point because of the divergences of the first-order perturbation $\boldsymbol{h}$ at the small body's position. A regularization procedure to cure these divergences is known [137], but it has not yet been applied in practical calculations.

An alternative to the solution of the full second-order perturbation equations entails introducing the deviations from geodesic motion in the right-hand-side of eq. (4.10). This approach is clearly not consistent, but hopefully accurate enough if the ratio m/M and consequently the deviations from geodesic motion are sufficiently small. This is indeed what was done by Drasco and Hughes [41], who used the adiabatic approximation and a simplified formula for $\dot{Q}$ to compute the deviations from geodesic motion, inserting them in the right-hand-side of the Teukolsky equation [120] and then solving for *first-order* perturbations.

While very appealing, as it provides a simple way to improve upon a purely first-order calculation, we will not follow this approach here. Rather, we will perform our calculations within a semirelativistic ("kludge") approximation to eq. (4.10), using however as a background spacetime a non-trivial departure from a pure-Kerr solution. The properties of this spacetime and of alternative formulations of non-Kerr spacetimes will be discussed in detail in sec. 4.3, while a brief description of our semi-relativistic approach will be presented in sec. 4.4.

4.3 Modelling the background spacetime

The discussion made in the previous section assumes that a background spacetime $\boldsymbol{g}$ is known and this is traditionally assumed to be a "pure-Kerr" solution. However, this is not the only possibility. Indeed, in order to investigate LISA's ability to detect deviations from Kerr, a number of attempts have been made recently to replace the Kerr metric with

other stationary solutions representing reasonable deviations from a single rotating black hole in vacuum. In what follows we will briefly review these attempts and discuss a novel one based on the use of highly-accurate numerical solutions of the Einstein equations for spacetimes containing a black hole and a compact torus (see sec. 4.3.3).

4.3.1 Approximate non-Kerr spacetimes

One first attempt to go beyond a pure-Kerr model for the central massive object was suggested by Ryan [86, 87, 88], who considered a general stationary, axisymmetric, asymptotically flat, vacuum spacetime, which can be used to describe the gravitational field around a central distribution of matter, and its expansion in terms of the mass multipoles M_ℓ and of the current multipoles S_ℓ [138]. If one assumes reflection symmetry, the odd M-moments and even S-moments are identically zero [139, 140], so that the non-vanishing moments are the mass $M_0 = M$, the mass quadrupole M_2 and the higher-order even multipoles $M_4, M_6, \ldots$, as well as the angular momentum $S_1 = J$, the current octupole S_3 and the higher-order odd multipoles $S_5, S_7, \ldots$. The metric can then be written as

$$ds^2 = -e^{\gamma+\delta}\, dt^2 + e^{2\alpha}\,(dr^2 + r^2\, d\theta^2) + e^{\gamma-\delta}\, r^2 \sin\theta^2 (d\phi - \omega dt)^2 \,, \tag{4.15}$$

where the potentials $\gamma, \delta, \omega, \alpha$ depend only on r and θ. Each of them can expanded in terms of the multipole moments: for example

$$\delta = \sum_{n=0}^{+\infty} -2\frac{M_{2n}}{r^{2n+1}}\, P_{2n}(\cos\theta) + (\text{higher order terms}) \,, \tag{4.16}$$

$$\omega = \sum_{n=1}^{+\infty} -\frac{2}{2n-1}\,\frac{S_{2n-1}}{r^{2n+1}}\,\frac{P^1_{2n-1}(\cos\theta)}{\sin\theta} + (\text{higher order terms}) \,, \tag{4.17}$$

where $P_{2n},\ P^1_{2n-1}$ are the Legendre and the associated Legendre polynomials and where only the lowest-order $1/r$-dependence of each multipole moment is shown.

The multipoles are related to the interior matter distribution and could in principle be computed by solving the Einstein equations. In the particular case of a Kerr spacetime, all the multipole moments are trivially related to the first two, mass and angular momentum, by the following relation:

$$M_\ell + \mathrm{i} S_\ell = M \left(\mathrm{i}\frac{J}{M}\right)^\ell \,. \tag{4.18}$$

This is the celebrated "no hair" theorem: the spacetime of an (uncharged) stationary black hole is uniquely determined by its mass and spin. Deviations from the Kerr metric can be therefore detected by measuring the mass, spin and higher order moments of the central massive object.

While general and very elegant, this approach has serious drawbacks in the strong-

field region near the central massive object, which is clearly the most interesting one. In fact, this is the region which will be mapped by LISA and where the spacetime could be significantly different from Kerr. The origins of these drawbacks are rather apparent when looking at eqs. (4.16)–(4.17), which give in practice an expansion in powers of $1/r$ around a Minkowski spacetime. As a result, an accurate representation of the strong field region necessarily requires the inclusion of many multipoles.

Another approach to the modelling of a non-Kerr background spacetime was recently suggested by Babak and Glampedakis in ref. [92], and is based on the use of the Hartle-Thorne metric [141]. This metric describes the spacetime outside slowly rotating stars, includes as a special case the Kerr metric at order $O(a^2)$, where $a \equiv J/M^2$, and is accurate up to the mass quadrupole moment. In order to isolate the quadrupolar deviation with respect to Kerr, the Hartle-Thorne metric can be rewritten in terms of the parameter ϵ defined as

$$Q = Q^{\rm Kerr} - \epsilon\, M^3 \,, \qquad Q^{\rm Kerr} = -\frac{J^2}{M} \tag{4.19}$$

where M, J and $Q \equiv M_2$ are the mass, the angular momentum and the mass quadrupole moment, respectively. Since for Kerr one has $\epsilon = 0$, ϵ can be used as a lowest-order measure of the deviation of the spacetime from a Kerr solution. The metric expressed in this way can be further rewritten in "quasi-Boyer-Lindquist coordinates", *i.e.* coordinates reducing to Boyer-Lindquist coordinates if $\epsilon = 0$. This procedure then leads to the "quasi-Kerr" metric

$$g_{\mu\nu}^{\rm quasi-Kerr} = g_{\mu\nu}^{\rm Kerr} + \epsilon\, h_{\mu\nu} + O(a\,\epsilon,\, \epsilon^2) + O(\delta M_{\ell\geq 4}, \delta S_{\ell\geq 3}) \,, \tag{4.20}$$

where $g_{\mu\nu}^{\rm Kerr}$ is the Kerr metric in Boyer-Lindquist coordinates, $\epsilon h_{\mu\nu}$ is the deviation from it and $\delta M_{\ell\geq 4}$, $\delta S_{\ell\geq 3}$ are the deviations of the higher-order multipoles from those of a Kerr spacetime. Stated differently, the quasi-Kerr metric consists of a Kerr solution plus a small difference in the mass quadrupole expressed by the parameter ϵ, while neglecting any deviations from Kerr in the higher-order multipoles $M_4, M_6, \ldots$, and $S_3, S_5, \ldots$, *etc.*

Because this approach does not involve any expansion in powers of $1/r$, it can be used in the strong-field regions as long as the central massive object is slowly rotating. Furthermore, it has the great advantage of being straightforward to implement, leaving the mass quadrupole parameter ϵ as the only adjustable one. However, it has the drawback that it does not include any deviations in the multipoles higher than the quadrupole with respect to the multipoles of pure Kerr, which could be important in the strong field regime.

4.3.2 Exact non-Kerr spacetimes

A different approach to the modelling of the background consists instead of using *exact* solutions of the Einstein equations: these spacetimes of course behave well in the strong field regime, since they are not based on any series expansions.

Few attempts have been made in this direction. However, Kesden, Gair and Ka-

mionkowski [89] considered spacetimes containing non-rotating boson stars and found that the gravitational waves produced by EMRIs look qualitatively different from the pure black hole case. The spherical boson stars which they consider have spacetimes which are in fact identical to Schwarzschild spacetimes outside their surfaces, making them indistinguishable from black holes during the initial stages of an EMRI. However, for a black hole the event horizon prevents any observations of the inspirals after the final plunge. Because boson stars are horizonless however, many orbits inside the interior are expected if the small body interacts only gravitationally with the scalar field out of which the star is made: the "smoking gun" for a boson star would therefore be that gravitational waves from the inspiral are observed after the plunge. Gravitational waves from such an event could not be interpreted as an inspiral into a black hole with different parameters, because the first part of the inspiral is identical to the usual black-hole inspiral.

Another attempt was made by Collins and Hughes in ref. [90] or by Gair, Li and Mandel in ref. [91]. The analytical "bumpy black holes" they consider are objects that are *almost* Schwarzschild or Kerr black holes, but have some multipoles with a 'wrong' value. These spacetimes reduce to the usual Schwarzschild or Kerr black hole spacetimes in a natural way, by setting the "bumpiness" of the black hole to zero, but unfortunately they require naked singularities: although they are not expected to exist in nature, "bumpy black holes" could be useful as "straw-men" to set up null experiments and test deviations from pure Kerr using EMRIs.

4.3.3 A self-gravitating torus around a rotating black hole

Another different and novel approach to the modelling of a background, non-Kerr spacetime is also possible and will be the one adopted in this chapter. In particular, we exploit the consistent numerical solution of the full Einstein equations describing a spacetime with an axisymmetric black hole and a compact, self-gravitating torus of comparable mass and spin. These solutions have been recently obtained to great accuracy by Ansorg and Petroff [130] with a numerical code using spectral methods. In general, Ansorg and Petroff's code will produce a numerical solution of the Einstein equations representing an axisymmetric and stationary spacetime containing a rotating black hole and a constant-density, uniformly rotating torus of adjustable mass and spin. The metric of this *non-pure Kerr spacetime* in quasi-isotropic (QI) coordinates is generically given by

$$ds^2 = -e^{2\nu}dt^2 + {r_{\rm QI}}^2 \sin^2\theta B^2 e^{-2\nu}\left(d\phi - \omega dt\right)^2 + e^{2\mu}\left({dr_{QI}}^2 + {r_{\rm QI}}^2 d\theta^2\right) \ , \qquad (4.21)$$

where ν, μ, B and ω are functions of the radial quasi-isotropic coordinate $r_{\rm QI}$ and θ. The procedure for obtaining these numerical solutions is described in detail in ref. [130] and we here provide only a summary of the main ideas.

The entire spacetime outside the horizon is described by a metric in Weyl - Lewis - Papapetrou coordinates as in eq. (4.21) or (4.15). We fix our coordinates uniquely by stipulating that the first derivatives of the metric functions should be continuous at the surface of the torus and by choosing the location of the horizon to be a coordinate sphere

$r_{\rm QI}$ = constant $\equiv r_{+,\rm QI}$. Specifying the boundary conditions $B = 0$, $e^{2\nu} = 0$ and $\omega =$ constant on this sphere ensures that it is indeed a black hole horizon. We further assume reflection symmetry with respect to the equatorial plane.

We are interested only in the metric outside of the black hole and determine it using a multi-domain spectral method. One of the domains coincides precisely with the interior of the homogeneous, uniformly rotating perfect fluid torus, the boundary of which must be solved for as part of the global problem. This choice is important in order to avoid Gibbs phenomena. The vacuum region (outside the horizon) is divided up into four subdomains with three fixed boundaries separating them. This somewhat arbitrary choice enables us to resolve functions more accurately in the vicinities of both the torus and the black hole according to the scale determined by each object itself. One of the four vacuum domains extends out to infinity and is then compactified. A mapping of each domain onto a square is chosen in such a way as to avoid steep gradients in the functions being solved for.

The Einstein equations together with the specification of asymptotic flatness and the aforementioned boundary conditions provide us with a complete set of equations to be solved for. The metric functions and the function describing the boundary of the torus are expanded in terms of a finite number of Chebyshev polynomials. By specifying physical parameters to describe a configuration and demanding that the equations be satisfied exactly at collocation points on these five domains, we get a non-linear system of algebraic equations determining the coefficients in the expansion of the functions. We solve this system using a Newton-Raphson method where an existing neighbouring solution provides the initial guess (see ref. [130] for more details and for a discussion of how to obtain the first "initial guess").

Note that throughout this chapter, the masses and angular momenta of the black hole, $M_{\rm BH}$ and $J_{\rm BH}$, of the torus, $M_{\rm Torus}$ and $J_{\rm Torus}$, and of the whole system, $M_{\rm tot} \equiv M_{\rm BH} + M_{\rm Torus}$ and $J_{\rm tot} \equiv J_{\rm BH} + J_{\rm Torus}$, are the "Komar" masses and angular momenta [142, 143]. We note that the definition of the mass of a single object in General Relativity can be quite slippery, especially when this measure is not an asymptotic one. We also recall that while the *total* Komar mass of the system coincides with the familiar "ADM" mass [144], other definitions are possible for the *single* masses of the torus and the black hole. As an example, it is possible to define the "irreducible mass" of the black hole as $M_{\rm irr} \equiv [A_+/(16\pi)]^{1/2}$, where A_+ is the horizon's area [145], and then define the total mass of the black hole as $M_{\rm hole} \equiv [M_{\rm irr}^2 + (J_{\rm BH}/(2M_{\rm irr}))^2]^{1/2}$ (Note that this latter definition coincides with the Komar mass for an isolated Kerr black hole.). Similarly, the mass of the torus can also be measured in terms of the "baryonic" mass $M_{\rm baryon} = \int \rho\, u^t \sqrt{-g}\, d^3x$ (ρ being the baryonic mass density and $\boldsymbol{u}$ the 4-velocity of the fluid of the torus). This mass is simply a measure of the number of baryons, it does not include the gravitational binding of the object, and thus can also be rather different from the corresponding Komar mass.

Overall, we have found that even in our non-pure Kerr spacetimes, all the definitions of the mass of the black hole agree rather well. In particular, in the spacetimes A and B which we will consider in sections 4.5.1-4.5.2 (*cf.* table 4.1) we have $M_{\rm BH} = 0.413$, $M_{\rm irr} = 0.457$, $M_{\rm hole} = 0.468$ and $M_{\rm BH} = 0.1$, $M_{\rm irr} = 0.1007$, $M_{\rm hole} = 0.1007$, respectively.

On the other hand, the Komar mass and the baryonic mass of the torus have been found to be different with $M_{\rm Torus} = 0.121$ and $M_{\rm baryon} = 0.0578$ in spacetime A and $M_{\rm Torus} = 0.007$ and $M_{\rm baryon} = 0.00656$ in spacetime B. As mentioned above, there is no reason to expect these two measures to be close, but it is interesting that this happens under certain circumstances (as in spacetime B, for example). Furthermore, these differences are not going to affect our analysis, which will never use the single mass of the torus.

4.4 The semi-relativistic approach

Although the procedure outlined in sec. 4.2 to calculate the waveforms from an EMRI in a non-vacuum spacetime is the only mathematically correct one, it has never been applied in practice, not even to first order. Such an approach, in fact, involves the solution of a complicated system of 14 coupled partial differential equations [eqs. (4.10) and (4.12)] and while this can in principle be solved, alternative solutions have traditionally been sought in the literature. A very popular one is the "semi-relativistic" approach, which leads to the so-called "kludge" waveforms [146, 147, 12] and which we will also adopt hereafter.

In essence, the semi-relativistic approach consists of considering geodesic motion for the small body (including, when possible, corrections to account at least approximately for the effects of radiation reaction) and in calculating the emitted gravitational waves as if the small body were moving in a Minkowski spacetime. This latter assumption requires a mapping between the real spacetime and the Minkowski spacetime: in the pure Kerr case, this is obtained by identifying Boyer-Lindquist coordinates with the spherical coordinates of the Minkowski spacetime. The waveforms are then computed using the standard quadrupole, octupole or higher order formulae[4]. Waveforms obtained in this way are commonly referred to as "kludge" waveforms [146, 147, 12]

A justification of this procedure in terms of the Einstein equations is given in the Appendix. However, the strongest motivation for introducing kludge waveforms is the surprising agreement that they show with the accurate waveforms that can be computed in a Kerr spacetime using the Teukolsky formalism [12]. In view of this, kludge waveforms represent the natural first approach to model the emission from EMRIs in non-pure Kerr spacetimes and will be used throughout this work.

As mentioned in sec. 4.2, the adiabatic approximation offers a simple way to include radiation-reaction effects in a Kerr spacetime. More specifically, if we denote Kerr geodesics by $x^\mu_{\rm geod}(t, E, L_z, Q)$, the trajectory of the small body is then corrected to be $x^\mu(t) = x^\mu_{\rm geod}(t, E(t), L_z(t), Q(t))$, that is, a geodesic with varying parameters. The accurate calculation of the fluxes $\dot{E}$, $\dot{L}_z$ and $\dot{Q}$ is rather involved [135, 41], but approximate ways to compute them have also been suggested [104, 115, 148, 119]. Although Barack and Cutler [93] have recently proposed including radiation reaction in quasi-Kerr spacetimes by

[4]Note that comparisons with Teukolsky-based waveforms in Kerr show that the inclusion of multipoles higher than the octupole does not improve kludge waveforms [12]. Because of this, contributions only up to the octupole are used here to calculate kludge waveforms.

using post-Newtonian fluxes in which the leading-order effect of the quadrupole of the spacetime is taken into account, it is still unclear at this stage how accurately the fluxes for a Kerr or a quasi-Kerr spacetime could describe the non-geodesic motion of an EMRI around our black hole-torus systems. Because of this, we have here preferred to consider the simplest scenario and thus model the motion of the small body as a pure geodesic with equations of motion that in the spacetime given by eq. (4.21) are

$$\frac{dt}{d\tau} = -g^{tt}\tilde{\epsilon} + g^{t\phi}\tilde{\ell}\,, \tag{4.22}$$

$$\frac{d\phi}{d\tau} = -g^{t\phi}\tilde{\epsilon} + g^{\phi\phi}\tilde{\ell}\,, \tag{4.23}$$

$$\begin{aligned}\frac{d^2r}{d\tau^2} = &-\Gamma^r_{rr}\left(\frac{dr}{d\tau}\right)^2 - \Gamma^r_{\theta\theta}\left(\frac{d\theta}{d\tau}\right)^2 - 2\Gamma^r_{r\theta}\frac{dr}{d\tau}\frac{d\theta}{d\tau} \\ &-\Gamma^r_{tt}\left(\frac{dt}{d\tau}\right)^2 - \Gamma^r_{\phi\phi}\left(\frac{d\phi}{d\tau}\right)^2 - 2\Gamma^r_{t\phi}\frac{dt}{d\tau}\frac{d\phi}{d\tau}\,,\end{aligned} \tag{4.24}$$

$$\begin{aligned}\frac{d^2\theta}{d\tau^2} = &-\Gamma^\theta_{rr}\left(\frac{dr}{d\tau}\right)^2 - \Gamma^\theta_{\theta\theta}\left(\frac{d\theta}{d\tau}\right)^2 - 2\Gamma^\theta_{r\theta}\frac{dr}{d\tau}\frac{d\theta}{d\tau} \\ &-\Gamma^\theta_{tt}\left(\frac{dt}{d\tau}\right)^2 - \Gamma^\theta_{\phi\phi}\left(\frac{d\phi}{d\tau}\right)^2 - 2\Gamma^\theta_{t\phi}\frac{dt}{d\tau}\frac{d\phi}{d\tau}\,,\end{aligned} \tag{4.25}$$

where $r \equiv r_{\rm QI}$ is the radial quasi-isotropic coordinate, τ is the proper time, the Γ's are the Christoffel symbols and $\tilde{\epsilon}$ and $\tilde{\ell}$ are the energy and angular momentum per unit mass as measured by an observer at infinity.

The resulting geodesics can be labelled with seven parameters: four refer to the initial position $t_0, \phi_0, r_0, \theta_0$ and the remaining three identify the initial 4-velocity. In the case, which we will consider in this chapter, of bound stable orbits in the equatorial plane, only five parameters would remain. However, because of stationarity and axisymmetry it is not restrictive to fix $t_0 = \phi_0 = 0$ and $r_0 = r_p$, with r_p being the periastron radius. Therefore, except for a sign to distinguish between prograde ($\dot{\phi} > 0$) and retrograde ($\dot{\phi} < 0$) orbits, equatorial bound stable geodesics can be characterised by only two parameters, which we can choose to be the semi-latus rectum $p_{\rm QI}$ and the eccentricity $e_{\rm QI}$, which are related to the coordinate radii at apoastron and periastron by $r_a \equiv p_{\rm QI}/(1 - e_{\rm QI})$ and $r_p \equiv p_{\rm QI}/(1 + e_{\rm QI})$.

Clearly, kludge waveforms computed from pure geodesic motion are expected to be accurate only below the timescale over which radiation-reaction effects become apparent and make our waveforms differ significantly from the real signal. A simple way to estimate this timescale exploits the concept of "overlap" between two waveforms, which will be introduced in sec. 4.4.1.

An important comment is instead needed here about the coordinate mapping used in calculating kludge waveforms. As already mentioned, this mapping has a straightforward realization in a Kerr spacetime, where the BL coordinates are associated with the spherical coordinates of a Minkowski spacetime. In a similar manner, in our non-pure

Kerr spacetimes we transform the solution of the geodesic equations from QI coordinates to "quasi-Boyer-Lindquist" (QBL) coordinates, *i.e.* coordinates that reduce to BL coordinates in the absence of the torus. These coordinates are then identified with the spherical coordinates of a Minkowski spacetime as in ref. [92] and used to compute kludge waveforms.

Fortunately, the transformation from QI to QBL coordinates is straightforward and involves only a change in the radial coordinate:

$$r_{\rm QBL} = r_{\rm QI} + \widetilde{M} + \frac{r_{+,\rm QI}^2}{r_{\rm QI}} \,, \tag{4.26}$$

where $\widetilde{M}$ is a parameter that reduces to the mass of the central black hole in the absence of the torus. Clearly, this mapping suffers from an intrinsic ambiguity as the mass $\widetilde{M}$ could be associated either with the mass of the black hole or with the total mass of the system, or even with a combination of the two. Although all of the choices are essentially equivalent when the torus is very light, this is not necessarily the case for some of the configurations considered here, for which the torus has a mass comparable with that of the black hole. Since the parameter $\widetilde{M}$ is, at least in a Newtonian sense, the gravitational mass experienced by the small body, we have here followed a pragmatic approach and set $\widetilde{M} = M_{\rm tot}$ for equatorial orbits with periastron larger than the outer edge of the torus, which we will refer to as the *"external orbits"*. Conversely, we have set $\widetilde{M} = M_{\rm BH}$ for what we will refer to as the *"internal orbits"*, that is equatorial orbits with both periastron and apoastron between the inner edge of the torus and the horizon. This classification is summarised schematically in Fig. 4.1, which shows the two regions into which the spacetime has been divided and the corresponding values of $\widetilde{M}$. This choice is clearly an operative ansatz, but we have checked to see that its influence on our results is indeed negligible and a detailed discussion of this will be presented in sec. 4.5.

Finally, we note that we have not considered here orbits crossing the torus because the non-gravitational interaction between the small body and the fluid would cause deviations from geodesic motion which are not easy to model [*cf.* chapter 3].

4.4.1 Overlap and dephasing time

In order to compare (kludge) waveforms computed in non-pure Kerr spacetimes with (kludge) waveforms computed in Kerr spacetimes, we follow the procedure proposed in ref. [92] and make use of the so-called *overlap function*. Its meaning can be best understood through the more familiar concept of SNR.

As we have seen in sec. 1.3, if a signal is the sum of a gravitational wave $h(t)$ and of some Gaussian noise $n(t)$, the SNR for a template $\hat{h}(t)$ is given by

$$\frac{S}{N}[\hat{h}] = \frac{(\hat{h},h)}{(\hat{h},\hat{h})^{1/2}} + \frac{(\hat{h},n)}{(\hat{h},\hat{h})^{1/2}} \approx \frac{(\hat{h},h)}{(\hat{h},\hat{h})^{1/2}} \,, \tag{4.27}$$

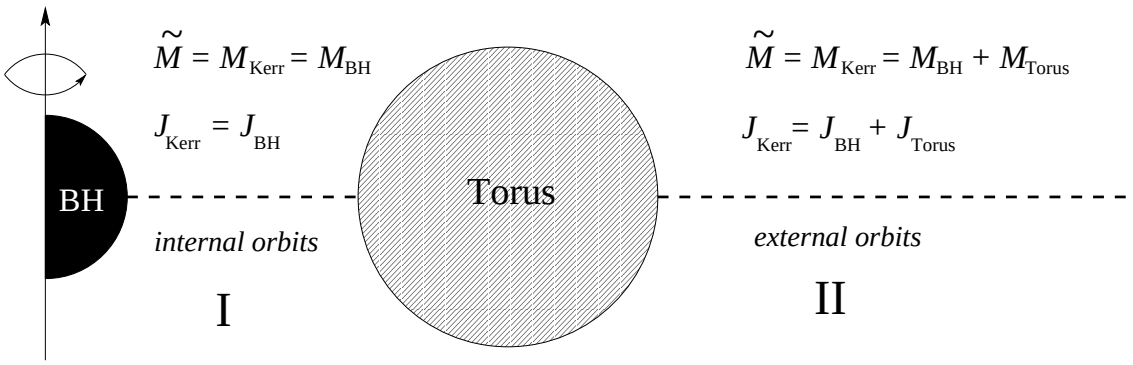

Figure 4.1: *Schematic classification of the two regions of the spacetime. For equatorial orbits in region I (i.e. internal orbits) the mass and angular momentum of the Kerr spacetime coincide with the mass and angular momentum of the black hole. For equatorial orbits in region II (i.e. external orbits) the mass and angular momentum of the Kerr spacetime coincide with the total mass and angular momentum of the black hole-torus system.*

[*cf.* eq. (1.25)], where the internal product "(,)" can be defined in terms of the Fourier transforms (which are denoted by a "tilde"):

$$(h_1, h_2) \equiv 2 \int_0^\infty \frac{\tilde{h}_1^*(f)\tilde{h}_2(f) + \tilde{h}_1(f)\tilde{h}_2^*(f)}{S_n(f)} df \tag{4.28}$$

[$S_n(f)$ is the spectral sensitivity of the detector].

If α measures the SNR for a template $\hat{h}(t)$ "matching" the gravitational wave $h(t)$ perfectly, *i.e.* $S/N = (h,h)^{1/2} \equiv \alpha$, any "mismatch" between $\hat{h}(t)$ and $h(t)$ will degrade the SNR ratio to $S/N = \alpha\, \mathcal{O}(h, \hat{h})$, where the overlap function $\mathcal{O}$ is defined as

$$\mathcal{O}(h, \hat{h}) \equiv \frac{(h, \hat{h})}{(\hat{h}, \hat{h})^{1/2}(h,h)^{1/2}} \ . \tag{4.29}$$

The same logic can now be used to quantify the differences between kludge waveforms computed in different spacetimes. More specifically, if we label with "1" a waveform computed in a non-pure Kerr spacetime and with "2" the closest equivalent in a Kerr spacetime, the overlap between the two $\mathcal{O}\,(h_1, h_2) \equiv (h_1, h_2)/[(h_1, h_2)^{1/2}(h_1, h_2)^{1/2}]$ will express how much SNR is lost by an observer matched-filtering a black hole-torus signal with a pure Kerr template. Stated differently, $\mathcal{O}(h_1, h_2) = 1$ if the two waveforms are

identical, while $\mathcal{O}(h_1, h_2) = 0$ if they are totally uncorrelated and $\mathcal{O}(h_1, h_2) = -1$ if they are perfectly anticorrelated.

Having introduced the concept of overlap function, we can proceed to an operative definition of the timescale below which kludge waveforms computed from pure geodesic motion are expected to be accurate. This timescale, usually referred to as the "dephasing time" $\tau_{\rm d}$, is defined as the time at which the overlap between two waveforms in the Kerr spacetime, one computed considering geodesic motion and the other one including radiation reaction effects, drops below 0.95 (this is indeed the threshold used to build template banks [149]). Clearly, the dephasing time will be different for external and internal orbits and also in this case attention needs to be paid to the mappings between non-pure and pure Kerr spacetimes. Following the same logic discussed in the previous section, we calculate $\tau_{\rm d}$ for an external equatorial orbit in our non-pure Kerr spacetime by considering the equatorial orbit with the same semi-latus rectum and eccentricity in the Kerr spacetime[5] with mass $M_{\rm Kerr} = M_{\rm tot}$ and spin $J_{\rm Kerr} = J_{\rm tot}$. On the other hand, for an internal orbit we calculate $\tau_{\rm d}$ by considering the orbit with the same semi-latus rectum and eccentricity in the Kerr spacetime with mass $M_{\rm Kerr} = M_{\rm BH}$ and spin $J_{\rm Kerr} = J_{\rm BH}$. As we will explain, in this case we have also looked into the influence that this association has on the overall results presented in sec. 4.5.

In order to compute the dephasing time, we used the approximate Kerr fluxes proposed in ref. [119], which are based on post-Newtonian expansions and fits to fluxes computed rigorously with the Teukolsky formalism.

4.5 Comparing pure and non-pure Kerr spacetimes

The set of tools introduced in the previous sections, namely: the kludge waveforms, the numerical solution of the Einstein equations for spacetimes containing a black hole and a torus, and the overlap function, can now be applied to determine to what extent LISA can detect a difference between a pure and a non-pure Kerr spacetime.

Hereafter we will restrict our attention to equatorial, bound and stable orbits, choosing the values of the mass and angular momentum of the pure Kerr spacetime using the same logic discussed in the previous sections, *i.e.*

$$\left.\begin{array}{ll} M_{\rm Kerr} & = M_{\rm BH} = \widetilde{M} \\ J_{\rm Kerr} & = J_{\rm BH} \end{array}\right\} \quad \text{internal orbits,}$$

$$\left.\begin{array}{ll} M_{\rm Kerr} & = M_{\rm tot} = \widetilde{M} \\ J_{\rm Kerr} & = J_{\rm tot} \end{array}\right\} \quad \text{external orbits.} \tag{4.30}$$

Note that for internal orbits we did try to compare our non-pure Kerr spacetimes with pure Kerr spacetimes having $M_{\rm Kerr} = M_{\rm tot} = \widetilde{M}$ and $J_{\rm Kerr} = J_{\rm tot}$ (using these values also

[5] The semi-latus rectum and the eccentricity are assumed to be in BL coordinates in pure Kerr and in QBL in non-pure Kerr spacetimes.

	spacetime A	spacetime B
$M_{\rm BH}$	0.413	0.100
$M_{\rm Torus}$	0.121	0.007
$M_{\rm BH}/M_{\rm Torus}$	3.4	14.3
$J_{\rm BH}$	9.02×10^{-2}	-1.74×10^{-5}
$J_{\rm Torus}$	1.17×10^{-1}	2.58×10^{-3}
$J_{\rm BH}/J_{\rm Torus}$	7.69×10^{-1}	-6.74×10^{-3}
$J_{\rm BH}/M_{\rm BH}^2$	5.28×10^{-1}	-1.74×10^{-3}
$J_{\rm tot}/M_{\rm tot}^2$	0.728	0.224
ρ	2.637	0.198
$r_{+,\rm QI}$	0.179	0.050
$r_{\rm in,QI}$	0.6064	0.9156
$r_{\rm out,QI}$	0.6305	1.0000
ϵ	0.11	2.63

Table 4.1: *Parameters of the spacetimes A and B analysed in section 4.5, in units in which $10^7 M_\odot = G = c = 1$. $r_{\rm in,QI}$ and $r_{\rm out,QI}$ are the inner and outer edges of the torus in QI coordinates, ρ is the baryonic mass density of the torus and the parameter ϵ provides a lowest-order measure of the deviation of the spacetime away from a Kerr solution [cf. eq.* (4.19)*]. Note that ϵ is more sensitive to the ratio between the angular momenta than to that between the masses.*

to compute the dephasing time, *cf.* sec. 4.4.1), but this turned out not to be a good choice[6].

Once a non-pure and a pure Kerr spacetime have been built and the orbits have been isolated according to the relations (4.30), further care needs to be paid to selecting corresponding geodesics. As mentioned in sec. 4.4, equatorial geodesics can be labelled by two parameters, which can be chosen to be, for instance, the semi-latus rectum and the eccentricity $p_{_{(\rm Q)BL}}$ and $e_{_{(\rm Q)BL}}$, calculated in QBL coordinates for the non-pure Kerr spacetime and in BL coordinates for the Kerr spacetime.

However, as already pointed out in ref. [92], waveforms produced by geodesics having the same $p_{_{(\rm Q)BL}}$ and $e_{_{(\rm Q)BL}}$ are significantly different because they do not have comparable orbital frequencies, and give overlaps $\mathcal{O} \lesssim 0.4$. A similar conclusion can be drawn in the case in which the free parameters are chosen to be the periastron radius and the (tangential) velocity measured at the periastron by a zero angular momentum observer (ZAMO): this choice gives overlaps $\mathcal{O} \simeq 0.1 - 0.2$. In view of this, any sensible comparison can be made only with geodesics in the two spacetimes that have the same orbital frequencies (this result was already pointed out in ref. [92]).

We recall that an equatorial geodesic in a generic stationary, axisymmetric spacetime has an r-motion that is periodic in the coordinate time t. To see this, it is sufficient to combine eqs. (4.22), (4.23) and the normalisation condition $u_\mu u^\mu = -1$ for an equatorial motion $\theta = \pi/2$ so that

$$(dr/dt)^2 = V(r, \tilde{\epsilon}, \tilde{\ell}) \,, \tag{4.31}$$

with $V(r, \tilde{\epsilon}, \tilde{\ell})$ being a function of r and of the two constants of motion $\tilde{\epsilon}$ and $\tilde{\ell}$. Clearly, eq. (4.31) has a periodic solution with a frequency that we will denote as ω_r. A similar analysis can be carried out for the motion in the ϕ direction, which, combining eqs. (4.22) and (4.23) for $\theta = \pi/2$, satisfies an equation of the type

$$d\phi/dt = G(r, \tilde{\epsilon}, \tilde{\ell}) \,, \tag{4.32}$$

where $G(r)$ is again a function of r, $\tilde{\epsilon}$ and $\tilde{\ell}$. Integrating eq. (4.32) with $\phi_0 = t_0 = 0$ leads to

$$\phi(t) = \langle G \rangle t + \int_0^t (G(r(t), \tilde{\epsilon}, \tilde{\ell}) - \langle G \rangle) dt \,, \tag{4.33}$$

where $\langle G \rangle$ is the time average of $G(r(t), \tilde{\epsilon}, \tilde{\ell})$ over an r-period. The second term on the right-hand-side of eq. (4.33) is clearly periodic in t (with zero average) so that the ϕ-motion has a linearly growing term and an oscillating one. The overall frequency content of the ϕ motion is therefore determined by $\omega_\phi = \langle G \rangle$.

The orbital frequencies ω_r and ω_ϕ can therefore be used to characterise equatorial geodesics (and hence waveforms) that are expected to be as similar as possible (*i.e.* have the largest possible overlap) in the two spacetimes. In practice, given a geodesic (and therefore a waveform) characterised by ω_r and ω_ϕ in the non-pure Kerr spacetime, we can compare it to the waveform produced in the Kerr spacetime by the orbit which has

[6] *i.e.*, for many bound stable orbits in the non-pure Kerr spacetimes that we considered, it was impossible even to find bound stable orbits with the same semi-latus rectum and eccentricity in the Kerr spacetime.

the same r- and ϕ-frequencies. Since ω_r and ω_ϕ for equatorial orbits in a Kerr spacetime are functions of $M_{\rm Kerr}$, $J_{\rm Kerr}$, $p_{\rm BL}$ and $e_{\rm BL}$ (explicit expressions for these functions, which we will denote $\omega_r^{\rm Kerr}$ and $\omega_\phi^{\rm Kerr}$, are given in ref. [116]), matching the geodesics amounts to solving the following equations in the unknowns δp and δe

$$\omega_r^{\rm BH+Torus}(p_{\rm QBL}, e_{\rm QBL}) = \omega_r^{\rm Kerr}(p_{\rm BL}=p_{\rm QBL}+\delta p, e_{\rm BL}=e_{\rm QBL}+\delta e, M_{\rm Kerr}, J_{\rm Kerr})\,, \tag{4.34}$$

$$\omega_\phi^{\rm BH+Torus}(p_{\rm QBL}, e_{\rm QBL}) = \omega_\phi^{\rm Kerr}(p_{\rm BL}=p_{\rm QBL}+\delta p, e_{\rm BL}=e_{\rm QBL}+\delta e, M_{\rm Kerr}, J_{\rm Kerr})\,, \tag{4.35}$$

where $\omega_r^{\rm BH+Torus}(p_{\rm QBL}, e_{\rm QBL})$ and $\omega_\phi^{\rm BH+Torus}(p_{\rm QBL}, e_{\rm QBL})$ are the r- and ϕ-frequencies of the equatorial orbit with semi-latus rectum $p_{\rm QBL}$ and eccentricity $e_{\rm QBL}$ in the non-pure Kerr spacetime under consideration and where $M_{\rm Kerr}$ and $J_{\rm Kerr}$ follow the selection rule in eq. (4.30) to distinguish internal and external orbits. Indeed, this is the approach which was followed in ref. [92] and which highlighted the possibility of a degeneracy problem in non-pure Kerr spacetimes.

An important difference with respect to the work presented in ref. [92] is that we also considered a different way in which it is possible to identify geodesics that have the same orbital frequencies in a Kerr and in a non-pure Kerr spacetime. We can in fact consider the semi-latus rectum and eccentricity as fixed in (Q)BL and search for the values of the additional mass δM and angular momentum δJ of the Kerr spacetime which would yield the same r- and ϕ-frequencies, *i.e.*

$$\omega_r^{\rm BH+Torus}(p_{\rm QBL}, e_{\rm QBL}) = \omega_r^{\rm Kerr}(p_{\rm BL}=p_{\rm QBL}, e_{\rm BL}=e_{\rm QBL}, M_{\rm Kerr}+\delta M, J_{\rm Kerr}+\delta J)\,, \tag{4.36}$$

$$\omega_\phi^{\rm BH+Torus}(p_{\rm QBL}, e_{\rm QBL}) = \omega_\phi^{\rm Kerr}(p_{\rm BL}=p_{\rm QBL}, e_{\rm BL}=e_{\rm QBL}, M_{\rm Kerr}+\delta M, J_{\rm Kerr}+\delta J)\,. \tag{4.37}$$

Of course, a similar but distinct set of equations can also be built by considering orbits having the same semi-latus rectum and eccentricity in QI coordinates[7]

$$\omega_r^{\rm BH+Torus}(p_{\rm QI}, e_{\rm QI}) = \omega_r^{\rm Kerr}(p_{\rm QI}, e_{\rm QI}, M_{\rm Kerr}+\delta M, J_{\rm Kerr}+\delta J)\,, \tag{4.38}$$

$$\omega_\phi^{\rm BH+Torus}(p_{\rm QI}, e_{\rm QI}) = \omega_\phi^{\rm Kerr}(p_{\rm QI}, e_{\rm QI}, M_{\rm Kerr}+\delta M, J_{\rm Kerr}+\delta J)\,. \tag{4.39}$$

To illustrate how different correlations of orbits in the two spacetimes can lead to significantly different waveforms, we show in Fig. 4.2 some kludge waveforms for a small body with mass $m = 1M_\odot$ moving in the spacetime B whose parameters are listed in Table 4.1. The geodesics have been calculated up to the dephasing time (*i.e.* $\tau_{\rm d} \simeq 42$ d) and the figure shows a magnification of the waveforms around this time. In particular, the black solid line shows the waveform produced by a geodesic with $p_{\rm QBL}/M_{\rm tot} = 21.237$ and $e_{\rm QBL} = 0.212$ in spacetime B, while the red dot-dashed one refers to a geodesic with the same semi-latus rectum and eccentricity (in (Q)BL coordinates) in a Kerr spacetime with $M_{\rm Kerr} = M_{\rm tot}$ and $J_{\rm Kerr} = J_{\rm tot}$. The blue dotted line and the brown circles are instead

[7] The transformation from BL to QI coordinates in a Kerr spacetime is given for instance in ref. [150], eq. (80): the transformation turns out to be the inverse of eq. (4.26), with $r_{+\,\rm QI} = M(1-a^2)^{1/2}/2$ (M and a being the mass and the spin parameters of the Kerr spacetime under consideration).

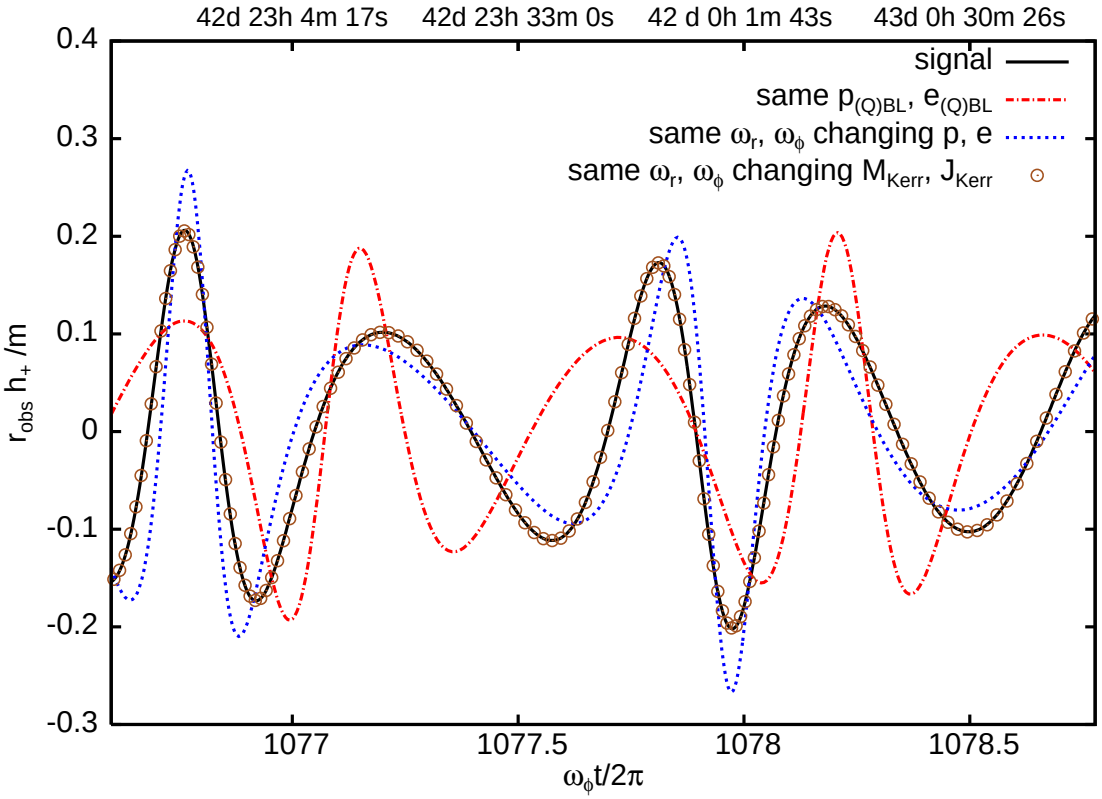

Figure 4.2: *Kludge waveforms around the dephasing time for a small body with mass $m = 1M_\odot$ moving in the spacetime B of Table 4.1. The black solid line shows the waveform produced by a geodesic with given semi-latus rectum and eccentricity in spacetime B, while the red dot-dashed one refers to a geodesic with the same semi-latus rectum and eccentricity (in (Q)BL coordinates) in a Kerr spacetime with $M_{\rm Kerr} = M_{\rm tot}$ and $J_{\rm Kerr} = J_{\rm tot}$. The blue dotted line and the brown circles are instead the waveforms produced by an orbit with the same r- and ϕ-frequencies as obtained by adjusting $(\delta p, \delta e)$ or $(\delta M, \delta J)$, respectively.*

the waveforms produced by an orbit with the same r- and ϕ-frequencies as obtained by adjusting $(\delta p, \delta e)$ or $(\delta M, \delta J)$, respectively. Clearly, fixing the same orbital parameters $p_{\rm (Q)BL}$ and $e_{\rm (Q)BL}$ in the two spacetimes would be misleading and will inevitably produce very small overlaps. On the other hand, ensuring that the orbital frequencies are the same by adjusting δM and δJ provides waveforms that are much more similar and even harder to distinguish over this timescale than if δp and δe are adjusted.

In the following sections we will discuss in detail the degeneracy problem when considering the two different ways in which the geodesics in the two spacetimes can be matched. Before doing that, however, we will now briefly recall the main properties of the numerically-generated spacetimes that we have considered here, and whose parameters are listed in Table 4.1. We note that because the investigation of each spacetime is a rather lengthy and computationally expensive operation, we have restricted our atten-

tion to two spacetimes only, but with rather different properties. More specifically, we have considered a first spacetime (denoted as A) having a torus with mass smaller than that of the black hole (but almost comparable to it) and slightly larger angular momentum (*i.e.* $M_{\rm BH} \gtrsim M_{\rm Torus}, |J_{\rm BH}| \lesssim |J_{\rm Torus}|$) and a second spacetime (denoted as B) having a torus with mass much smaller than that of the black hole but much larger angular momentum (*i.e.* $M_{\rm BH} \gg M_{\rm Torus}, |J_{\rm BH}| \ll |J_{\rm Torus}|$).

We also note that spacetime A has a rather small quadrupole parameter $\epsilon \simeq 0.1$ [*cf.* eq. (4.19) for the definition] and could therefore be used to validate the perturbative results of ref. [92] which, we recall, were formulated to the lowest order in ϵ. Interestingly, we will see that taking into account the higher-order multipoles can lead to important qualitative differences and weaken or even cancel (for orbits very close to the torus) the degeneracy problem found in ref. [92]. Spacetime B, on the other hand, has a considerably larger value for ϵ and cannot, therefore, be described satisfactorily by the metric (4.20). The spacetimes were computed to sufficiently high accuracy so as to ensure that the numerical errors do not affect the results. More specifically, for spacetime A we used 40×40 Chebyshev polynomials in the vacuum domain extending out to infinity (domain 1 of [130]) and 28×28 polynomials in the other 4 domains. For spacetime B we used 31×27 polynomials in each of the 5 domains. Typical physical quantities, such as mass and angular momentum, were thus accurate to about 10^{-6} in spacetime A and 10^{-7} in spacetime B. We note that these errors are orders of magnitude smaller than the ones of $O(a\,\epsilon,\, \epsilon^2) + O(\delta M_{\ell\geq 4}, \delta S_{\ell\geq 3})$ typically affecting the approximate metric (4.20). Moreover, the accuracy of our numerically generated spacetimes is sufficient for the present investigation, because the dephasing it introduces is comparable with the dephasing due to radiation reaction, as the latter scales with the mass ratio $m/M_{\rm BH} \approx 10^{-6} - 10^{-7}$. As a result, introducing a cut-off at the dephasing time not only makes the effects of radiation reaction negligible, but it also ensures that the numerical errors in the calculation of the spacetimes do not affect the results. As a further check, we have varied the number of Chebyshev polynomials and verified that the numerical errors inherent to the spacetimes have a negligible impact on our final results.

For all of the waveforms computed in this chapter, we have considered an observer located at $\phi_{obs} = 0, \theta_{obs} = \pi/4$ and have decomposed the incoming gravitational-wave signal into the usual "plus" and "cross" polarisations (see, for instance, refs. [12, 1] for details). Furthermore, labelling the gravitational waves computed in the two spacetimes with 1 and 2, we calculate the overlaps for both polarisations, $\mathcal{O}(h_1^+, h_2^+)$ and $\mathcal{O}(h_1^\times, h_2^\times)$, and in the discussion of our results we refer to the smaller of the two overlaps, *i.e.* $\mathcal{O}(h_1, h_2) \equiv \min[\mathcal{O}(h_1^+, h_2^+), \mathcal{O}(h_1^\times, h_2^\times)]$. In practice, however, the difference between $\mathcal{O}(h_1^+, h_2^+)$ and $\mathcal{O}(h_1^\times, h_2^\times)$ for the overlaps plotted in the figures of the next sections is typically smaller than 0.005 and in no case larger than 0.025.

Finally, we note that the results presented in the next sections refer to a small body with $m = 1 M_\odot$ and to a sensitivity function for LISA computed using the online generator [14] with its default parameters and, in particular, no white dwarf noise. As pointed out in ref. [92], including white-dwarf noise would only lead to a slight increase in the dephasing time.

4.5.1 The degeneracy problem when varying e and p

After excluding a comparison between geodesics (and hence waveforms) that have the same semi-latus rectum and eccentricity in the pure and non-pure Kerr spacetimes because of the very small overlap that they produce, we have compared waveforms having the same r- and ϕ-frequencies as obtained by changing the semi-latus rectum and eccentricity while keeping $M_{\rm Kerr}$ and $J_{\rm Kerr}$ fixed [*cf.* eqs. (4.34) and (4.35)]. More specifically, we already mention that the values of $\delta p/p_{\rm QBL}$ obtained in the regions of the parameter space $(p_{\rm QBL}, e_{\rm QBL})$ where the overlap between these waveforms is high ($\mathcal{O} > 0.95$) are $|\delta p/p_{\rm QBL}| \lesssim 0.05$ in spacetime A and $|\delta p/p_{\rm QBL}| \lesssim 0.16$ in spacetime B. Similarly, the values of δe obtained in the regions of the parameter space where $\mathcal{O} > 0.95$ are $|\delta e| \lesssim 0.06$ in spacetime A and $|\delta e| \lesssim 0.07$ in spacetime B.

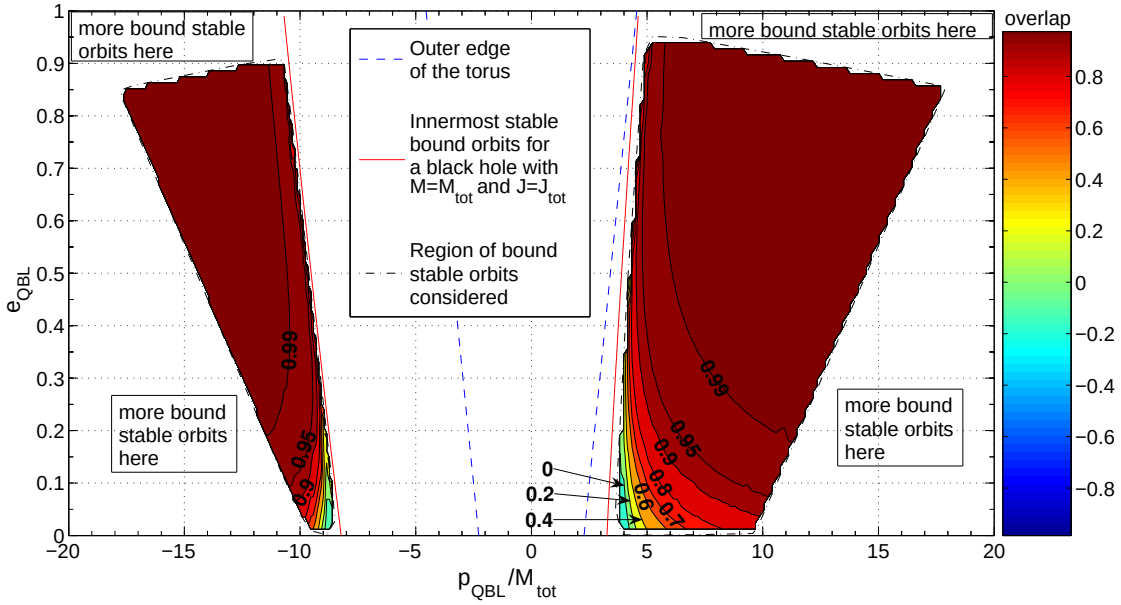

Figure 4.3: *Overlap between waveforms produced in spacetime A by* external *orbits and waveforms produced in a Kerr spacetime with mass $M_{\rm Kerr} = M_{\rm tot}$ and spin $J_{\rm Kerr} = J_{\rm tot}$. The orbits all have the same r- and ϕ-frequencies as obtained by suitably changing the semi-latus rectum and the eccentricity, with positive values of $p_{\rm QBL}$ referring to prograde orbits, and negative ones to retrograde orbits. The different lines mark the margins of the different relevant regions of the $(p_{\rm QBL}, e_{\rm QBL})$ plane, with the blue dashed line representing the outer "edge of the torus", the red solid line representing the innermost stable bound orbits for a Kerr spacetime with mass $M_{\rm Kerr} = M_{\rm tot}$ and spin $J_{\rm Kerr} = J_{\rm tot}$ and the black dot-dashed line delimiting the regions of the $(p_{\rm QBL}, e_{\rm QBL})$ plane where bound stable orbits have been studied. A high overlap in large regions of the parameter space indicates that a degeneracy problem is possible in this spacetime for observational timescales below or comparable to the dephasing time, although this degeneracy disappears for orbits with small eccentricities and close to the innermost bound stable orbits.*

We have computed the overlap between $h_{\rm BH+Torus}(p_{\rm QBL}, e_{\rm QBL})$ and $h_{\rm Kerr}(p_{\rm BL} = p_{\rm QBL} + \delta p, e_{\rm BL} = e_{\rm QBL} + \delta e, M_{\rm Kerr}, J_{\rm Kerr})$, and summarise the results of this comparison for a large set of orbits in Figs. 4.3, 4.4 and 4.5. In particular, Fig. 4.3 shows the colour-coded overlap between waveforms produced in spacetime A by external orbits in a $(p_{\rm QBL},\, e_{\rm QBL})$ plane, with positive values of $p_{\rm QBL}$ referring to prograde orbits, and negative ones to retrograde orbits. Note that *n*o internal orbits were found in spacetime A and this is due to the fact that in this case the torus is too close to the black hole for bound stable orbits to exist in region I of Fig. 4.1 without plunging into the black hole. The different lines in Fig. 4.3 mark the margins of the different regions of interest in the $(p_{\rm QBL},\, e_{\rm QBL})$ plane, with the blue dashed line representing the outer "edge of the torus", that is the set of points such that $p_{\rm QBL}/(1 + e_{\rm QBL}) = r_{\rm out,QBL}$. Similarly, the red solid line represents the innermost stable bound orbits (this line is also referred to as the "separatrix" in ref. [40]) for a Kerr spacetime with mass $M_{\rm Kerr} = M_{\rm tot}$ and spin $J_{\rm Kerr} = J_{\rm tot}$. Finally, the black dot-dashed line delimits the regions of the $(p_{\rm QBL},\, e_{\rm QBL})$ plane where bound stable orbits have been studied.

We underline that these are not the only regions in which bound stable orbits exist, but they rather represent the regions which we have investigated because of their being more directly related to LISA observations. In practice, we exploit the fact that there is a one-to-one correspondence between the semi-latus rectum $p_{\rm QBL}$ and the eccentricity $e_{\rm QBL}$ of bound stable orbits and their QI radius and tangential velocity (measured by a ZAMO) at periastron, r_p and v_ϕ. We therefore choose the initial radial QI position r_0 of the small body randomly in a limited range and vary its initial tangential velocity v_ϕ with small steps in the range of the velocities which result in energies per unit mass $\tilde{\epsilon} < 1$.[8] After integrating the geodesic equations (eqs. (4.22)-(4.24) with $\theta = \pi/2$) over and beyond the dephasing time, if the orbit does not intersect the torus and if r_0 actually corresponds to the periastron (and *not* to the apoastron) we extract the semi-latus rectum and eccentricity so as to populate the $(p_{\rm QBL},\, e_{\rm QBL})$ plane and compute the overlaps with pure-Kerr waveforms (the orbits in the Kerr spacetime are chosen to start at their periastron as well). Overall, a large number of bound stable orbits (*i.e.* $\gtrsim 2250$) has been integrated for each of the figures shown in this chapter. Notice that the requirement that r_0 correspond to the periastron is important because, as far as the overlaps are concerned, orbits having the same semi-latus rectum and eccentricity but different initial positions are not equivalent. We recall in fact that the overlaps are computed by putting a cutoff at the dephasing time and if the initial positions are different, the portions of the orbits contributing to the overlap are different.

Overall, because the waveforms agree very well with an overlap $\mathcal{O} > 0.95$ for most of the orbits which we have considered, the results in Fig. 4.3 clearly show that a degeneracy problem similar to the one presented in ref. [92] is indeed possible in this spacetime for observational timescales below or comparable to the dephasing time. As indicated by the

[8] We note that in both spacetimes A and B all of the equatorial bound stable orbits not crossing the torus have $\tilde{\epsilon} < 1$ [this can be verified by computing the values of $\tilde{\epsilon}$ for which the potential $V(r, \tilde{\epsilon}, \tilde{\ell})$ in eq. (4.31) is positive]. However, bound stable orbits which cross the torus and have $\tilde{\epsilon} > 1$ are present in both spacetimes.

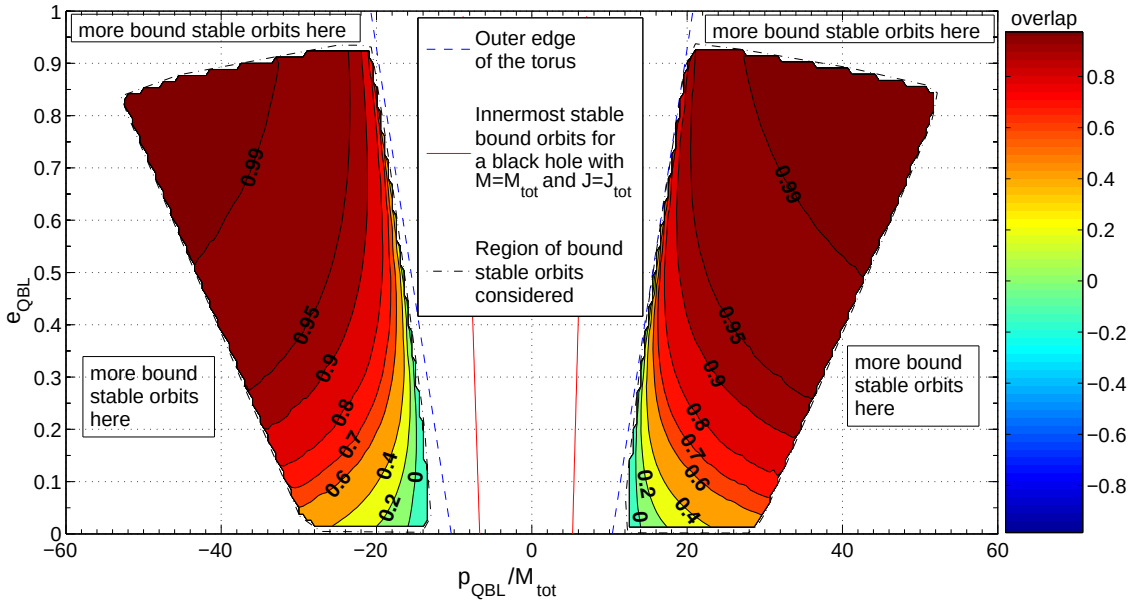

Figure 4.4: *The same as in Fig. 4.3 but for spacetime B. Note that in this case the degeneracy problem is less severe and indeed not present for orbits near the outer edge of the torus (i.e., with $p_{\rm QBL}/M_{\rm tot} \lesssim 30$) and with eccentricities $e_{\rm QBL} \lesssim 0.2$.*

colour-coding, the overlap has a drastic reduction only in a limited region of the parameter space and in particular for orbits with small eccentricity and close to the innermost bound stable orbits. This is not surprising since in these regions the local modifications of the spacetime due to the presence of the torus are the largest and have a more marked impact on the waveforms. Interestingly, prograde orbits produce overlaps that are smaller than those produced by retrograde orbits with comparable values of $p_{\rm QBL}$ and $e_{\rm QBL}$, and appear therefore to be better tracers of this spacetime.

It is important to underline that the presence of an albeit small region of the parameter space in which the overlap is small, and hence the dangers of a degeneracy problem is decreased, represents an important difference compared to the results presented in ref. [92]. We recall that spacetime A has a rather small quadrupole parameter ϵ (*cf.* Table 4.1), comparable with those used in ref. [92]. However, the small overlaps near to the innermost bound stable orbits indicate that taking into account the higher-order multipoles neglected in the metric (4.20) can lead to significant differences even far away from the black hole if a matter source is present.

Figure 4.4 summarises a set of results similar to those presented in Fig. 4.3 but for spacetime B. More specifically, it reports the colour-coded overlap between waveforms produced in spacetime B by *external* orbits and waveforms produced in a Kerr spacetime with mass $M_{\rm Kerr} = M_{\rm tot}$ and spin $J_{\rm Kerr} = J_{\rm tot}$. Here again, all of the orbits have the same orbital frequencies as obtained by adjusting δp and δe. It should be noted that in

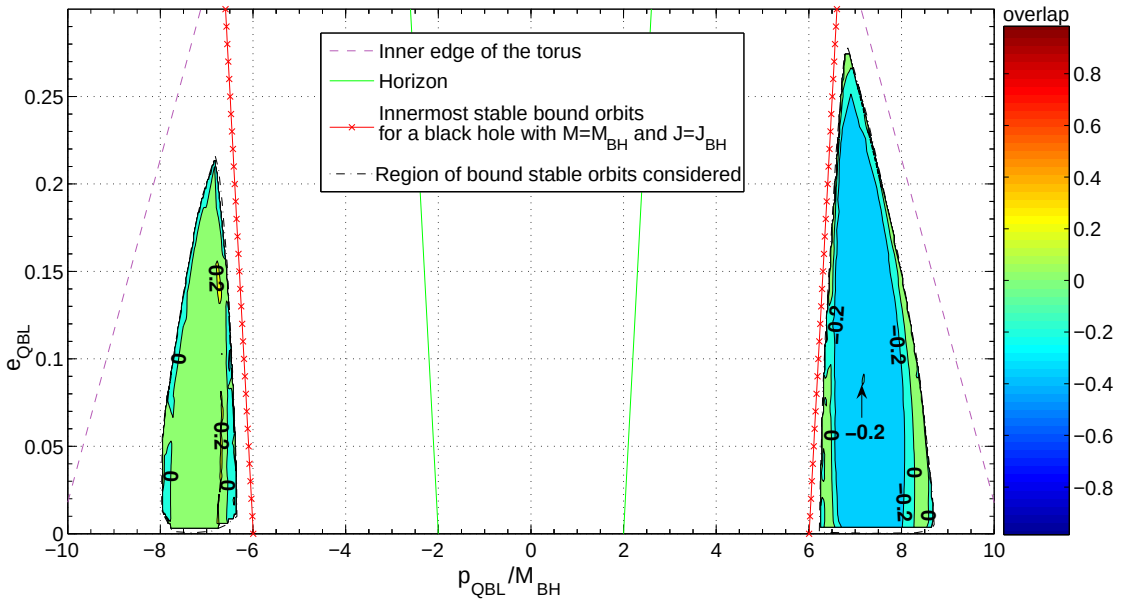

Figure 4.5: *The same as in Fig. 4.4 but for* internal *orbits, with the green solid line marking those orbits whose periastron lies on the event horizon, the purple dashed line representing the inner "edge of the torus" and finally the red crossed-solid line marking the innermost bound stable orbits in a Kerr spacetime with mass and spin $M_{\rm Kerr} = M_{\rm BH}$ and $J_{\rm Kerr} = J_{\rm BH}$. Again, the black dot-dashed line delimits the regions of the $(p_{\rm QBL}, e_{\rm QBL})$ plane where bound stable orbits have been studied, but in contrast to the case of external orbits, these regions correspond to practically all of the bound stable orbits not crossing the torus. Note that in this case the degeneracy problem is absent, with $\mathcal{O} \lesssim 0.2$.*

this case the degeneracy problem is less severe and indeed essentially absent for orbits near to the outer edge of the torus (*i.e.*, with $p_{\rm QBL}/M_{\rm tot} \lesssim 30$) and with eccentricities $e_{\rm QBL} \lesssim 0.2$. Finally, we report in Fig. 4.5 again results for spacetime B but this time for *internal* orbits. We recall, in fact, that in this case the torus is farther away from the black hole and thus bound stable orbits can be found in region I of Fig. 4.1. As in the previous figures, the black dot-dashed line delimits the regions of the plane $(p_{\rm QBL}, e_{\rm QBL})$ where bound stable orbits have been studied, but in contrast to the case of external orbits these regions correspond to practically all of the bound stable orbits not crossing the torus. On the other hand, the green solid line marks those orbits whose periastron lies on the event horizon, the purple dashed one marks those orbits whose apoastron lies on the inner edge of the torus and finally the red crossed-solid line indicates the innermost bound stable orbits in a Kerr spacetime with mass and spin $M_{\rm Kerr} = M_{\rm BH}$ and $J_{\rm Kerr} = J_{\rm BH}$. Clearly, no degeneracy problem is present for these orbits, because the overlap is always very small and never larger than $\simeq 0.2$.

In summary, the overlaps computed in the two spacetimes A and B containing a black-

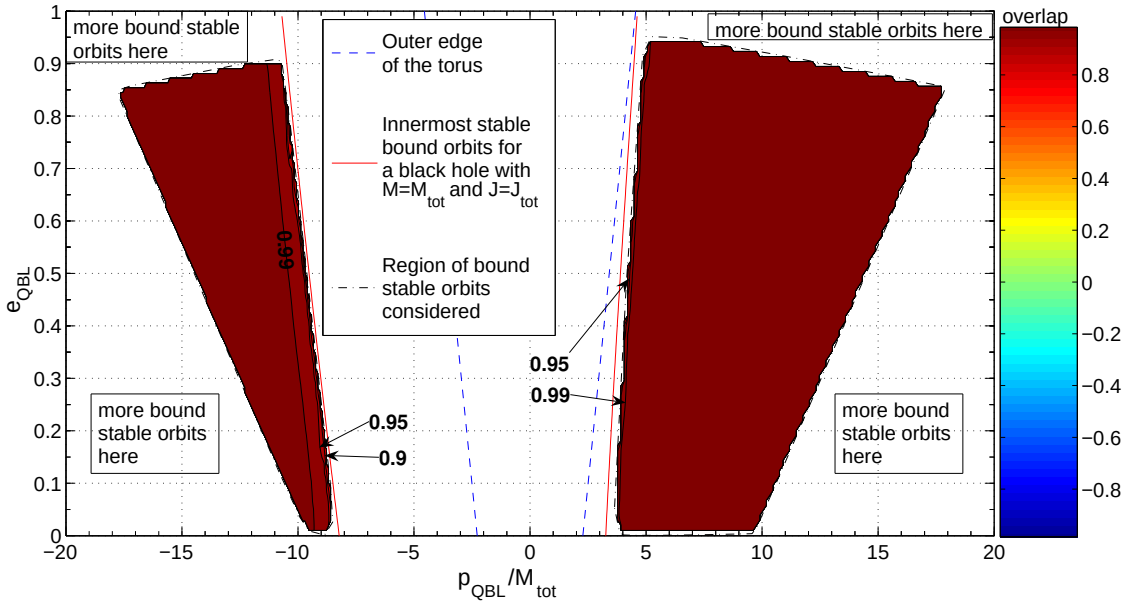

Figure 4.6: *Overlap between waveforms produced in spacetime A by* external *orbits and waveforms produced in a Kerr spacetime with mass $M_{\rm Kerr}+\delta M = M_{\rm tot}+\delta M$ and spin $J_{\rm Kerr}+\delta J = J_{\rm tot}+\delta J$ by orbits with the same semi-latus rectum and eccentricity [in (Q)BL coordinates] and the same r- and ϕ-frequencies. Here too, the blue dashed line represents the outer "edge of the torus", the red solid line marks the innermost stable bound orbits for a Kerr spacetime with mass $M_{\rm Kerr} = M_{\rm tot}$ and spin $J_{\rm Kerr} = J_{\rm tot}$ and the black dot-dashed line delimits the regions of the $(p_{\rm QBL}, e_{\rm QBL})$ plane where bound stable orbits have been studied. An overlap $\mathcal{O} > 0.95$ is present in all of the relevant regions of the $(p_{\rm QBL}, e_{\rm QBL})$ plane.*

hole and a torus by varying the semi-latus rectum and the eccentricity reveal that there are regions in which the non-pure Kerr spacetimes can be "confused" with Kerr spacetimes that are equivalent to them at the sensitivity of LISA. Clearly, this risk is concrete only for timescales over which radiation-reaction effects are negligible and it is not present for external orbits very close to the torus or for the orbits between the torus and the black hole, if they exist.

4.5.2 The degeneracy problem when varying M and J

Next, we consider the overlap obtained by comparing orbits having the same r- and ϕ-frequencies, achieved by changing the mass and spin of the Kerr black hole while keeping the semi-latus rectum and eccentricity fixed in either (Q)BL or QI coordinates [*cf.* eqs. (4.36)–(4.37) and (4.38)–(4.39)]. Doing this corresponds to considering a hypothetical scenario in which it would be possible to measure, by means of independent astronomical observations, the semi-latus rectum and eccentricity of the small body orbiting

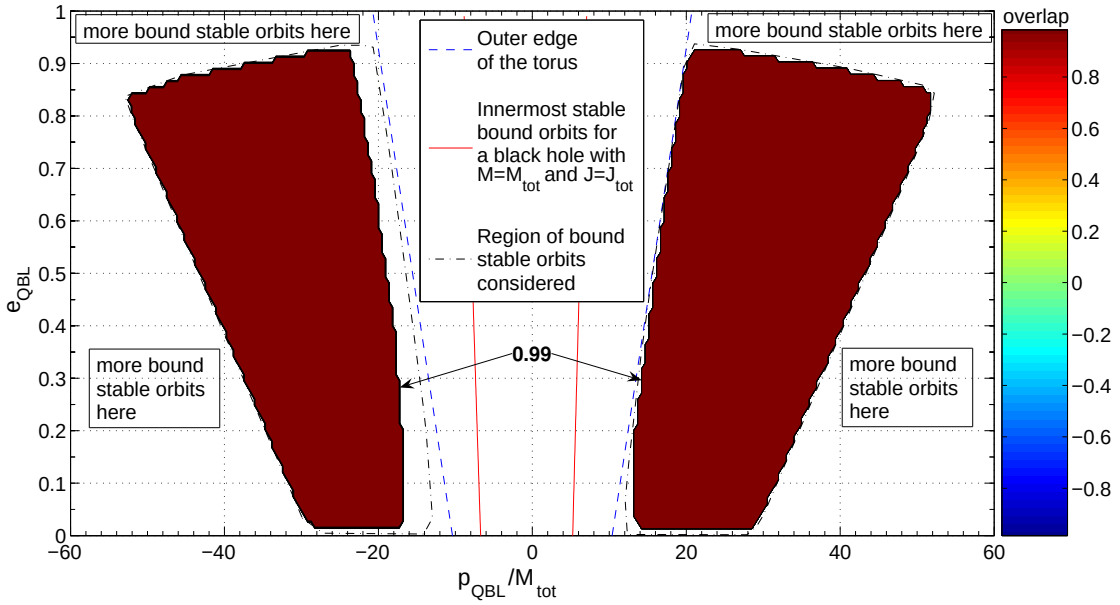

Figure 4.7: *The same as in Fig. 4.6 but for spacetime B. Note that also in this case the overlap is very high ($\mathcal{O} > 0.99$) in almost all of the relevant regions of the $(p_{\rm QBL}, e_{\rm QBL})$ plane, with the exception of a very small set of orbits very close to the torus, for which eqs.* (4.36)–(4.37) *have no solutions (these orbits correspond to the blank regions inside the black dot-dashed line).*

around the massive central black hole. In practice, and using the same compact notation introduced above, we have compared waveforms of type $h_{\rm BH+Torus}(p_{\rm QBL}, e_{\rm QBL})$ with $h_{\rm Kerr}(p_{\rm BL} = p_{\rm QBL}, e_{\rm BL} = e_{\rm QBL}, M_{\rm Kerr} + \delta M, J_{\rm Kerr} + \delta J)$ [*i.e.*, with semi-latus rectum and eccentricity fixed in (Q)BL coordinates, and δM and δJ being solutions to eqs. (4.36)–(4.37)] and $h_{\rm BH+Torus}(p_{\rm QI}, e_{\rm QI})$ to $h_{\rm Kerr}(p_{\rm QI}, e_{\rm QI}, M_{\rm Kerr} + \delta M, J_{\rm Kerr} + \delta J)$ [*i.e.*, semi-latus rectum and eccentricity fixed in QI coordinates, δM and δJ solutions to eqs. (4.38)–(4.39)].

While formally distinct, these two approaches yield essentially the same results quite irrespective of whether the semi-latus rectum and eccentricity are held fixed in (Q)BL or in QI coordinates. Because of this, from here on we will discuss only results obtained with $p_{\rm (Q)BL}$ and $e_{\rm (Q)BL}$ being kept fixed.

Figure 4.6 shows the overlap between waveforms produced in spacetime A by *external* orbits and waveforms produced in a Kerr spacetime with mass $M_{\rm Kerr} + \delta M = M_{\rm tot} + \delta M$ and spin $J_{\rm Kerr} + \delta J = J_{\rm tot} + \delta J$ by orbits with the same $p_{\rm (Q)BL}$ and $e_{\rm (Q)BL}$ and the same orbital frequencies. As in Fig. 4.3, the different lines mark the margins of the relevant regions of the $(p_{\rm QBL}, e_{\rm QBL})$ plane, with the blue dashed line representing the outer "edge of the torus", the red solid line representing the innermost stable bound orbits for a Kerr spacetime with mass $M_{\rm Kerr} = M_{\rm tot}$ and spin $J_{\rm Kerr} = J_{\rm tot}$ and the black dot-dashed line delimiting the regions of the $(p_{\rm QBL}, e_{\rm QBL})$ plane where bound stable orbits have been

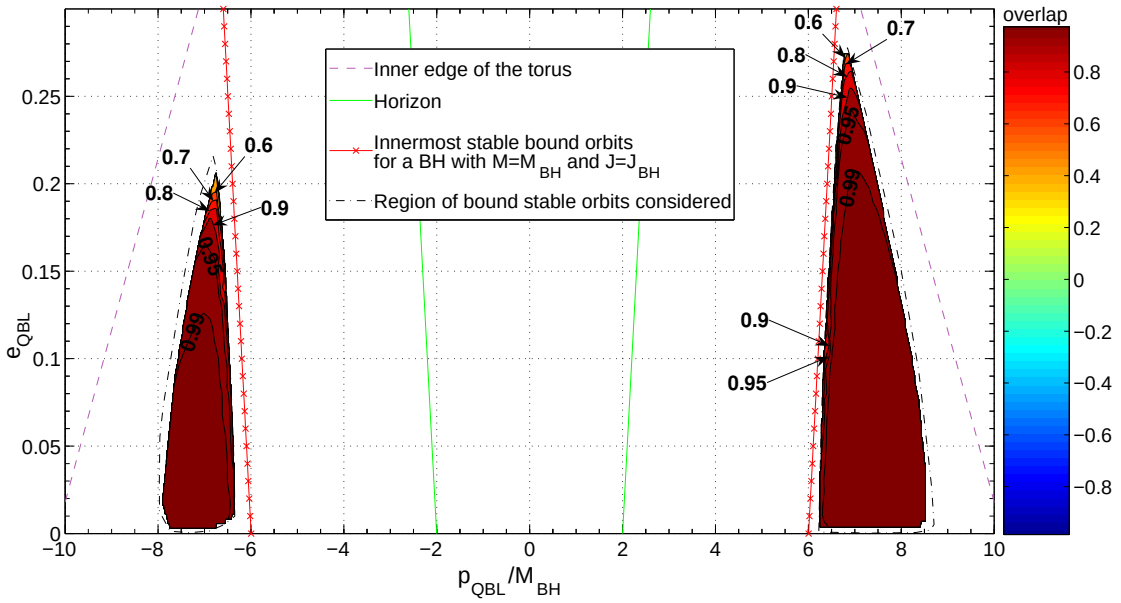

Figure 4.8: *The same as in Fig. 4.7 but for* internal *orbits, with the green solid line marking those orbits whose periastron lies on the event horizon, the purple dashed line representing the inner "edge of the torus" and finally the red crossed-solid line marking the innermost bound stable orbits in a Kerr spacetime with mass and spin* $M_{\rm Kerr} = M_{\rm BH}$ *and* $J_{\rm Kerr} = J_{\rm BH}$*. Again, the black dot-dashed line delimits the regions of the* $(p_{\rm QBL}, e_{\rm QBL})$ *plane where bound stable orbits have been studied, but in contrast to the case of external orbits these regions correspond to practically all of the bound stable orbits not crossing the torus. Note that in this case the degeneracy problem is present in most of the relevant regions of the* $(p_{\rm QBL}, e_{\rm QBL})$ *plane, becoming slightly less severe only for the largest allowed eccentricities and for a very small set of orbits, very close to the torus, for which eqs.* (4.36)–(4.37) *have no solutions (these orbits correspond to the blank regions inside the black dot-dashed line).*

studied. Note the very close match between the two waveforms, with an overlap $\mathcal{O} > 0.95$ in essentially all of the relevant regions of the $(p_{\rm QBL}, e_{\rm QBL})$ plane. This is a clear indication that a degeneracy problem is present for LISA measurements over a timescale below or comparable to the dephasing time.

Figures 4.7 and 4.8 provide complementary information for spacetime B, with the first one referring to *external* orbits and the second one to *internal* orbits (the meaning of the lines appearing in this figures is the same as in figures 4.4 and 4.5). In both cases it is apparent that the overlap is always very large. The only exceptions are the internal orbits with the largest allowed eccentricities, for which the overlap decreases slightly, and a very small set of orbits very close to the torus, for which eqs. (4.36)–(4.37) have no solutions (these orbits correspond to the blank regions inside the black dot-dashed line in figures 4.7 and 4.8).

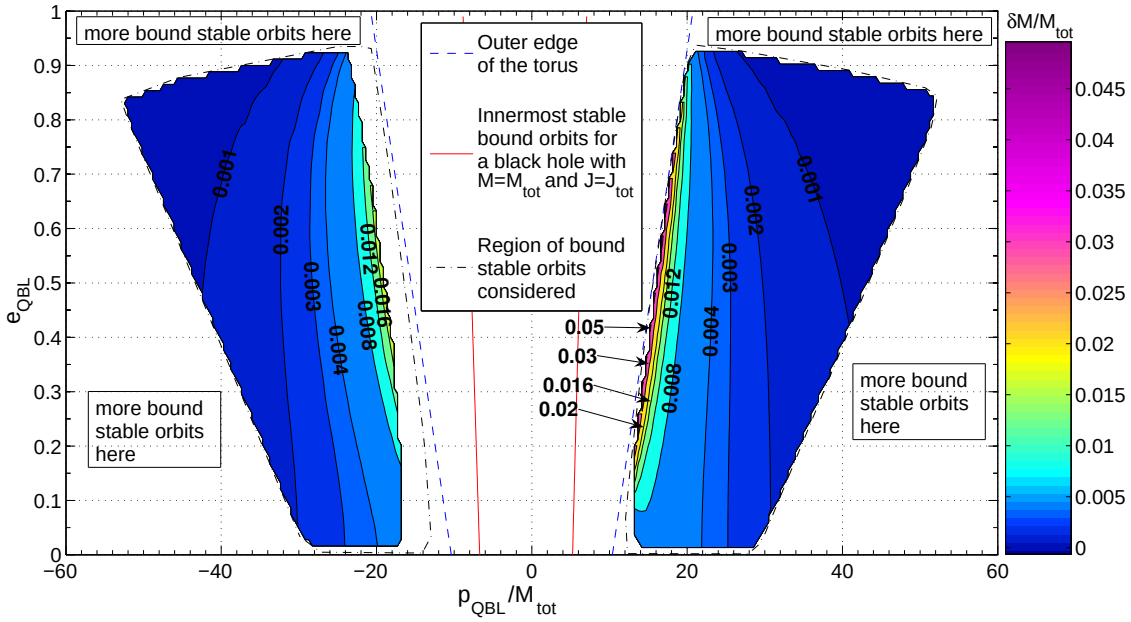

Figure 4.9: *Relative mass correction $\delta M/M_{\rm Kerr} = \delta M/M_{\rm tot}$ in the regions of the $(p_{\rm QBL}, e_{\rm QBL})$ plane where the overlap plotted in Fig. 4.7 is above 0.95. Note that far from the system $\delta M/M_{\rm tot}$ approaches zero, as one would expect.*

In summary, the overlap computed in the two spacetimes by varying the mass and spin of the black hole reveals that a LISA observation carried out over a timescale below or comparable to the dephasing time would not allow an observer to distinguish between a Kerr and a non-pure Kerr spacetime, even in the case in which the orbital parameters of the small body, such as the the semi-latus rectum and the eccentricity, were known through astronomical observations.

A simple explanation of why the overlap is always so large when calculated by varying the mass and spin of the Kerr black hole is already illustrated in Fig. 4.2. This shows that the waveform obtained in this way captures not only the proper orbital frequencies, but also the overall "form" of the signal, which is most sensitive to the values of the semi-latus rectum and of the eccentricity of the orbit (*cf.* the solid black line and the brown circles in Fig. 4.2).

The difficulty of distinguishing a Kerr spacetime from a non-pure Kerr one can also be expressed in terms of the mass $M_{\rm Kerr} + \delta M$ and spin $J_{\rm Kerr} + \delta J$ that would be measured by an observer analysing a gravitational wave from a black hole-torus system with pure Kerr templates. The corrections δM and δJ are those appearing in eqs. (4.36)–(4.37) and have been computed in order to determine the overlaps presented in this section. If they are small and slowly varying, it is hard to imagine a way in which the non-pure Kerr spacetime could be distinguished from a pure Kerr one, even with the help of additional

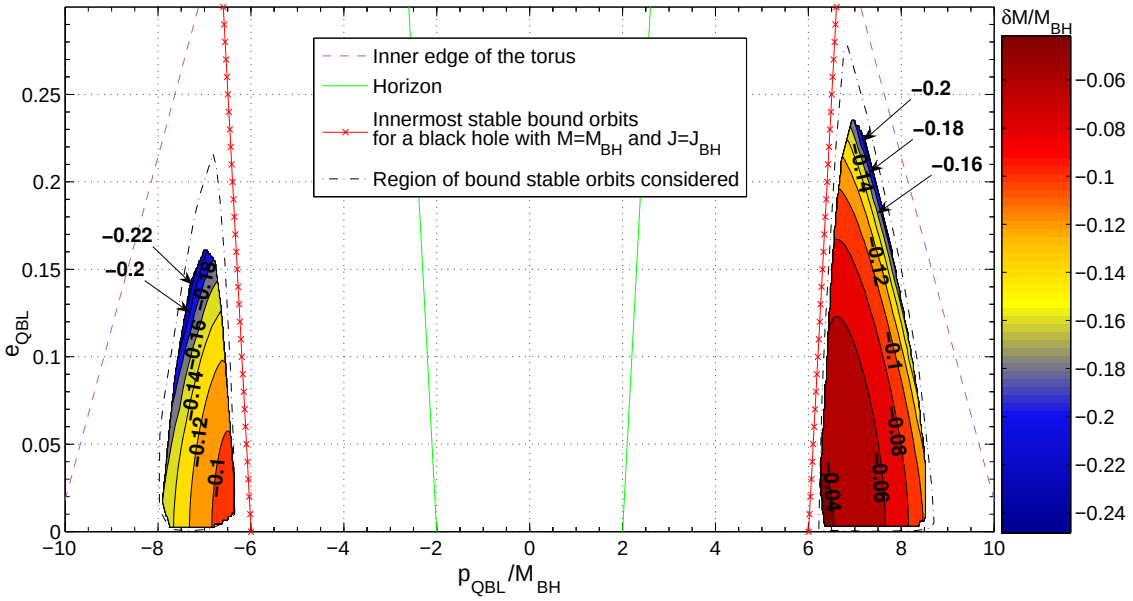

Figure 4.10: *The same as in Fig. 4.9 but for internal orbits. In this case the deviations are computed as* $\delta M/M_{\rm Kerr} = \delta M/M_{\rm BH}$ *in the regions of the* $(p_{\rm QBL}, e_{\rm QBL})$ *plane where the overlap plotted in Fig. 4.8 is above 0.95.*

astronomical observations. Conversely, if these corrections are large or rapidly varying it is possible that additional astronomical information about the system or an analysis of snapshots of the waveform taken at different times could be used to determine that the source is not an isolated Kerr black hole and therefore lessen the degeneracy problem which we find in our analysis.

A synthesis of these corrections for the determination of the mass of the black hole in the case of spacetime B is presented in Fig. 4.9 and Fig. 4.10, with the first one showing the relative error $\delta M/M_{\rm Kerr} = \delta M/M_{\rm tot}$ in the regions of the $(p_{\rm QBL}, e_{\rm QBL})$ plane where the overlap plotted for *external* orbits is above 0.95, and the second one showing the corresponding quantity ($\delta M/M_{\rm Kerr} = \delta M/M_{\rm BH}$) for *internal* orbits.

Clearly, the corrections are very small and slowly varying in almost all of the relevant parameter space for *external* orbits, meaning that an observer could not detect the presence of the torus using only these orbits. On the other hand, an observer could measure rather accurately the total mass of the system. Note in particular that the correction $\delta M/M_{\rm tot}$ goes to zero far from the system, as one would expect.

This situation is only slightly different for *internal* orbits, for which the correction increases to some percent: using internal orbits an observer could measure the mass of the central black hole quite accurately. Note therefore that a combination of observations of internal orbits (giving an estimate for $M_{\rm BH}$) and external orbits (giving an estimate for

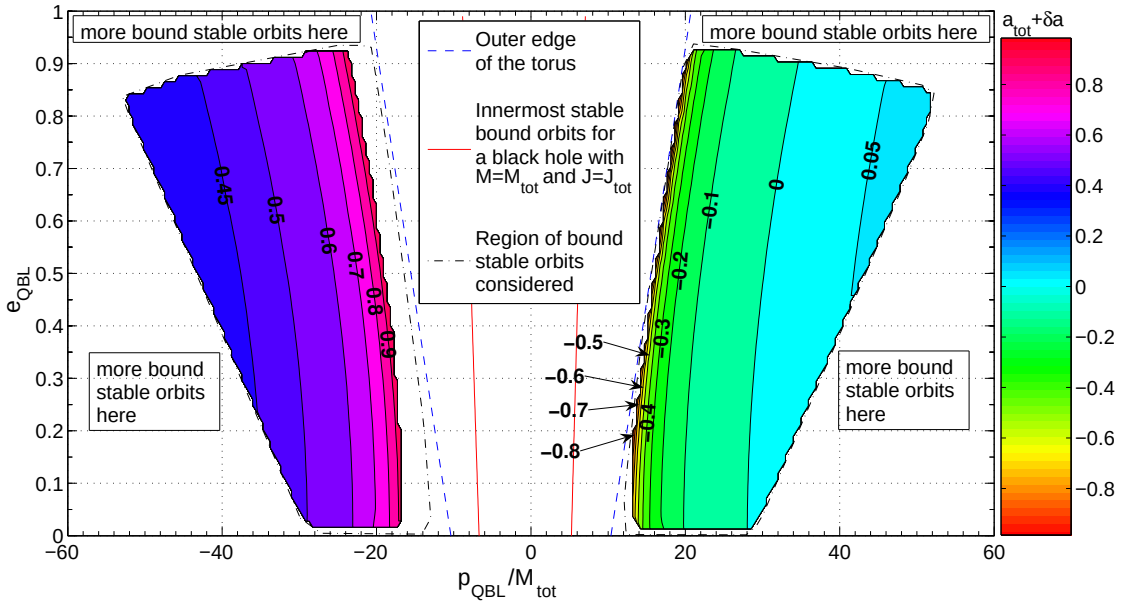

Figure 4.11: *Variations of the spin* $a_{\rm Kerr}+\delta a \equiv a_{\rm tot}+\delta a = (J_{\rm tot}+\delta J)/(M_{\rm tot}+\delta M)^2$ *in the regions of the* $(p_{\rm QBL}, e_{\rm QBL})$ *plane where the overlap plotted in Fig. 4.7 is above 0.95. We recall that for external orbits in spacetime* B*, we have* $a_{\rm Kerr} = a_{\rm tot} = 0.224$ *(cf. Table 4.1).*

$M_{\rm tot}$) could hint at the presence of a torus around the central black hole.

Similar behaviour has also been found for spacetime A. Because no internal bound stable orbits are present in this case, an observer could not measure the individual masses of the black hole and the torus, whereas he could measure accurately the total mass of the system. In fact, the corrections are always very small with $|\delta M/M_{\rm Kerr}| = |\delta M/M_{\rm tot}| \lesssim 0.02$; once again, the correction $\delta M/M_{\rm tot}$ goes to zero far from the system, as one would expect. Note that due to the absence of internal orbits in this spacetime and to the smallness and slow variations of $\delta M/M_{\rm tot}$, it is extremely difficult to distinguish spacetime A from a pure Kerr spacetime.

Information complementary to that given by the mass correction δM is provided by the spin correction δJ. In particular, for spacetime A the correction δa defined by $\delta a \equiv (J_{\rm Kerr}+\delta J)/(M_{\rm Kerr}+\delta M)^2 - a_{\rm Kerr}$ (with $a_{\rm Kerr} = J_{\rm Kerr}/M_{\rm Kerr}^2 = 0.728$) can be readily calculated to be $|\delta a/a_{\rm Kerr}| \lesssim 0.065$, going to zero, as one would expect, far from the system. This means that an observer could accurately measure the total spin of the black hole-torus system although, due to the absence of internal orbits in this system and to the slow variations of δa, a measurement of the individual spins of the torus and the black hole or even a simple detection of the torus seems unfeasible.

Spacetime B is considered in figures 4.11-4.12, in which we report the quantity $a_{\rm Kerr}+\delta a \equiv (J_{\rm Kerr}+\delta J)/(M_{\rm Kerr}+\delta M)^2$ for external orbits (with $a_{\rm Kerr} = J_{\rm Kerr}/M_{\rm Kerr}^2 = 0.224$)

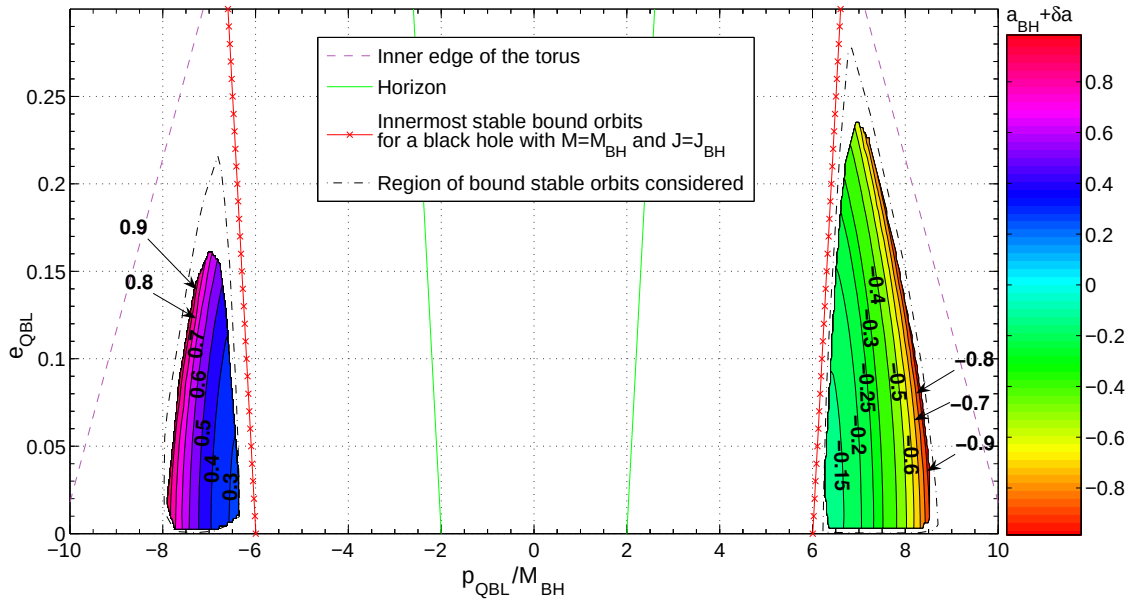

Figure 4.12: *The same as in Fig. 4.11 but for* internal *orbits. In this case the corrections are computed as* $a_{\rm Kerr}+\delta a = a_{\rm BH}+\delta a \equiv (J_{\rm BH}+\delta J)/(M_{\rm BH}+\delta M)^2$ *in the regions of the* $(p_{\rm QBL}, e_{\rm QBL})$ *plane where the overlap plotted in Fig. 4.8 is above 0.95. We recall that for* internal *orbits in spacetime* B*, we have* $a_{\rm Kerr} = a_{\rm BH} = -1.74\times 10^{-3}$ *(cf. Table 4.1).*

and internal orbits (with $a_{\rm Kerr} = J_{\rm Kerr}/M^2_{\rm Kerr} = -1.74\times 10^{-3}$), respectively. As can be seen, the corrections δa are, in both cases, rather large and rapidly varying: an observer could probably distinguish this spacetime from a pure Kerr one using estimates of the spin obtained by analysing the waveform at different times, but would have little chance to measure the spin of the central black hole correctly and should consider orbits very far from the system in order to achieve accurate measurements of the total spin. This was to be expected, since spacetime B has a large ratio $J_{\rm Torus}/J_{BH}$, which causes the quadrupole parameter ϵ to be large (*cf.* Table 4.1).

Before concluding this section, it is worth commenting on how robust and generic these results are. While we believe that they represent the first attempt to model consistently the gravitational-wave emission from spacetimes that deviate considerably for Kerr due to the presence of matter, the approach followed here has the obvious limitation of neglecting radiation-reaction effects and thus of considering waveforms only over a dephasing time which is typically of days or weeks. It is therefore possible, if not likely, that considering waveforms over a timescale comparable with LISA's planned lifetime (*i.e.* 3–5 years) would lower the overlaps computed here and thus reduce the impact of a degeneracy problem.

As already mentioned, a simple way to include radiation reaction would consist of

using the adiabatic approximation and thus considering motion along a geodesic with slowly changing parameters. In particular, approximate ("kludge") expressions for the fluxes $\dot{E}$, $\dot{L}_z$ and $\dot{Q}$ in Kerr have been derived using post-Newtonian expansions [104, 115, 148], recently corrected using fits to the fluxes computed rigorously with the Teukolsky formalism [119]. Likewise, it may be possible to adopt similar strategies in non-Kerr spacetimes. For instance, Cutler and Barack [93] recently proposed including radiation reaction in quasi-Kerr spacetimes by using post-Newtonian fluxes in which the leading-order effect of the quadrupole of the spacetime is taken into account, potentially eliminating the degeneracy problem. Nevertheless, it is still unclear at this stage whether post-Newtonian fluxes will be a good approximation for our spacetimes, where the parameters ϵ and a can be $O(1)$. We recall, indeed, that using post-Newtonian fluxes is not always a good approximation even in Kerr spacetimes and that the most accurate "kludge" fluxes for Kerr [119] are certainly based on post-Newtonian expansions, but are also corrected using fits to rigorous Teukolsky-based fluxes.

We also note than even with the radiation-reaction included, a "degeneracy" problem might in principle still be present, at least for equatorial orbits. In fact, requiring the equality of the r- and ϕ-frequencies fixes only two of the four free parameters characterising the geodesic, p, e, $M_{\rm Kerr}$ and $J_{\rm Kerr}$, while the remaining two could be used to obtain the equality of the time derivatives of the r- and ϕ-frequencies at the initial time [$\dot{\omega}_r^{\rm BH+Torus}(t_0) = \dot{\omega}_r^{\rm Kerr}(t_0)$, $\dot{\omega}_\phi^{\rm BH+Torus}(t_0) = \dot{\omega}_\phi^{\rm Kerr}(t_0)$], which could ensure, at least initially, a similar evolution under radiation reaction for the two waveforms.

Besides inclusion of radiation reaction, two other approaches to improve the estimates computed in this chapter are also worth considering. The first and most obvious one consists of replacing the "kludge" waveforms with more rigorous waveforms, given by solutions of eqs. (4.10) and (4.12), possibly neglecting the fluid perturbations appearing on the right-hand-side of eq. (4.10) (this could be a rather good approximation for orbits far enough from the torus). Doing this in practice is certainly not trivial since eqs. (4.10) have been solved only for a Schwarzschild spacetime so far [133]. The second possible improvement involves the extension of the present analysis to non-equatorial orbits. This is more complicated since one cannot require the strict equality of the orbital frequencies [in contrast to Kerr, eqs. (4.22)–(4.25) indicate that in general the r-, θ- and ϕ-motions are not periodic in the time coordinate t]. However, it is possible to check that these motions are *approximately* periodic, over the dephasing timescale, if the torus is not too massive, and then the present analysis can be extended straightforwardly in terms of these almost-periodic motions.

4.6 Summary

EMRIs are expected to be among the most important sources for LISA and, besides mapping accurately the spacetime around SMBHs, they might also shed light on the distribution of matter around them. We have here studied EMRIs and the corresponding gravitational-wave emission in spacetimes that are accurate numerical solutions of the

Einstein equations and consist of an SMBH and a compact torus with comparable mass and spin. We underline that the tori considered here *do not* represent a model for the accretion disks in AGNs but, rather, are a phenomenological model for a compact source of matter close to the SMBH. Our goal in this chapter has therefore been that of maximising the impact of this matter on the waveforms and investigating whether gravitational-wave observations will be able to reveal its presence. This hypothetical matter source, even if it exists, may not be detectable otherwise, being too close to the central SMBH and possibly "dark".

Using the semi-relativistic approach proposed in ref. [92], we have compared kludge waveforms produced by equatorial orbits in non-pure Kerr spacetimes with waveforms produced by equatorial orbits in Kerr spacetimes having the same mass and spin as the non-pure Kerr spacetimes. Because they are produced by purely geodesic motion, these waveforms are valid only over a rather short "dephasing" timescale. Overall, we find that waveforms produced by orbits having the same semi-latus rectum and eccentricity p and e are considerably different throughout the whole parameter space $(p,\, e)$. On the other hand, comparisons of waveforms produced by (equatorial) orbits having the same r- and ϕ-frequencies, with this condition being achieved by changing the semi-latus rectum and eccentricity of the orbits in the Kerr spacetime, produce overlaps $\mathcal{O} > 0.95$ for orbits far from the black hole-torus system, hence pointing out a degeneracy problem. This overlap decreases rapidly as one considers orbits which are close to the torus, indicating that in the strong-field region no degeneracy problem is present. Finally, if the equality of the r- and ϕ-frequencies is obtained by changing the mass and spin of the Kerr spacetime while maintaining fixed the semi-latus rectum and the eccentricity of the orbit, the resulting overlaps are very high, with $\mathcal{O} > 0.99$ for essentially all values of the orbital parameters p and e, indicating a degeneracy problem that is less severe only for a few orbits very close to the torus.

This degeneracy problem in the mass and the spin might therefore be more serious than the one involving the semi-latus rectum and eccentricity. Stated differently, an observer analysing below the dephasing timescale a gravitational waveform produced by an EMRI in a black hole-torus system would not be able to distinguish it from one produced in a pure Kerr spacetime. This observer would therefore associate the EMRI with a Kerr SMBH whose mass and spin would however be estimated incorrectly.

While these results represent the first attempt to model consistently the gravitational-wave emission from spacetimes that deviate considerably for Kerr, the approach followed here is based on four approximations, namely: *i)* the use of kludge waveforms in place of ones that are consistent solutions of the Einstein equations; *ii)* the use of a cut-off at the dephasing time beyond which radiation-reaction effects can no longer be ignored; *iii)* the restriction to purely equatorial orbits; *iv)* the use of tori that are very compact and close to the black hole. Relaxing one or more of these approximations could lead to a less serious degeneracy problem.

Finally, we stress that another possible improvement of the present analysis would be to use the Fisher information matrix to calculate the accuracy with which the orbital parameters and the parameters of the black hole-torus system could be measured. More-

over, the Fisher matrix would provide also the correlations among these parameters, thus revealing the presence (or the absence) of a degeneracy problem. However, such an analysis is presently not realistic since the construction of the Fisher matrix involves derivatives of the waveforms with respect to the parameters of the system, and these, in turn, require the construction of a very large number of spacetimes whose numerical calculation is still too expensive.

Appendix: From the Einstein equations to the semirelativistic approach

Although the main motivation for the semirelativistic approach which we use in this chapter is the surprising agreement that "kludge" waveforms show in Kerr with the rigorous waveforms computed using the Teukolsky formalism [12], one can also try to make sense of it using the Einstein equations.

We start by rewriting the Einstein equations in a more convenient form in which we isolate the perturbation as [1, 56]

$$\bar{H}^{\mu\nu} \equiv \eta^{\mu\nu} - (-\widetilde{g})^{1/2}\widetilde{g}^{\mu\nu} \ , \tag{4.40}$$

where $\eta^{\mu\nu}$ is the Minkowski metric. Since far from the source the spacetime reduces to Minkowski plus a small perturbation, *i.e.* $\boldsymbol{g} = \boldsymbol{\eta}$, the first-order perturbations there coincide with $\bar{\boldsymbol{H}}$, *i.e.* $\bar{H}^{\mu\nu} = \bar{h}^{\mu\nu} + \mathcal{O}(m/M)^2$, with $\bar{h}^{\mu\nu}$ being the trace-reversed potentials defined in eq. (4.8).

If we now restrict our attention to a region of the spacetime where it is possible to choose the harmonic gauge

$$\partial_\beta \bar{H}^{\alpha\beta} = 0 \tag{4.41}$$

(this is always possible far enough from the source), the *full* Einstein equations give [56]

$$\Box_{\rm flat}\bar{H}^{\alpha\beta} = -16\pi\tau^{\alpha\beta} \ , \tag{4.42}$$

where $\Box_{\rm flat} \equiv \eta^{\mu\nu}\partial_\mu\partial_\nu$ is the flat-spacetime wave operator. The right-hand side is given by the effective stress-energy pseudotensor

$$\tau^{\alpha\beta} = (-\widetilde{g})\widetilde{T}^{\alpha\beta} + (16\pi)^{-1}\Lambda^{\alpha\beta} \ , \tag{4.43}$$

where $\Lambda^{\alpha\beta}$ is given by

$$\Lambda^{\alpha\beta} = 16\pi(-\widetilde{g})t_{\rm LL}^{\alpha\beta} + (\bar{H}^{\alpha\mu}{}_{,\nu}\,\bar{H}^{\beta\nu}{}_{,\mu} - \bar{H}^{\alpha\beta}{}_{,\mu\nu}\,\bar{H}^{\mu\nu}) \ , \tag{4.44}$$

and $t_{\rm LL}^{\alpha\beta}$ is the Landau-Lifshitz pseudotensor

$$16\pi(-\widetilde{g})t_{\rm LL}^{\alpha\beta} \equiv \widetilde{g}_{\lambda\mu}\widetilde{g}^{\nu\rho}\bar{H}^{\alpha\lambda}_{,\nu}\bar{H}^{\beta\mu}_{,\rho} + \frac{1}{2}\widetilde{g}_{\lambda\mu}\widetilde{g}^{\alpha\beta}\bar{H}^{\lambda\nu}_{,\rho}\bar{H}^{\rho\mu}_{,\nu} - 2\widetilde{g}_{\mu\nu}\widetilde{g}^{\lambda(\alpha}\bar{H}^{\beta)\nu}_{,\rho}\bar{H}^{\rho\mu}_{,\lambda}$$
$$+\frac{1}{8}(2\widetilde{g}^{\alpha\lambda}\widetilde{g}^{\beta\mu} - \widetilde{g}^{\alpha\beta}\widetilde{g}^{\lambda\mu})(2\widetilde{g}_{\nu\rho}\widetilde{g}_{\sigma\tau} - \widetilde{g}_{\rho\sigma}\widetilde{g}_{\nu\tau})\bar{H}^{\nu\tau}_{,\lambda}\bar{H}^{\rho\sigma}_{,\mu} \ . \tag{4.45}$$

Because of the gauge condition (4.41), the source term of eq. (4.42) satisfies the conservation law

$$\tau^{\alpha\beta}{}_{,\beta} = 0 \ , \tag{4.46}$$

which is equivalent to the equations of motion of the matter

$$\widetilde{\nabla}_\beta \widetilde{T}^{\alpha\beta} = 0 \ . \tag{4.47}$$

Combining then eqs. (4.42) and (4.46), in the slow motion approximation one easily gets the usual quadrupole formula (see ref. [1] for details):

$$\bar{H}^{ij}(\vec{x},t) = \frac{2}{r}\left[\frac{d^2 I^{ij}}{dt'^2}\right]_{t'=t-r} \ , \tag{4.48}$$

$$I^{ij}(t') = \int \tau^{00}(\vec{x}',t')x'^i x'^j \mathrm{d}^3x' \ , \tag{4.49}$$

where $r^2 \equiv \vec{x}\cdot\vec{x}$. Note that one can easily relax the slow motion assumption by including the octupole terms [151] or even all of the higher order multipoles (the formula is due to Press [152]).

Eq. (4.48) clearly does not allow one to compute $\bar{H}^{ij}$ directly, because its right hand side depends on $\bar{H}^{\alpha\beta}$ [*cf.* eq. (4.43)]. The semirelativistic approximation consists indeed of *pretending* that $\bar{\boldsymbol{H}}$ is "small": making this assumption, one can neglect, in the expression (4.43) for the effective stress-energy tensor $\tau^{\alpha\beta}$, the terms quadratic in $\bar{H}^{\alpha\beta}$ and the terms in which $\bar{H}^{\alpha\beta}$ is multiplied by the mass m of the small body. In addition, the semirelativistic approximation also neglects all of the terms involving the stress-energy tensor of the fluid: with these assumptions, $\tau^{\alpha\beta}$ can be written as

$$\tau^{00}(\vec{x},t) = m\,\gamma(t)\,\delta^{(3)}(\vec{x}-\vec{z}(t)) \ , \tag{4.50}$$

$$\tau^{0i}(\vec{x},t) = m\,\gamma(t)\,\dot{z}^i(t)\,\delta^{(3)}(\vec{x}-\vec{z}(t)) \ , \tag{4.51}$$

$$\tau^{ij}(\vec{x},t) = m\,\gamma(t)\dot{z}^i(t)\,\dot{z}^j(t)\,\delta^{(3)}(\vec{x}-\vec{z}(t)) \ , \tag{4.52}$$

$$\gamma \equiv (1-\delta_{ij}\dot{z}^i\dot{z}^j)^{-1/2} \ ,$$

where the dot indicates a derivative with respect to the coordinate time t and the trajectory $z^i(t)$ of the small body is obtained by solving the geodesic equations, which are indeed contained in eq. (4.47). Note that eqs. (4.50)-(4.52) represent the stress-energy tensor of a small body moving along the trajectory $z^i(t)$ in a Minkowski spacetime, which constitutes exactly the assumption on which kludge waveforms are based. In particular,

the quadrupole moment (4.49) reduces, in the slow motion approximation, to its textbook version $I^{ij}(t) = mz^i(t)z^j(t)$, while analogous simplifications happen for the octupole and Press formulae (see ref. [12] for details).

Having calculated $\bar{H}^{ij} \approx \bar{h}^{ij}$, it is then a trivial task to project out the gauge invariant transverse traceless perturbations h_+ and $h_\times$ at infinity (see, for instance, refs. [1, 12] for details).

Chapter 5

Testing the Kerr metric with nearly horizon-skimming orbits?

> Experience is simply the name we give our mistakes.
>
> O. Wilde

In chapters 2, 3 and 4 we have analysed in detail whether the detection of gravitational waves from EMRIs can permit mapping the spacetime of SMBHs and allow one to detect the presence of astrophysical matter around them. In this chapter we will instead consider spacetime mapping from another point of view, because we will neglect the presence of matter and assume the SMBH spacetime is described exactly by the Kerr solution. In particular, we will perform a detailed analysis of orbital motion in the vicinity of a *nearly extremal* Kerr black hole, aiming at understanding whether the almost maximal SMBH spin could leave a peculiar imprint on the EMRI gravitational waveforms expected to be detected by LISA, as was conjectured by Hughes in ref. [153].

5.1 Introduction

Although the distribution of spins for observed astrophysical black holes is not very well known at present, very rapid spin is certainly plausible, as accretion tends to spin-up SMBHs [154]. Most models for quasi-periodic oscillations (QPOs) suggest this is indeed the case in all low-mass x-ray binaries for which data is available [155]. On the other hand, continuum spectral fitting of some high-mass x-ray binaries indicates that modest spins (spin parameter $a/M \equiv J/M^2 \sim 0.6 - 0.8$) are likewise plausible [156]. The continuum-fit technique *does* find an extremely high spin of $a/M \gtrsim 0.98$ for the galactic "microquasar" GRS1915+105 [157]. This argues for a wide variety of possible spins, depending on the detailed birth and growth history of a given black hole.

In the mass range corresponding to black holes in galactic centres, measurements of the broad iron Kα emission line in active galactic nuclei suggest that SMBHs can be very

rapidly rotating (see ref. [158] for a recent review). For instance, in the case of MCG-6-30-15, for which highly accurate observations are available, a has been found to be larger than $0.987M$ at 90% confidence [159]. Because gravitational waves from EMRIs are expected to yield a very precise determination of the spins of SMBHs [43], it is interesting to investigate whether EMRIs around very rapidly rotating black holes may possess peculiar features which would be observable by LISA. Should such features exist, they would provide unambiguous information about the spin of SMBHs and thus on the mechanisms leading to their formation [160].

For extremal Kerr black holes ($a = M$), the existence of a special class of "circular" orbits was pointed out long ago by Wilkins [161], who named them "horizon-skimming" orbits. ("Circular" here means that the orbits are at constant Boyer-Lindquist coordinate radius r.) These orbits have varying inclination angle with respect to the equatorial plane and have the same coordinate radius as the horizon, $r = M$. Despite this seemingly hazardous location, it can be shown that all of these $r = M$ orbits have finite separation from one another and from the event horizon [162]. Their somewhat pathological description is due to a singularity in the Boyer-Lindquist coordinates, which collapses a finite span of the spacetime into $r = M$.

Besides being circular and "horizon-skimming", these orbits also show peculiar behaviour in their relation between angular momentum and inclination. In Newtonian gravity, a generic orbit has $L_z = |\boldsymbol{L}| \cos\iota$, where ι is the inclination angle relative to the equatorial plane (going from $\iota = 0$ for equatorial prograde orbits to $\iota = \pi$ for equatorial retrograde orbits, passing through $\iota = \pi/2$ for polar orbits), and $\boldsymbol{L}$ is the orbital angular momentum vector. As a result, $\partial L_z(r, \iota)/\partial\iota < 0$, meaning that the angular momentum in the z-direction always decreases with increasing inclination if the radius of the orbit is kept constant. This intuitively reasonable decrease of L_z with ι when r is fixed is seen for almost all black hole orbits as well. Horizon-skimming orbits, by contrast, exhibit exactly the opposite behaviour: L_z increases with inclination angle.

Hughes, in ref. [153], asked whether the behaviour $\partial L_z/\partial\iota > 0$ could be extended to a broader class of circular orbits than just those at the radius $r = M$ for the spin value $a = M$. It was found that this condition is indeed more general, and extended over a range of radius from the "innermost stable circular orbit" to $r \simeq 1.8M$ for black holes with $a > 0.9524M$. Orbits that show this property have been named "nearly horizon-skimming". The Newtonian behaviour $\partial L_z(r, \iota)/\partial\iota < 0$ is recovered for all orbits at $r \gtrsim 1.8M$ [153].

A qualitative understanding of this behaviour comes from recalling that very close to the black hole all physical processes become "locked" to the event horizon of the black hole [163], with the orbital motion of point particles coupling to the rotation of the horizon. This locking dominates the "Keplerian" tendency of an orbit to move more quickly at smaller radii, forcing an orbiting particle to slow down in the innermost orbits. Locking is particularly strong for the most-bound (equatorial) orbits; the least-bound orbits (which have the largest inclination) do not strongly lock to the black hole spin until they have very nearly reached the innermost orbit [153]. The property $\partial L_z(r, \iota)/\partial\iota > 0$ reflects the different efficiency of nearly horizon-skimming orbits to lock with the horizon.

Hughes argued that this behaviour could have observational consequences [153]. It is well-known that the inclination angle of an inspiralling body generally increases due to

gravitational-wave emission [104, 105]. Since $dL_z/dt < 0$ because of the positive angular momentum carried away by the gravitational waves, and since "normal" orbits have $\partial L_z/\partial\iota < 0$, one would indeed expect $d\iota/dt > 0$. However, if during an evolution $\partial L_z/\partial\iota$ switches sign, then $d\iota/dt$ *might*, in principle, switch sign as well: An inspiralling body *could* evolve towards an equatorial orbit, signalling the presence of an "almost-extremal" Kerr black hole [153].

It should be emphasised that this argument is not rigorous at all. In particular, one needs to consider the joint evolution of orbital radius and inclination angle; and, one must include the dependence of these two quantities on orbital energy as well as angular momentum[1]. As such, $d\iota/dt$ depends not only on dL_z/dt and $\partial L_z/\partial\iota$, but also on dE/dt, $\partial E/\partial\iota$, $\partial E/\partial r$ and $\partial L_z/\partial r$.

In this sense, the argument made in ref. [153] amounts to claiming that the contribution coming from dL_z/dt and $\partial L_z/\partial\iota$ are simply the dominant ones. Using the numerical code described in [105] to compute the fluxes dL_z/dt and dE/dt, Hughes then found that a test-particle on a circular orbit passing through the nearly horizon-skimming region of a Kerr black hole with $a = 0.998M$ (the value at which the black hole spin tends to be buffered due to photon capture from thin disk accretion [121]) had its inclination angle decreased by $\delta\iota \approx 1^\circ - 2^\circ$ [153] in the adiabatic approximation [36]. It should be noted at this point that the rate of change of inclination angle, $d\iota/dt$, appears as the *difference* between two relatively small and expensive to compute rates of change [cf. eq. (3.8) of ref. [105]]. As such, small relative errors in those rates of change can lead to large relative errors in $d\iota/dt$. Finally, in ref. [153] Hughes speculated that the decrease could be even larger for eccentric orbits satisfying the condition $\partial L_z/\partial\iota > 0$, possibly leading to an observable imprint on EMRI gravitational waveforms.

The main purpose of this chapter is to extend the analysis in ref. [153] of nearly horizon-skimming orbits to include the effect of orbital eccentricity, and to thereby test the speculation that there may be an observable imprint on EMRI waveforms of nearly horizon-skimming behaviour. In doing so, we have revisited all of the calculations of ref. [153] using a more accurate Teukolsky solver, which was coded up by Drasco and Hughes and which serves as the engine for the analysis presented in ref. [41].

We have found that the critical spin value for circular nearly horizon-skimming orbits, $a > 0.9524M$, also delineates a family of eccentric orbits for which the condition $\partial L_z(p, e, \iota)/\partial\iota > 0$ holds. (More precisely, we consider variation with respect to an angle $\theta_{\rm inc}$ that is easier to work with in the extreme strong field, but that is easily related to ι.) The parameters p and e are the semi-latus rectum and eccentricity of the orbit, which have been defined in the chapters 3 and 4 and which we will briefly recall in sec. 5.2. These generic nearly horizon-skimming orbits all have $p \lesssim 2M$, deep in the extreme strong field of the black hole.

We next study the evolution of these orbits under gravitational-wave emission in the adiabatic approximation. We first revisited the evolution of circular, nearly horizon-

[1] In the general case, one must also include the dependence on the "Carter constant" Q [113], the third integral of black hole orbits (described more carefully in sec. 5.2). For circular orbits, $Q = Q(E, L_z)$: knowledge of E and L_z completely determines Q.

skimming orbits using the improved Teukolsky solver which was used for the analysis of ref. [41]. The results of this analysis were somewhat surprising: Just as for "normal" orbits, we found that orbital inclination *always* increases during inspiral, even in the nearly horizon-skimming regime. This is in stark contrast to the claims of ref. [153]. As noted above, the rate of change of the inclination depends on the difference of two expensive and difficult to compute numbers, and thus can be strongly impacted by small relative errors in those numbers. A primary result of this chapter is thus to amend the claim of ref. [153] that an important dynamic signature of the nearly horizon-skimming region is a reversal in the sign of inclination angle evolution: The inclination *always* grows under gravitational radiation emission.

We next extended this analysis to study the evolution of generic nearly horizon-skimming orbits. The Teukolsky code to which we have direct access can, at this point, only compute the radiated fluxes of energy E and angular momentum L_z; results for the evolution of the Carter constant Q are just now beginning to be understood [135], and have not yet been incorporated into this code. We instead use "kludge" expressions for dE/dt, dL_z/dt, and dQ/dt which were inspired by refs. [148, 119]. These expressions are based on post-Newtonian flux formulae, but we modify them in such a way that they fit strong-field radiation reaction results obtained from a Teukolsky integrator; see ref. [119] for further discussion. Our analysis indicates that, just as in the circular limit, the result $d\iota/dt > 0$ holds for generic nearly horizon-skimming orbits. Furthermore, and contrary to the speculation of ref. [153], we do *not* find a large amplification of $d\iota/dt$ as orbits are made more eccentric.

Our conclusion is that the nearly horizon-skimming regime, though an interesting curiosity of strong-field orbits of nearly extremal black holes, will *not* imprint any peculiar observational signature on EMRI waveforms.

The remainder of this chapter is organised as follows. In sec. 5.2, we review the properties of bound stable orbits in Kerr spacetimes, providing expressions for the constants of motion which we will use in sec. 5.3 to generalise nearly horizon-skimming orbits to the non-circular case. In sec. 5.4, we study the evolution of the inclination angle for circular nearly horizon-skimming orbits using Teukolsky-based fluxes; in sec. 5.5 we do the same for non-circular orbits and using kludge fluxes. We present and discuss our detailed conclusions in sec. 5.6. The fits and post-Newtonian fluxes used for the kludge fluxes are presented in the Appendix.

5.2 Bound stable orbits in Kerr spacetimes

The line element of a Kerr spacetime, written in Boyer-Lindquist coordinates is [1]

$$ds^2 = -\left(1-\frac{2Mr}{\Sigma}\right)\,dt^2 + \frac{\Sigma}{\Delta}\,dr^2 + \Sigma\,d\theta^2 + \left(r^2+a^2+\frac{2Ma^2r}{\Sigma}\sin^2\theta\right)\sin^2\theta\,d\phi^2 - \frac{4Mar}{\Sigma}\sin^2\theta\,dt\,d\phi, \quad (5.1)$$

where

$$\Sigma \equiv r^2 + a^2 \cos^2\theta, \qquad \Delta \equiv r^2 - 2Mr + a^2. \tag{5.2}$$

Up to initial conditions, geodesics can then be labelled by four constants of motion: the mass μ of the test particle, its energy E and angular momentum L_z as measured by an observer at infinity and the Carter constant Q [113]. The presence of these four conserved quantities makes the geodesic equations separable in Boyer-Lindquist coordinates. Introducing the Carter time λ, defined by

$$\frac{d\tau}{d\lambda} \equiv \Sigma \,, \tag{5.3}$$

the geodesic equations become

$$\begin{aligned} \left(\mu\frac{dr}{d\lambda}\right)^2 &= V_r(r), & \mu\frac{dt}{d\lambda} &= V_t(r,\theta), \\ \left(\mu\frac{d\theta}{d\lambda}\right)^2 &= V_\theta(\theta), & \mu\frac{d\phi}{d\lambda} &= V_\phi(r,\theta)\,, \end{aligned} \tag{5.4}$$

with

$$V_t(r,\theta) \equiv E\left(\frac{\varpi^4}{\Delta} - a^2\sin^2\theta\right) + aL_z\left(1 - \frac{\varpi^2}{\Delta}\right), \tag{5.5a}$$

$$V_r(r) \equiv \left(E\varpi^2 - aL_z\right)^2 - \Delta\left[\mu^2 r^2 + (L_z - aE)^2 + Q\right], \tag{5.5b}$$

$$V_\theta(\theta) \equiv Q - L_z^2\cot^2\theta - a^2(\mu^2 - E^2)\cos^2\theta, \tag{5.5c}$$

$$V_\phi(r,\theta) \equiv L_z\csc^2\theta + aE\left(\frac{\varpi^2}{\Delta} - 1\right) - \frac{a^2 L_z}{\Delta}, \tag{5.5d}$$

where we have defined

$$\varpi^2 \equiv r^2 + a^2\,. \tag{5.6}$$

The conserved parameters E, L_z, and Q can be remapped to other parameters that describe the geometry of the orbit. We have found it useful to describe the orbit in terms of an angle $\theta_{\rm min}$ — the minimum polar angle reached by the orbit — as well as the semi-latus rectum p and the eccentricity e. In the weak-field limit, p and e correspond exactly to the semi-latus rectum and eccentricity used to describe orbits in Newtonian gravity; in the strong field, they are essentially just a convenient remapping of the apoastron and periastron of the orbit:

$$r_{\rm ap} \equiv \frac{p}{1-e}\,, \quad r_{\rm peri} \equiv \frac{p}{1+e}\,. \tag{5.7}$$

Finally, in much of our analysis, it is useful to refer to

$$z_- \equiv \cos^2\theta_{\rm min}\,, \tag{5.8}$$

rather than to $\theta_{\rm min}$ directly.

To map (E, L_z, Q) to (p, e, z_-), one uses eq. (5.4) to impose $dr/d\lambda = 0$ at $r = r_{\rm ap}$ and $r = r_{\rm peri}$, and to impose $d\theta/d\lambda = 0$ at $\theta = \theta_{\rm min}$. (Note that for a circular orbit, $r_{\rm ap} = r_{\rm peri} = r_0$. In this case, one must apply the conditions $dr/d\lambda = 0$ and $d^2r/d\lambda^2 = 0$ at $r = r_0$.) Following this approach, Schmidt [116] was able to derive explicit expressions for E, L_z and Q in terms of p, e and z_-. We now briefly review Schmidt's results.

Let us first introduce the dimensionless quantities

$$\tilde{E} \equiv E/\mu \ , \quad \tilde{L}_z \equiv L_z/(\mu M) \ , \quad \tilde{Q} \equiv Q/(\mu M)^2 \ , \tag{5.9}$$

$$\tilde{a} \equiv a/M \ , \quad \tilde{r} \equiv r/M \ , \quad \tilde{\Delta} \equiv \Delta/M^2 \ , \tag{5.10}$$

and the functions

$$f(\tilde{r}) \equiv \tilde{r}^4 + \tilde{a}^2 \left[\tilde{r}(\tilde{r}+2) + z_- \tilde{\Delta}\right] \ , \tag{5.11}$$

$$g(\tilde{r}) \equiv 2\,\tilde{a}\,\tilde{r} \ , \tag{5.12}$$

$$h(\tilde{r}) \equiv \tilde{r}(\tilde{r}-2) + \frac{z_-}{1-z_-}\tilde{\Delta} \ , \tag{5.13}$$

$$d(\tilde{r}) \equiv (\tilde{r}^2 + \tilde{a}^2 z_-)\tilde{\Delta} \ . \tag{5.14}$$

Let us further define the set of functions

$$(f_1, g_1, h_1, d_1) \equiv \begin{cases} (f(\tilde{r}_{\rm p}), g(\tilde{r}_{\rm p}), h(\tilde{r}_{\rm p}), d(\tilde{r}_{\rm p})) & \text{if } e > 0 \ , \\ (f(\tilde{r}_0), g(\tilde{r}_0), h(\tilde{r}_0), d(\tilde{r}_0)) & \text{if } e = 0 \ , \end{cases} \tag{5.15}$$

$$(f_2, g_2, h_2, d_2) \equiv \begin{cases} (f(\tilde{r}_{\rm a}), g(\tilde{r}_{\rm a}), h(\tilde{r}_{\rm a}), d(\tilde{r}_{\rm a})) & \text{if } e > 0 \ , \\ (f'(\tilde{r}_0), g'(\tilde{r}_0), h'(\tilde{r}_0), d'(\tilde{r}_0)) & \text{if } e = 0 \ , \end{cases} \tag{5.16}$$

and the determinants

$$\kappa \equiv d_1 h_2 - d_2 h_1 \ , \tag{5.17}$$

$$\varepsilon \equiv d_1 g_2 - d_2 g_1 \ , \tag{5.18}$$

$$\rho \equiv f_1 h_2 - f_2 h_1 \ , \tag{5.19}$$

$$\eta \equiv f_1 g_2 - f_2 g_1 \ , \tag{5.20}$$

$$\sigma \equiv g_1 h_2 - g_2 h_1 \ . \tag{5.21}$$

The energy of the particle can then be written

$$\tilde{E} = \sqrt{\frac{\kappa\rho + 2\epsilon\sigma - 2D\sqrt{\sigma(\sigma\epsilon^2 + \rho\epsilon\kappa - \eta\kappa^2)}}{\rho^2 + 4\eta\sigma}} \ . \tag{5.22}$$

The parameter D takes the values ± 1. The angular momentum is a solution of the system

$$f_1\tilde{E}^2 - 2g_1\tilde{E}\tilde{L}_z - h_1\tilde{L}_z^2 - d_1 = 0\,, \tag{5.23}$$
$$f_2\tilde{E}^2 - 2g_2\tilde{E}\tilde{L}_z - h_2\tilde{L}_z^2 - d_2 = 0\,. \tag{5.24}$$

By eliminating the $\tilde{L}_z^2$ terms in these equations, one finds the solution

$$\tilde{L}_z = \frac{\rho\tilde{E}^2 - \kappa}{2\tilde{E}\sigma} \tag{5.25}$$

for the angular momentum. Using $d\theta/d\lambda = 0$ at $\theta = \theta_{\rm min}$, the Carter constant can be written

$$\tilde{Q} = z_- \left[\tilde{a}^2(1-\tilde{E}^2) + \frac{\tilde{L}_z^2}{1-z_-}\right]\,. \tag{5.26}$$

Additional constraints on p, e, z_- are needed for the orbits to be stable. Inspection of eq. (5.4) shows that an eccentric orbit is stable only if

$$\frac{\partial V_r}{\partial r}(r_{\rm peri}) > 0\,. \tag{5.27}$$

It is marginally stable if $\partial V_r/\partial r = 0$ at $r = r_{\rm peri}$. Similarly, the stability condition for circular orbits is

$$\frac{\partial^2 V_r}{\partial r^2}(r_0) < 0\,; \tag{5.28}$$

marginally stable orbits are set by $\partial^2 V_r/\partial r^2 = 0$ at $r = r_0$.

Finally, we note that one can manipulate the above solutions for the conserved orbital quantities of bound stable orbits to rewrite the solution for $\tilde{L}_z$ as

$$\tilde{L}_z = -\frac{g_1\tilde{E}}{h_1} + \frac{D}{h_1}\sqrt{g_1^2\tilde{E}^2 + (f_1\tilde{E}^2 - d_1)h_1}\,. \tag{5.29}$$

From this solution, we see that it is quite natural to refer to orbits with $D = 1$ as *prograde* and to orbits with $D = -1$ as *retrograde*. Note also that eq. (5.29) is a more useful form than the corresponding expression, eq. (A4), of ref. [41]. In that expression, the factor $1/h_1$ has been squared and moved inside the square root. This obscures the fact that h_1 changes sign for very strong field orbits. Differences between eq. (5.29) and eq. (A4) of [41] are apparent for $a \gtrsim 0.835$, although only for orbits close to the separatrix (*i.e.*, the surface in the parameter space (p, e, ι) where marginally stable bound orbits lie).

5.3 Non-circular nearly horizon-skimming orbits

With explicit expressions for E, L_z and Q as functions of p, e and z_-, we now examine how to generalise the condition $\partial L_z(r,\iota)/\partial\iota > 0$, which defined circular nearly horizon-

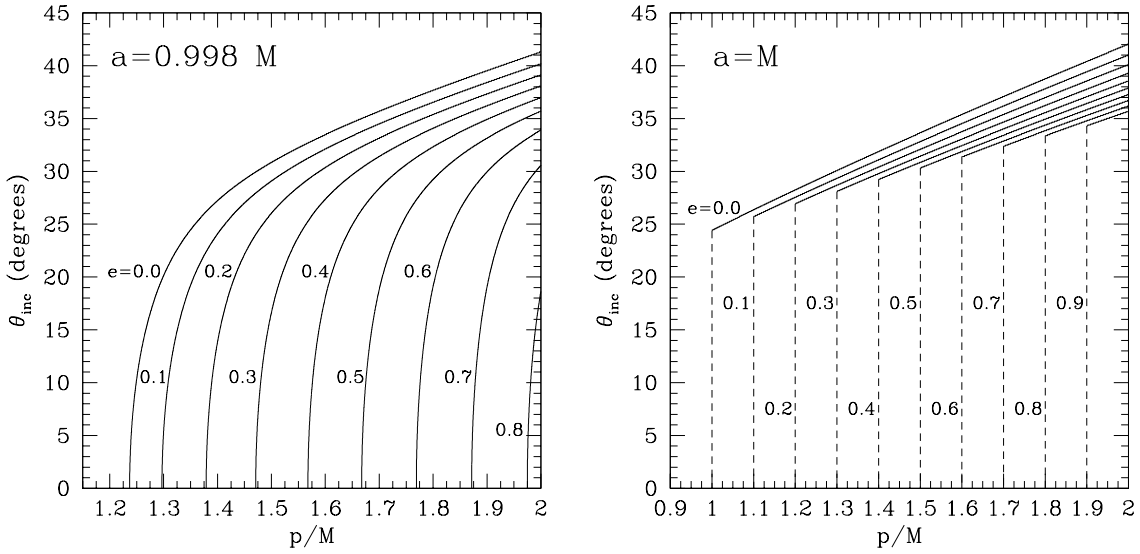

Figure 5.1: **Left panel**: *Inclination angles $\theta_{\rm inc}$ for which bound stable orbits exist for a black hole with spin $a = 0.998\,M$. The allowed range for $\theta_{\rm inc}$ goes from $\theta_{\rm inc} = 0$ to the curve corresponding to the eccentricity under consideration, $\theta_{\rm inc} = \theta_{\rm inc}^{\rm max}$.* **Right panel**: *Same as the left panel but for an extremal black hole, $a = M$. Note that in this case $\theta_{\rm inc}^{\rm max}$ never reaches zero.*

skimming orbits in ref. [153], to encompass the non-circular case. We recall that the inclination angle ι is defined as [153]

$$\cos\iota = \frac{L_z}{\sqrt{Q + L_z^2}} \,. \tag{5.30}$$

Such a definition is not always easy to handle in the case of eccentric orbits. In addition, ι does not have an obvious physical interpretation (even in the circular limit), but rather was introduced essentially to generalise (at least formally) the definition of inclination for Schwarzschild black hole orbits. In that case, one has $Q = L_x^2 + L_y^2$ and therefore $L_z = |\boldsymbol{L}| \cos\iota$.

A more useful definition for the inclination angle in a Kerr spacetime was introduced in ref. [41]:

$$\theta_{\rm inc} = \frac{\pi}{2} - D\,\theta_{\rm min} \,, \tag{5.31}$$

where $\theta_{\rm min}$ is the minimum reached by θ during the orbital motion. This angle is trivially related to z_- ($z_- = \sin^2\theta_{\rm inc}$) and ranges from 0 to $\pi/2$ for prograde orbits and from $\pi/2$ to π for retrograde orbits. It is a simple numerical calculation to convert between ι and $\theta_{\rm inc}$; doing so shows that the differences between ι and $\theta_{\rm inc}$ are very small, with the two coinciding for $a = 0$, and with a difference that is less than 2.6° for $a = M$ and circular orbits with $r = M$.

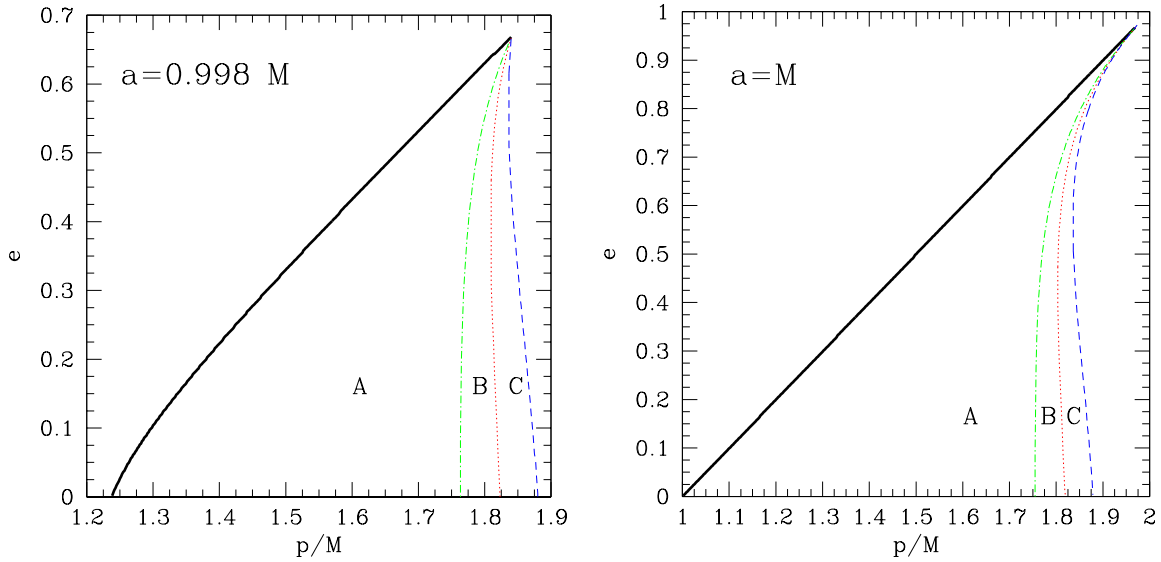

Figure 5.2: **Left panel**: *Non-circular nearly horizon-skimming orbits for $a = 0.998M$. The heavy solid line indicates the separatrix between stable and unstable orbits for equatorial orbits ($\iota = \theta_{\rm inc} = 0$). All orbits above and to the left of this line are unstable. The dot-dashed line (green in the colour version) bounds the region of the (p, e)-plane where $\partial L_z/\partial\theta_{\rm inc} > 0$ for all allowed inclination angles ("Region A"). All orbits between this line and the separatrix belong to Region A. The dotted line (red in the colour version) bounds the region $(L_z)_{\rm most\ bound} < (L_z)_{\rm least\ bound}$ ("Region B"). Note that B includes A. The dashed line (blue in the colour version) bounds the region where $\partial L_z/\partial\theta_{\rm inc} > 0$ for at least one inclination angle ("Region C"); note that C includes B. All three of these regions are candidate generalisations of the notion of nearly horizon-skimming orbits.* **Right panel**: *Same as the left panel, but for the extreme spin case, $a = M$. In this case the separatrix between stable and unstable equatorial orbits is given by the line $p/M = 1 + e$.*

Bearing all this in mind, the condition which we have adopted to generalise nearly horizon-skimming orbits is

$$\frac{\partial L_z(p, e, \theta_{\rm inc})}{\partial\theta_{\rm inc}} > 0 \ . \tag{5.32}$$

We have found that certain parts of this calculation, particularly the analysis of strong-field geodesic orbits, are best done using the angle $\theta_{\rm inc}$; other parts are more simply done using the angle ι, particularly the "kludge" computation of fluxes described in sec. 5.5. (This is because the kludge fluxes are based on an extension of post-Newtonian formulae to the strong-field regime, and these formulae use ι for inclination angle.) Accordingly, we often switch back and forth between these two notions of inclination, and in fact present our final results for inclination evolution using both $d\iota/dt$ and $d\theta_{\rm inc}/dt$.

Before mapping out the region corresponding to nearly horizon-skimming orbits, it is useful to examine stable orbits more generally in the strong field of rapidly rotating

black holes. We first fix a value for a, and then discretise the parameter space $(p, e, \theta_{\rm inc})$. We next identify the points in this space corresponding to bound stable geodesic orbits. Sufficiently close to the horizon, the bound stable orbits with specified values of p and e have an inclination angle $\theta_{\rm inc}$ ranging from 0 (equatorial orbit) to a maximum value $\theta_{\rm inc}^{\rm max}$. For given p and e, $\theta_{\rm inc}^{\rm max}$ defines the *separatrix* between stable and unstable orbits.

Example separatrices are shown in Fig. 5.1 for $a = 0.998M$ and $a = M$. This figure shows the behaviour of $\theta_{\rm inc}^{\rm max}$ as a function of the semi-latus rectum for the different values of the eccentricity indicated by the labels. Note that for $a = 0.998M$ the angle $\theta_{\rm inc}^{\rm max}$ eventually goes to zero. This is the general behaviour for $a < M$. On the other hand, for an extremal black hole, $a = M$, $\theta_{\rm inc}^{\rm max}$ never goes to zero. The orbits which reside at $r = M$ (the circular limit) are the "horizon-skimming orbits" identified by Wilkins [161]; the $a = M$ separatrix has a similar shape even for eccentric orbits. As expected, we find that for given semi-latus rectum and eccentricity the orbit with $\theta_{\rm inc} = 0$ is the one with the lowest energy E (and hence is the most-bound orbit), whereas the orbit with $\theta_{\rm inc} = \theta_{\rm inc}^{\rm max}$ has the highest E (and is least bound).

Having mapped out stable orbits in $(p, e, \theta_{\rm inc})$ space, we then computed the partial derivative $\partial L_z(p, e, \theta_{\rm inc})/\partial\theta_{\rm inc}$ and identified the following three overlapping regions:

- *Region A*: The portion of the (p, e) plane for which $\partial L_z(p, e, \theta_{\rm inc})/\partial\theta_{\rm inc} > 0$ for $0 \leq \theta_{\rm inc} \leq \theta_{\rm inc}^{\rm max}$. This region is illustrated in Fig. 5.2 as the area under the heavy solid line and to the left of the dot-dashed line (green in the colour version).

- *Region B*: The portion of the (p, e) plane for which $(L_z)_{\rm most\ bound}(p, e)$ is smaller than $(L_z)_{\rm least\ bound}(p, e)$. In other words,

$$L_z(p, e, 0) < L_z(p, e, \theta_{\rm inc}^{\rm max}) \tag{5.33}$$

  in Region *B*. Note that Region *B* contains Region *A*. It is illustrated in Fig. 5.2 as the area under the heavy solid line and to the left of the dotted line (red in the colour version).

- *Region C*: The portion of the (p, e) plane for which $\partial L_z(p, e, \theta_{\rm inc})/\partial\theta_{\rm inc} > 0$ for at least one angle $\theta_{\rm inc}$ between 0 and $\theta_{\rm inc}^{\rm max}$. Region *C* contains Region *B*, and is illustrated in Fig. 5.2 as the area under the heavy solid line and to the left of the dashed line (blue in the colour version).

Orbits in any of these three regions give possible generalisations of the nearly horizon-skimming circular orbits presented in ref. [153]. Notice, as illustrated in Fig. 5.2, that the size of these regions depends rather strongly on the spin of the black hole. All three regions disappear altogether for $a < 0.9524M$ (in agreement with [153]); their sizes grow with a, reaching maximal extent for $a = M$. These regions never extend beyond $p \simeq 2M$.

As we shall see, the difference between these three regions is not terribly important for assessing whether there is a strong signature of the nearly horizon-skimming regime on the inspiral dynamics. In view of this, it is perhaps most useful to use Region *C* as our definition, since it is the most inclusive.

5.4 Evolution of $\theta_{\rm inc}$: circular orbits

To ascertain whether nearly horizon-skimming orbits can affect an EMRI in such a way as to leave a clear imprint in the gravitational-wave signal, we have studied the time evolution of the inclination angle $\theta_{\rm inc}$. For doing this, we have used the so-called adiabatic approximation [36], in which the infalling body moves along a geodesic with slowly changing parameters. The evolution of the orbital parameters is computed using the time-averaged fluxes dE/dt, dL_z/dt and dQ/dt due to gravitational-wave emission ("radiation reaction"). As discussed in sec. 5.2, E, L_z and Q can be expressed in terms of p, e, and $\theta_{\rm inc}$. Given rates of change of E, L_z and Q, it is then straightforward [148] to calculate dp/dt, de/dt, and $d\theta_{\rm inc}/dt$ (or $d\iota/dt$).

We should note that although it is perfectly well-behaved for all bound stable geodesics, the adiabatic approximation breaks down in a small region of the orbital parameter space very close to the separatrix, where the transition from an inspiral to a plunging orbit takes place [164]. However, since this region is expected to be very small[2] and its impact on LISA waveforms rather hard to detect [164], we expect our results to be at least qualitatively correct also in this region of the parameter space.

Accurate calculation of dE/dt and dL_z/dt in the adiabatic approximation involves solving the Teukolsky and Sasaki-Nakamura equations [120]. For generic orbits this has been done for the first time in ref. [41]. The calculation of dQ/dt for generic orbits is more involved. As already mentioned, a formula for dQ/dt has been derived [135], but has not yet been implemented (at least in a code to which we have access).

On the other hand, it is well-known that a circular orbit will remain circular under radiation reaction [115, 114, 165]. This constraint means that Teukolsky-based fluxes for E and L_z are sufficient to compute dQ/dt. Considering this limit, the rate of change dQ/dt can be expressed in terms of dE/dt and dL/dt as

$$\left(\frac{dQ}{dt}\right)_{\rm circ} = -\frac{N_1(p,\iota)}{N_5(p,\iota)}\left(\frac{dE}{dt}\right)_{\rm circ} - \frac{N_4(p,\iota)}{N_5(p,\iota)}\left(\frac{dL_z}{dt}\right)_{\rm circ} \tag{5.34}$$

where

$$N_1(p,\iota) \equiv E(p,\iota)\,p^4 + a^2\,E(p,\iota)\,p^2 - 2\,a\,M\,(L_z(p,\iota) - a\,E(p,\iota))\,p\;, \tag{5.35}$$

$$N_4(p,\iota) \equiv (2\,M\,p - p^2)\,L_z(p,\iota) - 2\,M\,a\,E(p,\iota)\,p\;, \tag{5.36}$$

$$N_5(p,\iota) \equiv (2\,M\,p - p^2 - a^2)/2\;. \tag{5.37}$$

(These quantities are for a circular orbit of radius p.) Using this, it is simple to compute $d\theta_{\rm inc}/dt$ (or $d\iota/dt$).

This procedure was followed in ref. [153], using the code presented in ref. [105], to determine the evolution of ι; this analysis indicated that $d\iota/dt < 0$ for circular nearly horizon-skimming orbits. As a first step to our more general analysis, we have repeated

[2] Its width in p/M is expected to be of the order of $\Delta p/M \sim (\mu/M)^{2/5}$, where μ is the mass of the infalling body [164].

this calculation but using the improved Sasaki-Nakamura-Teukolsky code presented in ref. [41]; we focused on the case $a = 0.998M$.

Rather to our surprise, we discovered that the fluxes dE/dt and dL_z/dt computed with this more accurate code indicate that $d\iota/dt > 0$ (and $d\theta_{\rm inc}/dt > 0$) for *all* circular nearly horizon-skimming orbits — in contrast with what was found in ref. [153]. As mentioned in the introduction, the rate of change of inclination angle appears as the difference of two quantities. These quantities nearly cancel (and indeed cancel exactly in the limit $a = 0$); as such, small relative errors in their values can lead to large relative error in the inferred inclination evolution. Values for dE/dt, dL_z/dt, $d\iota/dt$, and $d\theta_{\rm inc}/dt$ computed using the present code are shown in Table 5.1 in the columns with the header "Teukolsky".

5.5 Evolution of $\theta_{\rm inc}$: non-circular orbits

The corrected behaviour of circular nearly horizon-skimming orbits has naturally led us to investigate the evolution of non-circular nearly horizon-skimming orbits. Since our code cannot be used to compute dQ/dt, we have resorted to a "kludge" approach, based on those described in refs. [148, 119]. In particular, we mostly follow the procedure developed by Gair & Glampedakis [119], although (as described below) importantly modified.

The basic idea of the "kludge" procedure is to use the functional form of 2PN fluxes E, L_z and Q, but to correct the circular part of these fluxes using fits to circular Teukolsky data. As developed in ref. [119], the fluxes are

$$\left(\frac{dE}{dt}\right)_{\rm GG} = (1-e^2)^{3/2}\left[(1-e^2)^{-3/2}\left(\frac{dE}{dt}\right)_{\rm 2PN}(p,e,\iota) - \left(\frac{dE}{dt}\right)_{\rm 2PN}(p,0,\iota) + \left(\frac{dE}{dt}\right)_{\rm fit\,circ}(p,\iota)\right], \quad (5.38)$$

$$\left(\frac{dL_z}{dt}\right)_{\rm GG} = (1-e^2)^{3/2}\left[(1-e^2)^{-3/2}\left(\frac{dL_z}{dt}\right)_{\rm 2PN}(p,e,\iota) - \left(\frac{dL_z}{dt}\right)_{\rm 2PN}(p,0,\iota) + \left(\frac{dL_z}{dt}\right)_{\rm fit\,circ}(p,\iota)\right], \quad (5.39)$$

$$\left(\frac{dQ}{dt}\right)_{\rm GG} = (1-e^2)^{3/2}\sqrt{Q(p,e,\iota)}\times \left[(1-e^2)^{-3/2}\left(\frac{dQ/dt}{\sqrt{Q}}\right)_{\rm 2PN}(p,e,\iota) - \left(\frac{dQ/dt}{\sqrt{Q}}\right)_{\rm 2PN}(p,0,\iota) + \left(\frac{dQ/dt}{\sqrt{Q}}\right)_{\rm fit\,circ}(p,\iota)\right]. \quad (5.40)$$

The post-Newtonian fluxes $(dE/dt)_{\rm 2PN}$, $(dL_z/dt)_{\rm 2PN}$ and $(dQ/dt)_{\rm 2PN}$ are given in the Appendix [eqs. (5.45), (5.46), and (5.47)].

Since for circular orbits the fluxes dE/dt, dL_z/dt and dQ/dt are related through eq. (5.34), only two fits to circular Teukolsky data are needed. One possible choice is to fit dL_z/dt and $d\iota/dt$, and then use the circularity constraint to obtain[3] [119]

$$\left(\frac{dQ/dt}{\sqrt{Q}}\right)_{\rm fit\,circ}(p,\iota) = 2\,\tan\iota\left[\left(\frac{dL_z}{dt}\right)_{\rm fit\,circ} + \frac{\sqrt{Q(p,0,\iota)}}{\sin^2\iota}\left(\frac{d\iota}{dt}\right)_{\rm fit\,circ}\right], \tag{5.41}$$

$$\left(\frac{dE}{dt}\right)_{\rm fit\,circ}(p,\iota) = -\frac{N_4(p,\iota)}{N_1(p,\iota)}\left(\frac{dL_z}{dt}\right)_{\rm fit\,circ}(p,\iota) - \frac{N_5(p,\iota)}{N_1(p,\iota)}\sqrt{Q(p,0,\iota)}\left(\frac{dQ/dt}{\sqrt{Q}}\right)_{\rm fit\,circ}(p,\iota)\,. \tag{5.42}$$

As stressed in ref. [119], one does not expect these fluxes to work well in the strong field, both because the post-Newtonian approximation breaks down close to the black hole, and because the circular Teukolsky data used for the fits in ref. [119] was computed for $3M \leq p \leq 30M$. As a first attempt to improve their behaviour in the nearly horizon-skimming region, we have made fits using circular Teukolsky data for orbits with $M < p \leq 2M$. In particular, for a black hole with $a = 0.998M$, we computed the circular Teukolsky-based fluxes dL_z/dt and $d\iota/dt$ listed in Table 5.1 (columns 8 and 10). These results were fitted with error $\lesssim 0.2\%$, and the fits are given by eqs. (5.48) and (5.49) in the Appendix.

Despite using strong-field Teukolsky fluxes for our fit, we found fairly poor behaviour of these rates of change, particularly as a function of eccentricity. To compensate for this, we introduced a kludge-type fit to correct the equatorial part of the flux, in addition to the circular part. We fitted, as a function of p and e, Teukolsky-based fluxes for dE/dt and dL_z/dt for orbits in the equatorial plane, and then introduced the following kludge fluxes for E and L_z:

$$\frac{dE}{dt}(p,e,\iota) = \left(\frac{dE}{dt}\right)_{\rm GG}(p,e,\iota) - \left(\frac{dE}{dt}\right)_{\rm GG}(p,e,0) + \left(\frac{dE}{dt}\right)_{\rm fit\,eq}(p,e) \tag{5.43}$$

$$\frac{dL_z}{dt}(p,e,\iota) = \left(\frac{dL_z}{dt}\right)_{\rm GG}(p,e,\iota) - \left(\frac{dL_z}{dt}\right)_{\rm GG}(p,e,0) + \left(\frac{dL_z}{dt}\right)_{\rm fit\,eq}(p,e)\,. \tag{5.44}$$

[Note that eq. (5.40) for dQ/dt is not modified by this procedure since $dQ/dt = 0$ for equatorial orbits.] Using equatorial non-circular Teukolsky data provided by Drasco [41, 166] for $a = 0.998$ and $M < p \leq 2M$ (the $\iota = 0$ "Teukolsky" data in Tables 5.2, 5.3 and 5.4), we found fits (with error $\lesssim 1.5\%$); see eqs. (5.52) and (5.53). Note that the fits for equatorial fluxes are significantly less accurate than the fits for circular fluxes. This appears to be due to the fact that, close to the black hole, *many* harmonics are needed in order for the Teukolsky-based fluxes to converge, especially for eccentric orbits (cf. Figs. 2 and 3 of ref. [41], noting the number of radial harmonics that have significant contribution to the flux). Truncation of these sums is probably a source of some error in

[3] This choice might seem more involved than fitting directly dL_z/dt and dQ/dt, but, as noted by Gair & Glampedakis, it ensures more sensible results for the evolution of the inclination angle. This generates more physically realistic inspirals [119].

the fluxes themselves, making it difficult to make a fit of as high quality as we could in the circular case.

These fits were then finally used in eqs. (5.43) and (5.44) to calculate the kludge fluxes dE/dt and dL_z/dt for generic orbits. This kludge reproduces to high accuracy our fits to the Teukolsky-based fluxes for circular orbits ($e = 0$) or equatorial orbits ($\iota = 0$). Some residual error remains because the $\iota = 0$ limit of the circular fits does not precisely equal the $e = 0$ limit of the equatorial fits.

Table 5.1 compares our kludge to Teukolsky-based fluxes for circular orbits; the two methods agree to several digits. Tables 5.2, 5.3 and 5.4 compare our kludge to the generic Teukolsky-based fluxes for dE/dt and dL_z/dt provided by Drasco [41, 166]. In all cases, the kludge fluxes dE/dt and dL_z/dt have the correct qualitative behaviour, being negative for all of the orbital parameters under consideration ($a = 0.998M$, $1 < p/M \leq 2$, $0 \leq e \leq 0.5$ and $0^\circ \leq \iota \leq 41^\circ$). The relative difference between the kludge and Teukolsky fluxes is always less than 25% for $e = 0$ and $e = 0.1$ (even for orbits very close to separatrix). The accuracy remains good at larger eccentricity, although it degrades somewhat as orbits come close to the separatrix.

Tables 5.1, 5.2, 5.3 and 5.4 also present the kludge values of $d\iota/dt$ and $d\theta_{\rm inc}/dt$ as computed using eqs. (5.43) and (5.44) for dE/dt and dL_z/dt, plus eq. (5.40) for dQ/dt. Although certainly not the last word on inclination evolution (pending rigorous computation of dQ/dt), these rates of change probably represent a better approximation than the results published to date in the literature. (Indeed, prior work has often used the crude approximation $d\iota/dt = 0$ [41] to estimate dQ/dt given dE/dt and dL_z/dt.)

Most significantly, we find that $(d\iota/dt)_{\rm kludge} > 0$ and $(d\theta_{\rm inc}/dt)_{\rm kludge} > 0$ for all of the orbital parameters which we consider. In other words, we find that $d\iota/dt$ and $d\theta_{\rm inc}/dt$ never change sign.

Finally, in Table 5.5 we compute the changes in $\theta_{\rm inc}$ and ι for the inspiral with mass ratio $\mu/M = 10^{-6}$. In all cases, we start at $p/M = 1.9$. The small body then inspirals through the nearly horizon-skimming region until it reaches the separatrix; at this point, the small body will fall into the large black hole in a dynamical timescale $\sim M$, and so we terminate the calculation. The evolution of circular orbits is computed using our fits to the circular-Teukolsky fluxes of E and L_z; for eccentric orbits we use the kludge fluxes (5.40), (5.43) and (5.44). As this exercise demonstrates, the change in inclination during inspiral is never larger than a few degrees. Not only is there no sign change in the nearly horizon-skimming region, but the magnitude of the inclination change remains very small. This leaves little room for the possibility that this class of orbits may have a clear observational imprint on the EMRI-waveforms to be detected by LISA.

5.6 Conclusions

We have performed a detailed analysis of the orbital motion near to the horizon of near-extremal Kerr black holes. We have demonstrated the existence of a class of orbits, which we have named "non-circular nearly horizon-skimming orbits", for which the angular

momentum L_z increases with the inclination of the orbit, while keeping the semi-latus rectum and eccentricity fixed. This behaviour, in contrast to that of Newtonian orbits, generalises earlier results for circular orbits [153].

Furthermore, to assess whether this class of orbits can produce a unique imprint on EMRI waveforms (an important source for future LISA observations), we have studied, in the adiabatic approximation, the radiative evolution of inclination angle for a small body orbiting in the nearly horizon-skimming region. For circular orbits, we have re-examined the analysis of ref. [153] using an improved code for computing Teukolsky-based fluxes of the energy and angular momentum. Significantly correcting the results of ref. [153], we found *no* decrease in the inclination angle of the orbit. Inclination always increases during inspiral.

We next carried out a similar analysis for eccentric nearly horizon-skimming orbits. In this case, we used "kludge" fluxes to evolve the constants of motion E, L_z and Q [119]. We found that these fluxes are fairly accurate when compared with the available Teukolsky-based fluxes, indicating that they should provide at least qualitatively correct information regarding inclination evolution. As for circular orbits, we found that the orbital inclination never decreases. For both circular and non-circular orbits, we found that the magnitude of the inclination change is quite small — only a few degrees at most.

Quite generically, therefore, we found that the inclination angle of both circular and eccentric nearly horizon-skimming orbits never decreases during the inspiral. Revising the results obtained in ref. [153], we thus conclude that such orbits are not likely to yield a peculiar, unique imprint on the EMRI-waveforms detectable by LISA.

Appendix

In this Appendix we report the expressions for the post-Newtonian fluxes and the fits to the Teukolsky data necessary for computing the kludge fluxes introduced in sec. 5.5. In particular the 2PN fluxes are given by [119]

$$\left(\frac{dE}{dt}\right)_{\rm 2PN} = -\frac{32}{5}\frac{\mu^2}{M^2}\left(\frac{M}{p}\right)^5 (1-e^2)^{3/2}\left[g_1(e) - \tilde{a}\left(\frac{M}{p}\right)^{3/2} g_2(e)\cos\iota - \left(\frac{M}{p}\right) g_3(e) + \pi\left(\frac{M}{p}\right)^{3/2} g_4(e) - \left(\frac{M}{p}\right)^2 g_5(e) + \tilde{a}^2\left(\frac{M}{p}\right)^2 g_6(e) - \frac{527}{96}\tilde{a}^2\left(\frac{M}{p}\right)^2 \sin^2\iota\right] , \quad (5.45)$$

$$\left(\frac{dL_z}{dt}\right)_{\rm 2PN} = -\frac{32}{5}\frac{\mu^2}{M}\left(\frac{M}{p}\right)^{7/2} (1-e^2)^{3/2}\left[g_9(e)\cos\iota + \tilde{a}\left(\frac{M}{p}\right)^{3/2}(g^a_{10}(e) - \cos^2\iota g^b_{10}(e)) - \left(\frac{M}{p}\right) g_{11}(e)\cos\iota + \pi\left(\frac{M}{p}\right)^{3/2} g_{12}(e)\cos\iota - \left(\frac{M}{p}\right)^2 g_{13}(e)\cos\iota + \tilde{a}^2\left(\frac{M}{p}\right)^2 \cos\iota\left(g_{14}(e) - \frac{45}{8}\sin^2\iota\right)\right] , \quad (5.46)$$

$$\left(\frac{dQ}{dt}\right)_{\rm 2PN} = -\frac{64}{5}\frac{\mu^2}{M}\left(\frac{M}{p}\right)^{7/2}\sqrt{Q}\,\sin\iota\,(1-e^2)^{3/2}\times \left[g_9(e) - \tilde{a}\left(\frac{M}{p}\right)^{3/2}\cos\iota\, g^b_{10}(e) - \left(\frac{M}{p}\right) g_{11}(e) + \pi\left(\frac{M}{p}\right)^{3/2} g_{12}(e) - \left(\frac{M}{p}\right)^2 g_{13}(e) + \tilde{a}^2\left(\frac{M}{p}\right)^2\left(g_{14}(e) - \frac{45}{8}\,\sin^2\iota\right)\right]\,, \quad (5.47)$$

where μ is the mass of the infalling body and where the various e-dependent coefficients are

$$g_1(e) \equiv 1 + \frac{73}{24}e^2 + \frac{37}{96}e^4\,, \qquad g_2(e) \equiv \frac{73}{12} + \frac{823}{24}e^2 + \frac{949}{32}e^4 + \frac{491}{192}e^6\,,$$

$$g_3(e) \equiv \frac{1247}{336} + \frac{9181}{672}e^2\,, \qquad g_4(e) \equiv 4 + \frac{1375}{48}e^2\,,$$

$$g_5(e) \equiv \frac{44711}{9072} + \frac{172157}{2592}e^2\,, \qquad g_6(e) \equiv \frac{33}{16} + \frac{359}{32}e^2\,,$$

$$g_9(e) \equiv 1 + \frac{7}{8}e^2\,, \qquad g^a_{10}(e) \equiv \frac{61}{24} + \frac{63}{8}e^2 + \frac{95}{64}e^4\,,$$

$$g^b_{10}(e) \equiv \frac{61}{8} + \frac{91}{4}e^2 + \frac{461}{64}e^4\,, \qquad g_{11}(e) \equiv \frac{1247}{336} + \frac{425}{336}e^2\,,$$

$$g_{12}(e) \equiv 4 + \frac{97}{8}e^2\,, \qquad g_{13}(e) \equiv \frac{44711}{9072} + \frac{302893}{6048}e^2\,,$$

$$g_{14}(e) \equiv \frac{33}{16} + \frac{95}{16}e^2\,,$$

The fits to the circular-Teukolsky data of Table 5.1 are instead given by

$$\left(\frac{dL_z}{dt}\right)_{\rm fit\,circ}(p,\iota) = -\frac{32}{5}\frac{\mu^2}{M}\left(\frac{M}{p}\right)^{7/2}\left\{\cos\iota + \left(\frac{M}{p}\right)^{3/2}\left(\frac{61}{24} - \frac{61}{8}\,\cos^2\iota + 4\pi\cos\iota\right) - \frac{1247}{336}\left(\frac{M}{p}\right)\cos\iota + \left(\frac{M}{p}\right)^2\cos\iota\left(-\frac{1625}{567} - \frac{45}{8}\,\sin^2\iota\right) + \left(\frac{M}{p}\right)^{\frac{5}{2}}\left[\widetilde{d}_1(p/M) + \widetilde{d}_2(p/M)\cos\iota + \widetilde{d}_3(p/M)\cos^2\iota + \widetilde{d}_4(p/M)\cos^3\iota + \widetilde{d}_5(p/M)\cos^4\iota + \widetilde{d}_6(p/M)\cos^5\iota + \cos\iota\left(\frac{M}{p}\right)^{3/2}\left(A + B\cos^2\iota\right)\right]\right\}\,, \quad (5.48)$$

$$\left(\frac{d\iota}{dt}\right)_{\text{fit circ}}(p,\iota) = \frac{32}{5}\frac{\mu^2}{M}\frac{\sin^2\iota}{\sqrt{Q(p,0,\iota)}}\left(\frac{M}{p}\right)^5\left\{\frac{61}{24}+\left(\frac{M}{p}\right)\widetilde{d}_1(p/M)+\right.$$
$$\cos\iota\left(\frac{M}{p}\right)^{1/2}\left[a_d^7+b_d^7\left(\frac{M}{p}\right)+c_d^7\left(\frac{M}{p}\right)^{3/2}\right]+\cos^2\iota\left(\frac{M}{p}\right)\widetilde{d}_8(p/M)$$
$$\left.+\ \cos\iota\left(\frac{M}{p}\right)^{5/2}\left[\widetilde{h}_1(p/M)+\cos^2\iota\,\widetilde{h}_2(p/M)\right]\right\}, \quad (5.49)$$

where

$$\widetilde{d}_i(x) \equiv a_d^i + b_d^i\,x^{-1/2} + c_d^i\,x^{-1}\,, \qquad i=1,\ldots,8,$$
$$\widetilde{h}_i(x) \equiv a_h^i + b_h^i\,x^{-1/2}\,, \quad i=1,2 \quad (5.50)$$

and the numerical coefficients are given by

$$a_h^1 = -278.9387\,, \quad b_h^1 = 84.1414\,, \quad a_h^2 = 8.6679\,,$$
$$b_h^2 = -9.2401\,, \quad A = -18.3362\,, \quad B = 24.9034\,, \quad (5.51)$$

and by the following table

i	1	2	3	4	5	6	7	8
a_d^i	15.8363	445.4418	−2027.7797	3089.1709	−2045.2248	498.6411	−8.7220	50.8345
b_d^i	−55.6777	−1333.2461	5940.4831	−9103.4472	6113.1165	−1515.8506	−50.8950	−131.6422
c_d^i	38.6405	1049.5637	−4513.0879	6926.3191	-4714.9633	1183.5875	251.4025	83.0834

Note that the functional form of these fits was obtained from eqs. (57) and (58) of ref. [119] by setting $\tilde{a}$ (*i.e.*, q in their notation) to 1. Finally, we give expressions for the fits to the equatorial Teukolsky data of tables 5.2, 5.3 and 5.4 (data with $\iota = 0$, columns with header "Teukolsky"):

$$\left(\frac{dE}{dt}\right)_{\text{fit eq}}(p,e) = \left(\frac{dE}{dt}\right)_{2PN}(p,e,0) - \frac{32}{5}\left(\frac{\mu}{M}\right)^2\left(\frac{M}{p}\right)^5(1-e^2)^{3/2}\times$$
$$\left[\widetilde{g}_1(e)+\widetilde{g}_2(e)\left(\frac{M}{p}\right)^{1/2}+\widetilde{g}_3(e)\left(\frac{M}{p}\right)+\widetilde{g}_4(e)\left(\frac{M}{p}\right)^{3/2}+\widetilde{g}_5(e)\left(\frac{M}{p}\right)^2\right], \quad (5.52)$$
$$\left(\frac{L_z}{dt}\right)_{\text{fit eq}}(p,e) = \left(\frac{L_z}{dt}\right)_{2PN}(p,e,0) - \frac{32}{5}\frac{\mu^2}{M}\left(\frac{M}{p}\right)^{7/2}(1-e^2)^{3/2}\times$$
$$\left[\widetilde{f}_1(e)+\widetilde{f}_2(e)\left(\frac{M}{p}\right)^{1/2}+\widetilde{f}_3(e)\left(\frac{M}{p}\right)+\widetilde{f}_4(e)\left(\frac{M}{p}\right)^{3/2}+\widetilde{f}_5(e)\left(\frac{M}{p}\right)^2\right], \quad (5.53)$$

$$\widetilde{g}_i(e) \equiv a_g^i + b_g^i\, e^2 + c_g^i\, e^4 + d_g^i\, e^6\ , \quad \widetilde{f}_i(e) \equiv a_f^i + b_f^i\, e^2 + c_f^i\, e^4 + d_f^i\, e^6\ , \quad i = 1, \ldots, 5 \tag{5.54}$$

where the numerical coefficients are given by the following table

i	a_g^i	b_g^i	c_g^i	d_g^i	a_f^i	b_f^i	c_f^i	d_f^i
1	6.4590	-2038.7301	6639.9843	227709.2187	5.4577	-3116.4034	4711.7065	214332.2907
2	-31.2215	10390.6778	-27505.7295	-1224376.5294	-26.6519	15958.6191	-16390.4868	-1147201.4687
3	57.1208	-19800.4891	39527.8397	2463977.3622	50.4374	-30579.3129	15749.9411	2296989.5466
4	-49.7051	16684.4629	-21714.7941	-2199231.9494	-46.7816	25968.8743	656.3460	-2038650.9838
5	16.4697	-5234.2077	2936.2391	734454.5696	15.6660	-8226.3892	-4903.9260	676553.2755

$\frac{p}{M}$	e	$\theta_{\rm inc}$ (deg.)	ι (deg.)	$\frac{dE}{dt}\times\frac{M^2}{\mu^2}$ (kludge)	$\frac{dE}{dt}\times\frac{M^2}{\mu^2}$ (Teukolsky)	$\frac{dL_z}{dt}\times\frac{M}{\mu^2}$ (kludge)	$\frac{dL_z}{dt}\times\frac{M}{\mu^2}$ (Teukolsky)	$\frac{d\iota}{dt}\times\frac{M}{\mu^2}$ (kludge)	$\frac{d\iota}{dt}\times\frac{M}{\mu^2}$ (Teukolsky)	$\frac{d\theta_{\rm inc}}{dt}\times\frac{M}{\mu^2}$ (kludge)	$\frac{d\theta_{\rm inc}}{dt}\times\frac{M}{\mu^2}$ (Teukolsky)
1.3	0	0	0	-9.108×10^{-2}	-9.109×10^{-2}	-2.258×10^{-1}	-2.259×10^{-1}	0	0	0	0
1.3	0	10.4870	11.6773	-9.328×10^{-2}	-9.332×10^{-2}	-2.304×10^{-1}	-2.306×10^{-1}	1.837×10^{-2}	1.839×10^{-2}	6.462×10^{-3}	6.475×10^{-3}
1.3	0	14.6406	16.1303	-9.588×10^{-2}	-9.588×10^{-2}	-2.359×10^{-1}	-2.360×10^{-1}	2.397×10^{-2}	2.400×10^{-2}	8.645×10^{-3}	8.667×10^{-3}
1.3	0	17.7000	19.3172	-9.875×10^{-2}	-9.876×10^{-2}	-2.420×10^{-1}	-2.421×10^{-1}	2.728×10^{-2}	2.731×10^{-2}	1.007×10^{-2}	1.010×10^{-2}
1.3	0	20.1636	21.8210	-1.019×10^{-1}	-1.019×10^{-1}	-2.486×10^{-1}	-2.488×10^{-1}	2.943×10^{-2}	2.950×10^{-2}	1.111×10^{-2}	1.117×10^{-2}
1.4	0	0	0	-8.700×10^{-2}	-8.709×10^{-2}	-2.311×10^{-1}	-2.312×10^{-1}	0	0	0	0
1.4	0	14.5992	16.0005	-9.062×10^{-2}	-9.070×10^{-2}	-2.386×10^{-1}	-2.386×10^{-1}	2.316×10^{-2}	2.319×10^{-2}	8.823×10^{-3}	8.848×10^{-3}
1.4	0	20.1756	21.7815	-9.520×10^{-2}	-9.526×10^{-2}	-2.482×10^{-1}	-2.482×10^{-1}	2.875×10^{-2}	2.877×10^{-2}	1.141×10^{-2}	1.143×10^{-2}
1.4	0	24.1503	25.7517	-1.006×10^{-1}	-1.007×10^{-1}	-2.595×10^{-1}	-2.596×10^{-1}	3.140×10^{-2}	3.141×10^{-2}	1.289×10^{-2}	1.288×10^{-2}
1.4	0	27.2489	28.7604	-1.067×10^{-1}	-1.068×10^{-1}	-2.725×10^{-1}	-2.725×10^{-1}	3.274×10^{-2}	3.275×10^{-2}	1.378×10^{-2}	1.377×10^{-2}
1.5	0	0	0	-8.009×10^{-2}	-7.989×10^{-2}	-2.270×10^{-1}	-2.265×10^{-1}	0	0	0	0
1.5	0	16.7836	18.1857	-8.401×10^{-2}	-8.383×10^{-2}	-2.348×10^{-1}	-2.343×10^{-1}	2.360×10^{-2}	2.351×10^{-2}	9.602×10^{-3}	9.545×10^{-3}
1.5	0	23.0755	24.6167	-8.917×10^{-2}	-8.897×10^{-2}	-2.454×10^{-1}	-2.449×10^{-1}	2.872×10^{-2}	2.863×10^{-2}	1.228×10^{-2}	1.222×10^{-2}
1.5	0	27.4892	28.9670	-9.537×10^{-2}	-9.516×10^{-2}	-2.583×10^{-1}	-2.579×10^{-1}	3.091×10^{-2}	3.082×10^{-2}	1.372×10^{-2}	1.367×10^{-2}
1.5	0	30.8795	32.2231	-1.025×10^{-1}	-1.023×10^{-1}	-2.733×10^{-1}	-2.728×10^{-1}	3.184×10^{-2}	3.173×10^{-2}	1.452×10^{-2}	1.443×10^{-2}
1.6	0	0	0	-7.181×10^{-2}	-7.156×10^{-2}	-2.168×10^{-1}	-2.162×10^{-1}	0	0	0	0
1.6	0	18.3669	19.7220	-7.568×10^{-2}	-7.545×10^{-2}	-2.242×10^{-1}	-2.237×10^{-1}	2.240×10^{-2}	2.229×10^{-2}	9.600×10^{-3}	9.515×10^{-3}
1.6	0	25.1720	26.6245	-8.084×10^{-2}	-8.062×10^{-2}	-2.346×10^{-1}	-2.341×10^{-1}	2.701×10^{-2}	2.685×10^{-2}	1.223×10^{-2}	1.210×10^{-2}
1.6	0	29.9014	31.2625	-8.708×10^{-2}	-8.687×10^{-2}	-2.474×10^{-1}	-2.470×10^{-1}	2.889×10^{-2}	2.872×10^{-2}	1.363×10^{-2}	1.349×10^{-2}
1.6	0	33.5053	34.7164	-9.425×10^{-2}	-9.399×10^{-2}	-2.622×10^{-1}	-2.616×10^{-1}	2.964×10^{-2}	2.951×10^{-2}	1.441×10^{-2}	1.432×10^{-2}
1.7	0	0	0	-6.332×10^{-2}	-6.317×10^{-2}	-2.034×10^{-1}	-2.031×10^{-1}	0	0	0	0
1.7	0	19.6910	20.9859	-6.702×10^{-2}	-6.687×10^{-2}	-2.101×10^{-1}	-2.098×10^{-1}	2.057×10^{-2}	2.052×10^{-2}	9.202×10^{-3}	9.171×10^{-3}
1.7	0	26.9252	28.2884	-7.197×10^{-2}	-7.184×10^{-2}	-2.199×10^{-1}	-2.196×10^{-1}	2.467×10^{-2}	2.456×10^{-2}	1.170×10^{-2}	1.162×10^{-2}
1.7	0	31.9218	33.1786	-7.794×10^{-2}	-7.782×10^{-2}	-2.319×10^{-1}	-2.316×10^{-1}	2.632×10^{-2}	2.620×10^{-2}	1.306×10^{-2}	1.296×10^{-2}
1.7	0	35.7100	36.8118	-8.475×10^{-2}	-8.465×10^{-2}	-2.457×10^{-1}	-2.455×10^{-1}	2.698×10^{-2}	2.686×10^{-2}	1.384×10^{-2}	1.373×10^{-2}
1.8	0	0	0	-5.531×10^{-2}	-5.528×10^{-2}	-1.888×10^{-1}	-1.887×10^{-1}	0	0	0	0
1.8	0	20.8804	22.1128	-5.879×10^{-2}	-5.874×10^{-2}	-1.948×10^{-1}	-1.946×10^{-1}	1.858×10^{-2}	1.858×10^{-2}	8.635×10^{-3}	8.639×10^{-3}
1.8	0	28.5007	29.7791	-6.343×10^{-2}	-6.336×10^{-2}	-2.036×10^{-1}	-2.035×10^{-1}	2.221×10^{-2}	2.223×10^{-2}	1.098×10^{-2}	1.101×10^{-2}
1.8	0	33.7400	34.9034	-6.901×10^{-2}	-6.894×10^{-2}	-2.146×10^{-1}	-2.144×10^{-1}	2.368×10^{-2}	2.371×10^{-2}	1.228×10^{-2}	1.232×10^{-2}
1.8	0	37.6985	38.7065	-7.533×10^{-2}	-7.533×10^{-2}	-2.271×10^{-1}	-2.271×10^{-1}	2.429×10^{-2}	2.427×10^{-2}	1.306×10^{-2}	1.303×10^{-2}
1.9	0	0	0	-4.809×10^{-2}	-4.811×10^{-2}	-1.740×10^{-1}	-1.740×10^{-1}	0	0	0	0
1.9	0	21.9900	23.1615	-5.132×10^{-2}	-5.134×10^{-2}	-1.792×10^{-1}	-1.793×10^{-1}	1.666×10^{-2}	1.664×10^{-2}	8.022×10^{-3}	8.007×10^{-3}
1.9	0	29.9708	31.1702	-5.562×10^{-2}	-5.564×10^{-2}	-1.872×10^{-1}	-1.872×10^{-1}	1.986×10^{-2}	1.987×10^{-2}	1.019×10^{-2}	1.020×10^{-2}
1.9	0	35.4385	36.5176	-6.078×10^{-2}	-6.077×10^{-2}	-1.971×10^{-1}	-1.970×10^{-1}	2.118×10^{-2}	2.122×10^{-2}	1.143×10^{-2}	1.148×10^{-2}
1.9	0	39.5592	40.4847	-6.659×10^{-2}	-6.658×10^{-2}	-2.082×10^{-1}	-2.082×10^{-1}	2.177×10^{-2}	2.182×10^{-2}	1.222×10^{-2}	1.228×10^{-2}
2.0	0	0	0	-4.174×10^{-2}	-4.175×10^{-2}	-1.598×10^{-1}	-1.598×10^{-1}	0	0	0	0
2.0	0	23.0471	24.1605	-4.471×10^{-2}	-4.472×10^{-2}	-1.643×10^{-1}	-1.643×10^{-1}	1.489×10^{-2}	1.489×10^{-2}	7.425×10^{-3}	7.424×10^{-3}
2.0	0	31.3715	32.4978	-4.867×10^{-2}	-4.871×10^{-2}	-1.713×10^{-1}	-1.714×10^{-1}	1.773×10^{-2}	1.770×10^{-2}	9.436×10^{-3}	9.411×10^{-3}
2.0	0	37.0583	38.0608	-5.341×10^{-2}	-5.345×10^{-2}	-1.801×10^{-1}	-1.801×10^{-1}	1.893×10^{-2}	1.889×10^{-2}	1.062×10^{-2}	1.057×10^{-2}
2.0	0	41.3358	42.1876	-5.873×10^{-2}	-5.875×10^{-2}	-1.900×10^{-1}	-1.900×10^{-1}	1.950×10^{-2}	1.948×10^{-2}	1.141×10^{-2}	1.138×10^{-2}

Table 5.1: *Teukolsky-based fluxes and kludge fluxes [computed using eqs. (5.40), (5.43) and (5.44)] for circular orbits about a black hole with* $a = 0.998M$*;* μ *represents the mass of the infalling body. The Teukolsky-based fluxes have an accuracy of* 10^{-6}.

$\frac{p}{M}$	e	$\theta_{\rm inc}$ (deg.)	ι (deg.)	$\frac{dE}{dt}\times\frac{M^2}{\mu^2}$ (kludge)	$\frac{dE}{dt}\times\frac{M^2}{\mu^2}$ (Teukolsky)	$\frac{dL_z}{dt}\times\frac{M}{\mu^2}$ (kludge)	$\frac{dL_z}{dt}\times\frac{M}{\mu^2}$ (Teukolsky)	$\frac{d\iota}{dt}\times\frac{M}{\mu^2}$ (kludge)	$\frac{d\theta_{\rm inc}}{dt}\times\frac{M}{\mu^2}$ (kludge)
1.3	0.1	0	0	-8.804×10^{-2}	-8.804×10^{-2}	-2.098×10^{-1}	-2.098×10^{-1}	0	0
1.4	0.1	0	0	-8.728×10^{-2}	-8.719×10^{-2}	-2.274×10^{-1}	-2.275×10^{-1}	0	0
1.4	0.1	8	8.8664	-9.110×10^{-2}	-8.736×10^{-2}	-2.355×10^{-1}	-2.273×10^{-1}	4.066×10^{-2}	2.938×10^{-2}
1.4	0.1	16	17.4519	-1.030×10^{-1}	-8.958×10^{-2}	-2.602×10^{-1}	-2.309×10^{-1}	7.428×10^{-2}	5.475×10^{-2}
1.4	0.1	24	25.5784	-1.243×10^{-1}	-9.771×10^{-2}	-3.037×10^{-1}	-2.415×10^{-1}	9.663×10^{-2}	7.316×10^{-2}
1.5	0.1	0	0	-8.069×10^{-2}	-8.095×10^{-2}	-2.255×10^{-1}	-2.260×10^{-1}	0	0
1.5	0.1	8	8.7910	-8.323×10^{-2}	-8.133×10^{-2}	-2.310×10^{-1}	-2.264×10^{-1}	2.996×10^{-2}	2.070×10^{-2}
1.5	0.1	16	17.3490	-9.121×10^{-2}	-8.395×10^{-2}	-2.483×10^{-1}	-2.314×10^{-1}	5.512×10^{-2}	3.888×10^{-2}
1.5	0.1	24	25.5197	-1.059×10^{-1}	-8.980×10^{-2}	-2.792×10^{-1}	-2.423×10^{-1}	7.255×10^{-2}	5.264×10^{-2}
1.6	0.1	0	0	-7.255×10^{-2}	-7.281×10^{-2}	-2.161×10^{-1}	-2.168×10^{-1}	0	0
1.6	0.1	8	8.7195	-7.430×10^{-2}	-7.321×10^{-2}	-2.201×10^{-1}	-2.173×10^{-1}	2.258×10^{-2}	1.502×10^{-2}
1.6	0.1	16	17.2437	-7.986×10^{-2}	-7.533×10^{-2}	-2.323×10^{-1}	-2.212×10^{-1}	4.179×10^{-2}	2.839×10^{-2}
1.6	0.1	24	25.4388	-9.025×10^{-2}	-8.040×10^{-2}	-2.547×10^{-1}	-2.309×10^{-1}	5.554×10^{-2}	3.886×10^{-2}
1.6	0.1	32	33.2683	-1.082×10^{-1}	-9.435×10^{-2}	-2.920×10^{-1}	-2.551×10^{-1}	6.316×10^{-2}	4.559×10^{-2}
1.7	0.1	0	0	-6.427×10^{-2}	-6.440×10^{-2}	-2.036×10^{-1}	-2.040×10^{-1}	0	0
1.7	0.1	8	8.6555	-6.552×10^{-2}	-6.478×10^{-2}	-2.065×10^{-1}	-2.045×10^{-1}	1.742×10^{-2}	1.124×10^{-2}
1.7	0.1	16	17.1454	-6.953×10^{-2}	-6.651×10^{-2}	-2.154×10^{-1}	-2.075×10^{-1}	3.240×10^{-2}	2.134×10^{-2}
1.7	0.1	24	25.3531	-7.707×10^{-2}	-7.052×10^{-2}	-2.317×10^{-1}	-2.150×10^{-1}	4.342×10^{-2}	2.948×10^{-2}
1.7	0.1	32	33.2416	-9.009×10^{-2}	-7.959×10^{-2}	-2.590×10^{-1}	-2.324×10^{-1}	4.998×10^{-2}	3.512×10^{-2}
1.8	0.1	0	0	-5.640×10^{-2}	-5.640×10^{-2}	-1.897×10^{-1}	-1.897×10^{-1}	0	0
1.8	0.1	8	8.5991	-5.732×10^{-2}	-5.676×10^{-2}	-1.918×10^{-1}	-1.902×10^{-1}	1.371×10^{-2}	8.640×10^{-3}
1.8	0.1	16	17.0562	-6.028×10^{-2}	-5.817×10^{-2}	-1.984×10^{-1}	-1.925×10^{-1}	2.562×10^{-2}	1.647×10^{-2}
1.8	0.1	24	25.2693	-6.588×10^{-2}	-6.139×10^{-2}	-2.105×10^{-1}	-1.983×10^{-1}	3.456×10^{-2}	2.291×10^{-2}
1.8	0.1	32	33.2018	-7.555×10^{-2}	-6.849×10^{-2}	-2.307×10^{-1}	-2.120×10^{-1}	4.020×10^{-2}	2.765×10^{-2}
1.9	0.1	0	0	-4.915×10^{-2}	-4.911×10^{-2}	-1.753×10^{-1}	-1.751×10^{-1}	0	0
1.9	0.1	8	8.5494	-4.985×10^{-2}	-4.945×10^{-2}	-1.768×10^{-1}	-1.755×10^{-1}	1.097×10^{-2}	6.791×10^{-3}
1.9	0.1	16	16.9760	-5.208×10^{-2}	-5.064×10^{-2}	-1.817×10^{-1}	-1.774×10^{-1}	2.055×10^{-2}	1.298×10^{-2}
1.9	0.1	24	25.1898	-5.633×10^{-2}	-5.328×10^{-2}	-1.908×10^{-1}	-1.819×10^{-1}	2.788×10^{-2}	1.816×10^{-2}
1.9	0.1	32	33.1555	-6.364×10^{-2}	-5.870×10^{-2}	-2.059×10^{-1}	-1.920×10^{-1}	3.272×10^{-2}	2.214×10^{-2}
2.0	0.1	0	0	-4.263×10^{-2}	-4.264×10^{-2}	-1.607×10^{-1}	-1.608×10^{-1}	0	0
2.0	0.1	8	8.5057	-4.316×10^{-2}	-4.292×10^{-2}	-1.619×10^{-1}	-1.611×10^{-1}	8.862×10^{-3}	5.424×10^{-3}
2.0	0.1	16	16.9042	-4.488×10^{-2}	-4.390×10^{-2}	-1.656×10^{-1}	-1.625×10^{-1}	1.666×10^{-2}	1.039×10^{-2}
2.0	0.1	24	25.1156	-4.815×10^{-2}	-4.604×10^{-2}	-1.724×10^{-1}	-1.660×10^{-1}	2.271×10^{-2}	1.459×10^{-2}
2.0	0.1	32	33.1064	-5.376×10^{-2}	-5.031×10^{-2}	-1.838×10^{-1}	-1.736×10^{-1}	2.684×10^{-2}	1.793×10^{-2}
2.0	0.1	40	40.8954	-6.339×10^{-2}	-6.236×10^{-2}	-2.027×10^{-1}	-1.967×10^{-1}	2.917×10^{-2}	2.036×10^{-2}

Table 5.2: *As in Table 5.1 but for non-circular orbits; the Teukolsky-based fluxes for E and L_z have an accuracy of 10^{-3}. Note that the code that we use, with all of the Teukolsky-based codes that we are aware of, does not at present have the capability to compute inclination angle evolution for generic orbits.*

$\frac{p}{M}$	e	$\theta_{\rm inc}$ (deg.)	ι (deg.)	$\frac{dE}{dt}\times\frac{M^2}{\mu^2}$ (kludge)	$\frac{dE}{dt}\times\frac{M^2}{\mu^2}$ (Teukolsky)	$\frac{dL_z}{dt}\times\frac{M}{\mu^2}$ (kludge)	$\frac{dL_z}{dt}\times\frac{M}{\mu^2}$ (Teukolsky)	$\frac{d\iota}{dt}\times\frac{M}{\mu^2}$ (kludge)	$\frac{d\theta_{\rm inc}}{dt}\times\frac{M}{\mu^2}$ (kludge)
1.4	0.2	0	0	-8.636×10^{-2}	-8.642×10^{-2}	-2.119×10^{-1}	-2.121×10^{-1}	0	0
1.4	0.2	8	8.8215	-9.853×10^{-2}	-8.240×10^{-2}	-2.374×10^{-1}	-2.015×10^{-1}	1.148×10^{-1}	9.714×10^{-2}
1.5	0.2	0	0	-8.362×10^{-2}	-8.349×10^{-2}	-2.236×10^{-1}	-2.230×10^{-1}	0	0
1.5	0.2	8	8.7595	-9.141×10^{-2}	-8.276×10^{-2}	-2.410×10^{-1}	-2.206×10^{-1}	7.893×10^{-2}	6.549×10^{-2}
1.5	0.2	16	17.2957	-1.145×10^{-1}	-8.394×10^{-2}	-2.915×10^{-1}	-2.215×10^{-1}	1.466×10^{-1}	1.230×10^{-1}
1.5	0.2	24	25.4608	-1.524×10^{-1}	-9.230×10^{-2}	-3.712×10^{-1}	-2.357×10^{-1}	1.952×10^{-1}	1.661×10^{-1}
1.6	0.2	0	0	-7.596×10^{-2}	-7.616×10^{-2}	-2.171×10^{-1}	-2.176×10^{-1}	0	0
1.6	0.2	8	8.6935	-8.111×10^{-2}	-7.641×10^{-2}	-2.292×10^{-1}	-2.177×10^{-1}	5.520×10^{-2}	4.502×10^{-2}
1.6	0.2	16	17.1994	-9.649×10^{-2}	-7.798×10^{-2}	-2.647×10^{-1}	-2.198×10^{-1}	1.032×10^{-1}	8.500×10^{-2}
1.6	0.2	24	25.3891	-1.221×10^{-1}	-8.314×10^{-2}	-3.212×10^{-1}	-2.288×10^{-1}	1.388×10^{-1}	1.160×10^{-1}
1.7	0.2	0	0	-6.765×10^{-2}	-6.799×10^{-2}	-2.057×10^{-1}	-2.068×10^{-1}	0	0
1.7	0.2	8	8.6329	-7.116×10^{-2}	-6.813×10^{-2}	-2.144×10^{-1}	-2.066×10^{-1}	3.963×10^{-2}	3.176×10^{-2}
1.7	0.2	16	17.1064	-8.171×10^{-2}	-6.995×10^{-2}	-2.398×10^{-1}	-2.096×10^{-1}	7.441×10^{-2}	6.024×10^{-2}
1.7	0.2	24	25.3085	-9.948×10^{-2}	-7.443×10^{-2}	-2.806×10^{-1}	-2.178×10^{-1}	1.009×10^{-1}	8.290×10^{-2}
1.7	0.2	32	33.2037	-1.257×10^{-1}	-8.558×10^{-2}	-3.371×10^{-1}	-2.366×10^{-1}	1.175×10^{-1}	9.806×10^{-2}
1.8	0.2	0	0	-5.965×10^{-2}	-5.962×10^{-2}	-1.927×10^{-1}	-1.926×10^{-1}	0	0
1.8	0.2	8	8.5789	-6.211×10^{-2}	-5.997×10^{-2}	-1.990×10^{-1}	-1.930×10^{-1}	2.919×10^{-2}	2.300×10^{-2}
1.8	0.2	16	17.0211	-6.953×10^{-2}	-6.147×10^{-2}	-2.175×10^{-1}	-1.954×10^{-1}	5.504×10^{-2}	4.380×10^{-2}
1.8	0.2	24	25.2283	-8.216×10^{-2}	-6.502×10^{-2}	-2.474×10^{-1}	-2.016×10^{-1}	7.515×10^{-2}	6.068×10^{-2}
1.8	0.2	32	33.1656	-1.009×10^{-1}	-7.410×10^{-2}	-2.890×10^{-1}	-2.190×10^{-1}	8.839×10^{-2}	7.258×10^{-2}
1.9	0.2	0	0	-5.218×10^{-2}	-5.210×10^{-2}	-1.786×10^{-1}	-1.783×10^{-1}	0	0
1.9	0.2	8	8.5312	-5.394×10^{-2}	-5.244×10^{-2}	-1.833×10^{-1}	-1.787×10^{-1}	2.197×10^{-2}	1.704×10^{-2}
1.9	0.2	16	16.9441	-5.928×10^{-2}	-5.373×10^{-2}	-1.970×10^{-1}	-1.807×10^{-1}	4.156×10^{-2}	3.254×10^{-2}
1.9	0.2	24	25.1518	-6.843×10^{-2}	-5.669×10^{-2}	-2.192×10^{-1}	-1.858×10^{-1}	5.706×10^{-2}	4.535×10^{-2}
1.9	0.2	32	33.1207	-8.213×10^{-2}	-6.277×10^{-2}	-2.502×10^{-1}	-1.966×10^{-1}	6.767×10^{-2}	5.475×10^{-2}
2.0	0.2	0	0	-4.528×10^{-2}	-4.530×10^{-2}	-1.637×10^{-1}	-1.638×10^{-1}	0	0
2.0	0.2	8	8.4891	-4.657×10^{-2}	-4.557×10^{-2}	-1.671×10^{-1}	-1.641×10^{-1}	1.679×10^{-2}	1.283×10^{-2}
2.0	0.2	16	16.8749	-5.049×10^{-2}	-4.664×10^{-2}	-1.774×10^{-1}	-1.657×10^{-1}	3.184×10^{-2}	2.457×10^{-2}
2.0	0.2	24	25.0802	-5.725×10^{-2}	-4.904×10^{-2}	-1.941×10^{-1}	-1.696×10^{-1}	4.391×10^{-2}	3.440×10^{-2}
2.0	0.2	32	33.0730	-6.743×10^{-2}	-5.427×10^{-2}	-2.175×10^{-1}	-1.793×10^{-1}	5.243×10^{-2}	4.184×10^{-2}
1.5	0.3	0	0	-8.481×10^{-2}	-8.478×10^{-2}	-2.094×10^{-1}	-2.094×10^{-1}	0	0
1.5	0.3	8	8.7037	-1.006×10^{-1}	-7.824×10^{-2}	-2.442×10^{-1}	-1.934×10^{-1}	1.484×10^{-1}	1.301×10^{-1}
1.5	0.3	16	17.2003	-1.469×10^{-1}	-7.811×10^{-2}	-3.435×10^{-1}	-1.864×10^{-1}	2.766×10^{-1}	2.440×10^{-1}
1.6	0.3	0	0	-8.144×10^{-2}	-8.123×10^{-2}	-2.183×10^{-1}	-2.178×10^{-1}	0	0
1.6	0.3	8	8.6498	-9.182×10^{-2}	-7.807×10^{-2}	-2.426×10^{-1}	-2.095×10^{-1}	1.028×10^{-1}	8.918×10^{-2}
1.6	0.3	16	17.1246	-1.223×10^{-1}	-8.089×10^{-2}	-3.122×10^{-1}	-2.144×10^{-1}	1.928×10^{-1}	1.683×10^{-1}
1.6	0.3	24	25.3046	-1.716×10^{-1}	-8.666×10^{-2}	-4.197×10^{-1}	-2.229×10^{-1}	2.607×10^{-1}	2.295×10^{-1}
1.7	0.3	0	0	-7.362×10^{-2}	-7.314×10^{-2}	-2.104×10^{-1}	-2.095×10^{-1}	0	0
1.7	0.3	8	8.5953	-8.060×10^{-2}	-7.224×10^{-2}	-2.277×10^{-1}	-2.065×10^{-1}	7.240×10^{-2}	6.224×10^{-2}
1.7	0.3	16	17.0415	-1.013×10^{-1}	-7.369×10^{-2}	-2.774×10^{-1}	-2.084×10^{-1}	1.365×10^{-1}	1.180×10^{-1}
1.7	0.3	24	25.2339	-1.349×10^{-1}	-7.800×10^{-2}	-3.547×10^{-1}	-2.153×10^{-1}	1.861×10^{-1}	1.622×10^{-1}
1.8	0.3	0	0	-6.488×10^{-2}	-6.484×10^{-2}	-1.973×10^{-1}	-1.972×10^{-1}	0	0
1.8	0.3	8	8.5454	-6.970×10^{-2}	-6.480×10^{-2}	-2.099×10^{-1}	-1.966×10^{-1}	5.206×10^{-2}	4.436×10^{-2}
1.8	0.3	16	16.9628	-8.402×10^{-2}	-6.671×10^{-2}	-2.461×10^{-1}	-1.998×10^{-1}	9.857×10^{-2}	8.445×10^{-2}
1.8	0.3	24	25.1601	-1.075×10^{-1}	-7.030×10^{-2}	-3.026×10^{-1}	-2.056×10^{-1}	1.353×10^{-1}	1.169×10^{-1}
1.8	0.3	32	33.1047	-1.404×10^{-1}	-8.153×10^{-2}	-3.762×10^{-1}	-2.255×10^{-1}	1.600×10^{-1}	1.394×10^{-1}
1.9	0.3	0	0	-5.669×10^{-2}	-5.690×10^{-2}	-1.829×10^{-1}	-1.832×10^{-1}	0	0
1.9	0.3	8	8.5010	-6.010×10^{-2}	-5.683×10^{-2}	-1.922×10^{-1}	-1.824×10^{-1}	3.823×10^{-2}	3.229×10^{-2}
1.9	0.3	16	16.8911	-7.025×10^{-2}	-5.818×10^{-2}	-2.189×10^{-1}	-1.844×10^{-1}	7.263×10^{-2}	6.165×10^{-2}
1.9	0.3	24	25.0887	-8.701×10^{-2}	-6.054×10^{-2}	-2.609×10^{-1}	-1.874×10^{-1}	1.003×10^{-1}	8.579×10^{-2}
1.9	0.3	32	33.0624	-1.106×10^{-1}	-6.912×10^{-2}	-3.157×10^{-1}	-2.034×10^{-1}	1.195×10^{-1}	1.032×10^{-1}
2.0	0.3	0	0	-4.953×10^{-2}	-4.946×10^{-2}	-1.683×10^{-1}	-1.683×10^{-1}	0	0
2.0	0.3	8	8.4616	-5.199×10^{-2}	-4.970×10^{-2}	-1.753×10^{-1}	-1.685×10^{-1}	2.862×10^{-2}	2.395×10^{-2}
2.0	0.3	16	16.8262	-5.932×10^{-2}	-5.079×10^{-2}	-1.954×10^{-1}	-1.699×10^{-1}	5.452×10^{-2}	4.585×10^{-2}
2.0	0.3	24	25.0215	-7.150×10^{-2}	-5.328×10^{-2}	-2.269×10^{-1}	-1.737×10^{-1}	7.564×10^{-2}	6.411×10^{-2}
2.0	0.3	32	33.0172	-8.878×10^{-2}	-6.003×10^{-2}	-2.682×10^{-1}	-1.864×10^{-1}	9.077×10^{-2}	7.771×10^{-2}

Table 5.3: *As in Table 5.2, but for additional values of the eccentricity e; the Teukolsky-based fluxes for E and L_z have an accuracy of 10^{-3}.*

$\frac{p}{M}$	e	$\theta_{\rm inc}$ (deg.)	ι (deg.)	$\frac{dE}{dt}\times\frac{M^2}{\mu^2}$ (kludge)	$\frac{dE}{dt}\times\frac{M^2}{\mu^2}$ (Teukolsky)	$\frac{dL_z}{dt}\times\frac{M}{\mu^2}$ (kludge)	$\frac{dL_z}{dt}\times\frac{M}{\mu^2}$ (Teukolsky)	$\frac{d\iota}{dt}\times\frac{M}{\mu^2}$ (kludge)	$\frac{d\theta_{\rm inc}}{dt}\times\frac{M}{\mu^2}$ (kludge)
1.6	0.4	0	0	-7.766×10^{-2}	-7.772×10^{-2}	-1.918×10^{-1}	-1.919×10^{-1}	0	0
1.6	0.4	8	8.5863	-9.433×10^{-2}	-7.645×10^{-2}	-2.297×10^{-1}	-1.881×10^{-1}	1.528×10^{-1}	1.370×10^{-1}
1.6	0.4	16	17.0151	-1.432×10^{-1}	-7.651×10^{-2}	-3.382×10^{-1}	-1.837×10^{-1}	2.873×10^{-1}	2.584×10^{-1}
1.7	0.4	0	0	-7.882×10^{-2}	-7.953×10^{-2}	-2.097×10^{-1}	-2.115×10^{-1}	0	0
1.7	0.4	8	8.5426	-9.002×10^{-2}	-7.408×10^{-2}	-2.367×10^{-1}	-1.978×10^{-1}	1.087×10^{-1}	9.656×10^{-2}
1.7	0.4	16	16.9502	-1.229×10^{-1}	-7.682×10^{-2}	-3.143×10^{-1}	-2.025×10^{-1}	2.054×10^{-1}	1.830×10^{-1}
1.7	0.4	24	25.1282	-1.760×10^{-1}	-8.090×10^{-2}	-4.336×10^{-1}	-2.075×10^{-1}	2.809×10^{-1}	2.514×10^{-1}
1.8	0.4	0	0	-7.107×10^{-2}	-7.007×10^{-2}	-2.013×10^{-1}	-1.988×10^{-1}	0	0
1.8	0.4	8	8.4989	-7.877×10^{-2}	-7.001×10^{-2}	-2.209×10^{-1}	-1.981×10^{-1}	7.788×10^{-2}	6.879×10^{-2}
1.8	0.4	16	16.8817	-1.015×10^{-1}	-7.009×10^{-2}	-2.774×10^{-1}	-1.965×10^{-1}	1.478×10^{-1}	1.309×10^{-1}
1.8	0.4	24	25.0646	-1.383×10^{-1}	-7.314×10^{-2}	-3.646×10^{-1}	-2.003×10^{-1}	2.036×10^{-1}	1.810×10^{-1}
1.8	0.4	32	33.0184	-1.887×10^{-1}	-9.193×10^{-2}	-4.755×10^{-1}	-2.319×10^{-1}	2.414×10^{-1}	2.156×10^{-1}
1.9	0.4	0	0	-6.187×10^{-2}	-6.267×10^{-2}	-1.861×10^{-1}	-1.881×10^{-1}	0	0
1.9	0.4	8	8.4591	-6.728×10^{-2}	-6.216×10^{-2}	-2.006×10^{-1}	-1.861×10^{-1}	5.666×10^{-2}	4.980×10^{-2}
1.9	0.4	16	16.8173	-8.328×10^{-2}	-6.222×10^{-2}	-2.424×10^{-1}	-1.844×10^{-1}	1.079×10^{-1}	9.506×10^{-2}
1.9	0.4	24	25.0006	-1.094×10^{-1}	-6.486×10^{-2}	-3.071×10^{-1}	-1.878×10^{-1}	1.495×10^{-1}	1.322×10^{-1}
1.9	0.4	32	32.9804	-1.452×10^{-1}	-7.884×10^{-2}	-3.896×10^{-1}	-2.158×10^{-1}	1.787×10^{-1}	1.588×10^{-1}
2.0	0.4	0	0	-5.483×10^{-2}	-5.457×10^{-2}	-1.735×10^{-1}	-1.729×10^{-1}	0	0
2.0	0.4	8	8.4235	-5.871×10^{-2}	-5.445×10^{-2}	-1.844×10^{-1}	-1.720×10^{-1}	4.222×10^{-2}	3.686×10^{-2}
2.0	0.4	16	16.7586	-7.020×10^{-2}	-5.555×10^{-2}	-2.158×10^{-1}	-1.733×10^{-1}	8.064×10^{-2}	7.057×10^{-2}
2.0	0.4	24	24.9396	-8.902×10^{-2}	-5.844×10^{-2}	-2.645×10^{-1}	-1.778×10^{-1}	1.122×10^{-1}	9.860×10^{-2}
2.0	0.4	32	32.9389	-1.150×10^{-1}	-6.536×10^{-2}	-3.267×10^{-1}	-1.896×10^{-1}	1.351×10^{-1}	1.193×10^{-1}
1.7	0.5	0	0	-7.421×10^{-2}	-7.401×10^{-2}	-1.815×10^{-1}	-1.810×10^{-1}	0	0
1.7	0.5	8	8.4736	-8.957×10^{-2}	-7.168×10^{-2}	-2.173×10^{-1}	-1.750×10^{-1}	1.379×10^{-1}	1.256×10^{-1}
1.7	0.5	16	16.8300	-1.347×10^{-1}	-6.999×10^{-2}	-3.201×10^{-1}	-1.676×10^{-1}	2.611×10^{-1}	2.378×10^{-1}
1.8	0.5	0	0	-7.589×10^{-2}	-7.620×10^{-2}	-1.993×10^{-1}	-2.000×10^{-1}	0	0
1.8	0.5	8	8.4395	-8.644×10^{-2}	-6.929×10^{-2}	-2.254×10^{-1}	-1.829×10^{-1}	1.005×10^{-1}	9.076×10^{-2}
1.8	0.5	16	16.7776	-1.175×10^{-1}	-7.210×10^{-2}	-3.004×10^{-1}	-1.880×10^{-1}	1.911×10^{-1}	1.726×10^{-1}
1.8	0.5	24	24.9413	-1.678×10^{-1}	-7.395×10^{-2}	-4.158×10^{-1}	-1.881×10^{-1}	2.638×10^{-1}	2.385×10^{-1}
1.9	0.5	0	0	-6.646×10^{-2}	-6.620×10^{-2}	-1.855×10^{-1}	-1.849×10^{-1}	0	0
1.9	0.5	8	8.4059	-7.386×10^{-2}	-6.320×10^{-2}	-2.048×10^{-1}	-1.768×10^{-1}	7.312×10^{-2}	6.579×10^{-2}
1.9	0.5	16	16.7233	-9.572×10^{-2}	-6.551×10^{-2}	-2.603×10^{-1}	-1.809×10^{-1}	1.395×10^{-1}	1.255×10^{-1}
1.9	0.5	24	24.8877	-1.312×10^{-1}	-7.087×10^{-2}	-3.461×10^{-1}	-1.909×10^{-1}	1.937×10^{-1}	1.744×10^{-1}
1.9	0.5	32	32.8741	-1.795×10^{-1}	-8.247×10^{-2}	-4.544×10^{-1}	-2.091×10^{-1}	2.320×10^{-1}	2.092×10^{-1}
2.0	0.5	0	0	-5.987×10^{-2}	-5.995×10^{-2}	-1.761×10^{-1}	-1.763×10^{-1}	0	0
2.0	0.5	8	8.3750	-6.516×10^{-2}	-5.918×10^{-2}	-1.906×10^{-1}	-1.738×10^{-1}	5.456×10^{-2}	4.882×10^{-2}
2.0	0.5	16	16.6725	-8.081×10^{-2}	-5.817×10^{-2}	-2.324×10^{-1}	-1.694×10^{-1}	1.044×10^{-1}	9.343×10^{-2}
2.0	0.5	24	24.8347	-1.063×10^{-1}	-6.254×10^{-2}	-2.970×10^{-1}	-1.776×10^{-1}	1.456×10^{-1}	1.304×10^{-1}
2.0	0.5	32	32.8378	-1.412×10^{-1}	-6.993×10^{-2}	-3.787×10^{-1}	-1.893×10^{-1}	1.756×10^{-1}	1.576×10^{-1}

Table 5.4: *As in Tables 5.2 and 5.3, but for different values of the eccentricity e; the Teukolsky-based fluxes for E and L_z have an accuracy of 10^{-3}.*

e	$\theta_{\rm inc}$ (deg.)	ι (deg.)	$\Delta t/M$	$\Delta\theta_{\rm inc}$ (deg.)	$\Delta\iota$ (deg.)
0	0	0	1.250×10^{6}	0	0
0	5	5.355510	1.217×10^{6}	1.949×10^{-1}	4.954×10^{-1}
0	10	10.679331	1.118×10^{6}	3.468×10^{-1}	8.631×10^{-1}
0	15	15.943192	9.574×10^{5}	4.236×10^{-1}	1.019
0	20	21.125167	7.446×10^{5}	4.109×10^{-1}	9.440×10^{-1}
0	25	26.211779	4.981×10^{5}	3.158×10^{-1}	6.860×10^{-1}
0	30	31.199048	2.528×10^{5}	1.732×10^{-1}	3.527×10^{-1}
0	35	36.092514	6.584×10^{4}	4.636×10^{-2}	8.806×10^{-2}
0.1	0	0	1.228×10^{6}	0	0
0.1	5	5.351602	1.198×10^{6}	4.517×10^{-1}	7.766×10^{-1}
0.1	10	10.671900	1.103×10^{6}	6.900×10^{-1}	1.236
0.1	15	15.932962	9.426×10^{5}	7.283×10^{-1}	1.344
0.1	20	21.113129	7.315×10^{5}	6.433×10^{-1}	1.187
0.1	25	26.199088	4.900×10^{5}	4.780×10^{-1}	8.547×10^{-1}
0.1	30	31.186915	2.513×10^{5}	2.730×10^{-1}	4.585×10^{-1}
0.1	35	36.082095	6.589×10^{4}	8.385×10^{-2}	1.279×10^{-1}
0.2	0	0	1.173×10^{6}	0	0
0.2	5	5.339916	1.150×10^{6}	1.204	1.598
0.2	10	10.649670	1.064×10^{6}	1.698	2.331
0.2	15	15.902348	9.043×10^{5}	1.618	2.293
0.2	20	21.077081	6.980×10^{5}	1.324	1.900
0.2	25	26.161046	4.693×10^{5}	9.545×10^{-1}	1.351
0.2	30	31.150481	2.486×10^{5}	5.674×10^{-1}	7.711×10^{-1}
0.2	35	36.050712	7.562×10^{4}	2.070×10^{-1}	2.648×10^{-1}
0.3	0	0	1.087×10^{6}	0	0
0.3	5	5.320559	1.069×10^{6}	2.307	2.788
0.3	10	10.612831	1.001×10^{6}	3.256	4.007
0.3	15	15.851572	8.454×10^{5}	2.984	3.741
0.3	20	21.017212	6.483×10^{5}	2.375	2.998
0.3	25	26.097732	4.408×10^{5}	1.700	2.129
0.3	30	31.089639	2.493×10^{5}	1.040	1.276
0.3	35	35.997987	1.108×10^{5}	4.626×10^{-1}	5.569×10^{-1}

Table 5.5: *Variation in the inclination angles ι and $\theta_{\rm inc}$, as well as the time needed to reach the separatrix, for several inspirals through the nearly horizon-skimming regime. In all of these cases, the mass ratio of the binary was fixed at $\mu/M = 10^{-6}$, the spin of the large black hole was fixed at $a = 0.998M$, and the orbits were begun at $p = 1.9M$. The time interval Δt is the total accumulated time taken for the inspiralling body to reach the separatrix (at which time it rapidly plunges into the black hole). The angles $\Delta\theta_{\rm inc}$ and $\Delta\iota$ are the total integrated change in these inclination angles that we compute. For the $e = 0$ cases, inspirals are computed using fits to the circular-Teukolsky fluxes of E and L_z; for eccentric orbits we use the kludge fluxes* (5.40), (5.43) *and* (5.44). *Notice that $\Delta\theta_{\rm inc}$ and $\Delta\iota$ are always positive — the inclination angle always increases during the inspiral through the nearly horizon-skimming region. The magnitude of this increase never exceeds a few degrees.*

Chapter 6

The final spin from the coalescence of two black holes

> L'essere eruditi e preparati ha avuto una sua necessità... rispetto al passato ci sono degli approcci sicuramente più veritieri di tante fantasie.
>
> G. Trapattoni

As we have mentioned in sec. 1.4, LISA will detect the gravitational waves emitted by EMRIs and by SMBH binaries and mergers, and will allow one to measure with high accuracy ($10^{-2} - 10^{-4}$) the masses and spins of SMBHs. Because there is now a broad consensus that galaxies form hierarchically [28], when two galaxies have merged, the SMBHs that they host are expected to form binary systems and eventually coalesce (*cf.* sec. 1.4.2). Mergers are therefore key events in the evolution of the masses and spins of the SMBH population, although a significant contribution to this evolution also comes from accretion onto the individual SMBHs (*cf.* ref. [33]). Because LISA will be able to measure the SMBH mass and spin distribution function up to high redshifts (even $z \sim 10$ and beyond, if SMBHs are already present then), it is of great importance to understand how the spin of an SMBH which originates from a binary merger is related to the masses and spins of the two progenitors. In this chapter we derive a formula which gives the spin of the black hole produced by the coalescence of two black holes following a quasi-circular inspiral. A comparison with simulations shows very accurate agreements with all of the numerical relativity data available to date, but we also suggest a number of ways in which our predictions can be further improved [167]. Our formula can be readily used to study the cosmological evolution of the SMBH spin distribution function [168, 169].

6.1 Motivation

To appreciate the spirit of our approach it can be convenient to think of the inspiral and merger of two black holes as a mechanism which takes, as input, two black holes of initial masses M_1, M_2 and spin vectors $\boldsymbol{S}_1$, $\boldsymbol{S}_2$ and produces, as output, a third black hole of mass $M_{\rm fin}$ and spin $\boldsymbol{S}_{\rm fin}$. In conditions of particular astrophysical interest, the inspiral takes place through quasi-circular orbits since the eccentricity is removed quickly by gravitational-radiation reaction [22]. Moreover, at least for nonspinning equal-mass black holes, the final spin does not depend on the value of the eccentricity as long as it is not too large [170]. The determination of $M_{\rm fin}$ and $\boldsymbol{S}_{\rm fin}$ from the knowledge of $M_{1,2}$ and $\boldsymbol{S}_{1,2}$, is of importance in several fields. In stellar astrophysics, it provides information about the properties of isolated stellar-mass black holes produced as a result of the merger of a black-hole binary at the end of the evolution of a binary system of massive stars. In cosmology, it can be used to model the distribution of masses and spins of the supermassive black holes produced through the merger of galaxies. A-priori knowledge of the final spin can help the detection of the gravitational waves from the ringdown after a binary black-hole merger. What makes this a difficult problem is clear: for binaries in quasi-circular orbits the space of initial parameters for the final spin has seven dimensions (*i.e.*, the mass-ratio $q \equiv M_2/M_1$ and the six components of the spin vectors). A number of analytical approaches have been developed over the years to determine the final spin, either exploiting the dynamics of point-particles [171, 172] or using more sophisticated approaches such as the effective-one-body approximation [173]. Ultimately, however, computing $\boldsymbol{a}_{\rm fin} \equiv \boldsymbol{S}_{\rm fin}/M_{\rm fin}^2$ accurately requires the solution of the full Einstein equations and thus the use of numerical-relativity simulations. Several groups have investigated this problem over the last few years [174, 175, 176, 177, 178, 179].

While the recent possibility of obtaining accurately the final spin through numerical-relativity calculations represents an important progress, the complete coverage of the full parameter space just through simulations is not a viable option. As a consequence, work has been done to derive analytic expressions for the final spin which would model the numerical-relativity data but also exploit as much information as possible either from perturbative studies, or from the symmetries of the system [175, 177, 178, 179, 180, 181]. In this sense, these approaches do not amount to a blind fitting of the numerical-relativity data, but, rather, use the data to construct a physically consistent and mathematically accurate modelling of the final spin. Despite a concentrated effort in this direction, the analytic expressions for the final spin could, at most, cover 3 of the 7 dimensions of the parameter space [179]. Here, we show that without additional fits and with a minimal set of assumptions it is possible to obtain an extension to the complete parameter space and reproduce all of the available numerical-relativity data. Our treatment is intrinsically approximate, but we suggest how it can be further improved.

6.2 The formula for the final spin

Analytic fitting expressions for $\boldsymbol{a}_{\rm fin}$ have so far been built using binaries having spins that are either *aligned* or *antialigned* with the initial orbital angular momentum. This is because in this case both the initial and final spins can be projected in the direction of the orbital angular momentum and it is possible to deal simply with the (pseudo)-scalar quantities a_1, a_2 and $a_{\rm fin}$ ranging between -1 and $+1$. If the black holes have *equal mass* but *unequal* spins that are either *parallel* or *antiparallel*, then the spin of the final black hole has been shown to be accurately described by the simple analytic fit [177]

$$a_{\rm fin}(a_1,a_2) = p_0 + p_1(a_1+a_2) + p_2(a_1+a_2)^2\,. \tag{6.1}$$

When seen as a power series in the initial spins, expression (6.1) suggests an interesting physical interpretation. Its zeroth-order term can be associated with the (dimensionless) orbital angular momentum not radiated in gravitational waves and amounting to $\sim 70\%$ of the final spin at most. The first-order term, on the other hand, can be seen as the contribution from the initial spins and from the spin-orbit coupling, amounting to $\sim 30\%$ at most. Finally, the second-order term, includes the spin-spin coupling, with a contribution to the final spin which is of $\sim 4\%$ at most.

If the black holes have *unequal mass* but spins that are *equal* and *parallel*, the final spin is instead given by the analytic fit [179]

$$a_{\rm fin}(a,\nu) = a + s_4 a^2\nu + s_5 a\nu^2 + t_0 a\nu + 2\sqrt{3}\nu + t_2\nu^2 + t_3\nu^3\,, \tag{6.2}$$

where ν is the symmetric mass ratio $\nu \equiv M_1M_2/(M_1+M_2)^2$. Although obtained independently in [177] and [179], expressions (6.1) and (6.2) are compatible as can be seen by considering (6.2) for equal-mass binaries ($\nu = 1/4$) and verifying that the following relations hold within the computed error-bars

$$p_0 = \frac{\sqrt{3}}{2} + \frac{t_2}{16} + \frac{t_3}{64}\,, \qquad p_1 = \frac{1}{2} + \frac{s_5}{32} + \frac{t_0}{8}\,, \qquad p_2 = \frac{s_4}{16}. \tag{6.3}$$

As long as the initial spins are aligned (or antialigned) with the orbital angular momentum, expression (6.2) can be extended to *unequal-spin, unequal-mass* binaries through the substitution

$$a \;\rightarrow\; \frac{a_1 + a_2 q^2}{1+q^2}\,. \tag{6.4}$$

To obtain this result, it is sufficient to consider (6.1) and (6.2) as polynomial expressions in the generic quantity

$$\tilde{a} \equiv a_{\rm tot}\frac{(1+q)^2}{1+q^2}\,. \tag{6.5}$$

where $a_{\rm tot} \equiv (a_1 + a_2q^2)/(1+q)^2$ is the total dimensionless spin for generic aligned binaries. In this way, expressions (6.1) and (6.2) are naturally compatible, since $\tilde{a} =$

$(a_1 + a_2)/2$ for equal-mass unequal-spin binaries, and $\tilde{a} = a$ for unequal-mass equal-spin binaries. Furthermore, the extreme mass-ratio limit (EMRL) of expression (6.2) with the substitution (6.4) yields the expected result: $a_{\rm fin}(a_1, a_2, \nu = 0) = a_1$.

As already commented above, the predictions of expressions (6.2) and (6.4) cover 3 of the 7 dimensions of the parameter space for binaries in quasi-circular orbits; we next show how to to cover the remaining 4 dimensions and derive an analytic expression for the dimensionless spin vector $\boldsymbol{a}_{\rm fin}$ of the black hole produced by the coalescence of two generic black holes in terms of the mass ratio q and of the initial dimensionless spin vectors $\boldsymbol{a}_{1,2}$. To make the problem tractable analytically, four assumptions are needed. While some of these are very natural, others can be relaxed if additional accuracy in the estimate of $\boldsymbol{a}_{\rm fin}$ is necessary. It should be noted, however, that removing any of these assumptions inevitably complicates the picture, introducing additional dimensions in the parameter space, such as the initial separation of the binary or the radiated mass.

As a result, in the simplest and yet accurate description the required assumptions are as follows:

(i) The mass radiated in gravitational waves $M_{\rm rad}$ can be neglected i.e., $M_{\rm fin} = M \equiv M_1 + M_2$. We note that $M_{\rm rad}/M = 1 - M_{\rm fin}/M \approx 5 - 7 \times 10^{-2}$ for most of the binaries evolved numerically. The same assumption was applied in the analyses of [177, 179], as well as in [172]. Relaxing this assumption would introduce a dependence on $M_{\rm fin}$ which can only be measured through a numerical simulation.

(ii) At a sufficiently large but finite initial separation the final spin vector $\boldsymbol{S}_{\rm fin}$ can be well approximated as the sum of the two initial spin vectors and of a third vector $\tilde{\boldsymbol{\ell}}$

$$\boldsymbol{S}_{\rm fin} = \boldsymbol{S}_1 + \boldsymbol{S}_2 + \tilde{\boldsymbol{\ell}}\,, \tag{6.6}$$

Differently from refs. [171] and [172], where a definition similar to (6.6) was also introduced, here we will constrain $\tilde{\boldsymbol{\ell}}$ by exploiting the results of numerical-relativity calculations rather than by relating it to the orbital angular momentum of a test particle at the innermost stable circular orbit (ISCO). When viewed as expressing the conservation of the total angular momentum, eq. (6.6) defines the vector $\tilde{\boldsymbol{\ell}}$ as the difference between the orbital angular momentum when the binary is widely separated $\boldsymbol{L}$, and the angular momentum radiated up to the merger $\boldsymbol{J}_{\rm rad}$, *i.e.*, $\tilde{\boldsymbol{\ell}} = \boldsymbol{L} - \boldsymbol{J}_{\rm rad}$.

(iii) The vector $\tilde{\boldsymbol{\ell}}$ is parallel to $\boldsymbol{L}$. This assumption is correct when $\boldsymbol{S}_1 = -\boldsymbol{S}_2$ and $q = 1$ [this can be seen from the post-Newtonian (PN) equations at 2.5 order], and by equatorial symmetry when the spins are aligned with $\boldsymbol{L}$ or when $\boldsymbol{S}_1 = \boldsymbol{S}_2 = 0$ (also these cases can be seen from the PN equations). For more general configurations one expects that $\tilde{\boldsymbol{\ell}}$ will also have a component orthogonal to $\boldsymbol{L}$ as a result, for instance, of spin-orbit or spin-spin couplings, which will produce in general a precession of $\tilde{\boldsymbol{\ell}}$. In practice, the component of $\tilde{\boldsymbol{\ell}}$ orthogonal to $\boldsymbol{L}$ will correspond to the angular momentum $\boldsymbol{J}^{\perp}_{\rm rad}$ radiated in a plane orthogonal to $\boldsymbol{L}$, with a resulting error in the estimate of $|\tilde{\boldsymbol{\ell}}|$ which is $\sim |\boldsymbol{J}^{\perp}_{\rm rad}|^2/|\tilde{\boldsymbol{\ell}}|^2 \sim |\boldsymbol{J}^{\perp}_{\rm rad}|^2/(2\sqrt{3}M_1M_2)^2$.[1] Although these errors are small in all the config-

[1] Assumption *(iii)* can be equivalently interpreted as enforcing that the component of the final spin $\boldsymbol{S}_{\rm fin}$ in

urations that we have analysed, they may be larger in general configurations. Measuring $\boldsymbol{J}^{\perp}_{\rm rad}$ via numerical-relativity simulations, or estimating it via high-order PN equations, is an obvious way to improve our approach. A similar assumption was also made in ref. [172].

(iv) When the initial spin vectors are equal and opposite ($\boldsymbol{S}_1 = -\boldsymbol{S}_2$) and the masses are equal ($q = 1$), the spin of the final black hole is the same as for nonspinning binaries. Stated differently, equal-mass binaries with equal and opposite spins behave like nonspinning binaries, at least concerning the properties of the final black hole. While this result cannot be derived from first principles, it reflects the expectation that if the spins are the same and opposite, their contributions to the final spin cancel exactly for equal-mass binaries. Besides being physically reasonable, this expectation is met by all of the simulations performed to date, both for spins aligned with $\boldsymbol{L}$ [177, 179] and orthogonal to $\boldsymbol{L}$ [176]. In addition, this expectation is met by the leading-order contributions to the spin-orbit and spin-spin point-particle Hamiltonians and spin-induced radiation flux [182, 173]. A similar assumption is also made, although not explicitly, in ref. [172] which, for $\boldsymbol{S}_{\rm tot} = 0$, predicts $\iota = 0$ and $|\boldsymbol{a}_{\rm fin}| = L_{\rm orb}(\iota = 0, |\boldsymbol{a}_{\rm fin}|)/M = \text{const}$. [*cf.* eqs. (12)–(13) in ref. [172]].

Using these assumptions we can now derive an analytic expression for the final spin. We start by expressing the vector relation (6.6) as

$$\boldsymbol{a}_{\rm fin} = \frac{1}{(1+q)^2}\left(\boldsymbol{a}_1 + \boldsymbol{a}_2 q^2 + \boldsymbol{\ell} q\right) , \tag{6.7}$$

where $\boldsymbol{a}_{\rm fin} = \boldsymbol{S}_{\rm fin}/M^2$ [*cf.* assumption *(i)*], $\boldsymbol{\ell} \equiv \tilde{\boldsymbol{\ell}}/(M_1 M_2)$, $\boldsymbol{a}_{1,2} \equiv \boldsymbol{S}_{1,2}/M^2_{1,2}$, and its norm is then given by

$$\begin{aligned} |\boldsymbol{a}_{\rm fin}| = \frac{1}{(1+q)^2}\Big[&|\boldsymbol{a}_1|^2 + |\boldsymbol{a}_2|^2 q^4 + 2|\boldsymbol{a}_2||\boldsymbol{a}_1| q^2 \cos\alpha + \\ &2\left(|\boldsymbol{a}_1|\cos\beta + |\boldsymbol{a}_2| q^2 \cos\gamma\right)|\boldsymbol{\ell}| q + |\boldsymbol{\ell}|^2 q^2\Big]^{1/2} , \end{aligned} \tag{6.8}$$

where the three (cosine) angles α, β and γ are defined by

$$\cos\alpha \equiv \hat{\boldsymbol{a}}_1 \cdot \hat{\boldsymbol{a}}_2 , \quad \cos\beta \equiv \hat{\boldsymbol{a}}_1 \cdot \hat{\boldsymbol{\ell}} , \quad \cos\gamma \equiv \hat{\boldsymbol{a}}_2 \cdot \hat{\boldsymbol{\ell}} . \tag{6.9}$$

Because $\boldsymbol{a}_1$ and $\boldsymbol{S}_1$, $\boldsymbol{a}_2$ and $\boldsymbol{S}_2$, and $\boldsymbol{\ell}$ and $\boldsymbol{L}$ are parallel [*cf.* assumption *(iii)*], the angles α, β and γ are also those between the initial spin vectors and the initial orbital angular momentum, so that it is possible to replace $\hat{\boldsymbol{a}}_{1,2}$ with $\hat{\boldsymbol{S}}_{1,2}$ and $\hat{\boldsymbol{\ell}}$ with $\hat{\boldsymbol{L}}$ in (6.9). Note that α, β and γ are well-defined if the initial separation of the two black holes is sufficiently large [*cf.* assumption *(ii)*] and that the error introduced by assumption *(iii)* in the measure of $\cos\alpha, \cos\beta$ and $\cos\gamma$ is also of the order of $|\boldsymbol{J}^{\perp}_{\rm rad}|/|\tilde{\boldsymbol{\ell}}|$.

The angle $\theta_{\rm fin}$ between the final spin vector and the initial orbital angular momentum can be easily calculated from $|\boldsymbol{a}_{\rm fin}|$. Because of assumption *(iii)*, the component of the

the orbital plane equals that of the total initial spin $\boldsymbol{S}_1 + \boldsymbol{S}_2$ in that plane.

final spin in the direction of $\boldsymbol{L}$ is [*cf.* eq. (6.7)]

$$a_{\rm fin}^{\parallel} \equiv \boldsymbol{a}_{\rm fin}\cdot\hat{\boldsymbol{\ell}} = \frac{|\boldsymbol{a}_1|\cos\beta + |\boldsymbol{a}_2|q^2\cos\gamma + |\boldsymbol{\ell}|q}{(1+q)^2}\,, \tag{6.10}$$

so that $\cos\theta_{\rm fin} = a_{\rm fin}^{\parallel}/|\boldsymbol{a}_{\rm fin}|$, and the component orthogonal to the initial orbital angular momentum is $a_{\rm fin}^{\perp} = |\boldsymbol{a}_{\rm fin}|\sin\theta_{\rm fin}$.

In essence, therefore, our approach consists of considering the dimensionless spin vector of the final black hole as the sum of the two initial spins and of a third vector parallel to the orbital angular momentum when the binaries were widely separated. Implicit in the assumptions made, and in the logic of mapping an initial-state of the binary into a final one, is the expectation that the length of this vector is an intrinsic "property" of the binary, depending on the initial spin vectors and mass ratio, but not on the initial separation. This is indeed a consequence of assumption *(ii)*: because the vector $\tilde{\boldsymbol{\ell}}$ measures the orbital angular momentum that cannot be radiated, it can be thought of as the angular momentum of the binary at the "effective" ISCO and, as such, it cannot be dependent on the initial separation.

An important consequence of our assumptions is that $\boldsymbol{a}_{\rm fin}$ for a black-hole binary is already fully determined by the set of coefficients s_4, s_5, t_0, t_2, t_3 computed to derive expression (6.2). The latter, in fact, is simply the final spin for a special set of values for the cosine angles; since the fitting coefficients are constant, they must hold also for generic binaries.

In view of this, all that is needed is to measure $|\boldsymbol{\ell}|$ in terms of the fitting coefficients computed in refs. [177, 179]. This can be done by matching expression (6.10) with (6.2) [with the condition (6.4)] for parallel and aligned spins ($\alpha=\beta=\gamma=0$), for parallel and antialigned spins ($\alpha=0$, $\beta=\gamma=\pi$), and for antiparallel spins which are aligned or antialigned ($\alpha=\beta=\pi$, $\gamma=0$ or $\alpha=\gamma=\pi$, $\beta=0$). This matching is not unique, but the degeneracy can be broken by exploiting assumption *(iv)* and by requiring that $|\boldsymbol{\ell}|$ depends linearly on $\cos\alpha$, $\cos\beta$ and $\cos\gamma$. We then obtain

$$\begin{aligned}|\boldsymbol{\ell}| = {}& \frac{s_4}{(1+q^2)^2}\left(|\boldsymbol{a}_1|^2 + |\boldsymbol{a}_2|^2q^4 + 2|\boldsymbol{a}_1||\boldsymbol{a}_2|q^2\cos\alpha\right) + \\ & \left(\frac{s_5\nu + t_0 + 2}{1+q^2}\right)\left(|\boldsymbol{a}_1|\cos\beta + |\boldsymbol{a}_2|q^2\cos\gamma\right) + 2\sqrt{3} + t_2\nu + t_3\nu^2\,. \end{aligned}\tag{6.11}$$

We now consider some limits of expressions (6.8) and (6.11). First of all, when $q\to 0$, (6.8) and (6.11) yield the correct EMRL, *i.e.*, $|\boldsymbol{a}_{\rm fin}| = |\boldsymbol{a}_1|$. Secondly, for equal-mass binaries having spins that are equal and antiparallel, (6.8) and (6.11) reduce to

$$|\boldsymbol{a}_{\rm fin}| = \frac{|\boldsymbol{\ell}|}{4} = \frac{\sqrt{3}}{2} + \frac{t_2}{16} + \frac{t_3}{64} = p_0 \simeq 0.688\,. \tag{6.12}$$

This result allows us now to qualify more precisely a comment made before: because for equal-mass black holes which are either nonspinning or have equal and opposite spins,

a_1^x	a_1^y	a_1^z	a_2^x	a_2^y	a_2^z	ν	$\lvert\boldsymbol{a}_{\rm fin}\rvert$	$\theta_{\rm fin}(^\circ)$
0.151	0.000	-0.563	0.000	0.000	0.583	0.250	0.692	2.29
0.151	0.000	0.564	0.000	0.151	0.564	0.250	0.846	3.97
0.413	0.000	0.413	0.000	0.413	0.413	0.250	0.815	7.86

Table 6.1: *Initial parameters of the new misaligned AEI binaries.*

the vector $|\boldsymbol{\ell}|$ does not depend on the initial spins, expression (6.12) states that $|\boldsymbol{\ell}|M_{\rm fin}^2/4 = |\boldsymbol{\ell}|M^2/4 = |\boldsymbol{\ell}|M_1M_2$ is, for such systems, the orbital angular momentum at the effective ISCO. We can take this a step further and conjecture that $|\boldsymbol{\ell}|M_1M_2 = |\tilde{\boldsymbol{\ell}}|$ is the series expansion of the dimensionless orbital angular momentum at the ISCO also for *unequal-mass* binaries which are either nonspinning or have equal and opposite spins. The zeroth-order term of this series (namely, the term $2\sqrt{3}M_1M_2$) is exactly the one predicted from the EMRL. We note that although numerical simulations do not reveal the presence of an ISCO, the concept of an effective ISCO can nevertheless be useful for the construction of gravitational-wave templates [27, 184].

Finally, we consider the case of equal, parallel and aligned/antialigned spins ($|\boldsymbol{a}_2| = |\boldsymbol{a}_1|$, $\alpha = 0$, $\beta = \gamma = 0,\ \pi$), for which expressions (6.10) and (6.11) become

$$\begin{aligned} a_{\rm fin} &= |\boldsymbol{a}_1|\cos\beta\,[1+\nu(s_4|\boldsymbol{a}_1|\cos\beta + t_0 + s_5\nu)] + \\ &\qquad \nu(2\sqrt{3} + t_2\nu + t_3\nu^2)\,, \end{aligned} \tag{6.13}$$

where $\cos\beta = \pm 1$ for aligned/antialigned spins. As expected, expression (6.13) coincides with (6.2) when $|\boldsymbol{a}_1|\cos\beta = a$ and with (6.1) [through the coefficients (6.3)] when $q = 1$ and $2|\boldsymbol{a}_1|\cos\beta = a_1 + a_2$. Similarly, (6.10) and (6.11) reduce to (6.2) for equal, antiparallel and aligned/antialigned spins ($|\boldsymbol{a}_2| = |\boldsymbol{a}_1|$, $\alpha = 0$, $\beta = 0, \gamma = \pi$, or $\beta = \pi, \gamma = 0$).

The only way to assess the validity of expressions (6.8) and (6.11) is to compare their predictions with the numerical-relativity data. This is done in Figs. 6.1 and 6.2, which collect all of the published data, together with the three additional binaries computed with the `CCATIE` code [175] and reported in Table 6.1. In these plots, the "binary order number" is just a dummy index labelling the different configurations. The left panel of Fig. 6.1 shows the rescaled residual, *i.e.*, $(|\boldsymbol{a}_{\rm fin}|_{\rm fit} - |\boldsymbol{a}_{\rm fin}|_{\rm num.}) \times 100$, for aligned binaries. The plot shows the numerical-relativity data with circles referring to equal-mass, equal-spin binaries from refs. [177, 178, 179, 185, 187, 188], triangles to equal-mass, unequal-spin binaries from refs. [177, 188], and squares to unequal-mass, equal-spin binaries from refs. [179, 185, 187, 188]. Although the data is from simulations with different truncation errors, the residuals are all very small and with a scatter of $\sim 1\%$.

A more stringent test is shown in the right panel of Fig. 6.1, which refers to mis-

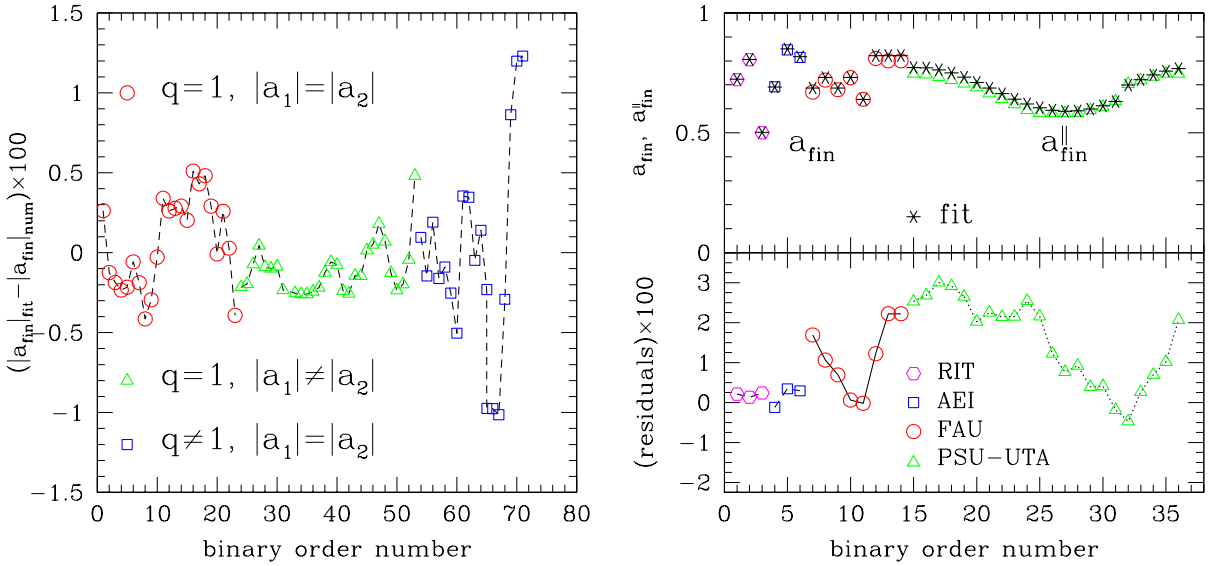

Figure 6.1: **Left panel:** *Rescaled residual for aligned binaries. The circles refer to equal-mass, equal-spin binaries presented in refs. [177, 178, 179, 185, 187, 188], triangles to equal-mass, unequal-spin binaries presented in ref. [177, 188], and squares to unequal-mass, equal-spin binaries presented in refs. [179, 185, 187, 188]. Here and in the right panel the "binary order number" is just a dummy index labelling the different configurations.* **Right panel:** *The top part reports the final spin computed for misaligned binaries. Hexagons refer to data from ref. [174] (labelled "RIT"), squares to the data in Table 6.1 (labelled "AEI"), circles to data from ref. [189] (labelled "FAU"), and triangles to data from ref. [183] (labelled "PSU-UTA"). Note that these latter data points refer to the aligned component $a^{\parallel}_{\rm fin}$ since this is the only component available from ref. [183]. The bottom part of this panel shows instead the rescaled residuals for these misaligned binaries.*

aligned binaries. In the top part, hexagons indicate the numerical values for $|\boldsymbol{a}_{\rm fin}|$ from ref. [174], squares the ones in Table 6.1, circles those from ref. [189] and triangles those from ref. [183]; note that these latter data points refer to the aligned component $a^{\parallel}_{\rm fin}$ since this is the only component available from ref. [183]. The agreement is again very good, with errors of a few percent (see bottom part of the same panel), even if the binaries are generic and for some the initial and final spins differ by almost 180° [174].

Finally, Fig. 6.2 reports the angle between the final spin vector and the initial orbital angular momentum $\theta_{\rm fin}$ using the same data (and convention for the symbols) as in the right panel of Fig. 6.1. Measuring the final angle accurately is not trivial, particularly due to the fact that the numerical evolutions start at a finite separation which does not account for earlier evolution. The values reported in [174] (and the relative error-bars) are shown with hexagons, while the squares refer to the binaries in Table 6.1, and have been computed using a new approach for the calculation of the Ricci scalar on the apparent horizon [186]. Shown with asterisks and circles are instead the values predicted for the numerical data (as taken from refs. [174, 183, 189] and from Table 6.1) by our analytic fit

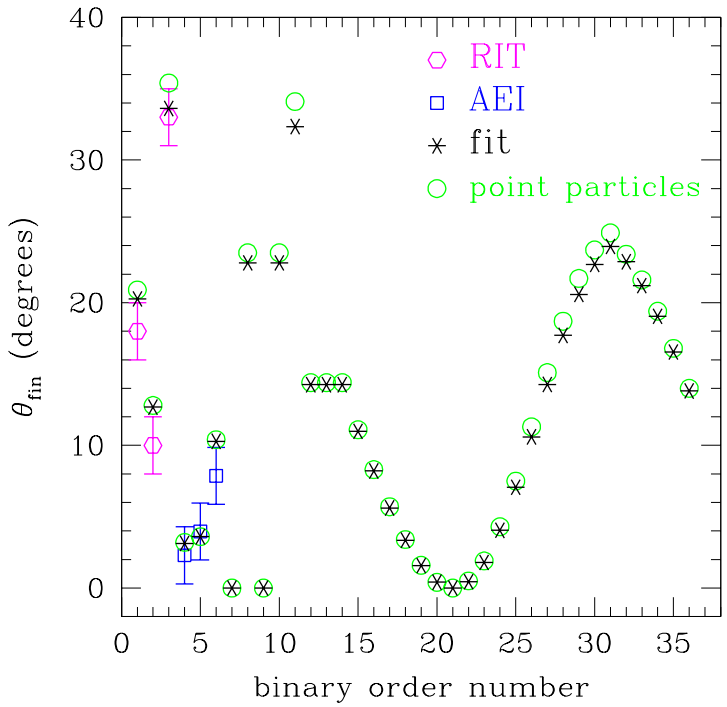

Figure 6.2: *Using the same data (and convention for the symbols) as in the right panel of Fig. 6.1, we here report the angle between the final spin vector and the initial orbital angular momentum $\theta_{\rm fin}$. Shown instead with asterisks and circles are the values predicted for the numerical data (as taken from refs. [174, 183, 189] and from Table 6.1) by our analytic fit (asterisks) and by the point-particle approach suggested in ref. [172] (circles).*

(asterisks) and by the point-particle approach suggested in ref. [172] (circles).

Clearly, when a comparison with numerical data is possible, the estimates of our fit are in reasonable agreement with the data and give residuals for the final angle (*i.e.*, $(\theta_{\rm fin})_{\rm fit} - (\theta_{\rm fin})_{\rm num.}$) which are generally smaller than those obtained with the point-particle approach of ref. [172]. However, for two of the three binaries from ref. [174] the estimates are slightly outside the error-bars. Note that the reported angles are relative to the orbital plane at a small initial binary-separation, and thus are likely to be underestimates as they do not take into account the evolution from asymptotic distances; work is in progress to clarify this. When comparison with the numerical data is not possible because $\theta_{\rm fin}$ is not reported (as for the data in ref. [183]), our approach and the one in ref. [172] yield very similar estimates.

In summary: we have considered the spin vector of the black hole produced by a black-hole binary merger as the sum of the two initial spins and of a third vector, parallel to the initial orbital angular momentum, whose norm depends only on the initial spin vectors

and the mass ratio, and measures the orbital angular momentum not radiated. Without additional fits with respect to those already available to model aligned/antialigned binaries, we have measured the unknown vector and derived a formula that accounts for all of the 7 parameters describing a black-hole binary inspiralling in quasi-circular orbits. The equations (6.8) and (6.11), encapsulate the near-zone physics to provide a convenient, but also robust and accurate determination of the merger product of rather generic black-hole binaries over a wide range of parameters.

Testing the formula against all of the available numerical data has revealed differences between the predicted and simulated values of a few percent at most. Our approach is intrinsically approximate and has been validated only on a small set of configurations, but it can be improved, for instance: by reducing the χ^2 of the fitting coefficients as new simulations are carried out; by using fitting functions that are of higher-order than those in expressions (6.1) and (6.2); by estimating $\boldsymbol{J}^{\perp}_{\rm rad}$ through PN expressions or by measuring it via numerical simulations.

6.3 Appendix: Mathematical and Numerical Setup

The data of the three binaries reported in Table 6.1, as well as those of the aligned binaries of ref. [175], were produced using the CCATIE code, a three-dimensional finite differencing code based on the Cactus Computational Toolkit [190, 191]. The current code is an evolution of previous versions which implemented an excision method and co-rotating coordinates [192, 193, 194]. The main features of the code, in particular the evolution equations, remain the same. However, some modifications have been introduced in the gauge evolution to accommodate "moving punctures" which has proven to be an effective way to evolve black hole spacetimes [195, 196]. This method simply removes any restrictions on movement of the punctures from their initial locations, allowing them to be advected on the grid.

In the following equations, we use Greek indices (running from 0 to 3) to denote components of four-dimensional objects and Latin indices (running from 1 to 3) for three-dimensional ones that are defined on space-like foliations of the space-time.

Evolution system

We evolve a conformal-traceless "$3+1$" formulation of the Einstein equations [192, 197, 198, 199], in which the spacetime is decomposed into three-dimensional spacelike slices, described by the intrinsic metric γ_{ij}, its embedding in the full spacetime, specified by the extrinsic curvature K_{ij}, and the gauge functions α (lapse) and β^i (shift) that specify a coordinate frame (see the next subsection for details on how gauges are treated and ref. [200] for a general description of the $3+1$ split). The metric therefore reads

$$ds^2 = (\gamma_{ij}\beta^i\beta^j - \alpha^2)dt^2 + 2\gamma_{ij}\beta^i dx^j dt + \gamma_{ij}dx^i dx^j \,. \tag{6.14}$$

The particular system which we evolve transforms the standard ADM variables as follows. The 3-metric γ_{ij} is conformally transformed via

$$\phi = \frac{1}{12}\ln\det\gamma_{ij}, \qquad \tilde{\gamma}_{ij} = e^{-4\phi}\gamma_{ij}, \tag{6.15}$$

and the conformal factor ϕ evolved as an independent variable, whereas $\tilde{\gamma}_{ij}$ is subject to the constraint $\det\tilde{\gamma}_{ij} = 1$. The extrinsic curvature is subjected to the same conformal transformation, and its trace $\mathrm{tr}\,K_{ij}$ is evolved as an independent variable. That is, in place of K_{ij} we evolve:

$$K \equiv \mathrm{tr}\,K_{ij} = g^{ij}K_{ij}, \qquad \tilde{A}_{ij} = e^{-4\phi}(K_{ij} - \frac{1}{3}\gamma_{ij}K), \tag{6.16}$$

with $\mathrm{tr}\,\tilde{A}_{ij} = 0$. Finally, new evolution variables

$$\tilde{\Gamma}^i = \tilde{\gamma}^{jk}\tilde{\Gamma}^i_{jk} \tag{6.17}$$

are introduced, defined in terms of the Christoffel symbols of the conformal 3-metric.

The Einstein equations specify a well known set of evolution equations for the listed variables and are given by

$$(\partial_t - \mathcal{L}_\beta)\,\tilde{\gamma}_{ij} = -2\alpha\tilde{A}_{ij}, \tag{6.18}$$

$$(\partial_t - \mathcal{L}_\beta)\,\phi = -\frac{1}{6}\alpha K, \tag{6.19}$$

$$(\partial_t - \mathcal{L}_\beta)\,\tilde{A}_{ij} = e^{-4\phi}[-D_iD_j\alpha + \alpha R_{ij}]^{TF} + \alpha(K\tilde{A}_{ij} - 2\tilde{A}_{ik}\tilde{A}^k{}_j), \tag{6.20}$$

$$(\partial_t - \mathcal{L}_\beta)\,K = -D^iD_i\alpha + \alpha(\tilde{A}_{ij}\tilde{A}^{ij} + \frac{1}{3}K^2), \tag{6.21}$$

$$\begin{aligned}\partial_t\tilde{\Gamma}^i = {}& \tilde{\gamma}^{jk}\partial_j\partial_k\beta^i + \frac{1}{3}\tilde{\gamma}^{ij}\partial_j\partial_k\beta^k + \beta^j\partial_j\tilde{\Gamma}^i - \tilde{\Gamma}^j\partial_j\beta^i + \frac{2}{3}\tilde{\Gamma}^i\partial_j\beta^j \\ & - 2\tilde{A}^{ij}\partial_j\alpha + 2\alpha(\tilde{\Gamma}^i{}_{jk}\tilde{A}^{jk} + 6\tilde{A}^{ij}\partial_j\phi - \frac{2}{3}\tilde{\gamma}^{ij}\partial_j K),\end{aligned} \tag{6.22}$$

where R_{ij} is the three-dimensional Ricci tensor, D_i is the covariant derivative associated with the three metric γ_{ij} and "TF" indicates the trace-free part of tensor objects. The Einstein equations also lead to a set of physical constraint equations that are satisfied within each spacelike slice,

$$\mathcal{H} \equiv R^{(3)} + K^2 - K_{ij}K^{ij} = 0, \tag{6.23}$$

$$\mathcal{M}^i \equiv D_j(K^{ij} - \gamma^{ij}K) = 0, \tag{6.24}$$

which are usually referred to as the Hamiltonian and momentum constraints. Here $R^{(3)} = R_{ij}\gamma^{ij}$ is the Ricci scalar on a three-dimensional time slice. Our specific choice

of evolution variables introduces five additional constraints,

$$\det \tilde{\gamma}_{ij} = 1, \tag{6.25}$$

$$\mathrm{tr}\, \tilde{A}_{ij} = 0, \tag{6.26}$$

$$\tilde{\Gamma}^i = \tilde{\gamma}^{jk}\tilde{\Gamma}^i_{jk}. \tag{6.27}$$

Our code actively enforces the algebraic constraints (6.25) and (6.26). The remaining constraints, $\mathcal{H}$, $\mathcal{M}^i$, and (6.27), are not actively enforced, and can be used as monitors of the accuracy of our numerical solution. See [193] for a more comprehensive discussion of the these points.

Gauges

We specify the gauge in terms of the standard ADM lapse function, α, and shift vector, β^a [1]. We evolve the lapse according to the "$1 + \log$" slicing condition:

$$\partial_t \alpha - \beta^i \partial_i \alpha = -2\alpha(K - K_0), \tag{6.28}$$

where K_0 is the initial value of the trace of the extrinsic curvature, and equals zero for the maximally sliced initial data which we consider here. The shift is evolved using the hyperbolic $\tilde{\Gamma}$-driver condition [193],

$$\partial_t \beta^i - \beta^j \partial_j \beta^i = \frac{3}{4}\alpha B^i\,, \tag{6.29}$$

$$\partial_t B^i - \beta^j \partial_j B^i = \partial_t \tilde{\Gamma}^i - \beta^j \partial_j \tilde{\Gamma}^i - \eta B^i\,, \tag{6.30}$$

where η is a parameter which acts as a damping coefficient. The advection terms on the right-hand-sides of these equations were not present in the original definitions of [193], where co-moving coordinates were used, but have been added following the experience of [201, 202], and are required for correct advection of the puncture in "moving-puncture" evolutions.

Numerical methods

Spatial differentiation of the evolution variables is performed via straightforward finite-differencing using fourth-order accurate centred stencils for all but the advection terms for each variable, which are upwinded in the direction of the shift. Vertex-centred adaptive mesh-refinement (AMR) is employed using nested grids [203, 204] with a $2:1$ refinement for successive grid levels, and with the highest resolution concentrated in the neighbourhood of the individual horizons. Individual apparent horizons are located every few time steps during the evolution [205, 206].

The time steps on each grid are set by the Courant condition and thus by the spatial grid resolution for that level, with the time evolution being carried out using fourth-order accurate Runge-Kutta integration steps. Boundary data for finer grids are calculated with

spatial prolongation operators employing 5th-order polynomials, and prolongation in time employing 2nd-order polynomials. The latter allows a significant memory saving, requiring only three time levels to be stored, with little loss of accuracy due to the long dynamical timescale relative to the typical grid time step.

Initial data

The initial data are constructed applying the "puncture" method [207], which uses the Bowen-York extrinsic curvature and solves the Hamiltonian constraint equation numerically as in [208]. For the orbital initial data parameters we use the effective potential method introduced in [209] and extended to spinning configurations in [210]. The effective potential method is a way of choosing the initial data parameters such that the required physical parameters (*e.g.* masses and spins) are obtained to describe a binary black-hole system on a quasi-circular orbit.

The free parameters to be chosen for the puncture initial data are: the puncture coordinate locations $\boldsymbol{C}_i$, the puncture mass parameters m_i, the linear momenta $\boldsymbol{p}_i$, and the individual spins $\boldsymbol{S}_i$. Since we are interested in quasi-circular orbits we work in the zero momentum frame and choose $\boldsymbol{p}_1 = -\boldsymbol{p}_2$ to be orthogonal to $\boldsymbol{C}_2 - \boldsymbol{C}_1$. The physical parameters which we want to control are: the black hole mass ratio M_1/M_2, the orbital angular momentum $\boldsymbol{L} = \boldsymbol{C}_1 \times \boldsymbol{p}_1 + \boldsymbol{C}_2 \times \boldsymbol{p}_2$ (see for example [150, 209, 210]) and the dimensionless spin parameters $\boldsymbol{a}_i = \boldsymbol{S}_i/M_i^2$. In order to choose the input parameters that correspond to the desired physical parameters we have to use a non-linear root finding procedure, since the physical parameters depend non-linearly on the input parameters and it is not possible to invert the problem analytically.

As detailed in [210], when the black-hole spins are taken as parameters, it is possible to reduce the number of independent input variables, so that at a given separation $\bar{\boldsymbol{C}} \equiv |\boldsymbol{C}_2 - \boldsymbol{C}_1|/m_1$, the independent input parameters are: $\bar{q} \equiv m_1/m_2$ and the dimensionless magnitude of the linear momentum p/m_1. Using a Newton-Raphson method, we solve for $\bar{q}$ and p/m_1 so that the system has a given mass ratio M_1/M_2 and a given dimensionless orbital angular momentum, $L/(\mu M)$ where $\mu = m_1 m_2/M^2$ is the reduced mass. For such a configuration the initial data solver [208] returns a very accurate value for $M_{\rm ADM}$, which together with the accurate irreducible mass calculated by the apparent horizon finder [205, 206] makes it possible to calculate an accurate value of the dimensionless binding energy

$$E_b/\mu = (M_{\rm ADM} - M_1 - M_2)/\mu. \tag{6.31}$$

The quasi-circular initial data parameters are then obtained by finding the minimum in E_b/μ for varying values of $\bar{\boldsymbol{C}}$ while keeping the required orbital angular momentum $L/(\mu M)$ constant.

Note that the physical mass M_i of a single puncture black hole increases when the spin parameter is increased if the mass parameter m_i is kept constant. For that reason obtaining $M_1 = M_2$ in general requires that $m_1 \neq m_2$. Even in the case where the spins have the same magnitude but different directions, the two black holes will have different

spin-orbit interactions leading to slightly different physical masses if $m_1 = m_2$.

Chapter 7

Why explore alternatives to General Relativity?

Everything popular is wrong.

O. Wilde

In the first part of this thesis, we have investigated whether future gravitational wave observations of EMRIs will allow one to map the spacetime around SMBHs, detecting possible deviations away from the pure Kerr solution of GR because of the presence of astrophysical matter (chapters 2, 3 and 4). In chapters 5 and 6, instead, we have assumed that the astrophysical matter can be neglected and we have studied some aspects of EMRIs (chapter 5) and of generic black-hole binaries (chapter 6) under this assumption. In particular, this latter analysis also amounts to analysing whether gravitational wave observations of these systems will allow one to validate the predictions of GR in the case in which the astrophysical matter can be neglected. In both cases, GR is assumed to be correct and possible observational consequences are worked out. In this sense, the tests that we have dealt with so far are *consistency* tests of GR, because they could (in principle) rule out GR, but in this case they would not give any hints at what the correct theory of gravity should be (see ref. [211] for more details on this point).

Nevertheless, distinguishing between competing gravity theories is becoming more and more important in view of the discoveries made by cosmologists in the last decade. The startling fact that 95% of the Universe seems to be made of unknown "dark components" (*Dark Matter* and *Dark Energy*), rather than of the normal matter of which ourselves, stars and galaxies are made, has triggered research both in Particle Physics – in order to understand what these dark components might be (especially Dark Matter) – and in Quantum Gravity and Superstring Theory – to understand whether at least some of the dark components that we see (especially Dark Energy) might be due to the failure of GR at cosmological scales.

Another possible approach, which has been widely explored in the literature (see for instance ref. [212] for a review), consists of considering *phenomenological* modifications to GR and checking whether they allow one to explain astrophysical and cosmological data without the inclusion of Dark Energy (or, in few cases, also Dark Matter). Although it is clear that the ultimate answer to the question of what is the correct theory of gravity will need a contribution from a fundamental high-energy theory, be it Quantum Gravity or Superstring Theory, this phenomenological approach may eventually give a direction to the theorists, because it could allow them to understand which kinds of gravity modifications may be expected on an experimental basis and which ones give instead unacceptable consequences. Unfortunately, most of the work in this direction so far has involved comparison of these theories only with cosmological observables, while the problem of whether they could give predictions which are very different from GR with a cosmological constant on smaller lengthscales seems to have been rather overlooked in the literature. In this thesis we try to (very partially) fill this gap by considering two popular modified theories of gravity, namely Palatini $f(R)$ gravity (chapter 8) and Gauss-Bonnet gravity (chapter 9), and by working out their predictions at the solar-system scale and at stellar scales, respectively. As we will see in one case (that of Palatini $f(R)$ gravity), the payoff of an investigation going beyond the cosmological level can even be that of ruling out the theory.

Before presenting these two specific examples, in this chapter we will first summarise very briefly the motivations for introducing modifications to Einstein's GR. Because these motivations lie in the interplay between GR, Quantum Field Theory (QFT) and cosmology, it is convenient to adopt, *only* in this chapter, units in which $\hbar = c = 1$ and in which, instead, G is not 1, but has the dimensions of a mass to the -2. In particular, in section 7.1 we briefly recall the main points of clash between GR and quantum mechanics, which reveal that GR, being a classical theory, cannot be the fundamental theory of gravity. In section 7.2 we review instead the experimental motivation for modifying GR. Because these motivations essentially come only from cosmology, in section 7.2.1 we introduce the basics of the ΛCDM model for the expansion and contents of the Universe. Although this model is widely accepted in the cosmological community (so much as to be referred to as the "concordance model"), it presents a number of theoretical flaws, especially when the possible nature of the so-called "Dark Energy" is analysed critically. The problems plaguing the concept of Dark Energy, and even more that of cosmological constant, are described in detail in sections 7.2.2 and 7.2.3 and give, in our view, compelling evidence that gravity should not be described using standard GR on cosmological scales.

7.1 Theoretical motivations

The main reason why GR cannot be the fundamental theory of gravity is that it is in conceptual clash with Quantum Field Theory (QFT). First of all, GR considers spacetime as dynamical, rather than pre-determined as in special relativity or Newtonian gravity.

This fact is often expressed by saying that GR is a diffeomorphism-invariant theory.[1] As a consequence, "time" in not well-defined because it is not fundamentally different from "space": both are coordinates on the spacetime manifold and can be mixed by means of coordinate transformations. There is no distinction between time and space in GR and both are dynamical quantities, because the spacetime structure itself is dynamical as it is governed by the Einstein equations. Conversely, in QFT time depends on the observer (because QFT is based on special relativity) but is not dynamical, because the underlying spacetime is kept fixed and is described by the flat Minkowski metric. In this sense, the concept of time in QFT resembles more the absolute Newtonian time rather than the general-relativistic concept.

Secondly, although time is a dynamical quantity, GR is a *deterministic* (and in this sense "classical") theory. Once the initial conditions on a Cauchy hypersurface have been fixed, the evolution of the spacetime is determined by the Einstein equations. The concept of spacetime is a global one: it keeps track of both the past and the future, with the latter necessarily determined by the former. This is clearly not the case in QFT due to the Heisenberg uncertainty principle, which makes quantum mechanics a *probabilistic* theory.

Of course, one could try to build a quantum theory of gravity using a perturbative expansion over the Minkowski background metric of QFT. In other words, one might try to introduce deviations from the Minkowski metric, which could in principle be quantised in a way similar to what is done for the matter fields (scalar fields, fermions). The resulting semi-classical theory of gravity is useful in many contexts (*e.g.*, to study the Hawking radiation of a black hole, to calculate the spectrum of the cosmological perturbations produced by inflation, etc.), but it will only be a low energy approximation of the complete theory. The reason is that gravity is not perturbatively renormalisable, because the coupling constant between gravitons and matter is dimensional (just like in the Fermi theory of weak interactions). This coupling constant is indeed the gravitational constant G, which has the dimensions of a mass to the power -2. More precisely, $G = 1/m_{\rm P}^2$, where $m_P = 1.2 \times 10^{19}$ GeV is the Planck mass. As such, on purely dimensional grounds, ones obtains that the amplitude for a two-body gravitational scattering will be of order $G[1 + Gk^2_{\rm cutoff} + (Gk^2_{\rm cutoff})^2 + ...]$, which clearly blows up when the cutoff energy $k_{\rm cutoff}$ becomes comparable to the Planck mass $m_{\rm P}$.

It would therefore seem that quantum corrections to GR should appear only at energies

[1] This does not simply mean that physics is independent from the choice of the coordinate system – these feature is shared also by Newtonian physics, classical electromagnetism, etc. – but also that physics does not change if one performs a "smooth" deformation of the spacetime manifold. More formally, in GR physics is described by a differentiable manifold (the "spacetime") $\mathcal{M}$, which has topological and differential properties (*i.e.*, one can do calculus), and a set of tensor fields $\mathcal{T}$ describing the geometrical and physical content of the spacetime. Diffeomorphism invariance means that if we "deform" in a particularly smooth way the manifold and we transform accordingly (through the so-called "push-forward" of the diffeomorphism) the tensor fields, physics does not change. This invariance is very important in GR and in some sense plays the role that invariance under time and space translations play in Newtonian mechanics: From diffeomorphism invariance one derives immediately the conservation of the stress energy tensor – see *e.g.* ref. [215], section 6.3 – while, similarly, in Newtonian mechanics one obtains the energy and momentum conservation from translation invariance.

comparable to the Planck mass. If such an assumption is correct, classical GR can be used to describe the evolution of the Universe back to very early times. In particular, GR would certainly be valid at the present time in the evolution of the Universe, because its energy density today is of the order of $\rho_{\rm c} \sim (10^{-3}{\rm eV})^4 \ll m_{\rm P}^4$. This point of view has been adopted for decades, but it leads to the surprising conclusion that the matter which we are made of is only 5 % of the mass-energy of the Universe, while the remaining 95 % consists of "dark" components. In the next subsection we will briefly review the cosmological observations leading to these conclusions (for a pedagogical review, see ref. [213]; for an extensive list of references on the observational evidence, see ref. [214]).

7.2 Experimental motivations

7.2.1 A brief introduction to the ΛCDM model

Our present understanding of cosmology is based on the basic assumption that the Universe is homogeneous and isotropic on large scales (*i.e.*, larger than $300h^{-1}$ Mpc, where $h \approx 0.72$ is the present Hubble constant expressed in $\mathrm{km\,s^{-1}\,Mpc^{-1}}$) at a "fixed time". Stated in this way, this assumption is ambiguous, but it can be made rigorous by requiring that the spacetime describing the Universe can be sliced in a family of spacelike hypersurfaces that are homogeneous and isotropic (*i.e.*, maximally symmetric). This assumption is hard to test experimentally, especially as far as homogeneity is concerned (although some interesting work has been done in this direction [216]), but reflects the "Copernican" philosophical expectation that there is nothing special about our position in the Universe. At any rate, accepting this basic assumption, which is known as "cosmological principle", the spacetime is described by the Robertson-Walker (RW) metric

$$ds^2 = -dt^2 + a(t)^2 \left(\frac{dr^2}{1-kr^2} + r^2 d\theta^2 + r^2 \sin^2\theta d\phi^2 \right) , \tag{7.1}$$

where k can be $0, \pm 1$ and $a(t)$ is the expansion parameter. Inserting this metric into the Einstein equations, in which we assume that the matter is given by a perfect fluid at rest with respect to the coordinates (*i.e.*, comoving with them):

$$R^{\mu\nu} - \frac{1}{2} R g^{\mu\nu} = 8\pi G T^{\mu\nu} , \tag{7.2}$$

$$T^{\mu\nu} = (p+\rho) u^\mu u^\nu + p g^{\mu\nu} , \quad u^\mu = \delta^\mu_t / \sqrt{-g_{tt}} = \delta^\mu_t , \tag{7.3}$$

one gets the Friedmann equations

$$\left(\frac{\dot{a}}{a} \right)^2 = \frac{8\pi G \rho}{3} - \frac{k}{a^2} , \tag{7.4}$$

$$\frac{\ddot{a}}{a} = -\frac{4\pi G}{3} (\rho + 3p) . \tag{7.5}$$

From them, or directly from the time component of the stress-energy tensor conservation ${T^{\mu\nu}}_{;\nu} = 0$, one gets

$$\dot{\rho} + 3\frac{\dot{a}}{a}(\rho + p) = 0 \ : \tag{7.6}$$

note that this equation can also be written as $d(\rho a^3) = -p\, da^3$ and is, therefore, just the first law of thermodynamics. Defining now the Hubble constant $H(t)$ and the critical density $\rho_c(t)$,

$$H(t) \equiv \frac{\dot{a}(t)}{a(t)}\,, \qquad \rho_c(t) \equiv \frac{3H(t)^2}{8\pi G}\,, \tag{7.7}$$

from eq. (7.4) one gets

$$\Omega - 1 = \frac{k}{a^2 H^2}\ , \tag{7.8}$$

where $\Omega \equiv \rho/\rho_c$ is called the "density parameter". Therefore, if the density is larger, smaller or equal to the critical density at a certain time, it is larger, smaller or equal to it at any later or earlier time.

Let us consider now an equation of state (EOS) $p = w\rho$ ($w \in [0, 1]$) for the cosmic fluid. This EOS includes physically relevant cases such as classical matter ($w = 0$) – *i.e.*, a fluid of non-relativistic particles[2], for which $p/\rho = k_B T/m \ll 1$ – or radiation ($w = 1/3$) – *i.e.*, a fluid of relativistic particles. Inserting this EOS into eq. (7.6), it is easy to find that

$$\rho = \rho_0 \left(\frac{a_0}{a}\right)^{3(1+w)}\ , \tag{7.9}$$

where a_0 is the scale factor at the present time. Using this equation, together with eq. (7.4) and (7.8), one gets

$$\dot{a}^2 = a_0^2 H_0^2 \left[\Omega_0 \left(\frac{a_0}{a}\right)^{1+3w} + 1 - \Omega_0\right]\,, \tag{7.10}$$

where the index 0 denotes again quantities evaluated at the present time. From eqs. (7.7), (7.8) and (7.9), it is then easy to check that the density parameter evolves as

$$\Omega^{-1} - 1 = \left(\Omega_0^{-1} - 1\right)\left(\frac{a}{a_0}\right)^{1+3w}\ . \tag{7.11}$$

Let us then note that eq. (7.10) can be integrated analytically in the "flat" case ($k = 0$, that is $\Omega = 1$): fixing the cosmic time such that for $t = 0$ one has $a = 0$[3] and exploiting the empirical observation, dating back to Hubble, that the universe is expanding rather than contracting, we have

$$a(t) = a_0 \left(\frac{t}{t_0}\right)^{2/[3(1+w)]}\ . \tag{7.12}$$

[2]Ones with mass $m \gg k_B T$, k_B and T being the Boltzmann constant and the temperature.

[3] This initial singularity ("big bang"), in which the spacetime curvature, the matter density and the matter temperature become infinite, comes about because $\ddot{a} < 0$ if $p > -\rho/3$ [*cf.* eq. (7.5)]. As such, if $\dot{a} > 0$ at a certain time, there must a finite time in the past at which $a = 0$.

It is also possible to show that for $\Omega < 1$ (*i.e.*, $k = -1$: "closed" universe) $a(t)$ initially grows from 0 (big bang) to a maximum and then decreases again to 0 (big crunch), while for $\Omega > 1$ (*i.e.*, $k = 1$: "open" universe) it increases indefinitely (and faster than in the flat case) after the big bang.

Let us consider again eq. (7.9): for matter that equation gives $\rho \propto a^{-3}$, while for radiation one has $\rho \propto a^{-4}$. This means that the energy density of radiation is diluted faster than that of matter as the Universe expands, and at sufficiently late times the matter energy density will be dominant over that of radiation. This is indeed what happens at redshift[4] $z \approx 4000$: at higher redshifts (earlier cosmic times) the universe is *radiation dominated*, while at smaller redshifts (more recent times) the universe is *matter dominated*. Therefore, in the matter dominated era it is possible (for some purposes) to neglect the presence of radiation. We should note, however, that all of the equations that we have derived in this section assume that GR is correct without any cosmological constant. Fortunately, a cosmological constant Λ would enter the Einstein equations through a term $\Lambda g_{\mu\nu}$ to be added to the left-hand side of eq. (7.2). Moving this term to the right-hand side, it is clear that a cosmological constant corresponds to a perfect fluid at rest with respect to the coordinates and with density $\rho_\Lambda = \Lambda/(8\pi G)$ and pressure $p_\Lambda = -\rho_\Lambda$ (*i.e.*, $w = -1$). Considering therefore a universe filled with matter and governed by the Einstein equations with a cosmological constant, eq. (7.10) becomes

$$\dot{a}^2 = a_0^2 H_0^2 \left[\Omega_{m0} \left(\frac{a_0}{a} \right) + \Omega_{\Lambda 0} \left(\frac{a_0}{a} \right)^{-2} + 1 - \Omega_0 \right] \tag{7.13}$$

(with $\Omega_0 = \Omega_{\Lambda 0} + \Omega_{m0}$), while eq. (7.5) becomes

$$\frac{\ddot{a}}{a} = -\frac{4\pi G}{3} \rho_m + \frac{\Lambda}{3} \, . \tag{7.14}$$

Of course, the energy density of the cosmological constant maintains constant during the universe expansion, while that of matter gets diluted as a^{-3} because eq. (7.9) keeps valid (as we have stressed, that equation follows from the first principle of thermodynamics).

In this simplistic view, therefore, the Universe at $z \ll 4000$ (*i.e.*, after the radiation-matter equivalence) can be described by a model with parameters H_0, $\Omega_{\Lambda 0}$ (or Λ) and Ω_{m0} (or $\Omega_0 = \Omega_{\Lambda 0} + \Omega_{m0}$).[5] Of course, other parameters would come about if we considered also the perturbations of our universe model over the homogeneous and isotropic background [this is clearly necessary in order to study the formation of cosmic structures – galaxies, groups, clusters, etc. – and the anisotropy spectrum of the cosmic microwave background (CMB)]. In particular, an additional parameter that we should consider is the fraction of matter in baryons: we will denote their density parameter with

[4] The redshift $z(t)$ is defined as $z(t) \equiv a_0/a(t) - 1$. Indeed, a photon emitted at a cosmic time t with frequency ν_0 at the present time has been redshifted to a frequency $\nu_0 = \nu/(1+z)$.

[5] It is clear that the present value of the scale factor a_0, can be set to 1 by redefining the spatial coordinates: *cf.* eq. (7.1).

Ω_{b0}, while the density parameter of Cold[6] Dark Matter (CDM) will of course be given by $\Omega_{CDM0} = \Omega_{m0} - \Omega_{b0}$.

The only way to determine the values of the four parameters H_0, $\Omega_{\Lambda 0}$, Ω_{m0} and Ω_{b0} is of course given by cosmological and astrophysical observations. Historically, the first parameter the determination of which was attempted was the Hubble constant at the present time H_0. It is in fact possible to show that the luminosity distance d_L of a source, defined as

$$d_L \equiv \sqrt{\frac{L}{4\pi\ell}} \,, \tag{7.15}$$

where L is the radiated power and ℓ the power flux per unit surface measured by an observer at the present time, depends on the redshift through

$$d_L = \begin{cases} \frac{1+z}{H_0\sqrt{|\Omega_0-1|}} \left[\int_0^z \frac{\sqrt{|\Omega_0-1|}dz'}{(\Omega_{m0}(1+z')^3+\Omega_{\Lambda 0}+(\Omega_0-1)(1+z')^2)^{1/2}}\right] & \text{for } \Omega_0 = 1\,, \\ \frac{1+z}{H_0\sqrt{|\Omega_0-1|}} \sin\left[\int_0^z \frac{\sqrt{|\Omega_0-1|}dz'}{(\Omega_{m0}(1+z')^3+\Omega_{\Lambda 0}+(\Omega_0-1)(1+z')^2)^{1/2}}\right] & \text{for } \Omega_0 < 1\,, \\ \frac{1+z}{H_0\sqrt{|\Omega_0-1|}} \sinh\left[\int_0^z \frac{\sqrt{|\Omega_0-1|}dz'}{(\Omega_{m0}(1+z')^3+\Omega_{\Lambda 0}+(\Omega_0-1)(1+z')^2)^{1/2}}\right] & \text{for } \Omega_0 > 1\,. \end{cases} \tag{7.16}$$

Expanding in a series around $z = 0$, one gets

$$d_L = \frac{1}{H_0}\left[z + \frac{z^2}{2}(1-q_0) + O\left(z^3\right)\right] \,, \tag{7.17}$$

where

$$q_0 = -\frac{\ddot{a}_0 a_0}{\dot{a_0}^2} = \frac{\Omega_{m0}}{2} - \Omega_{\Lambda 0} \tag{7.18}$$

is the *deceleration parameter*. Neglecting the terms quadratic in z, eq. (7.17) is the famous *Hubble law*: the redshift of a galaxy is proportional to its distance from us. This law permits measuring the Hubble constant H_0, if one can observe sources for which both the redshift and the luminosity distance are known. While the redshift of an object can be measured directly using the emission lines present in the spectrum, the luminosity distance can be derived from the observed luminosity ℓ only if one knows the intrinsic luminosity L [*cf.* eq. (7.15)]. Fortunately, there are classes of sources for which L is constant: these sources are known as "standard candles" and, once calibrated[7],

[6] By "cold", it is meant that Dark Matter particles are non-relativistic (*i.e.*, with $k_B T \ll m$). In the long history of the Dark Matter paradigm, the origin of which is due to Zwicky and dates back to the 30's (*cf.* for instance ref. [217]), models with Hot (*i.e.*, relativistic) Dark Matter were also put forward. However, these models were abandoned because they predicted that galaxies would form very late (at $z \lesssim 1$, while they are observed up to $z \gtrsim 6$).

[7] For instance, by comparison with classical Cepheids, which are periodic stars with a narrow relation between period and luminosity.

they can be used to measure or constrain the parameters entering eqs. (7.16) and (7.17). The best-known and most important standard candles are type Ia supernovae (SNe Ia), which form when a white dwarf explodes after overcoming the Chandrasekhar mass limit as a consequence of accretion from a companion. Low redshift SNe Ia (together with other standard candles) allow one to measure the Hubble constant with great precision: $H_0 = 72 \pm 8\ \mathrm{km\,s^{-1}Mpc^{-1}}$ [218]. Moreover, these sources are very luminous and can be observed up to $z > 1$, thus allowing one to determine, in addition to H_0, also a linear combination of Ω_{m0} and $\Omega_{\Lambda 0}$ [219, 220, 221]. From our approximate eq. (7.17), this combination would be $q_0 = \Omega_{m0}/2 - \Omega_{\Lambda 0}$, although a more rigorous analysis constrains a slightly different combination (for instance, ref. [220] gives $\Omega_{\Lambda 0} - 1.4\Omega_{m0} = 0.35 \pm 0.14$).

Having this constraint, all that we need to determine the individual value of $\Omega_{\Lambda 0}$ and Ω_{m0} is a constraint on another linear combination of these quantities. Fortunately, such a constraint is given by the measurement of the anisotropy spectrum of the temperature of the Cosmic Microwave Background (CMB). In particular, it is possible to show that the first peak of this spectrum gives a very precise measurement of the total density parameter $\Omega_0 = \Omega_{m0} + \Omega_{\Lambda 0}$: this quantity is found to be equal to 1 to within few percent [214]. This is in agreement with inflationary models, which predict that Ω_0 should be almost exactly 1 (flat universe). Combining this constraint with the one coming from SNe Ia, to which it is approximately orthogonal, one gets $\Omega_{m0} \approx 0.3$ and $\Omega_{\Lambda 0} \approx 0.7$ (*cf.* Fig. 7.1). We should mention, though, that the anisotropy spectrum of the CMB gives *much* more information than that, because the shape of the spectrum depends on all of the parameters of the ΛCDM model and a statistical analysis will therefore give constraints on all of them. Nevertheless, the best-determined parameters (that is, the parameters the variations of which have the most pronounced impact on the spectrum) are the already cited Ω_0 and the baryon density parameter Ω_{b0}. Indeed, it is found that $\Omega_{b0} \approx 0.045$, in agreement with the constraints coming from the Big Bang Nucleosynthesis model. As such, it turns out that most of the matter which enters the evolution of the Universe ($\Omega_{m0} \approx 0.3$) is not given by baryons but rather by CDM.

Further support to the above picture comes from measurements of Ω_{m0} and Ω_{b0} obtained by means of observations of the large scale structure of the universe. These observations include, for instance, measurements of the mass-luminosity ratio for galaxies, groups, clusters and superclusters [222], which can be converted into measurements of the total matter density using the luminosity function of galaxies[8]; measurements of the baryon fraction in clusters [223] (the baryon density can be measured using the Sunyaev-Zeldovich effect or x-ray observations; the latter also permits calculating the total density, if one assumes hydrostatic equilibrium); measurements of the cluster abundance as a function of redshift [224] (these constrain Ω_{m0}, because if Ω_{m0} is significantly less than

[8]The tricky point in these measurements is of course the inclusion of CDM in the measured masses. This is achieved with methods which are different from source to source: in disk galaxies one can measure the rotation curves of neutral hydrogen and reconstruct the mass profile; in elliptical galaxies one can infer the mass, for instance, from observations of hot x-ray emitting gas by assuming hydrostatic equilibrium; x-ray measurements or approaches based on the virial theorem can finally be applied also to groups, clusters and superclusters.

1 the cosmic structures do not evolve between $z = 1$ and $z = 0$); measurements of the correlation between the CMB temperature anisotropies and the distribution function of galaxies [225] (this correlation, known as Sachs-Wolfe effect, gives a measure of Ω_{m0}); measurements of the distortions of the galaxy correlation function in redshift space [226] (these distortions are due to the peculiar[9] velocities of galaxies and permit measuring Ω_{m0}); measurements of the bispectrum of the galaxy distribution [227] (these allow one to measure Ω_{m0}) and of its power spectrum [228] (these give both Ω_{m0} and, through the baryon acoustic oscillations, Ω_{b0}); measurements of the peculiar velocities of galaxies [229] (these allow mapping of the total matter density profile); etc.

At this point, it should be clear that a ΛCDM with $\Omega_0 \approx 1$, $\Omega_{\Lambda 0} \approx 0.7$, $\Omega_{m0} \approx 0.3$ and $\Omega_{b0} \approx 0.045$ is in agreement with basically all of the present cosmological observations (the ΛCDM is indeed known also as the "concordance model"). However, this model has an apparent drawback, namely the fact that 95% of the energy in the universe appears to be made of dark components. While the supersymmetric extensions of the Standard Model of particle physics predict the existence of many particles that could be the cosmological CDM, the situation is *much* worse for the cosmological constant, as we will see in the next two subsections.

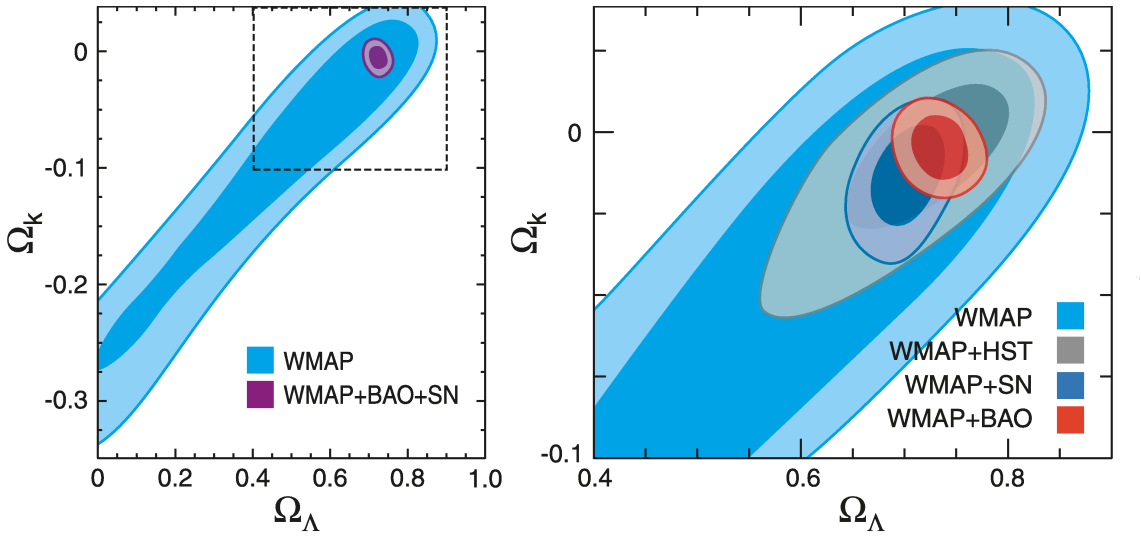

Figure 7.1: *Joint constraints from WMAP data alone and combined with large scale structure (baryon acoustic oscillations, BAO), SNe Ia (SN) and the Hubble Space telescope constraint for the Hubble constant (HST). Figure take from ref. [214].*

[9] *i.e.,* relative to an observer at rest with respect to the spatial coordinates used in eq. (7.1).

7.2.2 The cosmological constant: the standard lore before the 90's

As we have already mentioned, the addition of a cosmological constant Λ is the simplest possible modification of the Einstein equations, which become

$$R_{\mu\nu} - \frac{1}{2} R\, g_{\mu\nu} + \Lambda g_{\mu\nu} = 8\pi G\, T_{\mu\nu} \ . \tag{7.19}$$

These equations can be derived from the action

$$S = -\frac{1}{16\pi G} \int (R - 2\Lambda)\sqrt{-g}\, d^4x \ , \tag{7.20}$$

which replaces the Einstein-Hilbert action. As we have already stressed, $\Lambda g_{\mu\nu}$ can be viewed either as a geometrical term (in the absence of matter, the space-time is not Minkowski) or, once moved to the right hand side, as a perfect fluid with

$$T_{\mu\nu} = \frac{\Lambda}{8\pi G}\, g_{\mu\nu} \tag{7.21}$$

[that is, with $\rho_\Lambda = -p_\Lambda = \Lambda/(8\pi G)$].

However, in addition to this "geometrical" (or "bare") cosmological constant, there are other contributions (see ref. [230], to which we refer for the following discussion). In order to understand what they are, let us start with the simple case of a real scalar field ϕ, minimally coupled to gravity, with potential $V(\phi)$: its action is given by

$$S_\phi = \int d^4x \sqrt{-g} \left(-\frac{1}{2} \partial_\mu \phi \partial^\mu \phi - V(\phi) \right) \ , \tag{7.22}$$

from which the energy-momentum tensor follows:

$$T_{\mu\nu} = -2 \frac{\partial \mathcal{L}_\phi}{\partial g^{\mu\nu}} + \mathcal{L}_\phi g_{\mu\nu} = \partial_\mu \phi \partial_\nu \phi - \left(\frac{1}{2} \partial_\mu \phi \partial^\mu \phi + V(\phi) \right) g_{\mu\nu} \ . \tag{7.23}$$

Because in a neighbourhood of any fixed event $\bar{x}^\mu$ it is always possible to choose locally inertial coordinates, we can take, neglecting terms $\mathcal{O}((x - \bar{x})^2)$, $g_{\mu\nu} = \eta_{\mu\nu}$ in eqs. (7.22) and (7.23). In particular, we can quantise the action (7.22) as in a flat space-time and calculate the vacuum expectation value of $T_{\mu\nu}$, evaluated at $\bar{x}^\mu$.[10] If the vacuum is Lorentz invariant, we have

$$\langle 0 | T_{\mu\nu}(\bar{x}) | 0 \rangle = -\langle 0 | \rho | 0 \rangle \eta_{\mu\nu} \ , \tag{7.24}$$

which in generic coordinates gives

$$\langle 0 | T_{\mu\nu} | 0 \rangle = -\langle 0 | \rho | 0 \rangle g_{\mu\nu} \ . \tag{7.25}$$

[10] Of course the vacuum is not necessarily the state of the system: the vacuum energy is nevertheless the additive constant up to which the energies of all other states are defined. In special relativity this constant can be neglected, but this is not possible in GR, because an energy offset curves the space-time.

On the other hand, in order to quantise the action (7.22) we can expand the potential $V(\phi)$ around the value ϕ_0 of the scalar field for which it is minimal. Neglecting the self-interaction terms (*i.e.*, considering ϕ as a free field), the vacuum expectation value is $V(\phi_0)$, if we assume the normal ordering of the creation and destruction operators: this hypothesis, nevertheless, amounts to neglecting the *zero-point energy*, which, as we have stressed, is not possible in GR. Therefore, we have

$$\langle 0|\rho|0\rangle = V(\phi_0) + \int_0^{k_{\mathrm{cutoff}}} \frac{d^3\boldsymbol{k}}{(2\pi)^3}\frac{1}{2}\sqrt{k^2+m^2} \approx V(\phi_0) + \frac{k^4_{\mathrm{cutoff}}}{16\pi^2}\ , \tag{7.26}$$

where the cut-off depends on the scale up to which we consider quantum field theory to be valid.

Noting now that equation (7.25) has the same form as (7.21), it is clear that the "effective" cosmological constant (that is, the one relevant for experiments and observations) is given by the sum of three kinds of contribution:

$$\Lambda_{\mathrm{eff}} \sim \Lambda + 8\pi G\left(V(\phi_0) + \frac{k^4_{\mathrm{cutoff}}}{16\pi^2}\right)\ . \tag{7.27}$$

Of course, on the right hand side we must consider, instead of our toy scalar field, the vacuum energy densities of all of the degrees of freedom of quantum field theory: all of the fields contribute with their own zero-point fluctuations and the scalar fields contribute also with the minimum of their potential.

Let us now analyse what are the orders of magnitude of these different contributions. If we assume that quantum field theory is valid up to the Planck scale ($k_{\mathrm{cutoff}} \sim m_{\mathrm{P}}$), at which quantum-gravitational effects should begin to be important, the zero-point fluctuations should give a contribution of $\sim (10^{19}\,\mathrm{GeV})^4$ to $\rho_{\Lambda_{\mathrm{eff}}}$. Taking instead as cut-off the highest energy scale at which the standard model of particle physics has been experimentally tested (~ 100 GeV), we get, of course, a contribution of $\sim (100\,\mathrm{GeV})^4$.

Coming instead to the contributions from the minima of the potentials, we cannot estimate their absolute magnitude, but it is clear that they change significantly during spontaneous symmetry breakings. For instance, in the case of the Higgs field of the standard electroweak model (a weak isospin doublet $\Phi = (\phi_a, \phi_b)$, where ϕ_a and ϕ_b are complex scalar fields) the potential is

$$V(\Phi) = V_0 + \mu^2\Phi^\dagger\Phi + \lambda(\Phi^\dagger\Phi)^2\ . \tag{7.28}$$

Before the phase transition, μ^2 and λ are positive: the minimum of the potential is therefore V_0. After the phase transition, instead, μ^2 is negative: the potential is minimum [with value $V_0 - \mu^4/(4\lambda)$] for $\Phi^\dagger\Phi = -\mu^2/(2\lambda) \equiv v^2/2$. Although we do not know V_0, it can be shown that $v = (G_F\sqrt{2})^{-1/2}$ and $m_{\mathrm{H}} = \sqrt{2\lambda v^2}$, where $G_F = 1.166\cdot 10^{-5}\mathrm{GeV}^{-2}$ is the Fermi constant and m_{H} is the mass of the Higgs boson (unknown, but probably between 100 and 1000 GeV). We can then write the variation of the minimum value of the potential

as

$$\Delta V_{\min} = -\frac{\mu^4}{4\lambda} \approx -\frac{1}{8} m_{\rm H}^2 v^2 \approx -(100 - 300{\rm GeV})^4 \tag{7.29}$$

(using the given limits for $m_{\rm H}$). Of course, variations of the terms "of type $V(\phi_0)$" can happen also during the other phase transitions, which we believe the Universe has gone through during its history.

Coming finally to the bare cosmological constant Λ, we should note that in a classical context it is a free parameter, which could be estimated only experimentally (indeed, GR is based on the fundamental constants G, c, Λ, with which it is not possible to build any dimensionless combination). Anyway, we could hope that a quantum theory of gravity will predict its value: if we use, in addition to G, c and Λ, also the Planck constant $\hbar$, the simplest dimensionless combination that we can build is $\Lambda(G\hbar/c^3)$. Since it is reasonable to expect this to be ~ 1, we would have $\Lambda \sim L_{\rm P}^{-2}$, where $L_{\rm P} = (G\hbar/c^3)^{1/2} \approx 1.7 \times 10^{-33}{\rm cm}$ is the Planck length: in this case, the contribution to the energy density would be $\sim m_{\rm P}^4$.

In conclusion, the effective cosmological constant is due to the sum of several contributions. The trouble is that they are different in origin and in order of magnitude and they are much larger[11] than the present critical energy density $\rho_{c\,0} \sim (10^{-3}{\rm eV})^4$, which is of course the only allowed scale for an observed cosmological constant.

It therefore appears absolutely implausible (if not ridiculous) to think that all of these contribution could combine and give, at the present time, an effective cosmological constant which should be hundreds of orders of magnitude smaller than the single contributions. Indeed, until observations proved that $\Lambda \neq 0$, theorists used to think that there should be an unknown mechanism able of constraining the sum which we have considered to be exactly zero.

7.2.3 The coincidence problem

The observational evidence that we have briefly presented in section 7.2.1 gives rise to new problems. First of all, the cosmological constant is much smaller than the single contributions that we have listed in the last section: this is known as "first problem of the cosmological constant".

Also, there is a second problem ("second problem of the cosmological constant" or "coincidence problem"): why is ρ_Λ comparable to the energy density of matter at the present time? In other words, because ρ_Λ has been constant at least since the last phase transition (the quark-hadron transition, which happens at $T \approx 200 - 300{\rm MeV}$), whereas $\rho_m \propto a^{-3}$, the very fact that we observe $\Lambda \neq 0$ at the present time marks a fine tuning problem. Indeed, if ρ_Λ had been $\approx \rho_m$ much before the present time, cosmic structures would not have formed, whereas if $\rho_\Lambda \approx \rho_m$ in the far future, today we would not observe any cosmological constant. This "coincidence problem" is the most serious drawback of the ΛCDM model. Cosmologists tried then to think of other possible explanations for the observations of section 7.2.1. Indeed, those observations do not rule out a *dark energy*

[11] Note that $m_{\rm P}^4/\rho_{c\,0} \sim 10^{124}$ and $(100{\rm GeV})^4/\rho_{c\,0} \sim 10^{56}$.

component having equation of state $p = w_{DE}\,\rho$, with w_{DE} not necessarily being constant in time but being ≈ -1 at recent times.[12]

Among the models implementing this possibility, we will first address briefly the *quintessence* models (for a review see for instance ref. [213] and references therein), which have often been claimed to be able to alleviate, although not solve, the coincidence problem. In these models, dark energy is given by a scalar field (the *quintessence*) "rolling down a potential". Indeed, if we consider a uniform, real scalar field $\phi(t)$, minimally coupled to gravity, and if its potential is flat enough at recent times, we have $\dot{\phi}^2 \ll V(\phi)$ (slow-roll approximation) around the present time. As such,

$$w_{DE} = \frac{p_\phi}{\rho_\phi} = \frac{\frac{1}{2}\dot{\phi}^2 - V(\phi)}{\frac{1}{2}\dot{\phi}^2 + V(\phi)} \approx -1\ . \tag{7.30}$$

With this approach, dark energy at the present time is small because the universe is "old" (*i.e.*. quintessence has rolled down almost to the minimum of the potential).

In particular, by choosing suitable shapes for the potential it is possible to get the so called *tracker solutions*: in these models the energy density of quintessence is initially subdominant with respect to ρ_{rad} (the radiation density) and ρ_m, so as to avoid interference with primordial nucleosynthesis and structure formation, but eventually becomes comparable to ρ_m around the present time. The advantage of this is that all of the solutions with initial conditions in a wide "basin of attraction" join this tracker. In other words, the behaviour that we have sketched above does not depend on the initial conditions (*i.e.*, this model does not require fine tuning of initial conditions, unlike the "classical" cosmological constant)[13]. However, one still has to understand *why* the present matter density is comparable to the present energy density of quintessence : in fact, the latter depends strongly on the parameters of the potential.

Another possibility, not excluded by observations, is $w_{DE} < -1$, which would be impossible in, for instance, quintessence models. Indeed, in order to get this equation of state one must introduce fields with non-standard kinetic terms (*phantom fields*, see ref. [232]). In particular, it is easy to show that if $w_{DE} < -1$ is constant in time, there will be a future singularity (the so called "Big Rip" [233]) in the evolution of the universe. It could be shown that in such a universe the coincidence problem makes no sense: there is only a brief era in which cosmic structures exist and in which we must therefore necessarily live (no coincidence, then), and an era of phantom energy domination in which cosmic structures are destroyed. However, it has been demonstrated that this singularity does not occur if $w_{DE} < -1$ is not constant in time[14].

[12] Actually, another requirement is that dark energy must not cluster on small scales, otherwise it would be detected by the measurements of Ω_m performed with the large scale structure observations (*cf.* section 7.2.1).

[13] Actually, it has been shown [221] that the SNe Ia data require $d\,w_{DE}/d\,z = 0.6 \pm 0.5$ for $z = 0$: in order to have good trackers satisfying this constraint (*i.e.*, with a large basin of attraction), one has to choose potentials with rapidly varying curvature around the present time [231]. Of course this causes a new "coincidence problem".

[14] Of course, even if w_{DE} were < -1, there is certainly no reason to think that it is constant.

A completely different approach to the cosmological constant problem consists in using the "weak anthropic principle" [234]. In modern cosmological theories, the universe is *one* realization of a stochastic process (and not necessarily the only one, as happens in chaotic inflation or in the "superstring-inspired" landscape scenario); in other words, it can be considered as one element of a statistical ensemble. If we suppose that the cosmological constant is different in each element of the ensemble, we can treat it as a random variable. We could therefore wonder what its probability distribution is. Actually, as we exist, what is relevant is not the probability that Λ is in a given interval, but the probability that *it is observed and lies in the given interval*. More precisely, we would like to calculate the probability that an intelligent civilisation observes a universe with $\Omega_\Lambda \leq 0.7$ at the present time.

First of all, let us note that ρ_Λ must be much smaller than the energy densities typical of particle physics, otherwise galaxies would not form: we can therefore assume that the probability density $P_{a\,priori}(\rho_\Lambda)$ of having a certain ρ_Λ is approximately constant far from these energies. We can then reasonably assume that the probability that intelligent life develops is proportional to the fraction of baryons trapped in the galaxies [$N(\rho_\Lambda)$]. The probability of having a universe with an evolved civilisation whose astronomers measure a cosmological constant between Λ and $\Lambda + d\Lambda$ is therefore

$$dP(\rho_\Lambda) \approx \frac{N(\rho_\Lambda) P_{apriori}(\rho_\Lambda) d\rho_\Lambda}{\int N(\rho_\Lambda) P_{apriori}(\rho_\Lambda) d\rho_\Lambda} \approx \frac{N(\rho_\Lambda) d\rho_\Lambda}{\int N(\rho_\Lambda) d\rho_\Lambda} \,, \tag{7.31}$$

where $N(\rho_\Lambda)$ can be calculated using galaxy formation models: one finds a probability $P(\Omega_{\Lambda 0} \geq 0.7)$ between 5 and 12% (the result changes a bit according to the details of the calculation). Note that these values are rather small, but not implausible.

However, nothing guarantees that anthropic considerations are useful in theoretical physics. Let us consider an illustrative example: why does our universe have three spatial dimensions? A possible answer based on the anthropic principle is that if the number of spatial dimensions were not equal to three, the orbit of the Earth would not be closed and its climate would be too unstable to accommodate human life. This solution is a logically acceptable answer to the original question, but it is clear that it provides no insights for the compactification mechanism of extra dimensions, which is one of the central issues in higher-dimensional theories. Thus, in this sense this approach does not contribute to progress in theoretical physics.

A more fruitful approach, as we have already mentioned earlier in this chapter, may consist in interpreting the data pointing to the existence of a cosmological constant as being due to the failure of GR at cosmological scales, and in phenomenologically modifying GR to reproduce these data. In the next chapters we will examine the consequences of some of these phenomenological gravity theories at the lengthscales of stars.

Chapter 8

Stars in Palatini f(R) gravity

È pericoloso porre in modo sbagliato questioni sostanzialmente giuste.

I. Montanelli

8.1 Introduction

In this chapter we will focus on one specific generalisation of GR: Palatini $f(R)$ gravity [235] (see ref. [212] for a recent review of other attempts to generalise GR). As can be found in many textbooks (see *e.g.* ref. [1, 236]), Einstein's theory can be derived from the Einstein–Hilbert action not only by means of the standard metric variation, but also by taking independent variations with respect to the metric and the connection. In this approach, known as the *Palatini variational approach*, the metric and the connection are treated as independent quantities, and one has to vary the action with respect to both of them in order to obtain the field equations. The Riemann tensor $R^{\lambda}{}_{\mu\sigma\nu}$ and the Ricci tensor $R_{\mu\nu}$ are defined with respect to the now independent connection $\Gamma^{\lambda}{}_{\mu\nu}$ and do not necessarily coincide with the Riemann and Ricci tensors of the metric $g_{\mu\nu}$. Similarly, the Ricci scalar is defined as $R = g^{\mu\nu}R_{\mu\nu}$ and depends on the independent connection $\Gamma^{\lambda}{}_{\mu\nu}$, rather than on the Levi-Civita connection[1] of the metric as in standard GR. If the Lagrangian is linear in R (as in the Einstein–Hilbert action), variation with respect to the independent connection forces it to reduce to the Levi–Civita connection of the metric, whereas variation with respect to the metric gives the standard Einstein equations. Therefore, in the case of the Einstein–Hilbert action the outcome of Palatini variation is standard GR.

[1] We recall that the Levi-Civita connection is given by the familiar Christoffel symbols $\Gamma^{\lambda}{}_{\mu\nu} = g^{\lambda\sigma}(\partial_\mu g_{\nu\sigma} + \partial_\nu g_{\mu\sigma} - \partial_\sigma g_{\mu\nu})/2$.

However, clearly Einstein's theory is no longer recovered for a generic action

$$S = \frac{1}{16\,\pi}\int d^4x\sqrt{-g}f(R) + S_M(g_{\mu\nu},\psi), \tag{8.1}$$

where $f(R)$ is a function of R,[2] S_M is the matter action and ψ collectively denotes the matter fields. (We recall that we are using units in which $c = G = 1$). The resulting theory is then what is known as "$f(R)$ gravity in the Palatini formalism" or simply "Palatini $f(R)$ gravity". It is easy to see that independent variation of the action (8.1) with respect to the metric and the connection gives

$$F(R)R_{\mu\nu} - \frac{1}{2}f(R)g_{\mu\nu} = 8\,\pi\,T_{\mu\nu}, \tag{8.2}$$

$$\nabla_\sigma[\sqrt{-g}F(R)g^{\mu\nu}] = 0, \tag{8.3}$$

where $F(R) = \partial f/\partial R$, $T_{\mu\nu} \equiv -2(-g)^{-1/2}\delta S_M/\delta g^{\mu\nu}$ is the usual stress-energy tensor of the matter and ∇_μ is the covariant derivative built with the independent connection $\Gamma^\lambda{}_{\mu\nu}$. Note that a crucial assumption has been made in order to derive eqs. (8.2) and (8.3): the matter action has been taken to be independent of the connection $\Gamma^\lambda{}_{\mu\nu}$ [*cf.* eq. (8.1)]. This assumption is physically meaningful because it implies that the connection which defines parallel transport, and therefore the covariant derivative of matter fields, is the Levi-Civita connection of the metric. This demotes the independent connection to the role of an auxiliary field [238, 239, 240]. Additionally, under this assumption, the Levi-Civita connection becomes the one with respect to which the matter stress-energy tensor is conserved [241] (which implies, in particular, that test particles follow geodesics of the metric $g_{\mu\nu}$). In order to restore the geometrical nature of the independent connection, one has to allow it to couple to the matter. This leads to metric-affine $f(R)$ gravity [238], which is a different theory with enriched phenomenology [239, 240].

Specific choices for the function $f(R)$ in the action (8.1) have been shown to lead to models of Palatini $f(R)$ gravity which might be able to address dark-energy problems [237]. There is now an extensive literature on the cosmological aspects of such models and discussing their consistency with cosmological [242] and solar system constraints [243, 244]. In this chapter, we will focus on the less well-studied issue of finding consistent solutions for static spherically-symmetric matter configurations when $f(R) \neq R$.

In order to be able to treat the field equations analytically, we will assume a polytropic equation of state (EOS) for the matter, *i.e.*

$$p = \kappa\rho_0^\Gamma\,, \quad \Gamma > 3/2 \tag{8.4}$$

[2] As we will explain later in this chapter, there is no first principle from which one can derive the form of $f(R)$, the choice of which is a completely phenomenological one. *Ad hoc* choices which reproduce the acceleration of the expansion of the universe usually include, in addition to a term which is linear in R, a term proportional to $1/R$ [237].

(p and ρ_0 are the pressure and the rest-mass density, while κ and Γ are constants). This is a very common and useful choice for making simplified calculations both in GR and in Newtonian theory [245]. We will find that for a polytropic index in the range $3/2 < \Gamma < 2$ there exist *no* static and spherically-symmetric regular solutions to the field equations, because curvature singularities unavoidably arise at the surface.

Before presenting the derivation, there are four points that ought to be stressed about this result:

1. It holds also for any EOS which can be approximated, near to the surface, by a polytrope with $3/2 < \Gamma < 2$.

2. It is independent of the functional form of $f(R)$ (with the exception of some very specific cases, including standard GR). It is therefore applicable not only to specific models, but it reveals a generic aspect of Palatini $f(R)$ gravity as a class of theories.

3. The singularities appearing are true curvature singularities and not coordinate singularities, *i.e.* the curvature invariants of the metric diverge.

4. Apart from the assumptions already listed, concerning symmetries and the EOS, no other assumption or approximation has been used. The result therefore applies in all regimes ranging from Newtonian weak field to strong gravity.

This result therefore casts some serious doubt on the viability of Palatini $f(R)$ gravity. In the next sections, after presenting the proof of the result (sec. 8.2), we will further analyse the situation by considering gedanken experiments as a powerful tool to investigate the completeness of the theory (sec. 8.3). In sec. 8.3.1, we calculate the tidal forces due to the presence of the surface singularities, and reply to a recent criticism by Kainulainen *et al.* [246] about the idealised nature of the polytropic EOS and the validity of the fluid approximation at the lengthscales on which the singularities arise. In sec. 8.4, we then discuss the physical and mathematical nature of the problem. This analysis reveals that the presence of the singularities is not specifically related to the fluid description of matter, but rather is a feature of the differential structure of the equations of the theory and would, in general, become even more acute if the fluid approximation were to be abandoned. In the same section we also propose ways to generalise the theory in order to avoid these problems. In sec. 8.5 we present our conclusions.

8.2 A no-go theorem for polytropic spheres in Palatini f(R) gravity

As we have mentioned above, in this chapter we focus on the problem of finding consistent solutions for static spherically-symmetric stellar models in Palatini $f(R)$ gravity when $f(R) \neq R$. We first note that doing this is helped by the fact that Palatini $f(R)$ gravity retains a useful characteristic of GR: the exterior spherically symmetric solution

is unique (*Birkhoff's theorem*). To see this one must take the trace of eq. (8.2),

$$F(R)R - 2f(R) = 8\,\pi\,T, \tag{8.5}$$

where $T \equiv g^{\mu\nu}T_{\mu\nu}$. For a given $f(R)$, this is an algebraic equation in R and therefore it can be solved to give R as a function of T. We will not consider cases where this equation has no roots, since those do not give viable classical gravity theories [247]. Eq. (8.5) also implies that if $T = 0$, R must be constant[3]. If we denote the value of R when $T = 0$ by R_0 and insert it into eq. (8.3), this equation reduces to the covariant conservation of $g^{\mu\nu}$, fixing the independent connection to be the Levi-Civita one. This will be the situation in vacuum and in this case eq. (8.2) reduces to

$$\widetilde{R}_{\mu\nu} - \Lambda(R_0)g_{\mu\nu} = 0, \tag{8.6}$$

where $\widetilde{R}_{\mu\nu}$ is now indeed the Ricci tensor of the metric and $\Lambda(R_0) = R_0/4$. According to whether R_0 is zero or not, which of course depends on the choice of $f(R)$, the theory reduces in vacuum to GR without or with a cosmological constant. The vacuum spherically symmetric solution is unique in either case, being either Schwarzschild or Schwarzschild-(anti-)de Sitter.

Having determined an exterior solution, we then need to find an interior solution and perform a matching between the two. Recently, the generalisation of the Tolman–Oppenheimer–Volkoff (TOV) hydrostatic equilibrium equation for Palatini $f(R)$ gravity has been derived [248], opening the way for finding equilibrium interior solutions. We will consider here the matching of such interior solutions with exterior ones.

We begin by reviewing the formulas that we will need. Denoting the Ricci scalar of $g_{\mu\nu}$ by $\widetilde{R} \equiv g^{\mu\nu}\widetilde{R}_{\mu\nu}$ and setting $\widetilde{G}_{\mu\nu} = \widetilde{R}_{\mu\nu} - g_{\mu\nu}\widetilde{R}/2$, the field eqs. (8.2) and (8.3) can be rewritten as a single one

$$\begin{aligned}\widetilde{G}_{\mu\nu} = &\frac{8\pi}{F}T_{\mu\nu} - \frac{1}{2}g_{\mu\nu}\left(R - \frac{f}{F}\right) + \frac{1}{F}\left(\widetilde{\nabla}_\mu\widetilde{\nabla}_\nu - g_{\mu\nu}\widetilde{\Box}\right)F \\ &- \frac{3}{2}\frac{1}{F^2}\left((\widetilde{\nabla}_\mu F)(\widetilde{\nabla}_\nu F) - \frac{1}{2}g_{\mu\nu}(\widetilde{\nabla}F)^2\right),\end{aligned} \tag{8.7}$$

where $\widetilde{\nabla}_\mu$ is the covariant derivative with respect to the Levi-Civita connection of $g_{\mu\nu}$ and $\widetilde{\Box} \equiv g^{\mu\nu}\widetilde{\nabla}_\mu\widetilde{\nabla}_\nu$. To arrive at this equation, one has to solve eq. (8.3) for $\Gamma^\lambda{}_{\mu\nu}$, insert this into eq. (8.2) and express the resulting equation in terms only of metric quantities (for an alternative method, see ref. [239]).

Using the static spherically symmetric ansatz

$$ds^2 \equiv -e^{A(r)}dt^2 + e^{B(r)}dr^2 + r^2d\Omega^2, \tag{8.8}$$

[3]Indeed, if R_0 is the root of eq. (8.5) when $T = 0$ [*i.e.*, $F(R_0)R_0 - 2f(R_0) = 0$], one has $R(r) = R_0$ for any value of the radial coordinate r.

in eq. (8.7), considering perfect-fluid matter with $T_{\mu\nu} = (\rho + p)u_\mu u_\nu + p g_{\mu\nu}$ (where ρ is the energy density, p is the pressure and u^μ is the fluid 4-velocity) and representing d/dr with a prime, one arrives at the equations

$$A' = \frac{-1}{1+\gamma}\left(\frac{1-e^B}{r} - \frac{e^B}{F}8\pi G r p + \frac{\alpha}{r}\right), \tag{8.9}$$

$$B' = \frac{1}{1+\gamma}\left(\frac{1-e^B}{r} + \frac{e^B}{F}8\pi G r \rho + \frac{\alpha+\beta}{r}\right), \tag{8.10}$$

$$\alpha \equiv r^2\left(\frac{3}{4}\left(\frac{F'}{F}\right)^2 + \frac{2F'}{rF} + \frac{e^B}{2}\left(R - \frac{f}{F}\right)\right), \tag{8.11}$$

$$\beta \equiv r^2\left(\frac{F''}{F} - \frac{3}{2}\left(\frac{F'}{F}\right)^2\right), \qquad \gamma \equiv \frac{rF'}{2F}. \tag{8.12}$$

Defining $m_{\rm tot}(r) \equiv r(1-e^{-B})/2$ and using the Euler equation,

$$p' = -\frac{A'}{2}(p+\rho) \tag{8.13}$$

one gets the generalised TOV equations [248]:

$$p' = -\frac{1}{1+\gamma}\frac{(\rho+p)}{r(r-2m_{\rm tot})}\left(m_{\rm tot} + \frac{4\pi r^3 p}{F} - \frac{\alpha}{2}(r-2m_{\rm tot})\right), \tag{8.14}$$

$$m'_{\rm tot} = \frac{1}{1+\gamma}\left(\frac{4\pi r^2\rho}{F} + \frac{\alpha+\beta}{2} - \frac{m_{\rm tot}}{r}(\alpha+\beta-\gamma)\right). \tag{8.15}$$

We consider here matter which can be described by a one-parameter EOS $p = p(\rho)$. When this is specified, one can in principle solve the above equations and derive an interior solution. However, this is hard to do in practice because the equations are implicit, their right-hand sides effectively including through F' and F'' both first and second derivatives of the pressure, *e.g.*, $F' = d/dr\,[F(R(T))] = (dF/dR)\,(dR/dT)\,(dT/dp)\,p'$. We therefore first put them in an explicit form, which allows us not only to solve them numerically, but also to study their behaviour at the stellar surface.

Multiplying eq. (8.14) by dF/dp and using the definitions of α and γ, we get a quadratic equation in F', whose solution is

$$F' = \frac{-4rF(\mathcal{C}-F)(r-2m_{\rm tot}) + D\sqrt{2\Delta}}{r^2(3\mathcal{C}-4F)(r-2m_{\rm tot})} \tag{8.16}$$

where $D = \pm 1$ and where we have defined

$$\mathcal{C} = \frac{dF}{dp}(p+\rho) = \frac{dF}{d\rho}\frac{d\rho}{dp}(p+\rho), \tag{8.17}$$

$$\begin{aligned}\Delta = {} & Fr^2(r-2m_{\rm tot})\left[8F(\mathcal{C}-F)^2(r-2m_{\rm tot})\right. \\ & \left. -\mathcal{C}(4F-3\mathcal{C})\left((16\pi p - FR + f)r^3 + 4Fm_{\rm tot}\right)\right].\end{aligned} \tag{8.18}$$

We will now focus on polytropic EOSs given by $p = \kappa {\rho_0}^\Gamma$, noting that this can be rewritten as $\rho = (p/\kappa)^{1/\Gamma} + p/(\Gamma - 1)$, giving a direct link between p and ρ. In eq. (8.17), we have written $\mathcal{C}$ in terms of $dF/d\rho$ because this is finite at the stellar surface ($r = r_{\rm out}$ where $p = \rho = 0$). In fact, $dF/d\rho = (dF/dR)\,(dR/dT)\,(3dp/d\rho - 1)$, where dF/dR and dR/dT are in general finite even when $T = 3p - \rho$ goes to zero [check for instance the R^2 or $1/R$ models] and $dp/d\rho \to 0$ for $p \to 0$. Note also that while $d\rho/dp$ diverges when $p \to 0$, the product $(p+\rho)\,d\rho/dp$ goes to zero for $p \to 0$ if $\Gamma < 2$. Therefore, for a polytrope with $\Gamma < 2$, $\mathcal{C} = 0$ at the surface.

We now match the interior solution to the exterior one. For the latter, the general solution to eq. (8.6) is $\exp(-B(r)) = \ell \exp(A(r)) = 1 - 2m/r - R_0 r^2/12$, where ℓ and m are integration constants to be fixed by requiring continuity of the metric coefficients across the surface and R_0 is again the vacuum value of R. Using the definition of $m_{\rm tot}(r)$ this gives, in the exterior, $m_{\rm tot}(r) = m + r^3 R_0/24$. Besides continuity of the metric, one has to impose some junction conditions for A'. The exterior solution evaluated at the surface gives

$$A'(r_{\rm out}) = \frac{2\left(r_{\rm out}^3 R_0 - 12m\right)}{r_{\rm out}\left(R_0 r_{\rm out}^3 - 12 r_{\rm out} + 24m\right)}\,, \tag{8.19}$$

whereas the value of $A'(r_{\rm out})$ for the interior solution can be calculated with eq. (8.9). For this we need $F'(r_{\rm out})$. Evaluating eq. (8.16) at the surface, where $\mathcal{C} = p = 0$ and R, F and f take their constant vacuum values R_0, F_0 and $f_0 = F_0 R_0/2$, we get $F'(r_{\rm out}) = -(1+\widetilde{D})F_0/r_{\rm out}$, where $\widetilde{D} = D\,\mathrm{sign}[r_{\rm out} - 2m_{\rm tot}(r_{\rm out})]$ [4]. Choosing $\widetilde{D} = 1$ implies $\gamma = -1$ at the surface [*cf.* eq. (8.12)] giving $A' \to \infty$ for $r \to r_{\rm out}^-$ [*cf.* eq. (8.9)], whereas A' keeps finite for $r \to r_{\rm out}^+$ [eq. (8.19)]. Because $\widetilde{G}_{\mu\nu}$ involves A'', this infinite discontinuity leads to the presence of Dirac deltas in the field equations. These Dirac deltas cannot be cancelled by the derivatives of F' on the right-hand side, because the discontinuity of F' is only a finite one, and one should therefore invoke an infinite surface density at $r = r_{\rm out}$. Since this is unreasonable, we focus only on $\widetilde{D} = -1$, for which $F'(r_{\rm out}) = 0$ when $r \to r_{\rm out}^-$, making both F' and A' continuous across the surface.

In order to study the behaviour of $m_{\rm tot}$ at the surface, we need first to derive an explicit expression for F''. If we take the derivative of eq. (8.16), F'' appears on the left-hand side and also on the right-hand side [through $m'_{\rm tot}$, calculated from eq. (8.15) and the definition of β, eq. (8.12)], giving a linear equation in F''. The solution to this equation,

[4] Unlike in GR, one cannot prove that $r_{\rm out} > 2m_{\rm tot}(r_{\rm out})$ from eq. (8.14), because p' is not necessarily positive for $r < 2m_{\rm tot}$. However, one may expect $r_{\rm out} > 2m_{\rm tot}$ in sensible solutions.

evaluated at the surface, is

$$F''(r_{\rm out}) = \frac{\left(R_0 r_{\rm out}^3 - 8m_{\rm tot}\right)\mathcal{C}'}{8r_{\rm out}(r_{\rm out} - 2m_{\rm tot})} \tag{8.20}$$

Evaluating α, β and γ at the surface using $F' = 0$ and F'' given by eq. (8.20), and inserting into eq. (8.15) gives

$$m'_{\rm tot}(r_{\rm out}) = \frac{2F_0 R_0 r_{\rm out}^2 + \left(r_{\rm out}^3 R_0 - 8m_{\rm tot}\right)\mathcal{C}'}{16F_0} \ . \tag{8.21}$$

For $1 < \Gamma < 3/2$, $\mathcal{C}' = d\mathcal{C}/dp\, p' \propto d\mathcal{C}/dp\,(p+\rho) \to 0$ at the surface so that expression (8.21) is finite and it even gives continuity of $m'_{\rm tot}$ across the surface. However, for $3/2 < \Gamma < 2$, $\mathcal{C}' \to \infty$ as the surface is approached, provided that $dF/dR(R_0) \neq 0$ and $dR/dT(T_0) \neq 0$ (note that these conditions are satisfied by generic forms of $f(R)$, *i.e.* whenever an R^2 term or a term inversely proportional to R is present). While $m_{\rm tot}$ keeps finite [as can be shown using $p \sim (r_{\rm out} - r)^{\Gamma/(\Gamma-1)}$, which can be derived integrating eq. (8.14) near the surface], the divergence of $m'_{\rm tot}$ drives to infinity the Riemann tensor of the metric, $\widetilde{R}_{\mu\nu\sigma\lambda}$, and curvature invariants, such as $\widetilde{R}$ or $\widetilde{R}^{\mu\nu\sigma\lambda}\widetilde{R}_{\mu\nu\sigma\lambda}$, as can easily be checked [5]. This singular behaviour would cause unphysical phenomena, such as infinite tidal forces which would destroy anything present at the surface [*cf.* the geodesic deviation equation]. We can then conclude that no physically relevant solution exists for any polytropic EOS with $3/2 < \Gamma < 2$. Of course, polytropes give only simplified models for stars and the EOS in the outer layers is critical for the behaviour of $m'_{\rm tot}$ at the surface in the non-GR case. One would like to use a more accurate EOS, but while this can give regular solutions in many cases (*e.g.* if $p \propto \rho_0$ near the surface), the existence of counter-examples is worrying for the viability of the theory.

Setting aside the surface singularity, we next turn to the behaviour in the interior, focusing on models of neutron stars constructed using an analytical approximation to the FPS (Friedman-Pandharipande-Skyrme) EOS [250].[6] Adding positive powers of R to the Einstein-Hilbert action produces significant effects for compact stars while adding negative ones predominantly affects more diffuse stars. Generically, though, one would expect terms of both types to be added if there is a deviation away from GR. Since the $1/R$ term commonly used in cosmology would have a negligible effect in the interior of a neutron star, we used here $f(R) = R + \epsilon R^2$. As can be seen from eq. (8.7), the metric will be sensitive to derivatives of the matter fields, since R is a function of T. [7]. This

[5] This seems to have been missed in ref. [249].

[6] Since the FPS EOS is a tabulated EOS, its low density limit is not specified. Therefore, one can always build static spherically symmetric solutions which are not singular at the surface by imposing a suitable low-density behaviour (*e.g.,* assuming an isothermal outer layer for the system, which implies $p \propto \rho$ and therefore $\Gamma = 1$ near the surface).

[7] The unusual behaviour of this class of theories has been mentioned in a different context in ref. [251] However, we disagree with the claims made there about the violation of the equivalence principle, because they seem to be based on an ill-posed identification of the metric whose geodesics should coincide with

can be seen in Fig. 8.1: $m_{\rm tot}$, which in GR has a smooth profile, now develops peculiar features when $d\rho/dp$ and $d^2\rho/dp^2$ change rapidly in going from the core to the inner crust and from the inner crust to the outer crust. If $m_{\rm tot}$ were plotted against the radius, these features would look much more abrupt, because they occur in a small range of radii close to the surface. While $m_{\rm tot}$ does not represent a real mass in the interior, such a strong dependence of the metric on the derivatives of the matter fields is not very plausible and could have important consequences.

We have therefore found two unappealing characteristics of Palatini $f(R)$ gravity as applied to stellar models, each of which arises because of the dependence of the metric on higher order derivatives of the matter field. First: whether or not a regular solution can be found depends crucially on the microphysics through the EOS, because EOSs which can be approximated, near the surface, by polytropes with $3/2 < \Gamma < 2$ are ruled out for generic $f(R)$. Second: even if an EOS does allow a regular solution at the surface, the interior metric depends on the first and second derivatives of the density with respect to the pressure, giving a problematic behaviour.

8.3 The interpretation

Gedanken experiments and incompleteness

Clearly, a polytropic EOS is too idealised to give a detailed description for a matter configuration such as an astrophysical star. However, this does not at all make polytropes physically irrelevant. On the contrary, besides being widely used in GR and in Newtonian theory [245], there are at least two physical matter configurations which are *exactly* described by a $\Gamma = 5/3$ polytrope: a monatomic isentropic gas and a degenerate non-relativistic electron gas. Note that this value of the polytropic index lies well within the range $3/2 < \Gamma < 2$, for which surface singularities have been shown to appear, and so Palatini $f(R)$ gravity does not allow a physical solution for these configurations (a solution which is singular at the surface should be discarded as unphysical). One might, therefore, discard Palatini $f(R)$ gravity as a viable alternative to GR already on the basis of such *gedanken* experiments. Alternatively, one must at least accept that the theory, as it stands, is *incomplete*, being incapable of describing configurations, such as a cloud of monatomic gas, which are well-described even by Newtonian gravity. Note that this means in particular that Palatini $f(R)$ gravity does not even reproduce the Newtonian limit in these cases!

It should be stressed that although the fluid description of matter does indeed conceal information about the microphysics of the system, this is by no means the cause of the problem discussed here, nor will abandoning the fluid approximation solve the problem, as we will show in sec. 8.4. On the contrary, one naturally expects that systems such as a monatomic isentropic gas or a degenerate electron gas should be describable by a theory of gravity without resorting to a statistical description. In our opinion, the inability of a

free-fall trajectories.

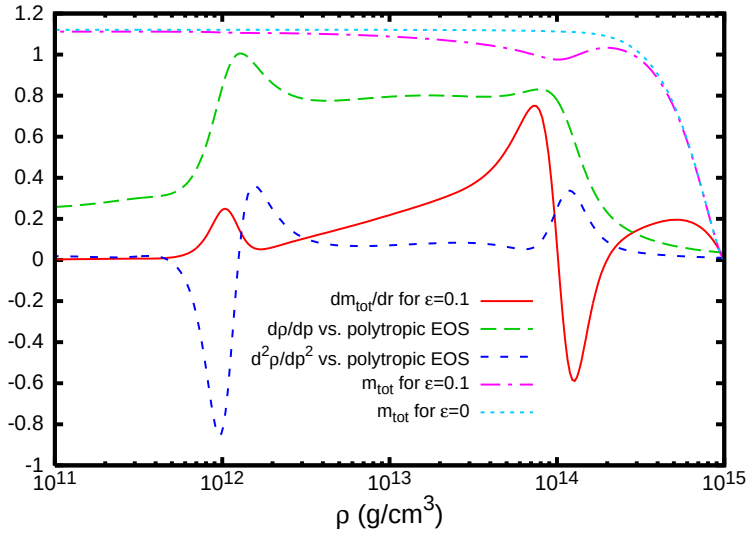

Figure 8.1: *Profiles of $m_{\rm tot}$ (in $M_\odot$) and other associated quantities plotted against density in the interior of a neutron-star with central density $10^{15}{\rm g/cm}^3$ and $p'=0$ in the centre as required by local flatness. We have used the FPS EOS [250] and $f(R)=R+\epsilon R^2$. The dot-dashed line shows $m_{\rm tot}$ as calculated with $\epsilon=0.1$ and the dotted line shows the equivalent curve in GR ($\epsilon=0$); the solid line shows $dm_{\rm tot}/dr$ (in $M_\odot/{\rm km}$) for $\epsilon=0.1$ (this value is orders of magnitude lower than solar system constraints [252]). Note the bumps in the $dm_{\rm tot}/dr$ curve resulting from rapid composition changes in the EOS (the corresponding features in the $m_{\rm tot}$ curve for $\epsilon=0.1$ are less apparent but a noticeable dip is seen at $\rho\sim 10^{14}{\rm g/cm}^3$). To make evident the influence of composition changes, we also show comparisons between the FPS EOS and a polytrope (with $\Gamma=4/3$ and $\kappa=10^{15}$ cgs): the long-dashed and short-dashed curves show $0.1\times(d\rho/dp)_{\rm FPS}/(d\rho/dp)_{\rm polytrope}$ and $0.01\times(d^2\rho/dp^2)_{\rm FPS}/(d^2\rho/dp^2)_{\rm polytrope}$, respectively.*

theory to provide a classical treatment of macroscopic systems without a precise microphysical description is already a very serious shortcoming. This problem does not arise in GR.

8.3.1 Stars and tidal forces

In this section we calculate the tidal forces arising due to the presence of the surface singularities which we discovered in sec. 8.2. A version of this calculation for a particular restricted form of $f(R)$ was performed by Kainulainen *et al.* [246], who found that the lengthscale on which the tidal forces diverge due to the curvature singularity was shorter than the mean free path (MFP) in that case, and concluded that the system was not then well-described using the fluid approximation. We will now show that while this is correct in the particular case which they considered, that is a very special one and is not representative of the general situation. Ref. [246] considered in fact the case of a

neutron star with $f(R) = R - \mu^4/R$ (where $\mu^2 \sim \Lambda$, Λ being the value of the cosmological constant as inferred from cosmological observations). Although $f(R) = R - \mu^4/R$ can be used to obtain the accelerated expansion of the Universe without resorting to Dark Energy or a cosmological constant, there is no basic principle from which to derive this functional form, and in order to justify it one has to invoke phenomenological arguments based on a series expansion of the unknown $f(R)$ coming from a consistent high energy theory. As such, there is no reason to exclude the presence of quadratic or cubic terms, and indeed the observational limits on these terms coming from solar system tests are very loose [252]. We will show that if one takes $f(R) = R - \mu^4/R + \varepsilon R^2$ even with ε being orders of magnitude smaller than the maximum allowed by the solar system constraints, the lengthscale on which the tidal forces diverge is *much* larger than the MFP, even in the case of neutron stars. Incidentally, this was expected because we have already shown in sec. 8.2 how important the effect of such a tiny ε can be in neutron star interiors. However, even if one cancels *by hand* all of the quadratic and cubic terms from the function $f(R)$, thus giving precisely $f(R) = R - \mu^4/R$, the result of ref. [246] still does not apply for sufficiently diffuse systems, where the lengthscale on which the tidal forces diverge is anyway *much* larger than the MFP.

We will now proceed to calculate in detail the tidal force experienced, because of the curvature singularities found in sec. 8.2, by a body falling radially into a polytropic sphere with $\Gamma = 5/3$, as soon as it crosses the surface. Our conclusions apply unchanged also to bodies moving on different orbits, *e.g.* circular ones just below the surface. Throughout the calculation, we use units in which $M_\odot = 1$ (besides, as usual, $G = c = 1$). If we consider the separation vector $\boldsymbol{\eta} = \eta^r \partial/\partial r$, the tidal acceleration in the radial direction is given by the geodesic deviation equation:

$$a \equiv \frac{D^2\eta^r}{D\tau^2} = R^r{}_{ttr}(u^t)^2\eta^r = -\frac{1}{4}e^{A-B}(A'^2 - A'B' + 2A'')(u^t)^2\eta^r \ , \tag{8.22}$$

where τ is the proper time and $D/D\tau$ is the total covariant derivative with respect to it. Using eqs. (8.9)-(8.12) and Mathematica [253], it is easy to show that the combination $A'^2 - A'B' + 2A''$ appearing in this equation depends linearly on F'':

$$A'^2 - A'B' + 2A'' = c_0 + c_1 F'' \ , \tag{8.23}$$

where

$$\begin{aligned} c_0 = \Big\{ & 16F^4 + 40rF'F^3 + 52r^2F'^2F^2 \\ & + 16e^{2B}\pi r^2\left[(f + 16\pi p - FR)r^2 + 2F\right](p+\rho)F^2 \\ & + 24r^3F'^3F - 2e^B\left(2F + rF'\right)\left[3(f + 12\pi p - 4\pi\rho)F'r^3\right. \\ & - F\left(r\left(r\left(f' + 2RF'\right) + 8\pi\left(p + \rho + 2rp'\right)\right) - 4F'\right)r \\ & \left. + F^2\left(R'r^3 + 4\right)\right]F + 3r^4F'^4\Big\} / \left[r^2F^2\left(2F + rF'\right)^2\right] \ , \end{aligned} \tag{8.24}$$

$$c_1 = -\frac{4}{2F + rF'} \,. \tag{8.25}$$

Note that both c_0 and c_1 are finite at the surface, whereas F'' diverges, as already mentioned. Keeping therefore only the divergent term $c_1 F''$, the ratio between the accelerations in the Palatini ("singular") and GR cases is

$$\left|\frac{a_{\rm sing}}{a_{\rm GR}}\right| \approx \frac{|c_1 F''| r_{\rm out}^2 (r_{\rm out} - 2m_{\rm tot})}{8 m_{\rm tot}} \tag{8.26}$$

Using now the fact that R_0 must be $\ll 1$ in our units in order to match the cosmological accelerated expansion (one needs to have $R_0 = 4\Lambda = 12\Omega_\Lambda H_0^2 \sim 10^{-45}$), eq. (8.20) gives $F'' \approx -m_{\rm tot}\mathcal{C}'/[r_{\rm out}(r_{\rm out} - 2m_{\rm tot})]$ and therefore

$$\left|\frac{a_{\rm sing}}{a_{\rm GR}}\right| \approx \frac{|c_1 \mathcal{C}'| r_{\rm out}}{8} \,. \tag{8.27}$$

The derivative of $\mathcal{C}$ with respect to r can easily be calculated from the definition $\mathcal{C} \equiv dF/dp\,(p+\rho)$: using the chain rule, the Euler equation (8.13) and the fact that the trace of the stress energy tensor for a perfect fluid is $T = 3p - \rho$, one has

$$\begin{aligned}
\mathcal{C}' &= \frac{d\mathcal{C}}{dp} p' = -\left[\frac{d^2F}{dp^2}(p+\rho)^2 + \frac{dF}{dp}(1 + \frac{d\rho}{dp})(p+\rho)\right]\frac{A'}{2} \\
&= -\frac{A'}{2}\Bigg\{\mathcal{C} + \frac{dF}{dR}\frac{dR}{dT}\frac{dT}{d\rho}\left(\frac{d\rho}{dp}\right)^2 (p+\rho) + (p+\rho)^2 \times \\
&\left[\frac{dF}{dR}\frac{dR}{dT}\left(-\frac{d^2\rho}{dp^2}\right) + \frac{dF}{dR}\frac{d^2R}{dT^2}\left(3 - \frac{d\rho}{dp}\right)^2 + \frac{d^2F}{dR^2}\left(\frac{dR}{dT}\right)^2\left(3 - \frac{d\rho}{dp}\right)^2\right]\Bigg\}.
\end{aligned} \tag{8.28}$$

Remembering now that $\mathcal{C} = 0$, $d\rho/dp(p+\rho) = 0$ and $dp/d\rho = 0$ at the surface for $\Gamma < 2$ (see sec. 8.2), one can easily rewrite the above equation keeping only the divergent terms:

$$\begin{aligned}
\mathcal{C}' = \frac{dF}{dR}\frac{dR}{dT}\frac{A'}{2}&\left[(p+\rho)\left(\frac{d\rho}{dp}\right)^2 + \frac{d^2\rho}{dp^2}(p+\rho)^2\right] \\
&+ \text{terms going to zero at the surface}
\end{aligned} \tag{8.29}$$

Taking $\Gamma = 5/3$ and using $A' \approx 2m_{\rm tot}/[r_{\rm out}(r_{\rm out} - 2m_{\rm tot})]$ [*cf.* eq. (8.19)], this equation becomes

$$\begin{aligned}
\mathcal{C}' &\approx \frac{dF}{dR}\frac{dR}{dT}\frac{A'}{2}\left[(p+\rho)\left(\frac{d\rho}{dp}\right)^2 + \frac{d^2\rho}{dp^2}(p+\rho)^2\right] \\
&\approx -8\pi\frac{dF}{dR}\frac{3m_{\rm tot}}{25 r_{\rm out}(r_{\rm out} - 2m_{\rm tot})\kappa^2}\left(\frac{p}{\kappa}\right)^{-1/5} \,,
\end{aligned} \tag{8.30}$$

where, in order to pass from the first to the second line, we have used the fact that $dR/dT \approx -8\pi$ close to the surface but at a finite distance below it, for a generic function $f(R) = R - \mu^4/R + \varepsilon R^2$. To see this, one can solve eq. (8.5) and obtain $R = -4\pi T \pm (3\mu^4 + 16\pi^2 T^2)^{1/2}$. Choosing the positive sign in order to have a positive cosmological constant in vacuum, one has $\mu^2 = R_0/\sqrt{3} \sim 10^{-45}$. Then, even very close to the surface, one has $|T| \gg \mu^2$ and $R \approx -8\pi T$.

Integrating the Euler equation (8.13) just below the surface one gets

$$p \approx \left(\frac{2}{5}\right)^{5/2} \left[\frac{m_{\rm tot}}{r_{\rm out}(r_{\rm out} - 2m_{\rm tot})}\right]^{5/2} (r_{\rm out} - r)^{5/2} \kappa^{-3/2} \tag{8.31}$$

hence

$$\rho \approx \left(\frac{2}{5}\right)^{3/2} \left[\frac{m_{\rm tot}}{r_{\rm out}(r_{\rm out} - 2m_{\rm tot})}\right]^{3/2} (r_{\rm out} - r)^{3/2} \kappa^{-3/2} \tag{8.32}$$

Therefore,

$$\left|\frac{a_{\rm sing}}{a_{\rm GR}}\right| \approx \frac{3\sqrt{5}}{25\sqrt{2}}\pi \left|c_1 \frac{dF}{dR}\right| \frac{\sqrt{m_{\rm tot}\, r_{\rm out}}}{\sqrt{r_{\rm out} - 2m_{\rm tot}}} \frac{\kappa^{-3/2}}{\sqrt{r_{\rm out} - r}} \tag{8.33}$$

To calculate the ratio given by eq. (8.33), let us first consider the general case $f(R) = R - \mu^4/R + \varepsilon R^2$. We stress again that one generically expects the presence of the term εR^2, because there is no first principle from which to derive the functional form of $f(R)$, and one has to think of it as the series expansion of an unknown $f(R)$ coming from a consistent high-energy theory of gravity. As can easily be seen from eq. (8.5), the quadratic term does not influence the vacuum value R_0 of the curvature scalar, which acts as the effective cosmological constant. Basically for this reason, the quadratic term is essentially unconstrained by cosmological data and solar system tests only allow weak constraints to be placed on it [252]. Taking now $\varepsilon \sim 0.1$ in our units (a value several orders of magnitude smaller than the upper limit coming from solar system tests [252]), just below the surface we have $dF/dR \approx 2\varepsilon \approx 0.2$ and $c_1 \approx -2/F_0 \approx -3/2$ (because $F' \sim 0$ near to the surface). From eq. (8.33), one then obtains

$$\left|\frac{a_{\rm sing}}{a_{\rm GR}}\right| \approx 0.2 \frac{\sqrt{m_{\rm tot}\, r_{\rm out}}}{\sqrt{r_{\rm out} - 2m_{\rm tot}}} \frac{\kappa^{-3/2}}{\sqrt{r_{\rm out} - r}} \,. \tag{8.34}$$

In the case of a neutron star as modelled with a polytropic EOS ($\kappa \approx 4$, $r_{\rm out} \approx 10$ and $m_{\rm tot} \approx 1$), one therefore has

$$\left|\frac{a_{\rm sing}}{a_{\rm GR}}\right| \approx 0.02 (r_{\rm out} - r)^{-1/2} \,, \tag{8.35}$$

and the ratio $|a_{\rm sing}/a_{\rm GR}|$ is large at distances below the surface at which the fluid approximation is certainly valid. For instance, $|a_{\rm sing}/a_{\rm GR}| \sim 20$ for $r_{\rm out} - r \sim 10^{-6} \sim 1.5$ mm, $|a_{\rm sing}/a_{\rm GR}| \sim 600$ for $r_{\rm out} - r \sim 10^{-9} \sim 1.5$ μm, $|a_{\rm sing}/a_{\rm GR}| \sim 2 \times 10^4$ for $r_{\rm out} - r \sim 10^{-12} \sim 1.5$ nm. Note also that the ratio $|a_{\rm sing}/a_{\rm GR}|$ scales proportionally with the value of

ε, which we have taken, as already mentioned, to be several orders of magnitude smaller than the upper limits coming from solar system tests [252].

Let us now consider instead the case $f(R) = R - \mu^4/R$, as used in ref. [246]. First, we need to evaluate c_1. Noting that $c_1 \to -2/F_0 = -3/2$ as $r \to r_{\rm out}$, because $F' = 0$ at the surface (*cf.* sec. 8.2), we have $c_1 \sim 1$ just below the surface. In order to see what happens instead at a finite distance below the surface, note first that $dF/dR \approx -2R_0^2/(3R^3)$. As already mentioned, solving eq. (8.5) and imposing that the cosmological constant $\Lambda = R_0/4$ in vacuum is positive, one gets $R = -4\pi T + (3\mu^4 + 16\pi^2 T^2)^{1/2} \approx 8\pi\rho$ for $\rho \gg R_0$. We can then write $dF/dR \approx -2/[3(8\pi)^3]R_0^2/\rho^3$ for $\rho \gg R_0$, and therefore $F' = (dF/dR)\,(dR/dT)\,(dT/d\rho)\,\rho' \sim \rho'\,(R_0/\rho)^3/R_0$. Because $R_0 \sim 10^{-45}$, it is clear $rF' \ll F$ even at finite distances below the surface. From eq. (8.25) it then follows that $c_1 \approx -2/F_0 = -3/2$ also at finite distances below the surface.

Let us evaluate eq. (8.33) for $\rho \gg R_0$: using $c_1 \approx -3/2$ and $dF/dR \approx -2/[3(8\pi)^3]R_0^2/\rho^3$, it becomes

$$\left|\frac{a_{\rm sing}}{a_{\rm GR}}\right| \approx \frac{3\pi}{25(8\pi)^3}\left(\frac{5}{2}\right)^5 R_0^2\kappa^3 m_{\rm tot}^{-4} r_{\rm out}^5 (r_{\rm out} - 2m_{\rm tot})^4 (r_{\rm out} - r)^{-5}. \tag{8.36}$$

It is therefore clear that tidal forces become increasingly more important, even in the particular case $f(R) = R - \mu^4/R$, for spheres with larger radius. As such, even for this particular form of $f(R)$, the lengthscale on which the tidal forces diverge is much larger than the lengthscale on which the fluid approximation is valid, if one considers less compact systems: some examples are worked out in the Appendix.

In conclusion, we have shown that the fluid approximation is still valid on the scale at which the tidal forces diverge just below the surface of a polytropic sphere in the case of the generic functions $f(R)$ likely to arise in practice in a cosmological scenario. Even in the special case considered by Kainulainen *et al.* [246], this continues to hold for configurations which are sufficiently diffuse.

8.4 Physical and mathematical nature of the problem

8.4.1 Differential structure and cumulativity

It is clear from the above that the nature of the problem discussed here does not lie in the fluid approximation or in the specifics of the approach followed in sec. 8.2, but is related to intrinsic characteristics of Palatini $f(R)$ gravity. These concern the differential structure of the action (8.1) and the resulting field equations.

We recall that the Lagrangian of the action (8.1) is an algebraic function of $R = g^{\mu\nu}R_{\mu\nu}$ and that $R_{\mu\nu}$ is constructed from the independent connection $\Gamma^\lambda{}_{\mu\nu}$. In more detail,

$$R^\mu{}_{\nu\sigma\lambda} = -\partial_\lambda\Gamma^\mu{}_{\nu\sigma} + \partial_\sigma\Gamma^\mu{}_{\nu\lambda} + \Gamma^\mu{}_{\alpha\sigma}\Gamma^\alpha{}_{\nu\lambda} - \Gamma^\mu{}_{\alpha\lambda}\Gamma^\alpha{}_{\nu\sigma}\,, \tag{8.37}$$

and contracting the first and the third index one gets (see refs. [212, 238] for further de-

tails)

$$R_{\mu\nu} = R^{\lambda}{}_{\mu\lambda\nu} = \partial_\lambda \Gamma^{\lambda}{}_{\mu\nu} - \partial_\nu \Gamma^{\lambda}{}_{\mu\lambda} + \Gamma^{\lambda}{}_{\sigma\lambda}\Gamma^{\sigma}{}_{\mu\nu} - \Gamma^{\lambda}{}_{\sigma\nu}\Gamma^{\sigma}{}_{\mu\lambda}. \tag{8.38}$$

It follows from this that $f(R)$ has no *a priori* dependence on derivatives of the metric. Also, R depends only linearly on the first derivatives of the connection *i.e.*, at least in the case where f is linear in R (which leads to GR), there are no $\partial\Gamma\partial\Gamma$ terms (indices suppressed) as there would usually be in a field theory! One might expect that allowing f to be non-linear in R would introduce $\partial\Gamma\partial\Gamma$ terms and solve this last problem, but we will see shortly that this is not the case. Note also that, since the metric has no *a priori* relation with the connection, one is dealing with a field theory with two independent fields, and so one cannot argue that having no quadratic terms in the connection is expected because the connection already includes derivatives of the metric.

This lack of dynamics in the action is also mirrored in the field equations (8.2) and (8.3). Variation with respect to the metric leads to eq. (8.2), which includes no derivatives of the metric. As already mentioned, contraction of eq. (8.2) gives eq. (8.5), which algebraically relates R and T for a given $f(R)$. Variation with respect to the connection leads to eq. (8.3), after some integration by parts to "free" the connection. For a linear function $f(R)$, this equation is just the definition of the Levi-Civita connection. When $f(R)$ is non-linear, instead, eq. (8.3) seems to include second derivatives of the connection. However, this is misleading because R can be completely eliminated in favour of T by using eq. (8.5) and, therefore, eq. (8.3) can be trivially solved to give the connection as a function of the metric and the matter fields. As already mentioned, following these steps one can completely eliminate the connection in favour of the metric and the matter fields, and turn eqs. (8.2) and (8.3) into the single-field representation (8.7). This representation of the theory is more convenient and more familiar for discussing the dynamics. It also highlights once more that the metric fully describes the geometry, which is indeed pseudo-Riemannian, and that the independent connection is just an auxiliary field [238, 239, 240].

It is also interesting to note that one could introduce an auxiliary scalar $\phi = F$ and re-write eq. (8.7) as

$$\begin{aligned}\widetilde{G}_{\mu\nu} = \frac{8\pi}{\phi}T_{\mu\nu} - \frac{1}{2}g_{\mu\nu}\left(R - \frac{f}{\phi}\right) + \frac{1}{\phi}\left(\widetilde{\nabla}_\mu\widetilde{\nabla}_\nu - g_{\mu\nu}\widetilde{\Box}\right)\phi \\ - \frac{3}{2}\frac{1}{\phi^2}\left((\widetilde{\nabla}_\mu\phi)(\widetilde{\nabla}_\nu\phi) - \frac{1}{2}g_{\mu\nu}(\widetilde{\nabla}\phi)^2\right),\end{aligned} \tag{8.39}$$

while, setting $V(\phi) = R\phi - f$, eq. (8.5) can be re-written as

$$2V(\phi) - \phi V'(\phi) = 8\,\pi\,T. \tag{8.40}$$

Expressions (8.39) and (8.40) are the field equations of a Brans–Dicke theory with Brans-Dicke parameter $\omega_0 = -3/2$, *i.e.* a theory described by the action

$$S = \frac{1}{16\,\pi}\int d^4x\sqrt{-g}\left(\phi\widetilde{R} + \frac{3}{2\phi}\partial_\mu\phi\partial^\mu\phi - V(\phi)\right) + S_M(g_{\mu\nu},\psi), \tag{8.41}$$

(see also refs. [239, 254, 255] for more details about the equivalence of Palatini $f(R)$ gravity and $\omega_0 = -3/2$ Brans-Dicke theory).

Returning to eq. (8.7), we note that this is a second order partial differential equation in the metric, just as in the case of GR, but that the left hand side includes up to second derivatives of F and consequently of T [$F = F(R)$ and $R = R(T)$]. Usually, the matter action includes derivatives of the matter fields ψ (if the equation of motion of the matter fields is to be of second order, the matter action has to be quadratic in the first derivatives of the matter fields). Therefore, generically one has $T = T(\partial\psi, \psi)$, implying that eq. (8.7) includes up to third derivatives of the matter fields!

In GR and in most of the proposed alternatives to it, the field equations include only first derivatives of the matter fields[8]. The higher differential order in the metric with respect to the differential order in the matter fields guarantees that the metric comes as an integral over the matter fields. Therefore, any discontinuities in the matter are "smoothed out" and are not inherited by the geometry (cumulativity of gravity). We recall that in general the metric is not allowed to become a delta function or a step function (although the latter is allowed if no Dirac deltas are produced in the field equations, *i.e.* if the metric, in spite of being discontinuous, is a solution of the field equations in the sense of distributions: see for instance ref. [256], section 3.7). However, this is clearly not true in Palatini $f(R)$ gravity or in $\omega_0 = -3/2$ Brans–Dicke theory, since the differential order of the field equations in the matter fields is actually higher than in the metric, implying that the latter is not necessarily an integral over the matter fields, but can be *algebraically* related to the matter fields and even to their derivatives. Because of this, a discontinuity in the matter fields or in their derivatives can lead to unacceptable singularities. A similar behaviour has been demonstrated in the post-Newtonian limit of the theory, where the post-Newtonian metric becomes algebraically dependent on the matter density [244].

This unusual differential structure of Palatini $f(R)$ gravity is at the root of the surface singularities discovered in sec. 8.2. The polytropic description of matter was used in sec. 8.2 only because this made it possible to find analytic solutions near the surface and demonstrate the problem without resorting to numerical techniques. In fact, a more detailed description of the matter would make the problem even more acute. To see this, note that in the case of a perfect fluid one has $T_{\mu\nu} = T_{\mu\nu}(\rho, p)$, *i.e.* the stress-energy tensor does not include any derivatives, unlike the case of a microscopic description of matter. The fluid approximation actually "smoothes out" the matter distribution with respect to the microscopic description. This also explains why no singularities appear for $1 < \Gamma < 3/2$: these values of Γ give a smooth passage from the interior to the exterior. In conclusion: abandoning the fluid approximation would just increase even further the differential order of the field equations in the matter fields and make it easier for singularities to appear.

As a further confirmation that the introduction of microphysics cannot solve the problems caused by the algebraic dependence of R on T [see eq. (8.5)] or, in the equivalent

[8] Adopting a "macroscopic" viewpoint, the field equations do not include any derivatives of the matter *variables* (*e.g.,* density, pressure), which depend on the *first* derivatives of the matter fields ψ.

action (8.41), by the algebraic dependence of ϕ on T [see eq. (8.40)], let us note that this feature of Palatini $f(R)$ gravity introduces corrections to the standard model of particle physics already at the meV energy scale (see ref. [254] and ref. [257]). Both the calculation of ref. [254] and that of ref. [257] are performed in the Einstein frame. Although the use of the Einstein frame has been criticised [258][9], this frame is equivalent to the Jordan frame and both are perfectly suitable for performing calculations [254]. However, one should remember that particles in vacuum follow geodesics of the Jordan frame metric, so this is the metric which becomes approximately Minkowski in the laboratory reference frame. This makes the Jordan frame calculation simpler and more transparent than the one in the Einstein frame. For this reason, and in order to highlight once again the problems caused by the algebraic dependence of R on T, we briefly redo the calculation of refs. [254] and [257] in the Jordan frame. Let us first consider the equivalent action (8.41) and take the matter to be represented by a scalar field H (*e.g.*, the Higgs boson), the Lagrangian of which reads

$$\mathcal{L}_m = \frac{1}{2\hbar}\left(g^{\mu\nu}\partial_\mu H \partial_\nu H - \frac{m_{\rm H}^2}{\hbar^2}H^2\right) \tag{8.42}$$

(we recall that we are using units in which $G = c = 1$). The vacuum of the action (8.41) with eq. (8.42) and $f(R) = R - \mu^4/R$ [which implies $V(\phi) = 2\mu^2(\phi-1)^{1/2}$] can easily be found to be $H = 0$, $\phi = 4/3$ [the solution of eq. (8.40) with $T = 0$] and

$$\begin{aligned} g_{\mu\nu}dx^\mu dx^\nu = &-\left(1 - \frac{2M_{\rm Earth}}{r} - \frac{\mu^2 r^2}{4\sqrt{3}}\right)dt^2 \\ &+ dr^2 \Big/ \left(1 - \frac{2M_{\rm Earth}}{r} - \frac{\mu^2 r^2}{4\sqrt{3}}\right) + r^2 d\Omega^2 \approx \eta_{\mu\nu}dx^\mu dx^\nu \end{aligned} \tag{8.43}$$

(which is indistinguishable from the Minkowski metric for the purposes of a particle physics experiment because $\mu^2 \sim \Lambda$ and $r \approx R_{\rm Earth}$). One can then expand the action to second order around this vacuum (as usual the first order action is identically zero because the field equations are satisfied to zeroth order). However, it is easy to show that perturbing eq. (8.40) one gets $\delta\phi \sim T/\mu^2 \sim m_{\rm H}^2 \delta H^2/(\hbar^3\mu^2)$ at energies lower than the Higgs mass ($m_{\rm H} \sim 100 - 1000$ GeV): replacing this expression in the action (8.41) perturbed to second order one immediately gets that the effective Lagrangian for the

[9] If the independent connection is allowed to enter the matter action, the results of refs. [254] and [257] will of course cease to hold, as pointed out in ref. [258]. In this case, also the surface singularities that we found in sec. 8.2 may disappear (see also sec. 8.4.2). However, such a theory would be a *generalisation* of Palatini $f(R)$ gravity [see the action (8.1)], known in the literature as *metric affine* $f(R)$ *gravity* [238].

Higgs scalar is

$$\mathcal{L}_m^{\text{effective}} \sim \frac{1}{2\hbar}\left(g^{\mu\nu}\partial_\mu\delta H\partial_\nu\delta H - \frac{m_{\rm H}^2}{\hbar^2}\delta H^2\right) \times\left[1+\frac{m_{\rm H}^2\delta H^2}{\mu^2\hbar^3}+\frac{m_{\rm H}^2(\partial\delta H)^2}{\mu^4\hbar^3}\right] \tag{8.44}$$

at energies $k \ll m_{\rm H}$. At an energy $k = 10^{-3}$ eV (corresponding to a lengthscale $L = \hbar/k = 2\times10^{-4}$ m), using the fact that $\mu^2 \sim \Lambda \sim 1/(H_0^{-1})^2$ (where $H_0^{-1} = 4000$ Mpc is the Hubble radius) and $\delta H \sim m_{\rm H}$ (because $k \ll m_{\rm H}$) and remembering that we are using units in which $G = c = 1$, it is easy to check that the first correction is of the order $m_{\rm H}^2\delta H^2/(\mu^2\hbar^3) \sim (H_0^{-1}/\lambda_{\rm H})^2(m_{\rm H}/M_{\rm P})^2 \gg 1$, where $\lambda_{\rm H} = \hbar/m_{\rm H} \sim 2\times10^{-19} - 2\times10^{-18}$ m is the Compton length of the Higgs and $M_{\rm P} = \hbar^{1/2} = (\hbar c^5/G)^{1/2} = 1.2\times10^{19}$ GeV is the Planck mass.[10] Similarly, the second correction is of the order $m_{\rm H}^2(\partial\delta H)^2/(\mu^4\hbar^3) \sim (H_0^{-1}/\lambda_{\rm H})^2(m_{\rm H}/M_{\rm P})^2(H_0^{-1}/L)^2 \gg 1$.

Note that replacing $\delta\phi \sim m_{\rm H}^2\delta H^2/(\hbar^3\mu^2)$ in eq. (8.41) gives also that the coupling of matter to gravity is described by the interaction Lagrangian

$$\mathcal{L}_{\rm int} \sim \frac{m_{\rm H}^2\delta H^2}{\hbar^3}\left(\delta g + \frac{\partial^2\delta g}{\mu^2}\right) \sim \frac{m_{\rm H}^2\delta H^2}{\hbar^3}\delta g\left[1+\left(\frac{H_0^{-1}}{L}\right)^2\right]. \tag{8.45}$$

It is therefore clear that also the coupling to gravity becomes non-perturbative at microscopic scales. This is, once again, a consequence of the algebraic dependence of ϕ on T, encoded in eq. (8.40), and this is in agreement with the singularities that we discuss in this chapter.

8.4.2 Overcoming the problem

In section 8.4.1 we have traced the root of the problem: it lies in the awkward differential structure of the field equations, in which the matter field derivatives are of higher order than the metric derivatives. This introduces non-cumulative effects and makes the metric extremely sensitive to the local characteristics of the matter. With this in mind, it is not difficult to propose a possible way out. Clearly, one would like to restore the cumulative nature of gravity. This requires the introduction of more dynamics into the gravitational sector of the theory. As an example of how to introduce more dynamics, let us consider a theory described by the action:

$$S = \frac{1}{16\,\pi}\int d^4x\sqrt{-g}\,(R + aR^{\mu\nu}R_{\mu\nu}) + S_M(g^{\mu\nu},\psi)\,, \tag{8.46}$$

where a should be chosen so as to have the correct dimensions. The term $R^{\mu\nu}R_{\mu\nu}$ is quadratic in the derivatives of the connection [see eq. (8.38)]. This implies that the action

[10] Equivalently, one can write the first correction as a self-interaction term $m_{\rm H}^4\delta H^4/(\mu^2\hbar^6)$: restoring the dependence on G this term becomes $Gm_{\rm H}^4\delta H^4/(\mu^2\hbar^6)$. In "particle physics units" $\hbar = c = 1$, the coupling constant is dimensionless and is given by $Gm_{\rm H}^4/\mu^2 \sim (H_0^{-1}/\lambda_{\rm H})^2(m_{\rm H}/M_{\rm P})^2 \gg 1$.

(8.46), even though linear in both R and $R^{\mu\nu}R_{\mu\nu}$, is quadratic in the derivatives of the connection and will not lead to an algebraic equation for the connection, unlike the action (8.1). Indeed, the field equations that one derives by varying the action (8.46) with respect to the metric and the connection are, respectively,

$$R_{(\mu\nu)} + 2aR^{\sigma}_{\mu}R_{\sigma\nu} - \frac{1}{2}\left(R + aR^{\sigma\lambda}R_{\sigma\lambda}\right) g_{\mu\nu} = 8\pi\, T_{\mu\nu}, \tag{8.47}$$

$$\nabla_{\lambda}\left[\sqrt{-g}\,(g^{\mu\nu} + 2aR^{\mu\nu})\right] = 0, \tag{8.48}$$

and eq. (8.48) cannot be algebraically solved for the connection. Also, this theory cannot be re-written as an $\omega_0 = -3/2$ Brans–Dicke theory. In summary, a theory described by action (8.46) does not seem to be sharing the unwanted characteristic of Palatini $f(R)$ gravity: that after eliminating the connection, one ends up with the matter field derivatives being of higher order than those of the metric. In particular, R cannot be expressed as an algebraic function of T through the trace of eq. (8.47), as in the case of eq. (8.5), nor can the independent connection be algebraically expressed simply in terms of the metric and derivatives of the matter fields (therefore introducing the higher differential order in the matter fields when it is replaced in the field equations).

Theories with higher order invariants in the action, such as $R_{\mu\nu}R^{\mu\nu}$, have recently been considered in the Palatini formalism in ref. [259]. Clearly, a more detailed analysis of the dynamics of such theories is needed in order to show in a clear way whether they exhibit the problem discussed here or other viability issues. Here we have used them solely to demonstrate that it might be possible to overcome the issues discussed here by generalising the action. This clarifies the following point: such shortcomings are not generic to Palatini variation, but seem to be a specific problem of Palatini variation when used with the specific choice of $f(R)$ actions.

8.5 Conclusions

In this chapter, we have discovered the presence of curvature singularities at the surface of polytropic spheres in Palatini $f(R)$ gravity. Simple gedanken experiments lead us to conclude that the presence of these singularities casts serious doubts on the viability of the gravity theory. Concerning the objection, raised in ref. [246], that polytropic EOS's are too idealised to allow one to rule out Palatini $f(R)$ gravity, we stress that among the EOS's not giving a regular static spherically symmetric solution there are perfectly physical cases such as a degenerate non-relativistic electron gas or an isentropic monatomic gas. Regular solutions for these configurations exist even in Newtonian mechanics, and we have argued that a theory not providing such solutions should be considered, at best, as being incomplete and as being disfavoured for giving viable alternatives to GR. We have also presented quantitative results for the magnitude of the tidal forces exerted just below the surface of polytropic spheres, showing that, for generic forms of $f(R)$, the lengthscale on which the tidal forces diverge due to the curvature singularities is *much* larger than the lengthscale at which the fluid approximation breaks down. This gener-

alises the calculation of Kainulainen *et al.* [246]: while their result (that the tidal forces only diverge at lengthscales on which the fluid approximation is not valid) is correct for their particular choice of $f(R)$ and for neutron stars, we find that it does not hold, even with their choice of $f(R)$, for more diffuse configurations and does not hold, even in the case of neutron stars, for more plausible choices of $f(R)$. Finally, an analysis of the differential structure of the field equations for the theory has been presented, which sheds light on the origin of the problem, showing that the appearance of singularities is not related to the fluid approximation. On the contrary, abandoning the fluid approximation would make the problem even more acute. Moreover, we have shown that the same problem should be expected for any theory which includes fields other than the metric for describing the gravitational interaction (*e.g.* scalar fields) which are algebraically related to matter rather than dynamically coupled. In this case one can always solve the field equations for the extra field and insert the solution into the field equation for the metric, inducing a dependence of the metric on higher derivatives of the matter fields. An example of such a theory is a scalar-tensor theory with Brans-Dicke parameter $\omega = -3/2$, which is anyway an equivalent representation of Palatini $f(R)$ gravity [239]. The addition of more dynamics to the theory seems to be a potential way out of this difficulty.

Appendix

In this appendix we evaluate eq. (8.36) – which gives the ratio $a_{\rm sing}/a_{\rm GR}$ in the special case of $f(R) = R - \mu^4/R$ – in several contexts. Our calculations will show that even with this special choice of $f(R)$, the fluid approximation is still valid on the scale at which the tidal forces diverge if the configuration under consideration is sufficiently diffuse. As in section 8.3.1, we use units in which $G = c = M_\odot = 1$.

Let us first consider a solar type star with mass $m_{\rm star} \approx 1$ surrounded by a gas cloud with mass $m_{\rm cloud} \approx 0.01$ and radius $r_{\rm out} \approx 10^{14}$ km, composed of monatomic isentropic gas. This is a perfectly physical configuration, although possibly not an *astrophysically* fully realistic one (note however that $r_{\rm out} \approx 10^{14}$ km is approximately the outer radius of the Oort cloud). The total mass of such a system is $m_{\rm tot} \approx m_{\rm star} + m_{\rm cloud} \approx 1$, and the polytropic constant of the cloud is $\kappa \approx 9 \times 10^{12}$. From eq. (8.36), one gets

$$\left|\frac{a_{\rm sing}}{a_{\rm GR}}\right| \approx 6 \times 10^{70} (r_{\rm out} - r)^{-5} \,, \tag{8.49}$$

and the tidal force becomes comparable to that of GR at a distance below the surface comparable to $r_{\rm out}$! Taking, for instance, a value of $r_{\rm out} - r \approx r_{\rm out}/10 \sim 10^{13}$, the tidal forces in Palatini $f(R)$ gravity would be 6 orders of magnitude larger than in GR. At this distance from the surface, the mean distance between the particles of the fluid is $\ell \approx 1/n^{1/3} \approx (m_{\rm p}/\rho)^{1/3} \approx 10^{-5}$ (where $n = \rho/m_{\rm p}$ is the number density and $m_{\rm p} \sim 10^{-57}$ is the mass of the proton). An upper limit for the MFP at this distance from the surface can be calculated assuming a cross section $\sigma \sim (1\,\text{Å})^2 \approx 5 \times 10^{-27}$, giving

$\ell_{\rm MFP} \sim 1/(n\sigma) \sim m_{\rm p}/(\rho\sigma) \sim 10^{11} \ll r_{\rm out} - r$ [11]. Also, note that the average velocity of the particles in the cloud can be evaluated from $p = nk_{\rm B}T$ ($k_{\rm B}$ and T being respectively Boltzmann's constant and the temperature) using eqs. (8.31) and (8.32), and is $v_{\rm av} \sim \{m_{\rm tot}(r_{\rm out}-r)/[r_{\rm out}(r_{\rm out}-2m_{\rm tot})]\}^{1/2}$. For $r_{\rm out}-r \sim r_{\rm out}/10$, one has $v_{\rm av} \sim 4\times 10^{-8}$, which is comparable with the virial velocity $v_{\rm virial} \sim (m_{\rm tot}/r)^{1/2} \sim 10^{-7}$, and so the polytropic coefficient κ needed to support the cloud is plausible. In conclusion: for this configuration, the lengthscale on which the tidal forces in Palatini $f(R)$ gravity are larger than in GR is certainly larger than the lengthscale on which the fluid approximation is valid, whether this scale is taken to be the mean interparticle distance or the MFP.

We would argue, however, that the relevant scale is actually the interparticle distance, because we are considering here static *equilibrium* configurations. A way to understand this point is to consider how one derives the hydrodynamic equations from the Vlasov equation (*i.e.*, the conservation equation for the phase-space distribution $f(\boldsymbol{x},\boldsymbol{v})$ in the case of a *collisionless* fluid, that is, one with *infinite* MFP; see for instance ref. [263], paragraph 27):

$$\frac{\partial f}{\partial t} + \frac{\partial f}{\partial x^i} v^i + \frac{\partial f}{\partial v^i}\frac{F^i}{m} = 0 \, , \tag{8.50}$$

where $v^i = dx^i/dt$ is the velocity, m is the mass of the particles and F^i is the force (thought of as dependent only on position and not on velocity). By integrating over all velocities, one easily obtains the mass conservation equation $\partial_t\rho + \boldsymbol{\nabla}\cdot(\rho\bar{\boldsymbol{v}}) = 0$, where $\rho = m\int f d^3v$ is the density and $\bar{v}^i = m\int f v^i d^3v/\rho$ is the average (*i.e.*, macroscopic) velocity. Similarly, one can multiply eq. (8.50) by v^i and integrate over all velocities. If the velocity distribution is isotropic [12] one then gets the Euler equation $(\partial_t + \bar{\boldsymbol{v}}\cdot\boldsymbol{\nabla})\bar{\boldsymbol{v}} = -(\boldsymbol{\nabla}p)/\rho + \boldsymbol{F}/m$, where one uses the isotropy of the velocity distribution to define the pressure as $p\delta_{ij} = m\int f(v^i-\bar{v}^i)(v^j-\bar{v}^j)d^3v$. If the phase-space distribution f is specified, the mass conservation and the Euler equations are clearly a closed system of equations. Therefore, one does not need to consider higher order moments of the Vlasov equation, and the system under consideration is a fluid in spite of the MFP being infinite. A typical example of this situation is, for instance, that of Dark Matter in a Friedmann-Robertson-Walker universe. Since the velocity distribution is isotropic because of the cosmological principle,

[11] This is an upper limit because it assumes a "geometrical" cross section for encounters between the atoms (1 Å is approximately the size of a hydrogen atom). However, for hydrogen-hydrogen collisions in the lab, $\sigma({\rm HH}) \sim 20$ Å^2 [260] while, for instance, hydrogen-lithium collisions have cross sections which are about 1200 Å^2 [261]. More importantly, if the fluid is (even partly) ionised, the cross section can be *much* larger, because Coulomb forces are long range (in strongly coupled plasmas it is actually common to have a MFP shorter than the interparticle distance [262]).

[12] Of course, one may object that if the fluid is collisionless there is no interaction which can make the velocity distribution isotropic. However, we are interested here in showing that for equilibrium configurations the MFP has nothing to do, from the conceptual point of view, with the lengthscale at which the fluid approximation breaks down. Moreover, one can always think of a tiny interaction between the particles (resulting in a *huge* MFP) which can make the velocity distribution isotropic in a sufficiently long time (comparable with the *mean free time*). From the conceptual point of view, one can also think of shooting a beam of collisionless particles into a box (or a potential well): the initially focused velocity distribution will become isotropic due to the small irregularities in the walls of the box or in the gravitational field.

Dark Matter can be treated, at the background level, as being a fluid (*cf.* for instance (3.10)–(3.12) of ref. [264]). Similarly, for a gas trapped in a box, the fluid approximation is valid on scales larger than the interparticle distance, whereas the MFP can be infinite if the fluid is non-collisional. This is indeed the case considered in the textbook derivation of the perfect gas law (see, for instance, Landau, Lifshitz and Pitaevskii [265], chapter 4), where the only necessary hypothesis is the isotropy of the velocity distribution. The role of the box is, in our case, played by the gravitational potential well.

Let us now consider a polytropic sphere with $m_{\rm tot} \approx 0.1$ and $r_{\rm out} \approx 200 R_\odot \approx 10^8$ ($R_\odot$ being the radius of the Sun). The polytropic constant is then $\kappa \approx 2 \times 10^7$, and eq. (8.36) becomes

$$\left| \frac{a_{\rm sing}}{a_{\rm GR}} \right| \approx 10^5 (r_{\rm out} - r)^{-5} \tag{8.51}$$

At a distance of ~ 1.5 km below the surface, therefore, tidal forces are $\sim 10^5$ times stronger in Palatini gravity than in GR, while the forces in the two cases become comparable at a distance $\gtrsim 15$ km. Now, from eq. (8.32), at a distance $r_{\rm out} - r \approx 1.5$ km ≈ 1 we have $\rho \approx 10^{-37} \sim 10^8 R_0$. Although $r_{\rm out} - r$ is certainly smaller than the *upper* MFP limit introduced above, at this density the mean distance between the particles of the fluid is $\ell \approx 1/n^{1/3} \approx (m_{\rm p}/\rho)^{1/3} \approx 10^{-7} \sim 0.1$ mm.

The same considerations apply, although marginally, for a polytropic sphere with $m_{\rm tot} \approx 1$ and $r_{\rm out} \approx R_\odot \approx 5 \times 10^5$. The polytropic constant is then $\kappa \approx 2 \times 10^5$, and eq. (8.36) becomes

$$\left| \frac{a_{\rm sing}}{a_{\rm GR}} \right| \approx 10^{-26} (r_{\rm out} - r)^{-5} \ , \tag{8.52}$$

from which it follows that the difference between the tidal forces becomes important for $r_{\rm out} - r \lesssim 7 \times 10^{-6} \sim 1$ cm. At this distance below the surface the density is $\rho \approx 5 \times 10^{-34} \sim 10^{11} R_0$, and the mean distance between the fluid particles is $\ell \approx 1/n^{1/3} \approx (m_{\rm p}/\rho)^{1/3} \approx 10^{-8} \sim 0.01$ mm.

Chapter 9

Testing Gauss-Bonnet gravity with solar system experiments

Oggi anche il cretino è specializzato.

E. Flaiano

In this chapter, we derive the parameterised post-Newtonian (PPN) expansion for gravitational theories with a scalar field coupled to the Gauss-Bonnet invariant and we discuss the comparison of these theories with solar system experiments.

9.1 The post-Newtonian expansion

As we have seen in chapter 7, the observed late time accelerated expansion of the universe, combined with the problems that arise when trying to rationalise it with the simplest of explanations, such as a cosmological constant, have triggered an increased interest in finding alternatives for the nature of dark energy. Scalar fields, widely used in the inflationary paradigm [266], constitute a familiar way of providing accelerated expansion. Scalar-tensor theory is therefore an appealing candidate as an alternative theory of gravity that can provide the desired cosmological dynamics [267]. However, there are motivations from String theory to believe that scalar fields might not be coupled to the Ricci scalar, as in scalar-tensor theory, but to the Gauss-Bonnet term,

$$\mathcal{G} = R^2 - 4R^{\mu\nu}R_{\mu\nu} + R^{\mu\nu\kappa\lambda}R_{\mu\nu\kappa\lambda}, \tag{9.1}$$

which is topologically invariant in four dimensions.

To be more precise, one expects to find two types of scalar fields in the low energy effective action of gravity coming from heterotic String theory: moduli, ϕ, which are related to the size and shape of the internal compactification manifold, and the dilaton

σ, which plays the role of the string loop expansion parameter. There are reasons to believe that moduli generally couple to curvature squared terms [268]. Moreover, since moduli dependent higher loop contributions (such as terms cubic or higher order in the Riemann tensor) vanish, a coupling of moduli with the Gauss-Bonnet term is particularly interesting [268, 269]. On the other hand the dilaton usually couples to the the Ricci scalar and consequently to matter in the Einstein frame, and there are reasons to believe that it might evolve in such a way as to settle to a constant [270]. Under these assumptions the effective low energy gravitational action takes the form

$$S = \int d^4x\sqrt{-g}\left[\frac{R}{2\kappa^2} - \frac{\lambda}{2}\partial_\mu\phi\partial^\mu\phi - V(\phi) + f(\phi)\mathcal{G}\right], \tag{9.2}$$

where $\kappa^2 = 8\pi G$, λ is $+1$ for a canonical scalar field and -1 for a phantom field ($c = \hbar = 1$), and where $V(\phi)$ and $f(\phi)$ are respectively the potential of the scalar field and its coupling to the Gauss-Bonnet invariant. A straightforward generalisation of the action is to include a kinetic term and a coupling with $\mathcal{G}$ for the dilaton σ. This will not concern us here but we will discuss how we expect it to affect our results.

Remarkably, it has been shown that action (9.2) can lead to a theory of gravity with desirable phenomenology, including inflation and accelerated expansion [271, 272]. Such a theory seems to fit observational data related to cosmology adequately [273] and avoid past and future singularities [269, 271]. However, a gravitational theory which can pose a viable alternative to GR should also have the correct Newtonian and post-Newtonian limits, since solar system tests provide stringent constraints and the most accurate measurements. This is the issue that will concern us here. Note that we will not consider the case where $\lambda = 0$ and the scalar field has no kinetic term in the action. Such actions are dynamically equivalent to an action with a general function of $\mathcal{G}$ added to the Ricci scalar and their Newtonian limit has already been considered in [274].

Let us start by reviewing the field equations that one derives from action (9.2) [271]. For the metric we have

$$\begin{aligned} G_{\mu\nu} \;=\; & \kappa^2\Big[T_{\mu\nu} + T^{\phi}_{\mu\nu} + 2(\nabla_\mu\nabla_\nu f(\phi))R - 2g_{\mu\nu}(\Box f(\phi))R \\ & -4(\nabla^\rho\nabla_\mu f(\phi))R_{\nu\rho} - 4(\nabla^\rho\nabla_\nu f(\phi))R_{\mu\rho} + 4(\Box f(\phi))R_{\mu\nu} \\ & +4g_{\mu\nu}(\nabla^\rho\nabla^\sigma f(\phi))R_{\rho\sigma} - 4(\nabla^\rho\nabla^\sigma f(\phi))R_{\mu\rho\nu\sigma}\Big], \end{aligned} \tag{9.3}$$

where $G_{\mu\nu} \equiv R_{\mu\nu} - \frac{1}{2}Rg_{\mu\nu}$ and

$$T^{\phi}_{\mu\nu} = \lambda\left(\frac{1}{2}\partial_\mu\phi\partial_\nu\phi - \frac{1}{4}g_{\mu\nu}\partial^\rho\phi\partial_\rho\phi\right) - \frac{1}{2}g_{\mu\nu}V(\phi), \tag{9.4}$$

and for the scalar field

$$\lambda\Box\phi - V'(\phi) + f'(\phi)\mathcal{G} = 0, \tag{9.5}$$

where $A'(x) \equiv \partial A/\partial x$ and $\Box \equiv g^{\mu\nu}\nabla_\nu\nabla_\mu$.

Let us bring eq. (9.3) to a more suitable form for our purposes. Taking the trace of eq. (9.3) one gets

$$R = \kappa^2 \left[-T - T^{\phi} + 2(\Box f(\phi))R - 4(\nabla^{\rho}\nabla^{\sigma} f(\phi))R_{\rho\sigma} \right], \tag{9.6}$$

where $T = g^{\mu\nu}T_{\mu\nu}$ and $T^{\phi} = g^{\mu\nu}T^{\phi}_{\mu\nu}$. Replacing eq. (9.6) back in eq. (9.3), the latter becomes:

$$\begin{aligned} R_{\mu\nu} &= \kappa^2 \Big[T_{\mu\nu} - \frac{1}{2} g_{\mu\nu} T + \frac{1}{2}\lambda \partial_{\mu}\phi\partial_{\nu}\phi + \frac{1}{2} g_{\mu\nu} V(\phi) + 2(\nabla_{\mu}\nabla_{\nu} f(\phi))R \\ &\quad - g_{\mu\nu}(\Box f(\phi))R - 4(\nabla^{\rho}\nabla_{\mu} f(\phi))R_{\nu\rho} - 4(\nabla^{\rho}\nabla_{\nu} f(\phi))R_{\mu\rho} \\ &\quad + 4(\Box f(\phi))R_{\mu\nu} + 2 g_{\mu\nu}(\nabla^{\rho}\nabla^{\sigma} f(\phi))R_{\rho\sigma} - 4(\nabla^{\rho}\nabla^{\sigma} f(\phi))R_{\mu\rho\nu\sigma} \Big] \end{aligned} \tag{9.7}$$

Following [275] we can choose a system of coordinates in which the metric can be perturbatively expanded around Minkowski spacetime. Therefore we write the metric as $g_{\mu\nu} = \eta_{\mu\nu} + h_{\mu\nu}$ (with $h_{\mu\nu} \ll 1$) and the scalar field as $\phi = \phi_0 + \delta\phi$ (with $\delta\phi \ll \phi_0$), where the value of ϕ_0 is determined by the cosmological solution. The perturbed field equations are

$$\begin{aligned} &\lambda[\Box_{\rm flat}\delta\phi + (\delta\Box)\delta\phi] - V''(\phi_0)\delta\phi - \frac{1}{2}V'''(\phi_0)(\delta\phi)^2 + f'(\phi_0)\mathcal{G} = \\ &\qquad\qquad \mathcal{O}(\delta\phi^3, \delta\phi(h_{\mu\nu})^2, h_{\mu\nu}\dot{\phi}_0, h_{\mu\nu}\ddot{\phi}_0), \end{aligned} \tag{9.8}$$

$$\begin{aligned} R_{00} &= \kappa^2 \Big\{ T_{00} + \frac{1}{2}T - \frac{1}{2}h_{00}T + \frac{1}{2}\lambda\partial_0\delta\phi\partial_0\delta\phi + \frac{1}{2}\lambda\,\dot{\phi}_0^2 - \frac{1}{2}V(\phi_0) + \frac{1}{2}V'(\phi_0)\delta\phi\,(h_{00} - 1) \\ &+ f'(\phi_0)\Big[2(\partial_0\partial_0\delta\phi)R + (\Box_{\rm flat}\delta\phi)R - 8(\partial^{\rho}\partial_0\delta\phi)R_{0\rho} + 4(\Box_{\rm flat}\delta\phi)R_{00} - 2(\partial^{\rho}\partial^{\sigma}\delta\phi)R_{\rho\sigma} \\ &- 4(\partial^{\rho}\partial^{\sigma}\delta\phi)R_{0\rho0\sigma} \Big] \Big\} + \mathcal{O}(\delta\phi^2 h_{\mu\nu}, \delta\phi^3, \dot{\phi}_0\delta\phi, \ddot{\phi}_0 h_{\mu\nu}, V(\phi_0)h_{00}), \end{aligned} \tag{9.9}$$

$$R_{0i} = \kappa^2 T_{0i} + \mathcal{O}(\delta\phi h_{\mu\nu}, \delta\phi^2, T h_{0i}, \dot{\phi}_0\delta\phi, \ddot{\phi}_0 h_{\mu\nu}, V(\phi_0)h_{0i}), \tag{9.10}$$

$$\begin{aligned} R_{ij} &= \kappa^2 \left[T_{ij} + \frac{1}{2}\delta_{ij}\left(-T + V'(\phi_0)\delta\phi + V(\phi_0) \right) \right] \\ &\qquad + \mathcal{O}(\delta\phi h_{\mu\nu}, \delta\phi^2, T h_{ij}, \ddot{\phi}_0 h_{\mu\nu}, V(\phi_0)h_{ij}), \end{aligned} \tag{9.11}$$

where $\Box_{\rm flat}$ denotes the d'Alembertian of flat spacetime. Notice that, as usually done in scalar-tensor theory [276, 277], we have neglected all of the terms containing derivatives of ϕ_0 multiplying perturbed quantities (e.g. $\dot{\phi}_0\delta\phi$). This is due to the fact that ϕ_0 changes on cosmological timescales and consequently one expects that it remains practically constant during local experiments. Therefore its time derivatives can be neglected as far as solar system tests are concerned. This can easily be verified by some order-

of-magnitude analysis. Take for instance Eq. (9.9): the terms containing a time derivative of ϕ_0 multiplying a perturbation are $\mathcal{O}(\ddot{f}(\phi_0)h_{\mu\nu}/(r^2M_p^2))$ and $\mathcal{O}(\dot{\phi}_0\delta\dot{\phi}/M_p^2)$, where $\dot{\phi}_0 \sim H_0M_p$ and $\ddot{f} \sim H_0^2$ ($M_p = 1/\kappa$ is the Planck mass and H_0 the present Hubble constant) and $h_{00} \sim h_{ij} \sim r\delta\phi \sim h_{0i}/v \sim r^2\delta\dot{\phi}/v \sim GM_\odot/r$ (r is the distance from the Sun and $v = \sqrt{GM_\odot/r}$). On the other hand, the $\mathcal{O}(v^4)$ post-Newtonian correction to R_{00} is $\sim (GM_\odot)^2/r^4 \sim 10^{-55}\mathcal{O}(\ddot{f}(\phi_0)h_{\mu\nu}/(r^2M_p^2), \dot{\phi}_0\delta\dot{\phi}/M_p^2)$ even if r is taken as large as 1000 AU. Therefore, the corrections coming from terms containing time derivatives of ϕ_0 multiplying perturbations are at least 55 orders of magnitude smaller than post-Newtonian corrections, and neglecting these terms cannot affect our results in any way. A similar treatment applies to the terms containing the potential V multiplying perturbed quantities (e.g.$V(\phi_0)h_{00}$): in order to give a reasonable cosmology, $V(\phi_0)$ should be of the same order as the energy density of the cosmological constant and these terms cannot therefore lead to any observable deviations at solar system scales.

We will instead adopt a different treatment required for the simple $V(\phi_0)$, $\frac{1}{2}\dot{\phi}^2$ terms appearing in the field equations: since they need to be of the same order as the energy density of the cosmological constant, they will not lead to any observational consequences (see [278] and references therein). However, for the sake of the argument we will keep track of them: due to their small value we can treat them as $\mathcal{O}(v^4)$ quantities following [278] and so they will not appear in the $\mathcal{O}(v^2)$ equations. As far as terms related to $V'(\phi_0)$ are concerned, we intend to just keep track of them for the time being and discuss their contribution later on.

If we now expand the perturbations in the metric and the scalar field in post-Newtonian orders, keeping in mind that the PPN expansion requires ϕ and h_{00} to $\mathcal{O}(v^4)$, h_{ij} to $\mathcal{O}(v^2)$ and h_{0i} to $\mathcal{O}(v^3)$, we can write

$$\delta\phi = {}_2\delta\phi + {}_4\delta\phi \ldots \tag{9.12}$$

$$h_{00} = {}_2h_{00} + {}_4h_{00} \ldots \tag{9.13}$$

$$h_{ij} = {}_2h_{ij} + \ldots \tag{9.14}$$

$$h_{0i} = {}_3h_{0i} + \ldots \tag{9.15}$$

where the subscript denotes the order in the velocity, *i.e.* quantities with a subscript ${}_2$ are $\mathcal{O}(v^2)$, quantities with a subscript ${}_3$ are $\mathcal{O}(v^3)$, *etc.*. So, to order $\mathcal{O}(v^2)$ this gives

$$\lambda\nabla^2({}_2\delta\phi) - V''(\phi_0){}_2\delta\phi = 0 \ : \tag{9.16}$$

where $\nabla^2 \equiv \delta_{ij}\partial_i\partial_j$. Note that since the metric is flat in the background $\mathcal{G} = \mathcal{O}(v^4)$. We want ϕ to take its cosmological value at distances far away from the sources. This is equivalent to saying that the perturbations due to the matter present in the solar system should vanish at cosmological distances, and this can be achieved by imposing asymptotic flatness for the solution of eq. (9.16), *i.e.* ${}_2\delta\phi \to 0$ for $r \to \infty$. This implies ${}_2\delta\phi = 0$.

To order $\mathcal{O}(v^2)$ for the components 00 and ij and $\mathcal{O}(v^3)$ for the components $0i$, and

after applying the standard gauge conditions

$$h^{\mu}_{i,\mu} - \frac{1}{2}h^{\mu}_{\mu,i} = 0\,, \qquad h^{\mu}_{0,\mu} - \frac{1}{2}h^{\mu}_{\mu,0} = \frac{1}{2}h^{0}_{0,0}\,, \tag{9.17}$$

the field equations for the metric take the form

$$\begin{aligned} -\nabla^2({}_2h_{00}) &= \kappa^2\rho\,, & (9.18)\\ -\nabla^2({}_2h_{ij}) &= \kappa^2\rho\delta_{ij}\,, & (9.19)\\ \frac{1}{2}\left(\nabla^2({}_3h_{0i}) + \frac{1}{2}({}_2h_{00,j0})\right) &= \kappa^2\rho v^i\,, & (9.20) \end{aligned}$$

which remarkably are exactly the same as in GR [275]. The well-known solutions are

$$\begin{aligned} {}_2h_{00} &= 2U,\,, & (9.21)\\ {}_2h_{ij} &= 2U\delta_{ij}\,, & (9.22)\\ {}_3h_{0i} &= -\frac{7}{2}V_i - \frac{1}{2}W_i\,, & (9.23) \end{aligned}$$

where following [275] we define

$$\begin{aligned} U &= G\int d^3x'\,\frac{\rho(x',t)}{|x-x'|}\,, & (9.24)\\ V_i &= G\int d^3x'\,\frac{\rho(x',t)v_i(x',t)}{|x-x'|}\,, & (9.25)\\ W_i &= G\int d^3x'\,\frac{\rho(x',t)v^k(x',t)(x-x')_k(x-x')_i}{|x-x'|^3}\,. & (9.26) \end{aligned}$$

We already see that the theory has no deviation from GR at order $\mathcal{O}(v^3)$: in particular it gives the correct Newtonian limit. It is now easy to go one step further and write down the perturbed equations that we need to $\mathcal{O}(v^4)$. For the scalar field, using ${}_2\delta\phi = 0$, we get

$$\lambda\nabla^2({}_4\delta\phi) - V''(\phi_0)\,{}_4\delta\phi + f'(\phi_0)\,{}_4\mathcal{G} = 0\,, \tag{9.27}$$

with

$$\begin{aligned} {}_4\mathcal{G} &= ({}_2h_{00,ij})({}_2h_{00,ij}) - ({}_2h_{00,ii})({}_2h_{00,jj}) + ({}_2h_{ij,ij})^2 + ({}_2h_{ij,kl})({}_2h_{ij,kl})\\ &\quad -({}_2h_{ij,kk})({}_2h_{ij,kk}) - 2({}_2h_{ij,kl})({}_2h_{il,jk}) + ({}_2h_{ij,kl})({}_2h_{kl,ij})\,, \end{aligned} \tag{9.28}$$

where we have again applied the gauge conditions (9.17). Using eqs. (9.21) and (9.22), eq. (9.28) becomes

$${}_4\mathcal{G} = 8\,U_{,kl}U_{,kl} - 8\,(U_{,kk})^2\,. \tag{9.29}$$

The solution of eq. (9.27) is therefore

$$ {}_4\delta\phi = \frac{f'(\phi_0)}{4\,\pi}\int d^3x' \frac{{}_4\mathcal{G}(x',t)}{|x-x'|} e^{-\sqrt{V''(\phi_0)}|x-x'|}\,. \tag{9.30} $$

The time-time component of the perturbed field equations for the metric to $\mathcal{O}(v^4)$ is

$$ {}_4R_{00} = \kappa^2\Big[({}_4T_{00}) + \frac{1}{2}({}_4T) - \frac{1}{2}({}_2h_{00})({}_2T) - \frac{1}{2}V'(\phi_0)({}_4\delta\phi) - \frac{1}{2}V(\phi_0) + \frac{1}{2}\lambda\dot{\phi}_0^2\Big], \tag{9.31} $$

where we have already used the fact that ${}_2\delta\phi = 0$. Note also that no contribution coming from the coupling between ϕ and the curvature terms in eq. (9.3) is present in the above equations. This should have been expected since in eq. (9.3) these terms always have the structure of two derivatives of ϕ times a curvature term, and so, due to the fact that in the background the metric is flat and ϕ_0 is slowly varying, they can only contribute to orders higher than $\mathcal{O}(v^4)$.

Let us discuss the contribution of the term proportional to $V'(\phi_0)$. Using eqs. (9.30) and (9.29) we can write this term as an integral over the sources times a dimensionless coefficient $\kappa^2 V'(\phi_0)f'(\phi_0)$. One can argue that $V'(\phi)$ should be practically zero as far as the post-Newtonian expansion is concerned [276, 277]. This is equivalent to saying that the cosmological solution corresponds to a minimum of the potential. Even though such assumptions are not exact, they are accurate enough for our purposes. Note that even in cases where V does not have a minimum, well motivated models usually introduce exponential forms for the potential and the coupling function, *i*.e. $V = V_0 e^{-a\kappa\phi}$ and $f = f_0 e^{b\kappa\phi}$ where a, b and f_0 are of order unity whereas V_0 is as small as the energy density of the cosmological constant in order to guarantee that the theory will fit observations related to the late time cosmological expansion. This implies that, since $\kappa^2 \sim 1/M_p^2$, $\kappa^2 V'(\phi_0)f'(\phi_0)$ is dimensionless and of the order of the now renowned 10^{-123}. Therefore, we will not take the term proportional to $V'(\phi_0)$ into account for what comes next but we will return to this discussion shortly.

We can use the solutions for ${}_2h_{00}$ and ${}_2h_{ij}$, the gauge conditions (9.17) and the standard post-Newtonian parametrisation for matter [275] to write eq. (9.31) as

$$ -\nabla^2({}_4h_{00} + 2U^2 - 8\mathbf{\Phi}_2) = \kappa^2\left[2\rho\left(v^2 - U + \frac{1}{2}\Pi - \frac{3p}{2\rho}\right) - V(\phi_0) + \frac{1}{2}\lambda\dot{\phi}_0^2\right], \tag{9.32} $$

where Π is the specific energy density (ratio of energy density to rest-mass density) [275] and Φ_2 is defined as

$$ \Phi_2 = G\int d^3x' \frac{\rho(x',t)U(x',t)}{|x-x'|}. \tag{9.33} $$

The solution to this equation is

$$ {}_4h_{00} = 2U^2 + 4\Phi_1 + 4\Phi_2 + 2\Phi_3 + 6\Phi_4 + \frac{\kappa^2}{6}\left(V(\phi_0) - \frac{1}{2}\lambda\dot{\phi}_0^2\right)|x|^2, \tag{9.34} $$

where

$$\Phi_1 = G\int d^3x' \frac{\rho(x',t)v(x',t)^2}{|x-x'|}, \tag{9.35}$$

$$\Phi_3 = G\int d^3x' \frac{\rho(x',t)\Pi(x',t)v(x',t)^2}{|x-x'|}, \tag{9.36}$$

$$\Phi_4 = G\int d^3x' \frac{p(x',t)}{|x-x'|}. \tag{9.37}$$

Therefore the metric, expanded in post-Newtonian orders is

$$g_{00} = -1+2U-2U^2+4\Phi_1+4\Phi_2 +2\Phi_3+6\Phi_4+\frac{\kappa^2}{6}\left(V(\phi_0)-\frac{1}{2}\lambda\dot{\phi}_0^2\right)|x|^2, \tag{9.38}$$

$$g_{0j} = -\frac{7}{2}V_i-\frac{1}{2}W_i, \tag{9.39}$$

$$g_{ij} = (1+2U)\delta_{ij}, \tag{9.40}$$

which, apart from the term related to $V(\phi_0)-1/2\lambda\dot{\phi}_0^2$, is exactly the result that one obtains for GR. This term corresponds to the standard correction normally arising from a cosmological constant, and since $V(\phi_0)-1/2\lambda\dot{\phi}_0^2$ should indeed be of the same order as the energy density of the cosmological constant, the contribution of this term is negligible on solar system scales. Since the metric is written in the standard PPN gauge one can read off the PPN parameters [275]. The only non-vanishing ones are γ and β, which are equal to 1. Therefore, the theory discussed here is indistinguishable from GR at the first post-Newtonian order.

9.2 Interpretation of the results

The calculation of the previous section implies that a gravitational theory with a scalar field coupled to the Gauss-Bonnet invariant trivially satisfies the constraints imposed on the post-Newtonian parameters by solar system tests. This is due to the fact that the terms arising in the field equation for the metric from the coupling between the scalar field and $\mathcal{G}$ in the action always have the structure of two derivatives of f times a curvature term. Such terms do not contribute to the post-Newtonian expansion to $\mathcal{O}(v^4)$. This is not the case for other possible couplings of a scalar to a quadratic curvature term, such as ϕR^2. Remarkably, the characteristic structure of such terms can be traced back to the special nature of $\mathcal{G}$, *i.e.* to the fact that it is a topological invariant in four dimensions.

However, note that our result strongly depends on the assumption that $V(\phi_0)$ and $V'(\phi_0)$ are reasonably small so as to give a negligible contribution. This assumption stems from the fact that $V(\phi_0)$ will play the role of an effective cosmological constant if the theory is to account for the late time accelerated expansion of the universe and should therefore be of the relevant order of magnitude. Additionally we expect that $V'(\phi_0)$ will

also be small enough so that its contribution can be considered negligible, based on the fact that either the field approaches a minimum at late times, or that the potential is of the form $V = V_0 e^{-a\kappa\phi}$, where a is of order unity, and therefore $V'(\phi_0) \sim \kappa V(\phi_0)$, which seem to be true in all reasonable models.

Another important aspect to be stressed is that the value of $f'(\phi_0)$ or $f''(\phi_0)$ should be suitable so that the post-Newtonian expansion remains trustworthy. From eq. (9.30) we see that non-trivial corrections will indeed be present at higher post-Newtonian orders and, even though such corrections are normally small, if $f'(\phi_0)$ or $f''(\phi_0)$ are sufficiently large they can become crucial for the viability of the theory. This was first noted in ref. [279], where the same theory, but without a potential V, was compared with solar system observations, considering a nearly Schwarzschild metric as an approximation. As mentioned before, the potential plays the role of an effective cosmological constant if one wants a theory that leads to a late time accelerated expansion as in [271, 272]. If this potential is not present, it is the coupling $f(\phi)$ between the scalar field and the Gauss-Bonnet term that will have to account for this phenomenology. In this case it turns out that $f''(\phi_0)$ has to be of the order of the inverse of the cosmological constant, and this is enough to make the post-Newtonian approximation break down. Fortunately, models with a potential do not suffer from this problem, and in fact f is usually assumed to be of the form $f = f_0 e^{b\kappa\phi}$ where both f_0 and b are of order unity. So, as predicted also in [279], all reasonable models with a potential will pass the solar system tests.

Concluding remarks and future prospects

> My interest is in the future because I am going to spend the rest of my life there.
>
> C. Kettering

In this thesis we have considered two different lines of research. In the first part, we have focused on binary systems of black holes as possible sources of gravitational waves for LISA. In particular, in chapters 2–4, we have investigated whether EMRIs (*i.e.*, systems composed of an SMBH and a stellar-mass black hole) could permit detecting and determining the properties of the astrophysical matter which could be present in galactic nuclei. In chapter 5, we have instead analysed whether gravitational waves from EMRIs could present any distinctive features when the SMBH is almost maximally rotating, as had been suggested in the literature. In chapter 6 we have considered SMBH binaries and studied how the spin of the final remnant is related to the spins of the progenitors. This study, combined with a suitable galaxy formation framework, will hopefully allow us, in the long term, to predict the distribution of the SMBH spins as a function of redshift [169]. In the second part of this thesis, we have instead considered gravity theories alternative to GR, motivating their introduction (chapter 7) and testing some of them using stars (chapter 8) and solar system tests (chapter 9).

These two lines of research have been kept separate in this thesis. As we have stressed several times, the only link between them is that they both aim at exploring gravity at the level of stars, black holes and compact objects. While this may seem quite a loose connection, a much more promising way to combine these two interests of mine has occurred to me during the last part of my PhD. The idea is that future gravitational-wave observations can do more than providing astrophysical information (detecting the matter in galactic nuclei, measuring the SMBH masses and spins, checking whether the number of SMBHs is that needed by galaxy formation models, *etc*.) or checking the predictions

of GR about gravitational waves. Indeed, gravitational-wave detectors, and LISA in particular, could also, at least potentially, discriminate between GR and alternative gravity theories *in the strong field regime*! An example of how to do this in practice is given by the discussion below.

In a recent paper [280], Psaltis *et al.* have pointed out that Kerr (Kerr-de Sitter) black hole solutions are not exclusive to GR, but are present also in several modified gravity theories. This has raised the concern that gravitational wave observations (and in particular the detection of EMRIs with LISA) might not be able to discriminate between these theories and GR. As we will show below, this is not really the case, and gravitational wave experiments can in principle distinguish between Kerr black holes in GR and in modified gravity theories.

The gravity theories considered by ref. [280] were $f(R)$ gravity, quadratic gravity and vector-tensor gravity. These theories are built so as to have maximally symmetric solutions in vacuum (Minkowski or de Sitter), and this is achieved by imposing that the field equations reduce to GR under the conditions $R_{,\mu}=0$, $R_{\mu\nu}=R\,g_{\mu\nu}/4$ and $T_{\mu\nu}=0$. Consequently, it had long been known that the Kerr-de Sitter solution, which satisfies these conditions, is a solution also in these theories. However, these theories also admit vacuum solutions different from Kerr, as mentioned also in ref. [280]. [The only exception is Palatini $f(R)$ gravity, which reduces exactly to GR (with a cosmological constant) in vacuum.] Astrophysical black holes form by gravitational collapse, and there is as yet no guarantee that this will lead to a Kerr black hole in theories in which there is no uniqueness theorem similar to that in GR. However, we set this (potentially important) issue aside, as done in ref. [280], and show that even a Kerr black hole permits probing deviations from GR. Indeed, the (vacuum) metric perturbations over a Kerr black hole in the theories considered in ref. [280] behave differently from GR. Again, the exception is Palatini $f(R)$ gravity, since this reduces to GR in vacuum.

We use metric $f(R)$ gravity in the metric formalism *as an example*. This theory is described by the action

$$S=\frac{1}{16\,\pi}\int d^4x\sqrt{-g}f(R)+S_M(g_{\mu\nu},\psi), \tag{C1}$$

where $f(R)$ is a function of R, S_M is the matter action and ψ collectively denotes the matter fields. (We recall that we are using units in which $c=G=1$). This action is clearly the same as in eq. (8.1), but now the connection is not thought of as an independent degree of freedom, as in the Palatini variational approach, but is rather assumed to be given by the Levi-Civita connection of the metric $g_{\mu\nu}$. The field equations can then be derived by taking variations of the action (C1) with respect to the metric, giving

$$f'(R)R_{\mu\nu}-\frac{1}{2}f(R)g_{\mu\nu}-(\nabla_\mu\nabla_\nu-g_{\mu\nu}\Box)f'(R)=8\pi T_{\mu\nu}. \tag{C2}$$

[with $\Box\equiv\nabla^\nu\nabla_\nu$ and $'\equiv\partial/\partial R$, while $T_{\mu\nu}\equiv-2(-g)^{-1/2}\delta S_M/\delta g^{\mu\nu}$ is the usual stress-energy tensor of the matter].

We will now perturb the field equations (C2) in vacuum ($T_{\mu\nu}=0$) and over a Kerr (and *not* Kerr-de Sitter) black hole, which has $R=R_{\mu\nu}=0$, thus simplifying the calculation considerably. Moreover, in order to have a Kerr (and not Kerr-de Sitter) solution, one needs to have a function $f(R)$ such that $f(0)=0$ [280]. We denote the metric perturbation by $h_{\mu\nu}$ and use the *Lorenz gauge*, defined by $\nabla_\nu \bar{h}^{\mu\nu}=0$, where $\bar{h}_{\mu\nu}\equiv h_{\mu\nu}-hg_{\mu\nu}/2$. Such a gauge is always attainable: $\bar{h}^{\mu\nu}$ transforms as

$$\hat{\bar{h}}_{\mu\nu}=\bar{h}_{\mu\nu}-\nabla_\mu\xi_\nu-\nabla_\nu\xi_\mu+g_{\mu\nu}\nabla_\alpha\xi^\alpha\,, \tag{C3}$$

and we only need to impose $\Box\xi^\mu=\nabla_\nu\bar{h}^{\mu\nu}$ [11]. Using this gauge and perturbing eq. (C2) with $T_{\mu\nu}=0$ over a Kerr background, we have

$$\Box\bar{h}_{\mu\nu}+2R_{\mu\alpha\nu\beta}\bar{h}^{\alpha\beta}=-\lambda\left(\nabla_\mu\nabla_\nu-g_{\mu\nu}\Box\right)\Box\bar{h}\,, \tag{C4}$$

where $\lambda\equiv f''(0)/f'(0)$. In GR $f'(0)=1$ and $f''(0)=0$, and thus $\lambda=0$. Furthermore, in GR it is possible to set $\bar{h}=0$, although only in a globally vacuum spacetime, using the residual freedom of the Lorenz gauge (one can perform a transformation with ξ^μ satisfying $\Box\xi^\mu=0$) [11]. From eq. (C3) it follows that we need $\nabla_\mu\xi^\mu+\bar{h}/2=0$ in order to have $\hat{\bar{h}}=0$. Taking the d'Alembertian of $\nabla_\mu\xi^\mu+\bar{h}/2$, and using the trace of eq. (C4) and $\Box\xi^\mu=R=R_{\mu\nu}=0$, one can show that $\nabla_\mu\xi^\mu+\bar{h}/2$ satisfies the homogeneous wave equation only if $f''(0)=0$ (as in GR): it is then possible to choose initial data for ξ^μ on a Cauchy hypersurface such that $\nabla_\mu\xi^\mu+\bar{h}/2$ and its derivative normal to the hypersurface vanish, thus ensuring $\nabla_\mu\xi^\mu+\bar{h}/2=0$ everywhere. This is not possible if $f''(0)\neq 0$, and $\bar{h}$ cannot then be set to zero (even in globally vacuum spacetimes).

Thus, eq. (C4) differs from its GR analogue. For example, over a Minkowski background, besides the propagation modes of GR, eq. (C4) also has a plane-wave solution $\bar{h}_{\mu\nu}\propto(\eta_{\mu\nu}+k_\mu k_\mu/m^2)\exp(ik_\alpha x^\alpha)$, where $\boldsymbol{k}\equiv\omega(\kappa)\,\partial_t+\kappa\,\boldsymbol{n}$ ($\boldsymbol{n}$ being a unit vector in the propagation direction) and $\omega(\kappa)^2\equiv\kappa^2+m^2$ (with $m^2\equiv(3\lambda)^{-1}>0$: if $\lambda<0$ the gravity theory is non-viable [281]). These waves, which cannot be zeroed in the Lorenz gauge, correspond to massive gravitons with velocity $d\omega/d\kappa<1$. This feature will be detectable by LISA because modes with different wavelengths propagate at different velocities, thus distorting the waveforms during the propagation [282]. Moreover, their polarisation differs from GR, and in principle also this feature could be used to distinguish these modes from the standard GR ones. Note that this mode corresponds to scalar field excitations [*cf.* the equivalent Brans-Dicke theory with a potential, *e.g.* ref. [283, 239]], and that it is also present in a Brans-Dicke theory with no potential [284], for which it was shown to affect the orbital evolution of binary systems [282, 284].

Stated differently: while the Kerr solution is common to many gravity theories, its perturbations are not. Because the gravitational waves emitted by a perturbed Kerr black hole behave differently in these theories, their detection can be used to discriminate between them. Thus, the concerns of ref. [280] seem unjustified.

In summary: we have highlighted that a different gravity theory will in general predict emission mechanisms and propagation modes for gravitational waves different from

those of standard GR. Moreover, in many modified gravity theories there is no black-hole uniqueness theorem similar to that in GR, and black holes different from Kerr will in general be present. If these black-hole solutions were physical (*i.e.* if they could result from gravitational collapse) – which in general is unclear so far and which will depend on the particular theory under consideration – the consequences for typical LISA sources such as SMBH binaries or EMRIs will be potentially very important.

Considering that testing gravity is among the main goals of the LISA mission [3], but one on which little work has been done so far by the community, this line of research will be among those that I will be pursuing in the coming future.

Bibliography

[1] C. W. Misner, K. S. Thorne and J. A. Wheeler, *Gravitation* (Freeman, San Francisco, 1973).

[2] `http://lisa.nasa.gov/`; `http://sci.esa.int/home/lisa/`.

[3] Committee on NASA's Beyond Einstein Program, *An Architecture for Implementation*, The National Academies Press (Washington, D.C., 2007). Available online at `http://www.nap.edu/catalog.php?record$_$id=12006`

[4] `http://www.ligo.caltech.edu/`

[5] `http://www.ego-gw.it/`

[6] `http://geo600.aei.mpg.de/`

[7] `http://tamago.mtk.nao.ac.jp/`

[8] M. Tinto, F. B. Estabrook and J. W. Armstrong, Time-delay interferometry white paper webpage `http://www.srl.caltech.edu/lisa/tdi_wp`

[9] M. A. Vincent and P. L. Bender Proc. Astrodynamics Specialist Conf. (Kalispell, USA) **1**, 1346 (2007), San Diego CA, Univelt.

[10] W. M. Folkner, F. Hechler, T. H. Sweetser, M. A. Vincent and P. L. Bender, Class. Quant. Grav. **14** 1405 (1997); S. V. Dhurandhar, K. Rajesh Nayak, S. Koshti and J. Y. Vinet, Class. Quant. Grav. **22**, 481 (2005).

[11] E. E. Flanagan and S. A. Hughes, New J. Phys. **7**, 204 (2005).

[12] S. Babak, H. Fang, J. R. Gair , K. Glampedakis and S. A. Hughes , Phys. Rev. D **75**, 024005 (2007).

[13] F. B. Estabrook and H. D. Wahlquist, Gen. Rel. Grav. **6**, 439 (1975).

[14] `http://www.srl.caltech.edu/~shane/sensitivity/`; S. L. Larson, W. A. Hiscock and R. W. Hellings, Phys. Rev. D **62**, 062001 (2000); S. L. Larson, R. W. Hellings and W. A. Hiscock, Phys. Rev. D **66**, 062001 (2002).

[15] M. Tinto and S. V. Dhurandhar, Living Rev. Rel. **8**, 4 (2005).

[16] P. L. Bender and D. Hils, Class. Quant. Grav. **14**, 1439 (1997); W. A. Hiscock, S. L. Larson, J. R. Routzahn and B. Kulick, Astrophys. J. **540**, L5 (2000).

[17] J. R. Gair, L. Barack, T. Creighton, S. L. Larson, E. S. Phinney, and M. Vallisneri, Class. Quant. Grav. **21**, S1595 (2004).

[18] C. Cutler and É. E. Flanagan, Phys. Rev. D **49**, 2658 (1994).

[19] R. J. Adler, *The geometry of random fields* (Wiley & Sons, London, 1981.)

[20] P. Amaro-Seoane, J. R. Gair, M. Freitag, M. Coleman Miller, I. Mandel, C. J. Cutler and S. Babak, Class. Quant. Grav. **24**, R113 (2007).

[21] S. A. Hughes, arXiv:0711.0188 [gr-qc].

[22] P. C. Peters, Phys. Rev. **136**, B1224 (1964).

[23] P. C. Peters and J. Mathews, Phys. Rev. **131**, 435 (1963).

[24] G. Nelemans, AIP Conf. Proc. **873**, 397 (2006).

[25] A. Buonanno, Y. Pan, J. G. Baker, J. Centrella, B. J. Kelly, S. T. McWilliams and J. R. van Meter, Phys. Rev. D **76**, 104049 (2007).

[26] F. Pretorius, Phys. Rev. Lett. **95**, 121101 (2005); M. Campanelli, C. O. Lousto, P. Marronetti and Y. Zlochower, Phys. Rev. Lett. **96**, 111101 (2006); M. Campanelli, C. O. Lousto and Y. Zlochower, Phys. Rev. D **74**, 041501(R) (2006); J. G. Baker, J. Centrella, D. I. Choi, M. Koppitz and J. van Meter, Phys. Rev. D **73**, 104002 (2006); J. G. Baker, J. Centrella, D. I. Choi, M. Koppitz, J. R. van Meter and M. C. Miller, Astrophys. J. **653**, L93 (2006); J. G. Baker, M. Campanelli, F. Pretorius and Y. Zlochower, Class. Quant. Grav. **24**, S25 (2007); J. A. Gonzalez, U. Sperhake, B. Brügmann, M. Hannam and S. Husa, Phys. Rev. Lett. **98**, 091101 (2007); S. Husa, J. A. Gonzalez, M. Hannam, B. Brugmann and U. Sperhake, arXiv:0706.0740 [gr-qc]. M. Koppitz, D. Pollney, C. Reisswig, L. Rezzolla, J. Thornburg, P. Diener and E. Schnetter, Phys. Rev. Lett. **99**, 041102 (2007);

[27] P. Ajith *et al.*,Phys. Rev. D **77**, 104017 (2008).

[28] V. Springel, C. S. Frenk and S. D. M. White, Nature **440**, 1137 (2006).

[29] J. Kormendy and D. Richstone, Ann. Rev. Astron. Astrophys. **33**, 581 (1995).

[30] M. C. Begelman, R. D. Blandford and M. J. Rees, Nature **287**, 307 (1980).

[31] W. C. Saslaw, M. J. Valtonen and S. J. Aarseth, Astrophys. J. **190**, 253 (1974).

[32] D. Merritt and M. Milosavljevic, Living Rev. Rel. **8**, 8 (2005).

[33] A. Sesana, F. Haardt, P. Madau and M. Volonteri, Astrophys. J. **611**, 623 (2004); A. Sesana, F. Haardt, P. Madau and M. Volonteri, Astrophys. J. **623**, 23 (2005).

[34] A. Vecchio, Phys. Rev. D **70**, 042001 (2004); E. Berti, A. Buonanno and C. M. Will, Class. Quant. Grav. **22**, S943 (2005).

[35] S. Drasco, Class. Quant. Grav. **23**, S769 (2006).

[36] Y. Mino, Phys. Rev. D **67**, 084027 (2003).

[37] A. Pound, E. Poisson and B. G. Nickel, Phys. Rev. D **72**, 124001 (2005).

[38] E. Poisson, Living Rev. Relativity **7**, 6 (2004).

[39] E. Poisson, arXiv:gr-qc/0410127.

[40] K. Glampedakis and D. Kennefick, Phys. Rev. D **66**, 044002 (2002).

[41] S. Drasco and S. A. Hughes, Phys. Rev. D **73**, 024027 (2006).

[42] L. Barack and N. Sago, Phys. Rev. D **75**, 064021 (2007).

[43] L. Barack and C. Cutler, Phys. Rev. D **69**, 082005 (2004).

[44] T. Alexander, Phys. Rept. **419** 65 (2005).

[45] A. P. Lightman and S. L. Shapiro, Astrophys. J. **211**, 244 (1977).

[46] C. Hopman and T. Alexander, Astrophys. J. **629**, 362 (2005).

[47] C. Hopman, AIP Conf. Proc. **873**, 241 (2006).

[48] K. P. Rauch and S. Tremaine, New Astronomy **1**, 149 (1996); K. P. Rauch and B. Ingalls, Mon. Not. Roy. Astron. Soc. **299**, 1231 (1998).

[49] C. Hopman and T. Alexander, Astrophys. J. **645**, 1152 (2006).

[50] J. N. Bahcall and R. A. Wolf, Astrophys. J. **216**, 833 (1977); H. Baumgardt, J. Makino and T. Ebisuzaki, Astrophys. J. **613**, 1143 (2004); M. Freitag, P. Amaro-Seoane and V. Kalogera, Astrophys. J. **649**, 91 (2006), C. Hopman and T. Alexander, Astrophys. J. **645**, L133 (2006).

[51] Y. Levin, Mon. Not. Roy. Astron. Soc. **374**, 515 (2007); Y. Levin, arXiv:astro-ph/0307084.

[52] M. Coleman Miller, M. Freitag, D. P. Hamilton and V. M. Lauburg, Astrophys. J. **631**, L117 (2005).

[53] S. Chandrasekhar Astrophys. J. **97**, 255 (1943).

[54] J. Binney and S. Tremaine, *Galactic dynamics* (Princeton University Press, Princeton, 1987).

[55] M. Walker and C. M. Will, Astrophys. J. **242**, L129 (1980).

[56] M. E. Pati and C. M. Will, Phys. Rev. D **62**, 124015 (2000).

[57] E. P. Lee, Astrophys. J. **155**, 687 (1969).

[58] D. Syer, Mon. Not. Roy. Astron. Soc. **270**, 205 (1994).

[59] L. I. Petrich, S. L. Shapiro, R. F. Stark and S. A. Teukolsky, Astrophys. J. **336**, 313 (1989).

[60] N. I. Shakura and R. A. Sunyaev, Astron. Astrophys. **24**, 337 (1973).

[61] A. R. King , J. E. Pringle and M. Livio, Mon. Not. Roy. Astron. Soc. **376**, 1740 (2007).

[62] Y. Rephaeli and E. E. Salpeter, Astrophys. J. **240**, 20 (1980).

[63] M. A. Ruderman and E. A. Spiegel, Astrophys. J. **165**, 1 (1971).

[64] H. Bondi and F. Hoyle, Mon. Not. Roy. Astron. Soc. **104**, 273 (1944).

[65] H. Bondi, Mon. Not. Roy. Astron. Soc. **112**, 195 (1952).

[66] E. C. Ostriker, Astrophys. J. **513**, 252 (1999).

[67] F. J. Sanchez-Salcedo and A. Brandenburg, Astrophys. J. **522**, L35 (1999).

[68] H. Kim and W. T. Kim, Astrophys. J. **665**, 432 (2007).

[69] D. Vokrouhlicky and V. Karas, Mon. Not. Roy. Astron. Soc. **265**, 365 (1993).

[70] D. Vokrouhlicky and V. Karas, Mon. Not. Roy. Astron. Soc. **298**, 53 (1998).

[71] L. Subr and V. Karas, Astron. Astrophys. **352**, 452 (1999).

[72] V. Karas and L. Subr, Astron. Astrophys. **376**, 686 (2001).

[73] R. Narayan Astrophys. J. **536**, 663 (2000).

[74] R. Narayan and I. Yi, Astrophys. J. **428**, L13 (1994).

[75] R. D. Blandford and M. C. Begelman, Mon. Not. Roy. Astron. Soc. **303**, L1 (1999).

[76] S. K. Chakrabarti, Astrophys. J. **411**, 610 (1993).

[77] S. K. Chakrabarti, Phys. Rev. D **53**, 2901 (1996).

[78] J. M. Bardeen, Phys. Rev. D **22**, 1882 (1980).

[79] H. Kodama and M. Sasaki, Progr. Theor. Phys. Suppl. **78**, 1 (1984).

[80] V. F. Mukhanov, H. A. Feldman and R. H. Brandenberger Phys. Rept. **215**, 203 (1992).

[81] C.-P. Ma and E. Bertschinger, Astrophys. J. **455**, 7 (1995)

[82] L. Barack and A. Ori Phys. Rev. D **64**, 124003 (2001).

[83] M. Colpi, S. L. Shapiro and I. Wasserman, Phys. Rev. Lett. **57**, 2485 (1986); D. F. Torres, S. Capozziello and G. Lambiase, Phys. Rev. D **62**, 104012 (2000).

[84] F. Munyaneza, D. Tsiklauri and R. D. Viollier Astrophys. J. Lett. **509**, L105 (1998); R. Schodel *et al.*, Nature **419**, 694 (2002).

[85] P. O. Mazur and E. Mottola, Proc. Nat. Acad. Sci. **101**, 9545 (2004); C. B. M. Chirenti and L. Rezzolla, Class. Quant. Grav. **24**, 4191 (2007).

[86] F. D. Ryan, Phys. Rev. D **52**, 5707 (1995).

[87] F. D. Ryan, Phys. Rev. D **56**, 1845 (1997).

[88] F. D. Ryan, Phys. Rev. D **56**, 7732 (1997).

[89] M. Kesden, J. Gair and M. Kamionkowski, Phys. Rev. D **71**, 044015 (2005).

[90] N. A. Collins and S. A. Hughes, Phys. Rev. D **69**, 124022 (2004).

[91] J. R. Gair, C. Li and I. Mandel, Phys. Rev. D **77**, 024035 (2008).

[92] K. Glampedakis and S. Babak, Class. Quant. Grav. **23**, 4167 (2006).

[93] L. Barack and C. Cutler, Phys. Rev. D **75**, 042003 (2007).

[94] Y. Levin and A. M. Beloborodov, Astrophys. J. Lett. **590**, 33 (2003); R. Genzel *et al.*, Astrophys. J. **594**, 812 (2003).

[95] R. Antonucci, Ann. Rev. Astron. Astrophys. **31**, 473 (1993); C. M. Urry and P. Padovani, Publ. Astron. Soc. Pac. **107**, 803 (1995).

[96] S. Collin and J. M. Huré, Astron. Astrophys. **372**, 50 (2001); J. M. Huré, Astron. Astrophys. **395**, L21 (2002).

[97] E. Barausse, L. Rezzolla, D. Petroff and M. Ansorg, Phys. Rev. D **75**, 064026 (2007).

[98] J. A. Font and J. M. Ibanez, Astrophys. J. **494**, 297 (1998).

[99] J. A. Font and J. M. Ibanez, Mon. Not. Roy. Astron. Soc. **298**, 835 (1998); J. A. Font, J. M. Ibanez and P. Papadopoulos, Mon. Not. Roy. Astron. Soc. **305**, 920 (1999).

[100] E. Barausse, Mon. Not. Roy. Astron. Soc. **382**, 826 (2007).

[101] M. Kozlowski, M. Jaroszynski and M. A. Abramowicz, Astron. Astrophys. **63**, 209 (1978).

[102] M. A. Abramowicz, M. Jaroszynski and M. Sikora, Astron. Astrophys. **63**, 221 (1978).

[103] F. H. Seguin, Astrophys. J. **197**, 745 (1975).

[104] F. D. Ryan, Phys. Rev. D **52**, R3159 (1995).

[105] S. A. Hughes, Phys. Rev. D **61**, 084004 (2000).

[106] E. Barausse, S. A. Hughes and L. Rezzolla, Phys. Rev. D **76**, 044007 (2007).

[107] J. A. Font and F. Daigne, Mon. Not. Roy. Astron. Soc. **334**, 383 (2002); F. Daigne and J. A. Font, Mon. Not. Roy. Astron. Soc. **349**, 841 (2004).

[108] O. Zanotti, L. Rezzolla and J. A. Font, Mon. Not. Roy. Astron. Soc. **341**, 832 (2003).

[109] O. Zanotti, J. A. Font, L. Rezzolla and P. Montero, Mon. Not. Roy. Astron. Soc. **356**, 1371 (2005).

[110] S. L. Shapiro and S. A. Teukolsky, *Black holes, white dwarfs, and neutron stars: The physics of compact objects* (Wiley, New York, 1983).

[111] S. Drasco, E. E. Flanagan and S. A. Hughes, Class. Quant. Grav. **22**, S801 (2005).

[112] S. A. Hughes, S. Drasco, E. E. Flanagan and J. Franklin, Phys. Rev. Lett. **94**, 221101 (2005).

[113] B. Carter, Phys. Rev. **174**, 1559 (1968).

[114] D. Kennefick and A. Ori, Phys. Rev. D **53**, 4319 (1996).

[115] F. D. Ryan, Phys. Rev. D **53**, 3064 (1996).

[116] W. Schmidt, Class. Quant. Grav. **19**, 2743 (2002).

[117] S. Drasco and S. A. Hughes, Phys. Rev. D **69**, 044015 (2004).

[118] W. H. Press, S. A. Teukolsky, W. T. Vetterling, and B. P. Flannery, *Numerical Recipes* (Cambridge University Press, Cambridge, 1992).

[119] J. R. Gair and K. Glampedakis, Phys. Rev. D **73**, 064037 (2006).

[120] S. A. Teukolsky, Astrophys. J. **185**, 635 (1973); M. Sasaki and T. Nakamura, Prog. Theor. Phys. **67**, 1788 (1982).

[121] K. S. Thorne, Astrophys. J. **191**, 507 (1974).

[122] L. Rezzolla, P. Diener, E. N. Dorband, D. Pollney, C. Reisswig, E. Schnetter, J. Seiler, preprint `gr-qc/0708.3999`

[123] L. Rezzolla, E. N. Dorband, C. Reisswig, P. Diener, D. Pollney, E. Schnetter, B. Szilagyi, preprint `gr-qc/0710.3345`

[124] P. L. Bender and D. Hils, Class. Quant. Grav. **14**, 1439 (1997); G. Nelemans, L. R. Yungelson and S. F. Portegies Zwart, Astron. Astrophys. **375** 890 (2001); A. J. Farmer and E. S. Phinney, Mon. Not. Roy. Astron. Soc. **346**, 1197 (2003).

[125] L. Barack and C. Cutler, Phys. Rev. D **69**, 082005 (2004).

[126] L. D. Landau and E. M. Lifshitz, *Mechanics* (Pergamon Press, Oxford, 1976)

[127] L. Barack and C. Cutler, Phys. Rev. D **69**, 082005 (2004).

[128] A. A. Svidzinsky, JCAP **0710**, 018 (2007).

[129] A. E. Broderick and R. Narayan, Astrophys. J. **638**, L21 (2006)

[130] M. Ansorg and D. Petroff, Phys. Rev. D **72**, 024019 (2005).

[131] Y. Mino, M. Sasaki, and T. Tanaka, Phys. Rev. D **55**, 3457 (1997).

[132] T. C. Quinn and R. M. Wald, Phys. Rev. D **56**, 3381 (1997).

[133] L. Barack and C. O. Lousto, Phys. Rev. D **72**, 104026 (2005).

[134] D. V. Gal'tsov, J. Phys. A **15**, 3737 (1982).

[135] N. Sago, T. Tanaka, W. Hikida and H. Nakano, Progr. Theor. Phys. **114**, 509 (2005); N. Sago, T. Tanaka, W. Hikida, K. Ganz and H. Nakano, Progr. Theor. Phys. **115**, 873 (2006).

[136] M. J. Pfenning and E. Poisson, Phys. Rev. D **65**, 084001 (2002); D. W. Sciama, P. C. Waylen and R. C. Gilman, Phys. Rev. 187, 1762 (1969).

[137] E. Rosenthal, Phys. Rev. D **73**, 044034 (2006).

[138] R. Geroch, J. Math. Phys. **11**, 2580 (1970); R. Hansen, J. Math. Phys. **15**, 46 (1974); G. Fodor, C. Hoenselaers and Z. Perjés, J. Math. Phys. **30**, 2252 (1989).

[139] P. Kordas, Class. Quant. Grav. **12**, 2037 (1995).

[140] R. Meinel and G. Neugebauer, Class. Quant. Grav. **12**, 2045 (1995).

[141] J. B. Hartle, Astrophys. J. **150**, 1005 (1967); J. B. Hartle and K. S. Thorne Astrophys. J. **153**, 807 (1968).

[142] A. Komar, Phys. Rev. **113**, 934 (1959).

[143] J. M. Bardeen, *Rapidly rotating stars, disks and black holes*, in *Black Holes, Les astres occlus*, C. DeWitt and B. S. DeWitt eds. (Gordon and Breach Science Publishers, New York, 1973).

[144] R. Arnowitt, S. Deser, C. W. Misner, *The Dynamics of General Relativity*, in *Gravitation: an introduction to current research*, L. Witten ed., (Wiley, 1962) [arXiv:gr-qc/0405109].

[145] D. Christodoulou, Phys. Rev. Lett. **25**, 1596 (1970).

[146] R. Ruffini and M. Sasaki, Progr. Theor. Phys. **66**, 1627 (1981).

[147] K. Glampedakis, Class. Quant. Grav. **22**, 605 (2005).

[148] K. Glampedakis, S. A. Hughes and D. Kennefick Phys. Rev. D **66**, 064005 (2002).

[149] R. Balasubramanian, B. S. Sathyaprakash and S. V. Dhurandhar, Phys. Rev. D **53**, 3033 (1996).

[150] G. Cook, Living Rev. Relativity **3**, 5 (2000).

[151] J. D. Bekenstein, Astrophys. J. **183**, 657 (1973).

[152] W. H. Press, Phys. Rev. D **15**, 965 (1977).

[153] S. A. Hughes, Phys. Rev. D **63**, 064016 (2001).

[154] S. L. Shapiro, Astrophys. J. **620**, 59 (2005).

[155] L. Rezzolla, T. W. Maccarone, S. Yoshida, and O. Zanotti, Mon. Not. Roy. Astron. Soc. **344**, L37 (2003).

[156] R. Shafee, J. E. McClintock, R. Narayan, S. W. Davis, L.-X. Li, and R. A. Remilland, Astrophys. J. **636**, L113 (2006).

[157] J. E. McClintock, R. Shafee, R. Narayan, R. A. Remilland, S. W. Davis, and L.-X. Li, Astrophys. J. **652**, 518 (2006).

[158] A. C. Fabian and G. Miniutti, G. 2005, to appear in *Kerr Spacetime: Rotating Black Holes in General Relativity*, edited by D. L. Wiltshire, M. Visser, and S. M. Scott; astro-ph/0507409.

[159] L. W. Brenneman and C. S. Reynolds, Astrophys. J. **652**, 1028 (2006).

[160] M. Volonteri, P. Madau, E. Quataert, and M. J. Rees, Astrophys. J. **620**, 69 (2005).

[161] D. C. Wilkins, Phys. Rev. D **5**, 814 (1972).

[162] J. M. Bardeen, W. H. Press, and S. A. Teukolsky, Astrophys. J. **178**, 347 (1972).

[163] K. S. Thorne, R. H. Price, and D. A. MacDonald, *Black Holes: The Membrane Paradigm* (Yale University Press, New Haven, CT, 1986).

[164] A. Ori and K. S. Thorne, Phys. Rev. D **62**, 124022 (2000)

[165] Y. Mino, unpublished Ph. D. thesis, Kyoto University, 1996.

[166] Data available at `http://gmunu.mit.edu/sdrasco/snapshots/`

[167] E. Barausse and L. Rezzolla, in preparation.

[168] E. Berti and M. Volonteri, arXiv:0802.0025 [astro-ph].

[169] E. Barausse and M. Cook, in preparation.

[170] I. Hinder, B. Vaishnav, F. Herrmann, D. Shoemaker and P. Laguna, arXiv:0710.5167 [gr-qc].

[171] S. A. Hughes and R. D. Blandford, Astrophys. J. **585**, L101 (2003).

[172] A. Buonanno, L. E. Kidder and L. Lehner, Phys. Rev. D **77**, 026004 (2008).

[173] A. Buonanno, Y. Chen and T. Damour, Phys. Rev. D **74**, 104005 (2006).

[174] M. Campanelli, C. O. Lousto and Y. Zlochower, Phys. Rev. D **74**, 084023 (2006); M. Campanelli, C. O. Lousto, Y. Zlochower, B. Krishnan and D. Merritt, Phys. Rev. D **75**, 064030 (2007).

[175] D. Pollney *et al.*, Phys. Rev. D **76**, 124002 (2007).

[176] B. Bruegmann, J. A. Gonzalez, M. Hannam, S. Husa and U. Sperhake, arXiv:0707.0135 [gr-qc]..

[177] L. Rezzolla, E. N. Dorband, C. Reisswig, P. Diener, D. Pollney, E. Schnetter and B. Szilagyi, Astrophys. J. **708**, in press (2007) [arXiv:0708.3999 [gr-qc]].

[178] P. Marronetti, W. Tichy, B. Brugmann, J. Gonzalez and U. Sperhake, Phys. Rev. D **77**, 064010 (2008).

[179] L. Rezzolla, P. Diener, E. N. Dorband, D. Pollney, C. Reisswig, E. Schnetter and J. Seiler, Astrophys. J. **674**, L29 (2008).

[180] L. Boyle, M. Kesden and S. Nissanke, arXiv:0709.0299 [gr-qc].

[181] L. Boyle and M. Kesden, arXiv:0712.2819 [astro-ph].

[182] B. Barker and R. O'Connell, Phys. Rev. D **2**, 1428 (1970).

[183] F. Herrmann, I. Hinder, D. M. Shoemaker, P. Laguna and R. A. Matzner, Phys. Rev. D **76**, 084032 (2007).

[184] C. Hanna, M. Megevand, E. Ochsner and C. Palenzuela, arXiv:0801.4297 [gr-qc].

[185] A. Buonanno, Y. Pan, J. G. Baker, J. Centrella, B. J. Kelly, S. T. McWilliams and J. R. van Meter, Phys. Rev. D **76**, 104049 (2007).

[186] M. Jasiulek *et al.*, in preparation.

[187] E. Berti, V. Cardoso, J. A. Gonzalez, U. Sperhake, M. Hannam, S. Husa and B. Brueg-mann, Phys. Rev. D **76**, 064034 (2007).

[188] E. Berti, V. Cardoso, J. A. Gonzalez, U. Sperhake and B. Brugmann, arXiv:0711.1097 [gr-qc].

[189] W. Tichy and P. Marronetti, Phys. Rev. D **76**, 061502 (2007).

[190] T. Goodale, G. Allen, G. Lanfermann, J. Massó, T. Radke, E. Seidel and J. Shalf, in *Vector and Parallel Processing – VECPAR'2002, 5th International Conference, Lecture Notes in Computer Science* (Springer, Berlin, 2003).

[191] *Cactus Computational Toolkit home page,* `http://www.cactuscode.org/`.

[192] M. Alcubierre, B. Brügmann, T. Dramlitsch, J. A. Font, P. Papadopoulos, E. Seidel, N. Stergioulas and R. Takahashi, Phys. Rev. D **62**, 044034 (2000).

[193] M. Alcubierre, B. Brügmann, P. Diener, M. Koppitz, D. Pollney, E. Seidel and R. Takahashi, Phys. Rev. D **67**, 084023 (2003).

[194] M. Alcubierre, B. Brügmann, P. Diener, F. S. Guzmán, I. Hawke, S. Hawley, F. Her-rmann, M. Koppitz, D. Pollney, E. Seidel and J. Thornburg, Phys. Rev. D **72**, 044004 (2005).

[195] J. G. Baker, J. Centrella, D.-I. Choi, M. Koppitz and J. van Meter, Phys. Rev. D **73**, 104002 (2006).

[196] M. Campanelli, C. O. Lousto, P. Marronetti and Y. Zlochower, Phys. Rev. Lett. **96**, 111101 (2006).

[197] T. Nakamura, K. Oohara and Y. Kojima, Prog. Theor. Phys. Suppl. **90**, 1 (1987).

[198] M. Shibata and T. Nakamura, Phys. Rev. D **52**, 5428 (1995).

[199] T. W. Baumgarte and S. L. Shapiro, Phys. Rev. D **59**, 024007 (1999).

[200] J. W. York, in *Sources of gravitational radiation*, edited by L. L. Smarr (Cambridge University Press, Cambridge, UK, 1979).

[201] J. G. Baker, J. Centrella, D.-I. Choi, M. Koppitz and J. van Meter, Phys. Rev. Lett. **96**, 111102 (2006).

[202] J. van Meter, J. G. Baker, M. Koppitz and D.-I. Choi, arxiv:gr-qc/0605030.

[203] E. Schnetter, S. H. Hawley and I. Hawke, Class. Quant. Grav. **21**, 1465 (2004).

[204] *Mesh Refinement with Carpet*, `http://www.carpetcode.org/`.

[205] J. Thornburg, Phys. Rev. D **54**, 4899 (1996).

[206] J. Thornburg, Class. Quant. Grav. **21**, 743 (2004).

[207] S. Brandt and B. Brügmann, Phys. Rev. Lett. **78**, 3606 (1997).

[208] M. Ansorg, B. Brügmann and W. Tichy, Phys. Rev. D **70**, 064011 (2004).

[209] G. B. Cook, Phys. Rev. D **50**, 5025 (1994).

[210] H. P. Pfeiffer, S. A. Teukolsky and G. B. Cook, Phys. Rev. D **62**, 104018 (2000).

[211] S. A. Hughes, AIP Conf. Proc. **873**, 233 (2006).

[212] T. P. Sotiriou, PhD Thesis, arXiv:0710.4438 [gr-qc].

[213] S. M. Carroll, Living Rev. Rel. **4**, 1 (2001).

[214] E. Komatsu *et al.*, arXiv:0803.0547 [astro-ph].

[215] F. De Felice and C. J. S. Clarke, *Relativity on curved manifolds* (Cambridge University Press, Cambridge, 1990).

[216] J. Ehlers, P. Geren and R. K. Sachs, J. Math. Phys. **9**, 1344 (1968); C. A. Clarkson and R. K. Barret, Class. Quant. Grav. **16**, 3781 (1999); J. Goodman, Phys. Rev. D **52**, 1821 (1995); W. R. Stoeger, R. Maartens and G. F. R. Ellis, Astrophys. J. **443**, 1 (1995); U. S. Nilsson, J. Wainwright and W. C. Lim, Class. Quant. Grav. **18**, 5583 (2001); O. Lahav, *Observational Tests for the Cosmological Principle and World Models*, in *Structure Formation in the Universe* (Proceedings of the NATO Advanced Study Institute on Structure Formation in the Universe, Cambridge, UK, 26 July - 6 August 1999), eds. R. G. Crittenden, N. G. Turok, Kluwer Academic Publishers, 2001 (arXiv:astro-ph/0001061).

[217] S. Van Den Bergh, *The early history of dark matter*, Publ. Astron. Soc. Pac. **111**, 657 (1999) [arXiv: astro-ph/9904251].

[218] W. L. Freedman *et al.*, Astrophys. J. **553**, 47 (2001).

[219] B. P. Schmidt *et al.*, Astrophys. J. **507**, 46 (1998); A. G. Riess *et al.*, Astron. J. **116**, 1009 (1998); S. Perlmutter *et al.*,, Astrophys. J. **517**, 565 (1999); P. Astier *et al.*, Astron. Astrophys. **447**, 31 (2006); A. G. Riess *et al.*, Astrophys. J. **659**, 98 (2007); W. M. Wood-Vasey *et al.*, Astrophys. J. **666**, 694 (2007).

[220] J. L. Tonry *et al.*, Astrophys. J. **594**, 1 (2003).

[221] A. G. Riess *et al.*, Astrophys. J. **607**, 665 (2004).

[222] D. Zaritsky, R. Smith, C. Frenk and S. D. M. White, Astrophys. J. **405**, 464 (1993); D. Zaritsky, R. Smith, C. Frenk and S. D. M. White, Astrophys. J. **478**, 39 (1997); G. Wilson, N. Kaiser, G. A. Luppino and L. L. Cowie, Astrophys. J. **555**, 572 (2001); N. A. Bahcall, L. M. Lubin and V. Dorman, Astrophys. J. Lett. **447**, L81 (1995); C.-P. Ma, T. Small and W. Sargent, Astron. Soc. Pac. Conf. Ser. **151**, 89 (1998) [arXiv: astro-ph/9808034]; N. Kaiser *et al.*, arXiv: astro-ph/9809268; R. B. Tully and E. J. Shaya, *Antibiasing: high mass-to-light ratios in dense clusters*, in *Evolution of large scale structure : from recombination to Garching*, eds. A. J. Banday, R. K. Sheth, L. N. da Costa, 1999 [arXiv: astro-ph/9810298].

[223] J. Mohr, B. Mathiesen and G. Evrard, Astrophys. J. **517**, 627 (1999); L. Grego *et al.*, Astrophys. J. **552**, 2 (2001); S. W. Allen, R. W. Schmidt and A. C. Fabian, Mon. Not. Roy. Astron. Soc. **334**, L11 (2002).

[224] V. R. Eke, S. Cole and C. S. Frenk, Mon. Not. Roy. Astron. Soc. **282** 263 (1996); N. A. Bahcall, X. Fan and R. Cen, Astrophys. J. Lett. **485**, L53 (1997); N.A. Bahcall *et al.*, Astrophys. J. **585** 182 (2003)..

[225] A. Cabre *et al.*, Mon. Not. Roy. Astron. Soc. Lett. **372**, L23 (2006); P. Fosalba, E. Gaztanaga and F. J. Castander, Astrophys. J. Lett. **597** L89 (2003); N. Afshordi, Y. Loh and M. A. Strauss, *Cross-Correlation of the Cosmic Microwave Background with the 2MASS Galaxy Survey: Signatures of Dark Energy, Hot Gas, and Point Sources* , American Astronomical Society Meeting 203 [arXiv:astro-ph/0308260]; S. Boughn and R. Crittenden, Nature **427**, 45 (2004).

[226] J. A. Peacock *et al.*, Nature **410**, 169 (2001).

[227] L. Verde *et al.*, Mon. Not. Roy. Astron. Soc. **335**, 432 (2002).

[228] W. J. Percival *et al.*, Mon. Not. Roy. Astron. Soc. **381**, 1053 (2007); W. J. Percival *et al.*, Astrophys. J. **657**, 645 (2007);

[229] J. A. Willick, *Cosmic velocities 2000: a review*, in *Energy Densities in the Universe*, XXXVth Rencontres de Moriond [arXiv: astro-ph/0003232]; R. B. Tully, *The Cosmological Parameters H_0 and Ω_0*, in IAU Symp. 183, *Cosmological Parameters and Evolution of the Universe*, ed. K. Sato, Kluwer Academic Publishers [arXiv: astro-ph/9802026]; J. A. Willick *et al.*, Astrophys. J. Suppl. **109**, 333 (1997); J. A. Willick and M. A. Strauss, Astrophys. J. **507**, 64 (1998); E. Bertschinger, A. Dekel, Astrophys. J. Lett. **336**, L5 (1989); Y. Sigad *et al.*, Astrophys. J. **495**, 516 (1998); S. Zaroubi *et al.*, Mon. Not. Roy. Astron. Soc. **336**, 1234 (2002); M. Rowan-Robinson *et al.*, Mon. Not. Roy. Astron. Soc. **314**, 375 (2000)

[230] S. Weinberg, Rev. Mod. Phys. **61**, 1 (1989).

[231] S. Bludman, arXiv: astro-ph/0312450; S. Bludman, Phys. Rev. D **69**, 122002 (2004).

[232] R. R. Caldwell, Phys. Lett. B **545**, 23 (2002).

[233] R. R. Caldwell, M. Kamionkowski and N. N. Weinberg, Phys. Rev. Lett. **91**, 071301 (2003).

[234] S. Weinberg, *The Cosmological Constant Problems*, in *Sources and Detection of Dark Matter and Dark Energy in the Universe* (4th International Symposium, 23-25 February 2000, Marina del Rey, California, USA), Springer-Verlag, 2001 (arXiv: astro-ph/0005265).

[235] H. A. Buchdahl, Mon. Not. Roy. Ast. Soc. **150**, 1 (1970); M. Ferraris, M. Francaviglia and C. Reina, Gen. Rel. Grav. **14**, 243 (1982).

[236] R. M. Wald, *General Relativity*, (University of Chicago Press, Chicago, 1984).

[237] D. N. Vollick, Phys. Rev. D **68**, 063510 (2003).

[238] T. P. Sotiriou and S. Liberati, Ann. Phys. **322**, 935 (2007); T. P. Sotiriou and S. Liberati, J. Phys. Conf. Ser. **68**, 012022 (2007).

[239] T. P. Sotiriou, Class. Quant. Grav. **23** (2006) 5117

[240] T. P. Sotiriou, arXiv:gr-qc/0611158, to appear in *Proceedings of the Eleventh Marcel Grossmann Meeting on General Relativity*, edited by H. Kleinert, R.T. Jantzen and R. Ruffini, World Scientific, Singapore, 2008.

[241] T. Koivisto Class. Quant. Grav. **23**, 4289 (2006).

[242] D. Barraco, V. H. Hamity and H. Vucetich, Gen. Rel. Grav. **34**, 533 (2002); G. Allemandi, A. Borowiec and M. Francaviglia, Phys. Rev. D **70**, 043524 (2004); X. Meng and P. Wang, Class. Quant. Grav. **21**, 951 (2004); X. H. Meng and P. Wang, Phys. Lett. B **584**, 1 (2004); X. H. Meng and P. Wang, Class. Quant. Grav. **22**, 23 (2005); G. Allemandi *et al.*, Phys. Rev. D **72**, 063505 (2005); T. P. Sotiriou, Phys. Rev. D **73**, 063515 (2006); M. Amarzguioui *et al.*, Astron. Astrophys. **454**, 707 (2006); T. Koivisto and H. Kurki-Suonio, Class. Quant. Grav. **23**, 2355 (2006); T. Koivisto, Phys. Rev. D **73**, 083517 (2006); B. Li, K. C. Chan and M. C. Chu, Phys. Rev. D **76**, 024002 (2007).

[243] G. Allemandi *et al.*, Gen. Rel. Grav. **37**, 1891 (2005); J. A. R. Cembranos, Phys. Rev. D **73**, 064029 (2006); T. P. Sotiriou, Gen. Rel. Grav. **38**, 1407 (2006); T. P. Sotiriou, Phys. Lett. B **645**, 389 (2007); G. Allemandi and M. L. Ruggiero, Gen. Rel. Grav. **39**, 1381 (2007).

[244] G. J. Olmo, Phys. Rev. Lett. **95**, 261102 (2005).

[245] S. L. Shapiro and S. A. Teukolsky, *Black holes, white dwarfs, and neutron stars: The physics of compact objects* (Wiley, New York, 1983).

[246] K. Kainulainen, J. Piilonen, V. Reijonen and D. Sunhede, Phys. Rev. D **76**, 024020 (2007).

[247] M. Ferraris, M. Francaviglia and I. Volovich, arXiv: gr-qc/9303007.

[248] K. Kainulainen, V. Reijonen and D. Sunhede, Phys. Rev. D **76**, 043503 (2007).

[249] D. E. Barraco and V. H. Hamity, Phys. Rev. D **62**, 044027 (2000).

[250] P. Haensel and A. Y. Potekhin, Astron. Astroph. **428**, 191 (2004).

[251] G. J. Olmo, Phys. Rev. Lett. **98**, 061101 (2007).

[252] T. P. Sotiriou, Class. Quant. Grav. **23** 1253 (2006).

[253] Wolfram Research, Inc., Mathematica, Version 5.2, Champaign, IL (2005).

[254] E. E. Flanagan, Phys. Rev. Lett. **92**, 071101 (2004); E. E. Flanagan, Class. Quant. Grav. **21**, 3817 (2004).

[255] G. J. Olmo Phys. Rev. D **75** 023511 (2007).

[256] E. Poisson, *A Relativist's Toolkit: The Mathematics of Black-Hole Mechanics* (Cambridge University Press, Cambridge, 2004).

[257] A. Iglesias, N. Kaloper, A. Padilla and M. Park, Phys. Rev. D **76**, 104001 (2007).

[258] D. N. Vollick Class. Quant. Grav. **21**, 3813 (2004); D. N. Vollick Phys. Rev. D **71**, 044020 (2005).

[259] B. Li, J. D. Barrow and D. F. Mota, Phys. Rev. D **76**, 104047 (2007).

[260] H. Hellwig Phys. Rev. D **166**, 1 (1968); M. Desaintfuscien and C. Audoin Phys. Rev. A **13**, 6 (1976).

[261] R. Côté, M. J. Jamieson, Z-C. Yan, N. Geum, G.-H. Jeung and A. Dalgarno, Phys. Rev. Lett. **84**, 2806 (2000).

[262] T. J. M. Boyd and J. J. Sanderson, *The Physics of Plasmas* (Cambridge University Press, Cambridge, 2003).

[263] E. M. Lifshitz and L. P. Pitaevskii, *Physical Kinetics* (Butterworth-Heinemann, Oxford, 1984).

[264] E. W. Kolb and M. S. Turner *The Early universe* (Addison-Wesley, Redwood City, 1990).

[265] L. D. Landau, E. M. Lifshitz and L. P. Pitaevskii, *Statistical Physics, Part 1* (Butterworth-Heinemann, Oxford, 1984).

[266] A. H. Guth, *The inflationary universe*, (Perseus, Reading, MA, 1997).

[267] V. Faraoni, *Cosmology in Scalar-Tensor Gravity*, (Kluwer Academic Publishers, The Netherlands, 2004).

[268] I. Antoniadis, E. Gava and K. S. Narain, Phys. Lett. B **283**, 209 (1992); A. A. Tseytlin, Nucl. Phys. B **467**, 383 (1996).

[269] I. Antoniadis, J. Rizos and K. Tamvakis, Nucl. Phys. B **415**,497 (1994).

[270] I. Antoniadis, E. Gava and K. S. Narain, Nucl. Phys. B **383**, 93 (1992); T. Damour and A. M. Polyakov, Nucl. Phys. B **423**, 532 (1994)

[271] S. Nojiri, S. D. Odintsov, M. Sasaki, Phys. Rev. D **71**, 123509 (2005).

[272] S. Nojiri, S. D. Odintsov and M. Sami, Phys. Rev. D **74**, 046004 (2006); G. Cognola, E. Elizalde, S. Nojiri, S. D. Odintsov and S. Zerbini, arXiv:hep-th/0611198; B. M. N. Carter and I. P. Neupane, J. Cosm. Astropart. Phys, **06**, 004 (2006); I. P. Neupane, Class. Quant. Grav. **23**, 7493 (2006); S. Tsujikawa, Annalen Phys. **15**, 302 (2006); B. M. N. Carter and I. P. Neupane, Phys. Lett. B **638**, 94 (2006); I. P. Neupane, hep-th/0605265.

[273] T. Koivisto and D. F. Mota, Phys. Rev. D **75**, 023518 (2007); T. Koivisto and D. F. Mota, Phys. Lett. B **644**, 104 (2007).

[274] G. Cognola, E. Elizalde, S. Nojiri, S. D. Odintsov and S. Zerbini, Phys. Rev. D **73**, 084007 (2006).

[275] C. M. Will, *Theory and experiment in gravitational physics*, (Cambridge University Press, Cambridge, 1981).

[276] R. V. Wagoner, Phys. Rev. D **1**, 3209 (1970).

[277] P. J. Steinhardt and C. M. Will, Phys. Rev. D **52**, 628 (1995).

[278] P. Jetzer and M. Sereno, Phys. Rev. D **73**, 044015 (2006).

[279] G. Esposito-Farese, AIP Conf. Proc. **736**, 35 (2004).

[280] D. Psaltis *et al.*, Phys. Rev. Lett. **100**, 091101 (2008).

[281] A. D. Dolgov and M. Kawasaki, Phys. Lett. B **573**, 1 (2003).

[282] E. Berti, A. Buonanno and C. M. Will, Phys. Rev. D **71**, 084025 (2005); C. M. Will and N. Yunes, Class. Quant. Grav. **21**, 4367 (2004).

[283] D. Wands, Class. Quant. Grav. **11**, 269 (1994).

[284] C. M. Will and H. W. Zaglauer, Astrophys. J. **346**, 366 (1989).